Faculté des bioingénieurs
Institut de la Matière Condensée et Nanosciences

Modulation of extra-framework oxygen species in C12A7 catalyst for oxidation reactions

by

Isaac Meza Trujillo

Supervisor: Prof. Eric Gaigneaux

Thèse présentée en vue de l'obtention
du grade de docteur en sciences agronomiques
et ingénierie biologique

June 2023

Examining board:

Prof. Eric Gaigneaux (UCLouvain)	Supervisor
Prof. Yann Garcia (UCLouvain)	Chairperson
Prof. Damien Debecker (UCLouvain)	Secretary
Prof. Bénédicte Vertruyen (ULiege, Belgium)	
Prof. Renaud Cousin (ULCO Univ-littoral, France)	
Prof. Piotr Pietrzyk (Jagiellonian University, Poland)	

Acknowledgements/Remerciements/Agradecimientos

…ceci n'est pas qu'une thèse, car elle représente non seulement l'aboutissement de plusieurs années de recherche mais aussi le résultat de plusieurs obstacles surmontés, qui ont considérablement stimulé mon développement scientifique et personnel.

Un jour, j'ai lu dans un livre que la compagnie sur le chemin est plus importante que la destination, et je suis tout à fait d'accord. Je tiens donc à remercier tous ceux qui m'ont aidé au cours de ce parcours particulièrement vertigineux de doctorat.

Je tiens à exprimer mes sincères remerciements à mon promoteur de thèse, le Professeur Eric Gaigneaux, pour la confiance qu'il m'a accordée et pour m'avoir accueillie dans son laboratoire afin de réaliser ma thèse de doctorat. Je suis sûr que la personne qui est arrivée au laboratoire fin 2016 n'est plus la même, et cette évolution personnelle et professionnelle, c'est en partie grâce à toi. Ce parcours a été parsemé d'épreuves, mais tu as contribué à remonter le moral à plusieurs reprises. Merci, Eric.

I would like to express all my appreciation to the members of my thesis examining board, Professors Bénédicte Vertruyen, Renaud Cousin, Piotr Pietrzyk, and Damien Debecker. Thank you for agreeing to be part of the jury, for providing constructive criticism on my work, and for offering valuable advice to help me enhance it. I also express my thankfulness to Professor Yann Garcia for his role as President of the jury. I would like to extend my gratitude to Professors Michel Devillers and Juray de Wilde, who were part of my doctoral committee.

Additionally, I would like to thank Prof. Piotr Pietrzyk and Prof. Zbigniew Sojka for welcoming me to their laboratory at the Faculty of Chemistry of the Jagiellonian University (Krakow, Poland), where the Electron Paramagnetic Resonance (EPR) and Raman analyses were performed. Piotr, I extend my thanks for our fruitful exchanges, as well as for your invaluable assistance and kindness towards me and my family during my various stays in Krakow. I am also thankful to Aneta Krasowska and Dr. Kamila Sobanska for their precious technical support throughout the analyses. Furthermore, I would like to express my appreciation to Justyna for the enjoyable and enlightening discussions we had over coffee or tea, for being my tour guide, and for introducing me to the wonderful places in Krakow.

Je tiens à remercier Ir. Arnaud Mary et Ir. Pierre Decock pour leur travail acharné et leur contribution scientifique à cette recherche lors de leurs mémoires de maîtrise respectifs. Merci pour les bons moments passés ensemble et pour avoir toujours conservé un état d'esprit positif, ainsi que pour votre persévérance.

Acknowledgements/Remerciements/Agradecimientos

Este logro no podría haber sido posible sin la invaluable ayuda, el apoyo incondicional y el amor constante que mi amada familia me ha brindado. Mami Denne, tú has sido y sigues siendo mi roca, mi ejemplo de superación y perseverancia, una fuente inagotable de amor y mi refugio en momentos de desahogo. Dios te pague por siempre haberme reconfortado con palabras llenas de amor y sosiego cuando mi camino se volvía cuesta arriba, por recordarme que siempre debemos avanzar sin retroceder ni siquiera para tomar impulso. Mami Lauri (mi guambrita) y mi siempre recordado Papi Jorge, ustedes han sido y serán por siempre la piedra angular de nuestra familia. Su tesón, bondad, amor incondicional, calidez humana y humildad son virtudes que han dejado huella en mí y que me han impulsado perpetuamente a seguir luchando y conquistar nuevos horizontes. Pai, mis papis amados, gracias por siempre haber creído en mí y darme fuerza en mis momentos más difíciles. Mi ñaño Joe, te agradezco de todo corazón por nunca dudar de mis capacidades, incluso cuando yo te decía que no lo lograría. Gracias por siempre verme con admiración, no tienes idea de lo importante que eres para mí.

Mi Nathalie, mi amada esposa, este prolongado capítulo no habría encontrado su fin sin tu amor, guía, apoyo incondicional y sesiones personalizadas de coaching. Eres un ejemplo para mí en innumerables aspectos, te admiro y valoro infinitamente. Gracias por demostrarme día a día que en este camino llamado vida lo recorremos juntos codo a codo y que, si uno cae, el otro siempre está ahí para levantarlo. Gracias por nunca dejar de creer en mí y en mis capacidades, por motivarme siempre a continuar y luchar a pesar de las adversidades. Quiero expresar también mi profunda gratitud a mi enano, mi Emilio, por permitirme disfrutar de tu amor, tus travesuras y tus enseñanzas. Eres mi razón de lucha, mi fuerza motriz y mi pedacito de cielo. Contigo me siento un ser humano mejor, porque tú me enseñas a ver a través de mis debilidades. Nathie y Emilio, les agradezco por todos los sacrificios que han hecho durante este tiempo y por nunca permitirme rendirme. Además, quiero agradecer al resto de mi familia por su apoyo y sus palabras de ánimo: Papi David, Ñaño Rober, Ñaña Jenny y Rita, Ñaños Miguel, Victor y Lucho. También quiero agradecer a mi amigo, mentor y suegro, Ernesto, quien ha sido un ejemplo para mí y un impulso hacia nuevos horizontes, pai compadre. Asimismo, quiero agradecer a los miembros de mi otra familia: Susy, Ernesto (Pepi) y Anita, por los ánimos y palabras de afecto. Un agradecimiento especial a Ahmed, compañero de batallas y sufrimientos, gracias por esos grandes y valiosos momentos que hemos compartido juntos y por los que vendrán.

Le doctorat est une expérience complexe et extrêmement enrichissante dont les apprentissages dépassent les frontières du domaine scientifique pour toucher aux relations humaines et aux échanges culturels. Ainsi, dans ce

parcours bouleversé, passionnant et rempli d'épreuves, la vie a été très généreuse envers moi, en me permettant de croiser le chemin de personnes spéciales et précieuses. Dans un pays étranger que je considère maintenant comme le mien, loin de la terre qui m'a vu naître, j'ai eu la grande opportunité de me faire de nouveaux et grands amis qui ont joué un rôle fondamental dans la réalisation de cette réussite. Chacun d'entre vous, avec votre manière unique, a touché mon cœur et m'a donné l'élan nécessaire pour continuer à me battre et ne pas me laisser vaincre. C'est pourquoi je tiens à remercier Maximilien (Max), Solène, Quentin, Eliana, Gabriel, Charlotte, Matthew (merci pour ta touche culinaire), Chiara, François D., Ludivine (merci pour ta touche artistique), Carlitos, Graciela, Ward, Anilú, Valentin, Gaby, Danilo, Leticia, Maximiliano, Yoli, Celso, Mathilde, et Alex.

Je tiens à remercier tous mes collègues du laboratoire de catalyse hétérogène avec lesquels j'ai partagé de bons moments, ainsi que ceux avec qui j'ai eu la possibilité d'échanger sur des sujets scientifiques et de profiter de moments de détente pendant ces années de thèse à l'UCLouvain : Josefine, William, Anna, Ramesh, Palraj, Valentin, Arnaud, Paulina, Aleš, Vijay, Weiyi, Itika, Valeria, Sebastian, Margot, Dennis, Hippolyte, Fanny, Giovanni, Ali, Marty, Yingrui, Feilong et Diego.

Je voudrais également adresser mes remerciements au personnel logistique et technique du laboratoire pour leur aide et leur soutien dans toutes les tâches nécessaires au bon déroulement de cette recherche : Françoise Somers, Nathalie Blangenois, Audrey Dejean, François Devred, Pascal Valvassori, Pierre Eloy et Jean-Charles Godefroid.

Je tiens également à remercier les trois institutions, le Conseil d'Action Internationale, l'Académie de Recherche et d'Enseignement Supérieur (ARES) ainsi que la Fédération Wallonie-Bruxelles (FWB), de m'avoir accordé les bourses qui m'ont permis de mener à bien cette recherche scientifique et mon court séjour en Pologne (à Cracovie). En particulier, je souhaite exprimer ma gratitude envers Gabriela Bidegain pour ton aide précieuse et ton soutien (muchas gracias Gaby, sos un ángel).

Table of Contents

GENERAL INTRODUCTION

1 Research context

Since the modern usage of petroleum around the end of the 19th century, hydrocarbons have neverendingly gained importance in our society, not only because they power our industry and transport but also because they are the source of countless commodities used to sustain our current lifestyle. Paradoxically, they are also perceived as a threat to the planet and our health, considering that they largely contribute to anthropogenic global warming. In this regard, oxidation catalysis plays a fundamental role in a more sustainable chemical industry, either by transforming hydrocarbons into more profitable products or by their abatement towards less harmful by-products as a tool in emission control applications.[1] Nowadays, nearly 90% of all chemical products are fabricated by a catalytic process, among which 60% comes from the oxidative one.[1,2] Moreover, the most cost-effective and less-energetic way to control pollution emissions leverages catalytic oxidation technologies.[2]

In oxidation catalysis, related to the manufacture of high-value products by functionalizing hydrocarbons, the control of process selectivity is paramount in reaching high yields. Yet, achieving high selectivity in an oxidation reaction is particularly challenging. The latter is related to several factors. For instance, the desired product is often intermediate in a complex network of competing parallel and consecutive oxidation reactions. Besides, considering that C-H bonds in the initial hydrocarbons are usually more robust than those in the intermediate products, the oxidation process favors the ultimate by-products (carbon oxides and water), which are thermodynamically the most stable. Therefore, the catalyst must have the capability of controlling the relative rates between the different reactions, and favoring the pathway toward the desired product while avoiding its overoxidation.[3–5] In this regard, the nature of the active species available at the catalyst surface plays a pivotal role on the selectivity, reaction mechanism and kinetics.[6]

In most cases, catalysts involved in a heterogeneous gas-phase oxidation process are based on bulk or supported single/mixed oxides of transition metals. The latter preference is connected to their unique chemical coordination, tunable reducibility, stability under reaction conditions, and ability to activate molecular oxygen.[5–7] The surface of

a metal oxide can simultaneously present several oxygen species of different nature and reactivity, which can be regarded as the active sites of the catalyst. Surface oxygen species can be categorized as being either “electrophilic” or “nucleophilic” in character, being distinguished by their different electron affinity and correspondingly M-O bond strength.[3–5,7] Electrophilic oxygen species (peroxide/O_2^{2-}, superoxide/O_2^-, and oxygen radical/O^-) are described as adsorbed moieties, whereas nucleophilic ones (O^{2-}) correspond to lattice oxygens. The way these oxygen species are bonded to the metal center(s) depends on their nature and configuration (Figure i.1).

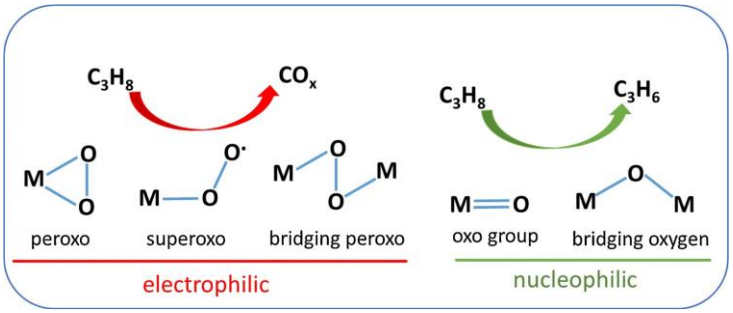

Figure i.1. Schematic representation of the different oxygen species available at the surface of a metal oxide-based catalyst and their interactions with light alkane in the gas phase depending on their nucleophilic or electrophilic nature, taken from[6].

Furthermore, the mentioned oxygen species are known to interact with the hydrocarbon molecule in different ways during the reaction process (Figure i.1). Electrophilic oxygen species, specifically oxygen radicals (O_2^- and O^-), are known for their high reactivity but limited selectivity. When these species interact with hydrocarbon molecules through hydrogen abstraction, alkyl radicals are formed. However, due to the inherent instability of these radicals, chain reactions are initiated, leading to the overoxidation of the hydrocarbon and resulting in the production of CO_x and H_2O as by-products. In certain cases, electrophilic oxygen species like peroxide anions can act as ligands that exhibit selectivity in promoting the formation of oxygenated products, by interacting with hydrocarbons like olefins or aromatics.[3] These electrophilic oxygen species target the region of the substrate with the highest electron density, the π bond, forming peroxo- and superoxo-complexes. These complexes then undergo further transformations to yield the desired oxygenated product. It is worth

noting that in certain scenarios, the higher reactivity of the product compared to the substrate can significantly influence the selectivity of the oxidation process.[3,4] Alternatively, the nucleophilic oxygen species (O^{2-}) are described as selective but much less active. These oxygen species, often regarded as nucleophilic reagents, interact with the substrate without affecting the C-C bond, abstracting a proton (H^+), and producing the desired partially oxidized product and water.[4,5] Hence, the required application (total or partial oxidation) determines the oxygen species needed and that the corresponding catalyst should contain. In general, heteroatom doping, thermal and chemical treatments of the bulk metal oxides, or the utilization of suitable support materials have been employed as strategies to modify the reactivity and selectivity of these materials.[6]

In this context, this thesis pretends to evaluate the possibility of modulating the activity and selectivity of an oxidation process by controlling the population distribution of extra-framework oxygen species of a mixed oxide known as Mayenite ($12CaO{\cdot}7Al_2O_3$). Interestingly, this peculiar material, based on earth-abundant raw components (calcium and aluminum), can host both nucleophilic and electrophilic oxygen species inside its structure.[8–14] Therefore, we argue that, depending on the nature of the predominant oxygen species in the population distribution, we may have the potential to favor total or partial oxidation reactions.

2 Mayenite: general aspects

2.1 Origins and classification

In 1915, Rankin *et al.*[15] were the first to report on the different phases of the $CaO\text{-}Al_2O_3$ binary system. They proposed a $5CaO{\cdot}3Al_2O_3$ stoichiometry for the calcium aluminate compound at the boundaries between $CaO{\cdot}Al_2O_3$ (monocalcium aluminate, $CaAl_2O_4$, CA) and $3CaO{\cdot}Al_2O_3$ (tricalcium aluminate, $Ca_3Al_2O_6$, C3A) phases (Figure i.2) —where C stands for CaO and A for Al_2O_3 according to the cement chemistry notation.[16] However, less than two decades after in 1937, the above-proposed stoichiometry was verified and corrected, corresponding to $12CaO{\cdot}7Al_2O_3$ or $Ca_{12}Al_{14}O_{33}$, which we all presently recognize.[17] It is, in fact, from these early reports in the concrete research field that the compound $12CaO{\cdot}7Al_2O_3$ acquired its most

frequently used acronym, C12A7. Eventually, Nurse *et al.*[18] determined that the C12A7 phase could not exist in a moisture-free atmosphere over 1050 °C (see inset Figure i.2), thus establishing the instability of this phase under anhydrous conditions. While the pentacalcium trialuminate (C5A3) compound possesses a close stoichiometry to C12A7, it is considered as a metastable phase either under dry or wet conditions (Figure i.2), and is as an intermediate phase in the formation-decomposition processes of $12CaO{\cdot}7Al_2O_3$ by solid-state reactions under specific experimental conditions.[16,19,20] Nowadays, C12A7 and C5A3 can be easily distinguished if they are simultaneously present in a material. Each calcium aluminate possesses a different crystal structure that can be identified by various characterization techniques, such as X-ray Diffraction (XRD) or Raman spectroscopy.[19,20]

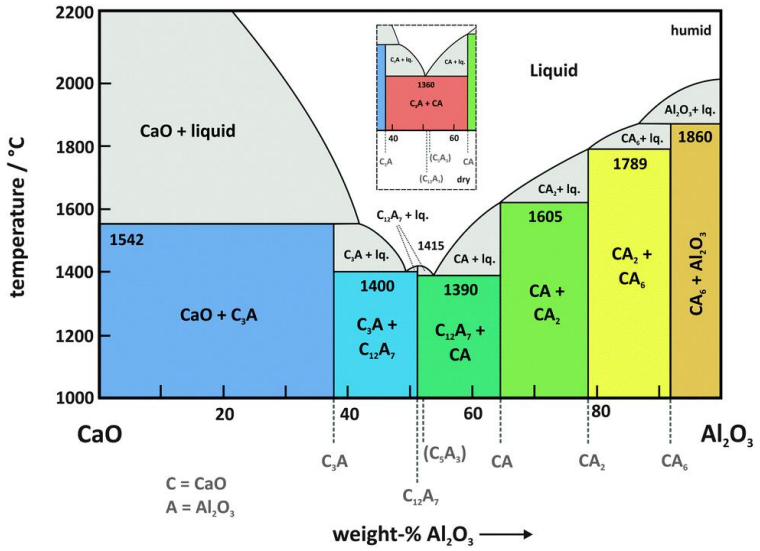

Figure i.2. Phase diagram of the binary system $CaO\text{-}Al_2O_3$ under humid conditions (inset under dry conditions) reproduced from [20]. Phases within parenthesis are considered as metastable. lq. is an abbreviation for liquid.

$Ca_{12}Al_{14}O_{33}$ is a mineral that rarely occurs naturally, but when it does, it often appears as scattered micro-sized crystals in volcanic rocks. It was in 1964 that Hentschel first discovered a mineral holotype presumably presenting the chemical structure of $12CaO{\cdot}7Al_2O_3$ in the locality of Eifel near Mayen (Germany), and thus called it mayenite.

Since then, this term has been widely employed in diverse research fields (materials science, catalysis, mineralogy, etc.).

Recently, the C12A7 mineral found in Eifel has been re-investigated and renamed as chlormayenite[21]—due to the presence of Cl^- rather than O^{2-} as extra-framework species (*vide infra*). Besides, different kinds of mayenite-type isostructural minerals bearing other elements (*e.g.*, Fe, Si, etc.) rather than only Ca and Al have also been discovered from terrestrial or meteoritic environments.[21,22] Galuskin *et al.*[22] have proposed the consolidation of these distinct minerals into a mayenite supergroup—containing two main groups: mayenite (oxides) and wadalite (silicates)—which can be represented by a simplified general formula $X_{12}T_{14}O_{32}[W_6]$, where each site is occupied by distinct elements as follows. The *X* site (octahedral) can be filled with divalent cations, generally Ca^{2+} (less frequent Sr^{2+}). The tetrahedral *T* unit, which represents the two tetrahedral sites *T1* and *T2*, can be occupied by tri- or tetravalent cations (Al^{3+}, Mg^{3+}, Fe^{3+}, Ti^{4+}, and Si^{4+}), irrespectively of the site. The *W* site can contain one or more monovalent anions ($X^- = Cl^-$, F^-, and OH^-), which are encapsulated as extra-framework ions within the mayenite structure (*see* Figure i.3). For instance, in the case of the mayenite group, *e.g.*, $Ca_{12}Al_{14}O_{32}[\boxdot_4X_2]$, the *W* site can be filled with a maximum of two monovalent anions, where $\boxdot$ represents the unoccupied *W* sites from a total of six. Alternatively, concerning the wadalite group, *e.g.*, $Ca_{12}Al_{10}Si_4O_{32}[X_6]$, the *W* site can host a more significant number of up to six monovalent anions.

Currently, the mayenite mineral containing oxygen anions in the *W* site has not yet been identified. Consequently, the term “mayenite” has been reserved for the isostructural synthetic derivative, $Ca_{12}Al_{14}O_{32}[\boxdot_5O]$, also denoted as $Ca_{12}Al_{14}O_{33}$, as will be addressed in the following section.

In the upcoming sections, the name mayenite, the abbreviation C12A7, and the chemical formulas $12CaO{\cdot}7Al_2O_3$ or $Ca_{12}Al_{14}O_{33}$ will be interchangeably employed throughout the document.

2.2 C12A7: crystal structure and properties

Back in 1936, Büssem *et al*.[23] were the first to report on the crystal structure of mayenite. Yet at that time, the chemical composition was not yet well established, as discussed in the previous section. Over the decades, the C12A7 crystal structure has been re-examined and refined by several consecutive studies.[24,25] Among them, one proposed crystal structure by Bartl *et al*.[15] is nowadays well accepted in the scientific community and often employed as a starting point for more dedicated studies (*e.g.*, structural models refinements by neutron and synchrotron XRD analyses)[26,27] or even as a reference pattern in crystallographic databases.[28,29] Hence, C12A7 crystal presents a body-centered cubic symmetry (Figure i.3) belonging to the space group I $\bar{4}$3d (n° 220), with Z (number of formula units per unit cell) = 2, and a lattice parameter a = 1.199 nm.[15]

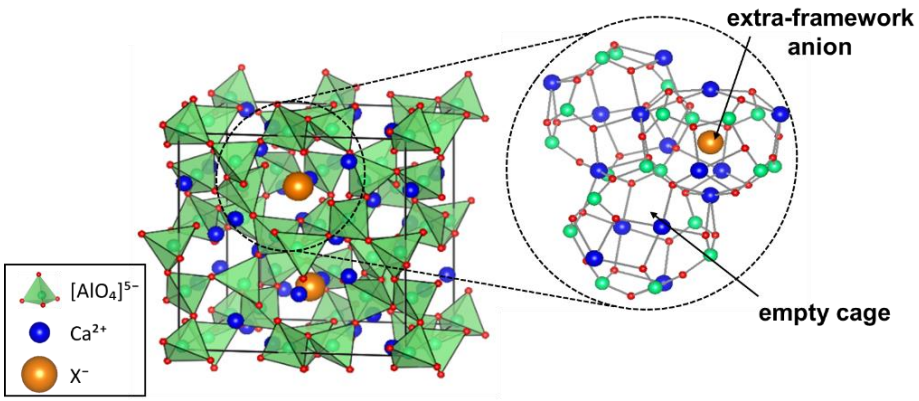

Figure i.3. C12A7 crystal structure. Left-side: C12A7 unit cell composed of interconnected $[AlO_4]^{5-}$ tetrahedra and intercalated Ca^{2+} ions (octahedrally coordinated). Right-side: expanded representation of three adjacent cages; two empty and one occupied by an anionic extra-framework species.

In contrast to the mineralogical notation of C12A7, in most of the reports referring to synthetic mayenite, its unit cell—composed of two $Ca_{12}Al_{14}O_{33}$ formula units—is generally represented as $[Ca_{24}Al_{28}O_{64}]^{4+}:4X^-$ to denote its capacity to clathrate anionic species inside its structure.[8,9,24] The left-side component embodies the three-dimensional positively charged framework, tailored by $[AlO_4]^{5-}$ tetrahedra partially interconnected by corner-sharing and some others via Ca bridges, where Ca^{2+} is octahedrally coordinated (Figure i.3).

This atypical structural conformation allows the creation of twelve cages (aforementioned as *W* sites) per unit cell (or six per formula unit). These cages are interconnected via hollow hexagonal “windows”—composed of a closed chain of Ca-O-Al-O-Al-O atoms—presenting an opening diameter of *ca.* 0.4 nm. The formal charge per cage is +1/3 giving rise to an absolute +4 charge for the entire framework per unit cell. The right-side component ($4X^-$) represents the maximum number of monovalent extra-framework anions that can be hosted inside the cavities to neutralize the total charge and stabilize the framework.

In the stoichiometric case,[8,9] the C12A7 framework is represented as $[Ca_{24}Al_{28}O_{64}]^{4+}\cdot 2O^{2-}$ (also denoted as C12A7:O^{2-}), where two O^{2-} extra-framework counter-anions are found per until cell, which are often referred to as "free" oxygen ions. These oxygen ions are stabilized inside the cages and loosely bound by electrostatic interactions between two Ca^{2+} ions. Hence, these peculiarities of C12A7 material provide it with several unique properties as will be addressed below.

One of the first assessments of C12A7 properties was its high oxide ionic conductivity. Lacerda *et al.*[30,31] discovered that C12A7 presented a comparable oxide ionic conductivity to yttria-stabilized zirconia (YSZ), being only one order of magnitude inferior to the latter. They understood that this high conductivity of C12A7 was associated with the mobility of the “free” oxygen species in its bulk in a wide range of temperatures (~500-1200 °C). Yet, they found that this property could be affected and significantly reduced when OH^- ions were incorporated into the framework by annealing the material in a humid atmosphere. The latter observation is related to one of the most remarkable features of mayenite, its anionic exchange[8,9,24,32] capacity. It has been demonstrated that by controlling the preparation or post-activation conditions (*i.e.*, atmosphere composition, heat-treatment temperature, etc.)[9,20,32,33], C12A7 can incorporate a broad assortment of foreign anions by totally or partially replacing its native counter-anions (O^{2-}) via an anionic exchange mechanism. By doing so, C12A7 has become a versatile platform functional material where several reactive oxygen species (O_2^-,[8–14] O^-,[9–11,13,14] O_2^{2-},[13,34] OH^-,[24,30,35,36]); mono-, di-, and tri-valent ions (F^-,[24] Cl^-,[20,24] H^-,[32,37] C_2^{2-},[38–40] S^{2-},[20] N^{3-},[20]); small molecules (CN^-, NO_2^-, NH_2^-, hydrazine)[20]; and even electrons (e^-)[32,33] can be accommodated in its nanocavities. The latter one has given rise to the

first stable inorganic electride, $[Ca_{24}Al_{28}O_{64}]^{4+}:4e^-$, exhibiting good electrical conductivity (~100 $S \cdot cm^{-1}$) and low work function (2.4 eV). This C12A7 electride derivative is currently a hot-topic subject of numerous studies; however, this falls apart from the scope of the present thesis. Alternatively, the reader is referred to the following references.[38,41,42] Last but not least, in contrast to anionic substitutions into C12A7, the Ca and/or Al replacement by cationic doping have shown to influence the structural and electronic features of C12A7.[43–47]

As can be seen, these functional properties displayed by C12A7 have encouraged the scientific community to look for potential applications. For instance, in materials science, C12A7 has been explored in application for fuel cells, sensors, hydrogen storage, electronic circuits, electron emitter, etc.[38,46,48–50] Alternatively, in catalysis, mayenite has been broadly studied as bulk catalyst[9,51–60] or active support[41,42,61–68] in several catalytic systems (*e.g.,* oxidation reactions, tar steam reforming, N_2O reduction, ammonia synthesis, CO_2 hydrogeneration, etc.). As in this work, the C12A7 catalytic behavior in oxidation reactions will be addressed (*see section 5.1, p. 36*).

3 Modulation and control over the extra-framework oxygen species entrapped inside C12A7 structure

As mentioned above, C12A7 can substitute its native extra-framework (O^{2-}) oxide ions with several oxygen species (O_2^-, O^-, and O_2^{2-}) of distinct natures. In this regard, it can be considered that C12A7 can display an assorted extra-framework population in which one or more of the aforementioned oxygen species can be simultaneously found. Therefore, to be capable of fine-tuning this extra-framework population distribution is of essential importance to understand under which specific conditions each of these oxygen species are formed.

3.1 Formation, stability, mobility, and regeneration of reactive oxygen species (ROS) in C12A7

In 1986, Hosono *et al.* discovered for the first time the existence of superoxide ions in C12A7. They confirmed, employing Electron Paramagnetic Resonance (EPR) spectroscopy, that O_2^- ions can be

formed within the C12A7 structure in concentrations up to *ca.* 4 x 10^{18} spin·g^{-1}.[8] Later, the same group unveiled the occurrence of O^- and O_2^{2-} anions by combining EPR, Raman, and thermogravimetric (TGA-MS) analyses.[9,10,13] This mayenite material containing ROS is often described as non-stoichiometric C12A7, $Ca_{12}Al_{14}O_{33+x}$., where an excess of oxygen over the stoichiometric composition can be found.[13] Either in stoichiometric or non-stoichiometric forms, the theoretical maximum concentration of extra-framework species that can be accommodated inside C12A7 cages corresponds to *ca.* 2.3 x 10^{21} spin·cm^{-3},[1] which is dictated by the overall charge (4+) of its framework.[10]

Regarding the stability of the oxygen species inside C12A7. Hosono and coworkers determined by EPR and Raman analyses that once these oxygen anions are clathrated inside C12A7, they remain stable for at least several months under ambient conditions.[10] Hence, they established that the inner cage provides an adsorption site for these oxygen species to stabilize and protect them from the ambient atmosphere. Consequently, their life span is prolonged, in contrast, to the typically very short lifetime of the same oxygen species found at the surface of other types of metal oxides under specific conditions (*e.g.*, MgO).[69]

Moreover, Hayashi *et al*.[9,10,14] proposed that the oxygen radicals formation can be described by Eq. (i.1). They suggested that more or less equivalent amounts of O_2^- and O^- can be formed in C12A7 when this material, initially containing O^{2-} ions, is calcined in a controlled atmosphere (*e.g.*, dry oxygen).

$$O^{2-}_{(cage)} + O_{2\,(atmosphere)} \rightleftharpoons O^{-}_{2\,(cage)} + O^{-}_{(cage)} \qquad \text{(i.1)}$$

[1] C12A7 theoretical maximum concentration = $\frac{C}{V}$ = 2.3 x 10^{21} spin·cm^{-3}

where,

V = unit cell volume, considering the C12A7 cubic structure; a^3 = (1.199 nm)^3 = 1.7 x 10^{-21} cm^3

C = C12A7 framework overall charge (4+)

They postulated that the oxygen radical formation mechanism is a three-step process. First, O^{2-} ions are mobilized to the outermost external layer of C12A7, and molecular oxygen is incorporated at the C12A7 superficial cages. Then, the clathrated O^{2-} ion is oxidized, transferring an electron to the incorporated neutral oxygen molecule to produce O_2^- and O^- ions. Finally, the oxygen radicals formed by the latter reaction diffuse inward the inner region of C12A7 (Figure i.4). This formation mechanism was then confirmed by annealing C12A7:O^{2-} in a ^{17}O isotope enriched oxygen atmosphere leading to the incorporation of $^{17}O_2^-$, which was corroborated by the presence of a $(^{17}O\cdot^{17}O)^-$ hyperfine structure employing EPR.[12]

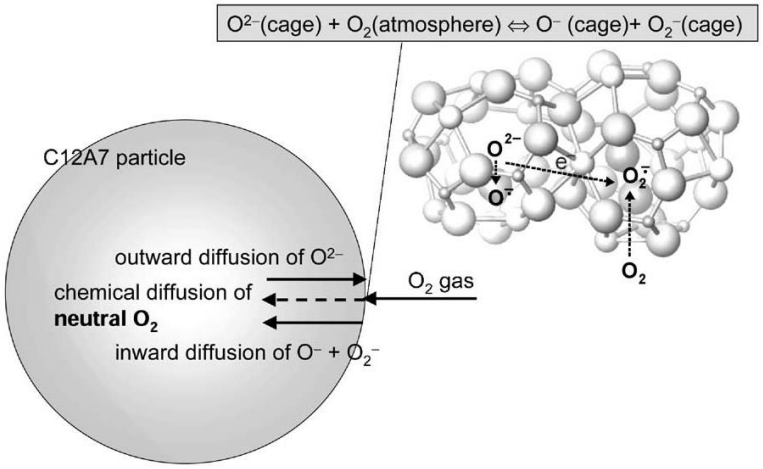

Figure i.4. Schematic representation of the oxygen radical formation process reproduced from [70].

Later on, Hosono's group established that the driving force behind the oxygen radical formation in C12A7 was the instability of O^{2-} ions.[14,70] By thermodynamic calculation, they compared the energy required for the oxygen radicals formation in the gas phase ($\Delta H° = -886.5$ kJ·mol^{-1}) and in C12A7 ($\Delta H° = -131$ kJ·mol^{-1}). The large negative value observed in the gas phase is assigned to the high instability of O^{2-} ions, which are easily oxidized by molecular oxygen. Thus, the same reasoning was assimilated in the case of the occluded O^{2-} ions in C12A7. Besides, the $\Delta H°$ smaller absolute value in C12A7 (compared to the one in the gas phase) was attributed to the interaction between the oxide ions and the lattice framework. Therefore, the "free"

extra-framework oxide ions seem to present an intermediate state between O^{2-} in the gas phase and that of an ordinary metal-oxide lattice.

Thus, when C12A7 is heat-treated under a dry oxygen atmosphere (pO_2 = 1 atm), O^{2-} ions are easily oxidized by molecular oxygen from the atmosphere. This surface reaction (Eq. (i.1)) is judged as a fast process. Hence, the inward diffusion of O_2^- and O^- species into the bulk was determined as the rate-limiting step in the oxygen radicals formation, likely governed by the lesser diffusivity of superoxide ions.[70]

The control over the heat-treatment temperature and O_2 and H_2O partial pressures during the preparation or post-activation of C12A7 has shown to be of pivotal importance in either the formation or regeneration of reactive oxygen species inside C12A7 cavities.[10,11] Hayashi *et al.* found that a significantly large quantity of O_2^- and O^- ions *ca.* 1.7 x 10^{21} spin·cm^{-3} was obtained when C12A7 was annealed at 1350 °C under an oxygen pressure of 400 atm and later cooled in the same atmosphere.[10] Therefore, this demonstrates that the total concentration of oxygen radicals can become close to the theoretical maximum by heat-treating C12A7 under high pressures of oxygen. Later on, Hayashi *et al.* evaluated the thermodynamics and kinetics of the oxygen radicals formation under a dry atmosphere. They noticed that the equilibrium concentration of O_2^- and O^- ions increases with decreasing temperature and rising oxygen partial pressure.[14] They also observed that for a given temperature, at the initial stage of the annealing, the oxygen radicals concentration increases proportionally to the square root of the annealing time, which then levels off at the equilibrium. In addition, it was determined that the time required to reach the equilibrium strongly depends on particle bulkiness.

Yang *et al.* found that the desorption of oxygen radicals happens inversely to their formation and established that it involves three consecutive steps.[11] First, outward diffusion of the oxygen species from the inner bulk to the surface (outermost external cages), then interconversion of the oxygen radicals into oxygen molecules, and finally, the desorption of oxygen into the surrounding atmosphere. Additionally, they established that the bulkiness of C12A7 plays a decisive role in the desorption of the oxygen species. They observed that the desorption temperature for the oxygen species depends on the

particle size of C12A7, as the mobility of oxygen species is limited by its diffusion in the C12A7 bulk. Subsequently, by *ab initio* calculation and isotope exchange experiments ($^{18}O_2$), Hosono's group suggested that the extra-framework oxygen diffusion mechanism in C12A7 bulk proceeds via an exchange process with oxygen from the cage wall rather than an interstitial route (via the interconnected openings of the cages).[71,72] The latter proposal was confirmed via a Neutron powder diffraction study conducted by Boysen *et al*.[26]

The team of Hosono has also looked into the regeneration of oxygen radicals.[11] Yang *et al.* noticed that oxygen radicals could be regenerated by annealing C12A7 in a dry oxygen atmosphere over 400°C. They noted that the O_2^- and O^- concentrations upsurge with rising temperature, indicating that a high temperature is essential for their regeneration. Furthermore, it was observed that O_2^- is formed more rapidly than O^- at lower temperatures in the regenerated C12A7. However, as the temperature was increased during the regeneration process, the $[O^-]/[O_2^-]$ ratio increased and approached unity (ideally equivalent proportions between O^- and O_2^- according to eq. (i.1)) at higher temperatures (*e.g.,* 900 °C). The authors suggested that the difference in the $[O^-]/[O_2^-]$ in samples regenerated at lower temperatures (400-800 °C) could be associated with the lower stability of O^- compared to O_2^-. In addition, this deviation from the ideal formation ratio may arise from interconversion reactions involving O^{2-}, O^-, and O_2^-, as well as reactions with H_2O leading to the formation of OH^- within the cages.[14] Yet, it seems that the reasons behind the variations in the $[O^-]/[O_2^-]$ under certain conditions are still unclear. In contrast, they evidenced that the presence of water during the annealing step significantly reduces and/or prevents the formation/regeneration of oxygen radicals,[9–11,14] as will be discussed in section 3.2 (*p. 28*).

Primary evidence of the peroxide anions (O_2^{2-}) occurrence in C12A7 was identified through a combination of EPR, TGA-MS, and Raman analyses.[13] Hayashi *et al.* observed that the excess oxygen (measured by TGA-MS), which could not be solely attributed to oxygen radicals (quantified by EPR), corresponded as well to another type of oxygen species. By comparing different C12A7 samples treated under various conditions, they found variations in the intensity of the Raman band at ca. 770 cm^{-1}, which is typically associated with the stretching

mode of AlO_4 tetrahedra in C12A7. These intensity variations indicated the superposition of an additional band, which was attributed to the vibration mode of O_2^{2-}.

Regarding the formation mechanism for O_2^{2-}, it was initially suggested that these species can be formed by two routes.[11,13] The first, through direct reaction between molecular oxygen and occluded oxide ions in C12A7 cages:

$$2O^{2-}_{(cage)} + O_{2\,(atmosphere)} \rightleftharpoons 2O^{2-}_{2\,(cage)} \quad \text{(i.2)}$$

or by the recombination of two encaged monoatomic oxygen radicals

$$2O^{-}_{(cage)} \rightleftharpoons O^{2-}_{2\,(cage)} \quad \text{(i.3)}$$

The authors suggested that regardless of the route, high temperature and high oxygen partial pressures were needed for peroxide ions formation. In a later study, Hosono and coworkers reevaluated the formation mechanism of O_2^{2-} employing *in situ* Raman spectroscopy under controlled atmospheres.[34] By employing *ex situ* Raman analysis (at room temperature), they corroborated that by heat-treating C12A7 at high temperature under pure oxygen, the concentration of O_2^{2-} consistently increased. However, no peroxide signal was detected at very high temperatures (1350 °C) during the *in situ* measurements. To address this inconsistency, they hypothesized that at elevated temperatures, transient atomic oxygen (O^o) is generated within C12A7 at interstitial or cage sites, potentially resulting from the thermal dissociation of atmospheric O_2. Subsequently, this atomic oxygen combines with entrapped O^{2-} ions within the cages to form peroxide ions.

$$2O^{0}_{(cage/interstitial)} + 2O^{2-}_{(cage)} \rightarrow 2O^{2-}_{2\,(cage)} \quad \text{(i.4)}$$

Thus, they proposed that O_2^{2-} ion is not immediately formed at high temperatures but instead is created during the cooling process to room temperature after C12A7 resided at very high temperature.[34] Moreover, they found that the equilibrium concentration of O_2^{2-} species decreased with decreasing annealing temperatures, mainly below 800 °C, and was also significantly impaired by the competing formation of O_2^{-} and

O^- radicals. The maximum concentration of peroxide anions was attained when C12A7 was annealed at 1350 °C under pure dry O_2 (pO_2 = 1 atm) and then quenched (*i.e.*, suddenly, and rapidly cooled).

3.2 Hydroxide anions in C12A7: a persistent species.

As stated in section 2.1 (*pp. 17-20*), C12A7 is a stable crystalline phase in the $CaO\text{-}Al_2O_3$ system in a wet atmosphere.[18,24] The latter is associated with the exceptionally high hydration enthalpy of C12A7 (-228 ± 40 $kJ{\cdot}mol^{-1}$)[35], which enables mayenite to stably incorporate and contain hydroxyl anions within its cages even at temperatures over ~1000 °C. Hence, mayenite prepared or annealed in an ambient atmosphere (*i.e.*, the presence of water) below the latter temperature can be regarded as a hydrated material (C12A7H), denoted as $C12A7{:}2OH^-$ when fully hydrated.[35,36] The formation reaction for the OH^- insertion inside C12A7 cages is described as follows, where the term [null] represents an empty cage.

$$O^{2-}_{(cage)} + [null]_{(cage)} + H_2O_{(atmosphere)} \rightleftharpoons 2OH^-_{(cage)} \qquad (i.5)$$

The hydroxide ion formation mechanism was determined to be very similar to the one previously described for the oxygen radicals (*see section 3.1, pp. 22-24*), as it also involves a three-step process. Yet, in this case, the limiting rate was determined to be the bulk inward diffusion of OH^-.[35] In addition, Li *et al.* showed that O_2^- and O^- ions could be substituted by OH^- when C12A7 containing oxygen radicals was sintered in a wet inert atmosphere (*i.e.,* flowing Ar/H_2O mixture). They proposed that, as in the case of oxide ions, the oxygen radicals react at the surface of C12A7 with water from the atmosphere and thus form hydroxyl anions, which are then incorporated in the cages and diffused inside the inner mass.[36]

Alternatively the reverse pathway, the dehydroxylation process (*i.e.,* the annihilation of encaged OH^- ions), can take place by thermally annealing $C12A7{:}OH^-$ between ~500-1350°C under dry oxygen or inert (*e.g.,* Ar) atmospheres.[20,35] It has been established that the equilibrium concentration of OH^- ions highly depends on the temperature and water partial pressure, whereas the complete dehydroxylation can be accomplished at temperatures over 1100 °C

under a dry oxygen atmosphere.[9,35] Besides, Boysen *et al.* described that clathrated OH^- and/or oxygen anions (O_2^{2-}, O_2^-, and O^-) can be removed at lower temperatures under vacuum conditions (*ca.* 10^{-6} bar).[26] They noticed that under specific conditions over 700 °C mayenite adopted its stoichiometric composition, *i.e.*, C12A7:O^{2-}. Later on, Inoue *et al.* corroborated that C12A7H can be dehydrated under vacuum conditions (*ca.* 10^{-9} bar) starting from 600°C, and the dehydration process was favored by raising the temperature.[73]

Besides, the C12A7 phase is unstable under dry conditions. In this manner, Eufinger *et al.* showed that by heat treating C12A7 under a dry atmosphere (*e.g.,* Ar with $pH_2O \approx 1x10^{-5}$ bar) over 1050°C, it was decomposed into other calcium aluminate phases (C3A, CA, and C3A5) due to the absence of any templating anion to compensate for the framework charge. However, at lower temperatures (<1000°C), the limited diffusivity of Ca stabilizes the C12A7 structure, and prevents its decomposition under dry conditions.[20]

As one can see, the hydroxyl formation reaction compulsory results in the partial or total suppression of the oxygen species inside C12A7. Conversely, the dehydroxylation pathway leads to the reinsertion of oxide ions or the regeneration of oxygen anions, depending on the treatment conditions. Consequently, controlling the partial pressure of water during the heat treatment of C12A7 is of pivotal importance, especially when oxygen anionic species are the target species.

4 C12A7 synthesis

In this section, the focus will be put on the preparation strategies to synthesize pristine and doped C12A7 containing oxygen species as counter-anions. The synthesis of the electride derivative (C12A7:e^-) will not be addressed here, yet the reader is referred to the following references[38,41].

4.1 C12A7 prepared by solid-state reaction

As previously stated in section 2.1, C12A7 is an intermediate compound found in the binary system CaO-Al_2O_3, in-between CA and C3A (Figure i.2), containing *ca.* 54wt.% Al_2O_3 and 46wt.% CaO. Since its origin,[15] synthetic polycrystalline mayenite has been commonly

prepared by solid-state reaction (ceramic route) between highly pure CaO (starting from $CaCO_3$ or $Ca(OH)_2$) and γ-Al_2O_3 (or sometimes $Al(OH)_3$) employing a stoichiometric molar ratio (*i.e.*, Ca/Al: 12/14). Nevertheless, to avoid the occurrence of side phases (CA and C3A), and thus, to promote the formation of a single C12A7 phase, this ceramic route unavoidably requires long calcination times (from several hours to days) at high temperatures (>1300°C), with intermediate crushing steps to homogenize the solid mixture.[8,19,24,26,31,38] Because of such protocol conditions, C12A7 obtained by this ceramic route shows a negligible porosity and a low specific surface area, rarely exceeding 1 $m^2 \cdot g^{-1}$. The latter properties could significantly impact the C12A7 catalytic performances (*e.g.,* low conversion) and limit its use as a potential support for other catalytic species. In this regard, some researchers have employed highly-energetic size reductions processes to enhance the texture of C12A7 obtained by the ceramic route. For example, Yang *et al.* used a jet milling procedure to yield mayenite with a higher specific surface area (S_{BET}) of about 14 $m^2 \cdot g^{-1}$.[11,63]

4.2 C12A7 obtained by wet-chemistry preparations

As previously illustrated, the ceramic route is intrinsically limited by the long-lasting diffusion, only favored at high temperatures, needed to reach desired stoichiometric homogeneity. In contrast, preparation strategies based on sol-gel[39,74–79] and hydrothermal[56,80–83] techniques have been instead employed to prepare polycrystalline C12A7 powder at milder conditions, especially at lower temperatures. In most cases, these methodologies aimed to guarantee better control of the mayenite textural and structural properties. In this matter, a selection of different wet-chemistry preparations has been summarized in Table i.1.

Table i.1. Summary of the wet-chemistry methods employed to produce C12A7

Preparation strategy	Formation Temp. (°C)	Calcination time (h)	S_{BET} ($m^2 \cdot g^{-1}$)	Observations	Ref.
Amorphous citrate route	850-900	3	14.9*	Presence of small pores	74 *84
Oxalate precursor	800	1-3	5	Micro structured powders	76,77
Sol-gel (ceramic) assisted ball milling	900 (1300)	24 (36)	48.9 (17.3)	Improved S_{BET} compared to ceramic powder	79
Hydrothermal synthesis	400-1000	4	5-70	Aggregates of spherical-alike nanoparticles with high S_{BET}	80
Topotactic synthesis	400-1000	1	12-63	Mesoporous microcubes with controlled porosity	85
Assisted-PMMA hydrothermal	600	4	35-47	Enhanced S_{BET} by the soft templating agent	56

For example, Ude *et al.*[74] showed that C12A7 could be prepared by a citrate route in shorter time, at a lower temperature, and without subsequent annealing steps. Intiso *et al.* later showed that C12A7 powders prepared by this citrate route by calcination at 1000°C under air for 4h presented a high surface area than those prepared by the ceramic method.[84] Moreover, Rashad *et al.* employed an oxalate precursor technique to prepare micro-structured C12A7 materials. They obtained C12A7 powders displaying sliced leaves or platelet-like forms as a function of the calcination temperature.

As an alternative approach, as mentioned above, extended periods of ball-milling have been applied to improve the specific surface area of the powders obtained from sol-gel routes. In this regard, Ozawa *et al.* demonstrated that C12A7 powders could develop high specific surface areas by applying a post-size reduction stage for at least 24 h.[79] They compared derived C12A7 materials from sol-gel and ceramic syntheses and found that the ball-milling step was more effective when the material was produced by a wet-chemistry method.

The hydrothermal approach has grown in popularity as a convenient technique to prepare mayenite with a high surface area at

low temperatures. It was first employed by Fujita *et al.* to prepare a calcium aluminosilicate ($Ca_{12}Al_{10}Si_4O_{35}$) from a hydrothermally synthesized hydrogarnet ($Ca_3Al_2(SiO_4)_{0.8}(OH)_{8.8}$). Thus, they obtained a Si-containing C12A7 derivative by calcining the hydrogarnet at 800 °C, displaying an S_{BET} of 7 $m^2 \cdot g^{-1}$. Later, Li *et al.* demonstrated that mayenite with a high specific surface area could be produced by this hydrothermal preparation. They prepared a hydrogarnet ($Ca_3Al_2(OH)_{12}$, denoted as C3AH6) precursor by hydrothermally treating a suspension mixture of $Ca(OH)_2$ and $Al(OH)_3$, which was previously ground in a planetary ball-mill. Then, the C3AH6 precursor was calcined between 400-1000 °C to yield C12A7 with surface area values (5-70 $m^2 \cdot g^{-1}$) ranging as a function of the calcination temperature. Recently, Intiso *et al.* employed an assisted polymethylmethacrylate (PMMA) hydrothermal procedure to produce porous C12A7. They used PMMA as a soft-templating agent leading to an increase in the specific surface area (35-47 $m^2 \cdot g^{-1}$) of the produced C12A7 materials.[56]

Lately, Hasegawa *et al.* informed on a topotactic strategy to produce mesoporous C12A7 mesocrystalline microcubes. They prepared these C12A7 microcubes by firing a hydrogarnet (C3AH6) precursor, followed by a washing step with 0.1 M NH_4Cl/methanol. The latter procedure was conducted to create porosity by washing out the excess CaO produced during the decomposition of C3AH6 upon heating. They showed that the atmosphere during the hydrogarnet precursor preparation influenced its crystallization and phase composition. Additionally, they revealed that the pore size and surface area could be controlled by tuning the temperature and the duration of the heat treatment.

Even though several of the above-exposed methods allowed the control of the textural and structural properties of C12A7, most of them require multiple synthetic steps to yield C12A7. Occasionally, a washing procedure has also been added to improve the C12A7 porosity, which only generates a waste byproduct, while others still require moderately high temperatures (> 800 °C) to obtain mayenite. In specific cases, a size reduction step, either during the synthesis or as a post-treatment, is needed to boost the surface area. This type of grinding (*e.g.,* planetary or jet milling) is a costly and energy-consuming process that involves specialized equipment.

Alternatively, solution combustion synthesis (SCS) emerges as a suitable and attractive method to produce C12A7 because it is a fast, cost- and energy-effective, and potentially scalable process.[78,86–94] Additionally, it is regarded as environmentally approachable—considering the chemical nature of combustion by-products (N_2, CO_2, and H_2O).[87] Moreover, it has been shown that nanostructured materials with tailored texture and morphologies can be obtained through this synthetic approach.[87,95] The SCS system is an amalgamation of three partners: oxidizer(s), fuel(s), and solvent. The role of the oxidizer is to provide the metal cations and the necessary amount of oxygen to burn off the fuel. The most frequently used oxidizers are hydrated metal nitrates. Yet, ammonium nitrate or nitric acid can also be employed when the related metal nitrate is not readily available.[87] The function of the fuel is not only to generate sufficient heat for the system but also to ensure the formation of stable complexes with the metal cations. Additionally, the fuel has to increase the oxidizer solubility and prevent the precipitation of the cations during the water evaporation upon heating. Therefore, fuel selection is not a trivial choice. The most used organic substances are urea, glycine, citric acid, hydrazine, etc. Finally, the solvent most commonly chosen is water, yet alcohols or hydrocarbons have also been employed.[87,95,96]

In short, the SCS approach relies on a self-sustained combustion reaction between oxidizer(s) and organic fuel(s), which is triggered once the solution is heated to the required temperature. Typically, the temperature of the employed heating devices (*i.e.*, preheated-furnace or hot plates) ranges from 250-500 °C. After the combustion reaction occurs, which lasts only a few seconds, a dry, frequently crystalline powder is obtained. [87]

Various authors have prepared C12A7 by SCS employing a single-fuel approach. For instance, Fumo *et al.* prepared several calcium aluminates using stoichiometric amounts of Ca and Al nitrates and urea (fuel) dissolved in water.[89] Later, Tas *et al.* showed that the C12A7 phase could be obtained by annealing for several hours at temperatures from 800 °C, the as-prepared solid obtained from the combustion reaction (500°C).[90] Raab *et al.* employed glycine as fuel and metal nitrates to prepare C12A7. The authors also compared the SCS strategy with a Pechini process and ceramic route. They found that C12A7 was produced after calcining the as-burnt solid from the combustion reaction at temperatures from 1000°C, while a metastable

calcium aluminate phase (C3A5) was depicted below this latter temperature. Alternatively, Gong *et al.* employed a citric acid sol-gel combustion method to produce C12A7:O^- powders. They relied on the sol-gel CS to obtain a xerogel precursor that was fired at 250 °C to produce an amorphous precursor. Later, this solid precursor was annealed between 900-1150°C to yield C12A7 phase. As one can see, none of these previous studies have produced mayenite directly after the combustion reaction. Meanwhile, an additional annealing treatment at high temperatures has unavoidably been applied to achieve the formation of the C12A7 phase.

In contrast, Ianoş *et al.* revealed that by employing a double-fuel mixture, the calcium aluminate phase (C3A) was directly obtained after the combustion reaction by SCS.[92] They showed that the appropriate fuels to interact with Al and Ca nitrates were urea and β-alanine, respectively. Thus, they noticed that C3A was immediately formed after triggering the combustion reaction at temperatures as low as 300 °C, whereas an additional firing step was no longer needed. Therefore, this approach could be extended to other calcium aluminates from the binary system $CaO\text{-}Al_2O_3$ such as C12A7.

5 C12A7 as catalyst

Pristine C12A7 and its derivatives (*i.e.,* electride or doped-C12A7) are suitable candidates for heterogeneous catalysis[41,55] because of their oxidative properties,[9,43,63,82,83] carbon deposition resistance[63,65,97], sulfur and chlorine poisoning tolerance[55,56,62,64,83,98], and electron donor capacity[41,66,73,99]. Therefore, C12A7 catalytic performances have been primarily evaluated in oxidation reactions (catalytic abatement of volatile organic compounds, soot, and so on)[44,53–55,58,81], steam or dry cracking/reforming[59,62], and as active support for Ru (and sometimes Co) in ammonia synthesis[42,66,73,85].

The first assessments of the C12A7 catalytic behavior were evaluated in the steam cracking (catalytic pyrolysis) of n-hexane[59], n-heptane[60], and methylcyclohexane[100]. For instance, Lemonidou *et al.* attributed the enhanced activity of C12A7, in contrast with other calcium aluminate catalysts, to the presence of peroxidic active oxygen species in its structure. They proposed that these oxygen ions promote

the initiation reactions of n-hexane, which are responsible for the extent of the pyrolysis.[59]

Hosono's group also assessed the oxidative properties of the clathrated oxygen anions in C12A7. Hayashi *et al*. found that when a Pt-metal plate was put in contact with the C12A7 surface, it was oxidized to Pt^{4+} during an annealing process at 1350°C in a dry oxygen atmosphere.[9] They initially postulated that the most likely active species for such an unusual oxidation process were O^- ions. However, in a recent report, Dong *et al.* from the same group proposed that the transcendent O^0 species are the mediating active species for Pt oxidation. The latter species are assumed to be produced by the thermal dissociation of molecular oxygen at 1350 °C at the surface of C12A7 and then dissolved into the mayenite lattice.[34]

Li *et al.* used mayenite as active support for Ni catalyst in the biomass tar steam reforming reaction.[62] They employed toluene as a tar destruction model compound. In comparison to Ni-supported commercial catalysts, it was noticed that Ni/C12A7 showed excellent performance and presented good coke and sulfur resistance, attributed to the entrapped reactive oxygen species (O_2^- and O_2^{2-}). In the latter case, the replacement of the extra-framework oxygen species by sulfur protected Ni from being poisoned to some extent. Yet, the regeneration of this S-substituted C12A7 to its oxidic form showed to be difficultly fulfilled.

In a recent study, Somekawa *et al.* reported on a Ni/$12CaO{\cdot}7Al_2O_3$ coated on a honeycomb-type catalyst for hydrogen production by methane decomposition.[68] They showed that this catalyst was active and stable under severe reaction conditions (high space velocity, high temperature, and reducing atmosphere) even in the presence of water. Hence, they proposed that Ni/C12A7 supported on honeycomb-type cordierite might be considered as a promising catalyst for future applications in hydrogen production.

Alternatively, Ruszak *et al.* reported on the high-temperature catalytic reduction of nitrous oxide (N_2O) using mayenite.[52] They indicated that C12A7 fulfilled the required performances to be industrially employed as a catalyst in the secondary abatement plants related to the production of nitric acid. They proposed that the deN_2O

reaction involved the dissociation and abstraction of oxygen from nitrous oxide (under anaerobic conditions) and further oxygen incorporation inside the superficial cages of C12A7.

5.1 C12A7 in catalytic oxidation reactions

As exposed above, the capacity of C12A7 i) to accommodate several oxygen species (O^{2-}, O_2^-, O^-, and O_2^{2-}) of distinct nature inside its structure, ii) to release them to the atmosphere, and iii) to regenerate them according to the external conditions (temperature and atmosphere composition), have placed this material as a worthy catalyst contender in oxidation reactions. Hence, C12A7 as a bulk oxidation catalyst or active support for various metals in oxidation reactions will be reviewed in the following paragraphs (see also summary in Table i.2). Additionally, the control over mayenite textural properties, its concentration of oxygen species, and the modification of its cationic sites (Ca^{2+} or Al^{3+}) by doping with foreign metal cations will also be addressed to highlight the influence of these parameters on its catalytic performance. On this matter, a few examples of the electride form (C12A7:e^-) will also be revised.

Table i.2. Summary of oxidation reactions employing C12A7 as bulk catalyst or support.

Catalyst	Tested reaction	Main findings	Ref.
		Mayenite as bulk catalyst	
Si-C12A7 derivative ($Ca_{12}Al_{14-x}Si_xO_{33+0.5x}$)	Total oxidation of hydrocarbons	- Si-C12A7 exhibited higher activity compared to thermal decomposition (T > 400 °C). - O_2^- and O_2^{2-} are the active species in this reaction.	58,98
Bare C12A7	Total oxidation of Trichloroethylene (TCE)	- C12A7 obtained 92% conversion at 500 °C thanks O_2^- and O_2^{2-} species. - Cl^- was incorporated into cages leading to deactivation. -Exposition of spent catalyst to humid air partially restored catalytical properties.	55
Bare C12A7	Total oxidation of TCE	- C12A7 synthesized by hydrothermal method showed the best textural properties and concentration of oxygen anions, which implies a high activity, selectivity (towards CO_2) and stability.	84
Bare C12A7 and (Cu, Cr, Co, Ni)-substituted C12A7	NO reduction with C_3H_6 in the absence of O_2	- Metal substituted C12A7 showed better catalytic activity compared to non-doped C12A7, which was attributed to an increased O_2^- reactivity caused by the substitution of Ca^{2+} by other metals.	43
Bare C12A7 and substituted C12A7	Catalytic oxidation of carbon black	- Si-C12A7 catalyst doped with Cu showed better performances than bare C12A7 and other dopants (Cr, Co, Ni), obtaining the highest combustion rate at T < 500°C.	44
		Mayenite as support	
Ni, Co, Pt, Pd, Ru / C12A7	Partial oxidation of CH_4 to syngas	-Pt/C12A7 and Ni/C12A7 showed the highest activity, selectivity, and stability. - Ni/C12A7 was the most active due to good NiO dispersion and active oxygen ions.	63
Co_3O_4/ Si-C12A7	Total oxidation of hydrocarbons	- Co_3O_4/ Si-C12A7 presents higher activity and stability than Co_3O_4/Al_2O_3 thanks to a good dispersion of the active phase. - Total conversion at T< 300 °C.	81
$La_{0.8}Sr_{0.2}MnO_3$ / C12A7	Total combustion of methyl methacrylate	- C12A7 enhances physic-chemical properties of monoliths, promoting good $La_{0.8}Sr_{0.2}MnO_3$ dispersion. - $La_{0.8}Sr_{0.2}MnO_3$ phase is stable in mayenite surface up to 1050 °C.	67

One of the only reported studies on a partial oxidation reaction using C12A7 was done by Yang *et al.* from Hosono's group.[63] They informed on the partial oxidation of methane with oxygen to syngas (H_2+CO) employing bare and promoted C12A7 catalysts. They used C12A7 as functional support for Ni, Co, Pt, Pd, and Ru active phases. They found that all the prepared catalysts were active. Pt/C12A7 and Ni/C12A7 were among the others the most active ones, presenting high activity, selectivity, and stability, even at low temperatures and low metal loading. When comparing Ni/C12A7 with other Ni-supported catalysts, the good dispersion of NiO and the presence of clathrated oxygen species in the former placed it as the most active with good coke resistance.

Concurrently, Fujita *et al.* appraised the role of a Si-containing C12A7 derivative ($Ca_{12}Al_{10}Si_4O_{35}$) hydrothermally prepared as a heterogeneous catalyst in the total oxidation of volatile organic compounds (VOCs).[98] They tested several hydrocarbons (propylene, benzene, toluene, and chlorobenzene) in concentration *ca.* 1000 ppmv. diluted in synthetic air as VOC probe molecules. They found that this calcium aluminosilicate exhibited high activity in the oxidation of the distinct hydrocarbons in comparison to their thermal decomposition, transforming these pollutants into carbon oxides (CO_2 and CO) at temperatures over 400 °C. During the propylene oxidation only CO_2 was observed as product. They suggested that encaged peroxide and superoxide anions were accountable for the catalytic activity. For non-chlorinated hydrocarbons, $Ca_{12}Al_{10}Si_4O_{35}$ showed time-on-stream stable activity for at least 600 min at 600 °C. However, for chlorobenzene, the activity decayed with time due to the replacement of O_2^- and O_2^{2-} by Cl^- leading to the deactivation of the catalyst. The same authors also prepared this calcium aluminate from a Co-containing hydrogarnets[81] and molten slag waste materials[83], and tested their catalytic activity in the catalytic combustion of non-chlorinated hydrocarbons. The Co-containing hydrogarnets led to the formation of materials composed of Co_3O_4 finely dispersed over Si-C12A7. These Co_3O_4/ Si-C12A7 catalysts exhibited better activity and stability than a conventional Co_3O_4/Al_2O_3 catalyst due to the better dispersion of the active phase.[81] Besides, the $Ca_{12}Al_{10}Si_4O_{35}$ prepared from molten-slag showed to be more active than the one prepared from pristine precursors. As exposed in section 2.1 *(pp. 17-20),* various metal cations can be found in the octahedral or tetrahedral sites of

C12A7 framework.[22] Hence, Fujita *et al.* attributed this improvement to the cationic substitution of Ca^{2+} and/or Al^{3+} by foreign cations found in the molten slag waste.[83]

Zhang *et al.* wash-coated mayenite materials (C12A7 and S12A7; S = SrO) on cordierite monoliths to support and stabilize $La_{0.8}Sr_{0.2}MnO_3$ perovskite (LSM) as active phase. They assessed the catalytic activity of the LSM/mayenite monoliths in the total combustion of methyl methacrylate (MMA).[67] They found that the thermal stability of LSM/mayenite monolith was improved, and the catalytic activity was enhanced in comparison to LSM/Al_2O_3 conventional catalyst. They revealed that mayenite (S12A7 or C12A7) as support promoted the dispersion of LSM and prevented the interactions between the monolith and the active phase even at high temperatures (1050 °C), as usually occurred when LSM is supported over γ-Al_2O_3.

Recently, Cucciniello *et al.* uncovered that mayenite is an active and efficient heterogenous catalyst for the oxidation of trichloroethylene (TCE) in the gas phase.[55] They assessed that C12A7 oxidized TCE starting from 200 °C and reached nearly total conversion (92%) at 500°C. They showed that TCE transformed into CO_x and that chlorine was not released into the atmosphere instead it was incorporated inside C12A7 structural cages. Nevertheless, as early noticed by Fujita *et al.*[98], the latter incorporation of Cl^- ions inside C12A7 led to a gradual deactivation with time-on-stream. In this matter, a regeneration procedure, by heat-treating the C12A7:Cl^- spent catalyst under humid air at 500 °C, showed to be capable of partially restoring the catalytic activity of C12A7. Furthermore, in line with previous reports, they suggested that the C12A7 high performance could be related to the presence of O_2^- and O_2^{2-}, which promoted the complete oxidation of TCE and avoid coke formation.

5.1.1 Effect of tuning the textural properties

As a general rule, the improvement of the catalyst texture is a well-established approach to promote its catalytic activity. In the case of C12A7, this is also valid. For instance, Yang *et al.* showed that the desorption of the oxygen species from the bulk to the atmosphere occurred at lower temperatures by reducing the C12A7 particle size via a jet milling process, which increased its surface area. Thus, they

noticed that the oxygen desorption from C12A7 strongly depends on the bulkiness of the material due to the mass transport limitations inside its bulk.[11] As a result, when Yang and coworkers used C12A7 as an active support for several metals in the partial oxidation of methane to syngas (H_2+CO), they employed a C12A7 material with a surface area of 14 $m^2 \cdot g^{-1}$ rather than a bulkier one (1 $m^2 \cdot g^{-1}$).[63]

Moreover, as reviewed in section 4.1, some research works have found new synthesis preparations to tune the C12A7 textural properties. In the following paragraphs, some examples will be covered where the effect of such modifications on the mayenite catalytic performance was evoked.

Intiso *et al.* compared the catalytic performance of C12A7 obtained by different synthesis methods in the TCE oxidation.[84] Precisely, they compared mayenite prepared by hydrothermal (35.5 $m^2 \cdot g^{-1}$), sol-gel (14.9 $m^2 \cdot g^{-1}$), and ceramic (11.7 $m^2 \cdot g^{-1}$) routes. They showed that the C12A7 catalyst obtained by the hydrothermal method was the most active, stable, and selective towards CO_2. They associated the latter improved behavior with the higher surface area and the higher concentration of oxygen anions. Even though they observed that the hydrothermally obtained C12A7 was more stable than the others, the former also suffered from the above-recalled deactivation process upon exposure to TCE.

The benefits of increasing the specific surface area have also been revealed in the ammonia synthesis from N_2 and H_2 employing Ru-supported C12A7 electride (C12A7:e^-) catalysts.[73,85] For instance, Inoue *et al.* demonstrated that a hydrothermally obtained high specific surface area Ru/C12A7 electride (20 $m^2 \cdot g^{-1}$) was more active than the one prepared by the traditional ceramic route (1 $m^2 \cdot g^{-1}$), revealing a two-fold reaction rate increase. They observed no substantial difference in the apparent activation energy between both Ru-supported catalysts, indicating they possessed comparable electron-donating capacities. Yet, they evidenced that Ru particles were smaller and better dispersed on C12A7 with improved texture than over the non-porous one, both containing equivalent Ru loading (2 wt.%). Therefore, they attributed this improvement in the catalytic activity to better dispersion of Ru nanoparticles on the electride support with a higher specific surface. Later, Hasegawa *et al.* reported on a topotactic

synthesis approach to prepare mesoporous C12A7 mesocrystalline microcubes as support for Ru and tested also in the NH_3 synthesis. They found that the better control over C12A7 morphology and texture achieved by this new protocol permitted these C12A7 microcubes to uphold a higher Ru loading while keeping a high dispersion. They also noticed that the usual reduction step needed for the electride formation was no longer mandatory for these C12A7 microcubes, as similar NH_3 synthesis rates were obtained using the oxidic or reduced C12A7 forms.

5.1.2 Effect of adjusting the concentration of oxygen species

Generally, the increase in the number of active sites typically results in higher conversion rates. Regarding the C12A7 catalyst, this fact can be translated into an increase in the concentration of the reactive oxygen species. In this matter, only a couple of reports have analyzed the influence of increasing the concentration of oxygen species, yet the reported results are divergent.

From mineralogic reports, one can recall that the wadalite group (calcium aluminum silicates) can host a higher number of counter-anions inside its cages because of the greater positive charge of its framework due to the partial substitution of Al^{3+} by Si^{4+}.[22] In this regard, Fujita *et al.* examined the catalytic performance of a Si-containing C12A7 derivative ($Ca_{12}Al_{10}Si_4O_{35}$) in the total combustion of several hydrocarbons, as presented above. Yet, they also explored a strategy to manipulate the number of oxygen species inside this material. They reported on several Si-containing C12A7 derivatives with ranging contents of active oxygen ions ($Ca_{12}Al_{14-x}Si_xO_{33+0.5x}$, $0 \leq x \leq 4$).[82] They observed that the total amount of occluded oxygen anions (O_2^- and O_2^{2-}) could be indeed controlled by changing the Si/Al molar ratio (assessed by Raman and Rietveld refinement analyses). They noticed that all Si-C12A7 catalysts were active in the catalytic total oxidation of propene and benzene, starting from 400°C. However, they remarked that as the Si content increased (*i.e.*, a higher number of oxygen anions), the activity of the Si-C12A7 derivatives did not improve. Instead, they noticed that pristine $Ca_{12}Al_{14}O_{33}$, presenting the lowest amount of active oxygen species, performed better than the one containing the highest number ($Ca_{12}Al_{10}Si_4O_{35}$). Additionally, they found that the pristine one was more selective to CO_2 than the other

Si-C12A7 catalysts in the benzene oxidation. Hence, they hypothesized that the oxidation ability of the different catalysts might be different, yet no further evidence was provided.[58]

On the opposite, as presented before, Intiso *et al*.[84] examined the catalytic performance of C12A7 prepared by different synthetic strategies for the TCE oxidation reaction. They proposed that apart from the positive influence of the texture in the C12A7 performance, the increase in the number of active species (superoxide radicals) also plays an important role. On this matter, they revealed that the hydrothermally prepared C12A7 presented the highest hydrogen consumption (measured by TPR analysis), which was attributed to an increased number of reactive oxygen species in contrast to those catalysts prepared by sol-gel and ceramic routes. Finally, Intiso *et al*. reported on a new synthesis strategy to further improve the activity of mayenite in the TCE catalytic combustion. They employed ranging amounts of PMMA as a soft-templating agent during the hydrothermal procedure to synthesize C12A7. They found that employing PMMA increased the surface area and the oxygen anions concentration (judged by Raman analysis). Hence, they concluded that a good combination of textural and redox properties could be advantageous for the catalytic performance of C12A7.

5.1.3 Effect of modifying C12A7 cationic sites

It has been reported that incorporating aliovalent and isovalent dopants on the cationic sites within the C12A7 framework can affect its structure and properties.[38,46] Thus, the insertion of several dopants and their effect on the catalytic performance of C12A7 will be briefly revised.

For instance, as described above (*see section 5.1.2*), the partial replacement of Al^{3+} by Si^{4+} improved the capability of mayenite to incorporate oxygen anionic species. In this regard, Sato *et al.* also reported on the cationic substitution of Ca^{2+} within this calcium aluminosilicate (Si-C12A7 derivative) and its effect on the reactivity of the occluded superoxide ions.[43] They prepared these catalysts by a hydrothermal approach and studied their reactivity in the NO reduction with C_3H_6 under anaerobic conditions. They found that a small fraction of Ca^{2+} could be replaced by Ni, Co, Cr, and Cu. They noticed that all

catalysts were active in the NO reduction in the absence of oxygen. While by contrasting the different doped-C12A7 specimens, they remarked that the O_2^- reactivity was increased with the following order $Cu^{2+} > Cr^{3+} > Co^{3+} > Ni^{2+} >> Ca^{2+}$.

Moreover, Sato and coworkers also evaluated the impact of the cationic substitution in the catalytic oxidation of soot employing carbon black (CB) as alternate substrate. They selected several C12A7 doped catalysts from their previous study and mixed them with CB in a weight content of 5 wt%.[44] They remarked that among the different dopants, the Si-C12A7 catalyst containing Cu exhibited the best performances achieving the highest CB combustion rate at 468 °C (T_{peak}) in contrast to the Si-C12A7 (not containing transition metals) at 530°C. Hence, Sato *et al.* suggested that the partial replacement of Ca^{2+} ions by foreign metal ions led to a reactivity enhancement of the occluded O_2^- species. Yet the nature of the copper species interacting with the reactive oxygen species remained uncertain. Moreover, Maurelli *et al*. studied the localization of Cu^{2+} ions and their interactions with native anions (O_2^- and OH^-) in a Cu-doped C12A7 using EPR spectroscopy.[45] Cu-substituted C12A7 was synthesized by impregnating an already-prepared undoped C12A7 (obtained via solid-state reaction) with an ethanolic solution containing Cu nitrate and calcining at 900 °C for 0.5 h. They revealed the existence of three different Cu(II) species inside the C12A7 framework, presenting axial symmetry and well-resolved parallel hyperfine structure, which is characteristic of isolated divalent copper species ($Cu^{2+}(d^9)$, $S = {}^1/_2$, $I = {}^3/_2$). They established that Cu^{2+} centers interacted directly with OH^- occluded ions located in the same or nearby cages, while O_2^- extra-framework species preferentially interacted with Ca^{2+} ions. Recently, a theoretical study suggested that the partial incorporation of copper in C12A7 electride form ($C12A7:e^-$) facilitates the formation of a conduction channel, which could boost the electronic conductivity of this material.[46] To the best of our knowledge, none of these previous reports have described the role of copper species in the catalytic activity enhancement of Cu-doped C12A7 in oxidation reactions. Nor was it reported on the nature of other kinds of copper species that could be formed during the synthesis of Cu-C12A7 materials, and whose presence could also influence the catalytic performances of these catalysts.

6 Critical consideration of literature survey

6.1 Step by step examination

- Hosono's group has extensively studied the conditions necessary to form, stabilize, desorb, and regenerate the reactive oxygen species within C12A7. However, in all these studies, the C12A7 samples were prepared by ceramic route or produced as single crystals. Therefore, they systematically obtained materials with negligible textural properties. Additionally, all the investigated C12A7 samples contained oxide ions as initial occluded species. Even though this ideal composition ($C12A7:O^{2-}$) can be easily obtained by solid-state synthesis at elevated temperatures (1350°C), this is hardly achieved by employing wet-chemistry strategies. The latter is related to the facility of OH^- ions to be incorporated inside C12A7 cages when it is prepared in the presence of water. Meanwhile, the total elimination of hydroxyl ions required high temperatures (1200 °C). Consequently, all the experimental conditions found by Hosono's group to modulate the oxygen species population can only be straightforwardly applicable when C12A7 presents a stoichiometric composition and also under a controlled oxidative dry atmosphere (*i.e.,* absence or limited presence of water).

- It has been unanimously agreed that enhancing the C12A7 textural and structural properties promotes its catalytic performance. However, the reasons behind this improvement, specifically related to the cationic replacement of the native cations, remained less explored or unclear. For instance, the employment of C12A7 as a support has been justified by the fact that the increase in the specific surface area favors the dispersion of the active phase. Besides, in the case of C12A7 as a bulk catalyst, a synergic effect between the texture and the oxygen species concentration has been evoked. In contrast, regarding cationic doping, Sato *et al.* proposed that the dopants influence the reactivity of the superoxide species inside C12A7, and copper was highlighted as the most effective one. However, the authors

did not go more in-depth in understanding this effect nor reported on the nature of these dopants within the C12A7 structure (*i.e.*, inserted in the matrix or dispersed on the solid) and their individual relationship with catalytic performance.

- Finally, contradictory findings have been reported regarding the influence of the oxygen species concentration on the C12A7 catalytic behavior, as recalled in section 5.1.2. Fujita *et al*., through XRD (Rietveld refinement), TGA, and Raman analyses, established that raising the concentrations of oxygen anions (O_2^- and O_2^{2-}) was obtained by increasing the number of Si^{4+} by partially replacing Al^{3+}. In opposition, Intiso *et al*., employing TPR-H_2, Raman, and BET analyses, suggested that enhancing the C12A7 textural properties promoted the concentration of entrapped oxygen species. Nevertheless, they neither considered utilizing EPR analysis to accurately evaluate the presence and amount of superoxide ions, which can be easily distinguished by this technique and quantitively estimated, nor did they consider the influence that the occurrence of CaO or $CaCO_3$ (depicted by XRD) in their samples could have in their Raman spectra interpretation. A recent study pointed out that lime-related materials presented characteristic Raman bands between 1070-1090 cm^{-1}.[101] Therefore, considering that both groups assigned bands at 1075 cm^{-1} (Fujita *et al.*) and 1085 cm^{-1} (Intiso *et al.*) to the occurrence of O_2^- ions, they might disregard the connection of the latter bands with CaO ($CaCO_3$). Besides, both groups' assignations are opposed to the most recognized Raman mode of superoxide ions in C12A7, which is rather observed between 1122-1135 cm^{-1}.[14,102,103] Regarding all the distinct extra-framework species that can be incorporated in C12A7, both groups considered that only reactive oxygen species were present inside C12A7 cages. Yet, both employed wet-chemistry strategies to prepare C12A7, namely a hydrothermal approach. Thus, it is possible to assume that a considerable number of OH^- ions were also incorporated with C12A7 due to the presence of water during its preparation.

6.2 General conclusion

In summary, the unique properties displayed by C12A7, mainly its capability to host reactive oxygen species within its structure, have proven that mayenite presents great potential as a heterogeneous catalyst in oxidation reactions. It has been shown that it is possible to modulate the nature of the extra-framework species within the C12A7 structure by controlling the preparation or post-activation conditions, such as annealing temperature and atmosphere composition (oxygen and water partial pressures). However, it seems that when C12A7 presents an initial extra-framework population composition distinct from the ideal one, *e.g.*, the presence of OH^- ions instead of only O^{2-}, the conditions reported in the literature to modulate the oxygen species distribution in C12A7 could not be blindly employed.

Additionally, it has been pointed out that C12A7 catalytic performances can be improved by controlling its textural and structural properties. In this regard, in many cases, the enhancement of the specific surface area appeared to be a crucial factor regarding mayenite utilization as a bulk catalyst or active support. In the same regard, the improvement of C12A7 catalytic performance by modifying its cationic sites was also illustrated. Yet, a more systematic study is still required to evaluate the role of the dopants, namely copper, which has been pointed out as the most promising one in oxidation reactions. Moreover, opposing regards related to the influence of the oxygen species concentration were evidenced. Consequently, this matter needs to be elucidated by a more comprehensive study to appraise whether or not the concentration of active oxygen anions can impact the performance of C12A7. Alternatively, evaluating the modulation of the extra-framework population distribution as a tool to control the C12A7 catalytic performance, mainly its selectivity in an oxidation process, has not been explored.

7 Objectives

As described at the beginning of this General Introduction, it is recognized that the nature of oxygen species present on the catalyst surface plays a crucial role in the overall catalytic process, particularly in terms of its selectivity. Thus, the main purpose of this thesis is to evaluate the possibility of controlling the catalytic activity and selectivity of C12A7 in an oxidation reaction by modulating its population distribution of extra-framework oxygen species. In addition, based on the literature review presented above, three specific objectives converging to support the main aim of this work or clarify some gray areas in the present state-of-the-art have been set:

i. Developing a new wet-chemistry strategy to produce pristine and doped C12A7 at lower temperatures with improved textural properties.
ii. Studying the modulation of the population distribution of oxygen species inside C12A7 produced by a wet-chemistry approach by controlling the synthesis or post-activation conditions.
iii. Examining the catalytic performances (activity and selectivity) of the C12A7 catalyst in the carbon black (CB) and propane oxidation reactions and studying the influence of the catalyst texture, speciation of extra-framework species, and structural modifications by cationic doping with copper.

8 Strategy

To meet the objectives exposed in the previous section, the strategy applied in this thesis is articulated as follows.

8.1 Choice of the synthesis methodology

As described in section 4.2, several wet-chemistry strategies have been employed to modify the textural or structural properties of C12A7. However, several drawbacks in these approaches were evidenced (*p. 31*). Since solution combustion synthesis (SCS) has been described as a promising approach to preparing solids with controlled textural and structural properties, especially at low temperatures, this

approach has been selected for the present work. Hence, C12A7 is synthesized by one-pot SCS employing a double-fuel approach with urea and β-alanine as fuels. Additionally, a second procedure is explored by introducing oxalic acid in the preceding solution combustion system, aiming to produce porous C12A7, thus partly tackling the first objective.

In contrast, as highlighted in the literature, copper appears as the most promising dopant influencing the catalytic behavior of mayenite in an oxidation reaction.[43–46] Therefore, the partial replacement of calcium by copper is also investigated by the SCS preparation to fulfill the first objective.

8.2 Modulation of the population distribution of extra-framework oxygen species

Section 3 evidenced that the modulation of the overall population distribution of extra-framework species toward a targeted oxygen species is a viable task. To do so, the fine-tuning of the heat-treatment temperature and atmosphere during either the formation or post-treatment of C12A7 can be exploited to promote the incorporation of electrophilic or nucleophilic oxygen species inside its structure. Consequently, to first settle the ground, the assessment of the population distribution of extra-framework species within the mayenite samples prepared by SCS under ambient conditions without controlling the atmosphere is evaluated. Next, the possibility of modulating the speciation and relative abundance of the extra-framework oxygen species by applying several condition arrangements is explored. At this stage, distinct parameters are varied, including the calcination temperature, partial pressures of oxygen and water, the mode of contact between the solid and the gas stream (primarily oxygen) employed during the annealing process, and the oxygen flow rate. The primary purpose of this section is to satisfy the second objective and, secondly, to provide several representative C12A7 samples presenting different extra-framework population profiles, which are meant to be used to evaluate the feasibility of the principal aim of this thesis.

8.3 Choice of the catalytic reactions

This section is conceived to tackle the third objective of this research work. Concerning the catalytic systems employed in this

thesis, two model oxidation reactions have been selected, utilizing carbon black (denoted CB, Printex-U from Degussa) and propane as substrates, where oxygen is the oxidant. The CB combustion reaction is used to obtain a general overview of the catalytic performance of the prepared C12A7 catalysts and to evaluate the influence of its textural properties. Additionally, leveraging on this reaction, the impact of the nature of distinct copper entities in C12A7 and the analysis of their relationship with the catalytic behavior of Cu-C12A7 catalysts is investigated.

Furthermore, it has been argued that the modulation of the population distribution of the extra-framework oxygen species may offer a way to influence the catalytic performance of C12A7 in an oxidation process. In this scenario, propane is selected as a model molecule to examine the viability of the proof-of-concept, considering that this hydrocarbon can be partially oxidized to propene or completely oxidized toward carbon oxides. Hence, different catalytic configurations are designed to favor the propane total or partial (selective) oxidation by controlling the reaction conditions, namely the feeding gases ratios. As a result, multiple sets of selected catalysts, with varying population distributions of extra-framework species, are examined in the propane oxidation to assess the impact of manipulating this distribution on the catalytic performance of C12A7.

9 Thesis structure

Supported by the heretofore exposed objectives and related strategic methodology, the structure of the thesis is presented below and schematized in Figure i.5. The present general introduction is immediately followed by the experimental section, which describes all the materials and relevant technical details required to perform the analytical techniques employed to characterize the C12A7 materials prepared in this work and to appraise their catalytic performances. Next, the experimental results obtained in this research, their interpretation, and discussion are disclosed in three separate chapters. The **first chapter** addresses the preparation of pristine C12A7 with enhanced textural properties by solution combustion synthesis (first objective). The focus is placed on evaluating the influence of the preparation parameters (temperature, fuel-to-oxidizer ratio, oxalic acid loading) on the textural and structural properties of C12A7. Next, the

effect of improving the C12A7 textural properties on its catalytic performance is evaluated in the carbon black (CB) combustion reaction which is typically employed in the literature as soot model substitute (third objective). The **second chapter** is subdivided into two parts, considering its complexity and extent. This chapter deals with the second and third objectives of this work. Precisely, it examines the feasibility of controlling the catalytic performance of C12A7 in an oxidation reaction by modulating its population distribution of extra-framework oxygen species. Here, the propane oxidation reaction is employed to appraise the proposed effect. The **third chapter** covers the preparation of Cu-doped C12A7 catalysts and the evaluation of their catalytic performances in the CB oxidation reaction (first and third objectives). Herein, the control over the dispersion of Cu, textural properties, and superoxide species concentration of the Cu-C12A7 catalysts is explored by adjusting the Cu loading and calcination temperature to appraise their effect on the catalytic behavior of these materials. Lastly, the general conclusions and the outlook for future work are presented.

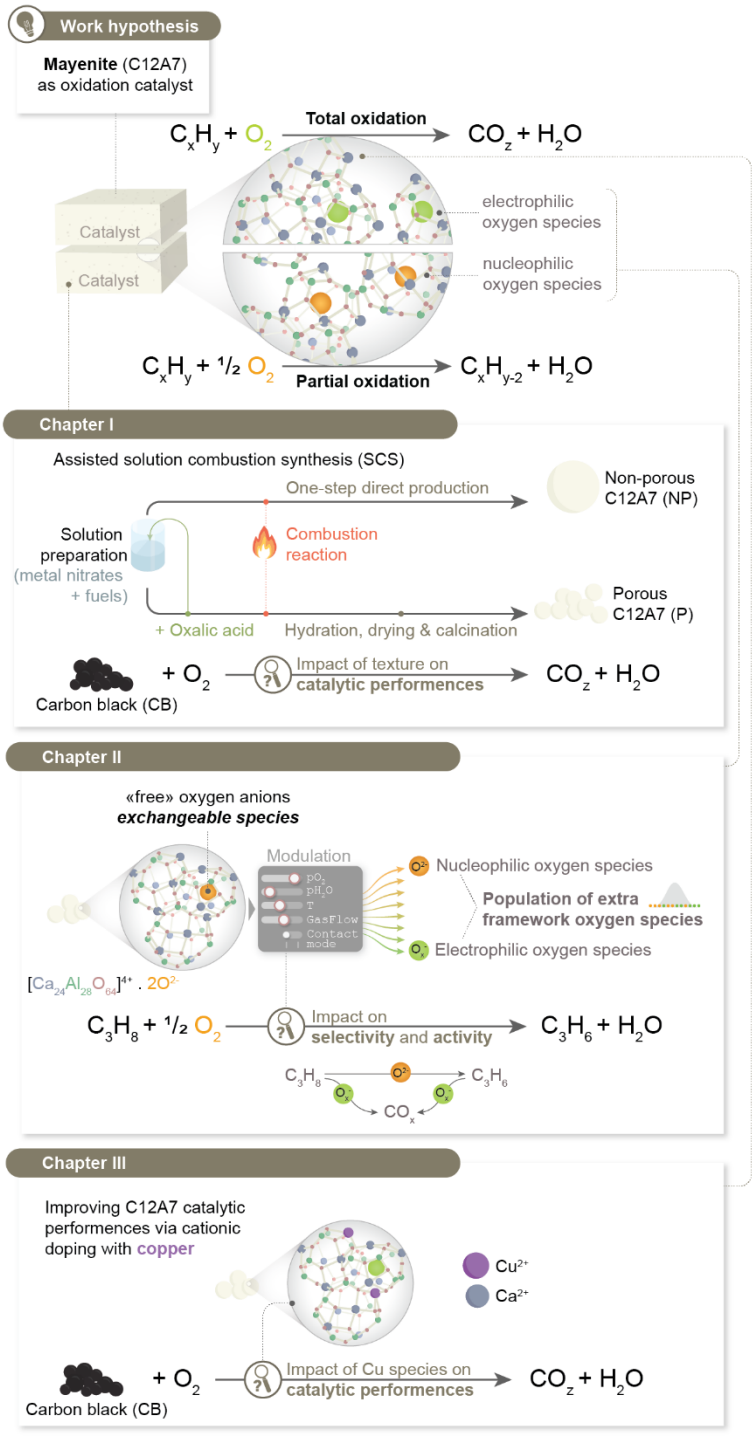

Figure i.5. Scheme representing the thesis structure and the objectives covered in each chapter.

EXPERIMENTAL SECTION

1 Materials

Calcium nitrate tetrahydrate [$Ca(NO_3)_2 \cdot 4H_2O$, 99.9%], aluminum nitrate nonahydrate [$Al(NO_3)_3 \cdot 9H_2O$, 98.5%], copper(II) nitrate hemi(pentahydrate) [$Cu(NO_3)_2 \cdot 2.5H_2O \geq 99\%$], urea ($CH_4N_2O$, 99.9%), and β-alanine ($C_3H_7NO_2$, 99%) were purchased from Merck. Anhydrous oxalic acid ($C_2H_2O_4$, 99.9%) was purchased from Sigma Aldrich. All reagents were used as delivered[2] without any further treatments in the preparation of pristine nonporous and porous C12A7 (Chapter I), and Cu-doped porous C12A7 (Chapter III). Carbon black (CB) (Printex U) from Degussa was employed as a diesel soot surrogate, and oxygen contained in Helium ($5\%O_2$/He) from Praxair was used as an oxidant in the catalytic tests reported in Chapters I and III. Propane (3000ppmv C_3H_8 in N_2), propane (industrial grade, 99.7%), oxygen (99.995%, denoted as dry oxygen in Chapter II), and nitrogen (99.995%) provided by Air Liquide were used in the catalytic tests and post-activation/preparation of C12A7 under controlled atmosphere conditions (Chapter II). Propene (industrial grade, Praxair), and oxygen (99.5%, Praxair) were used in the reactivity tests (see Chapter II for more details, pp. 111-113). In Chapter I, synthetic dry air (alphagaz1: 80% N_2, 20% O_2) from Airliquide was employed in the High temperature powder X-ray diffraction (HT-PXRD) analysis.

[2] It is important to note that the initial hydration water content of the various hydrated nitrates used in the C12A7 synthesis was not measured. Since these metal precursors are known to be hygroscopic, steps were taken to minimize the impact of moisture on the precise measurement of the precursor mass required for synthesis. All precursor containers were stored in desiccators containing silica gel desiccants, which were regularly replaced. However, the possible hydration of the metal nitrates was neglected since they were dissolved in water.

2 Methods

2.1 Catalyst synthesis

2.1.1 Preparation of pristine (undoped) nonporous and porous C12A7

In this thesis, mayenite materials with different textural properties were prepared based on the solution combustion synthesis (SCS). The details regarding the synthesis of nonporous and porous C12A7 can be found in the experimental part of Chapter I (*sections 2.4 and 2.5, pp. 73-75*).

2.1.2 Preparation of Cu-doped porous C12A7

Copper-doped mayenite materials were also prepared based on the SCS. In this case, the developed strategy to produce pristine porous C12A7 from Chapter I was adapted and used in Chapter III. The details regarding the synthesis of Cu-doped porous C12A7 can be found in the experimental part of *Chapter III* (*section 2.2, p. 159*).

2.2 Characterization techniques

Most of the experimental work reported in this thesis was carried out employing equipment from the laboratories of the Molecular Chemistry, Materials, and Catalysis (MOST) division of the Institute of Condensed Matter and Nanoscience (IMCN) (UCLouvain, Belgium). Nonetheless, Electron Paramagnetic Resonance (EPR) and Raman spectroscopic analyses were performed at the facilities of the Chemistry Faculty of the Jagiellonian University (Krakow, Poland), thanks to a mobility subvention granted by the Fédération Wallonie-Bruxelles (FW-B) to Isaac Meza Trujillo.

2.2.1 Powder X-ray diffraction (PXRD)

PXRD patterns were recorded on a Bruker-D8 advance diffractometer (Bragg-Brentano geometry) using Cu Kα radiation (λ=0.15418 nm), equipped with a LYNXEYE XE-T detector. The X-ray source was operated with a tension of 40 kV and a current of 30 mA. Diffractograms were collected between 10° and 80° (2θ) with a scan step size of 0.02°(2θ) and scanning rate of 3.8°·min^{-1}. The rotation

speed of the sample was set at 5 rpm. For analysis, all samples were placed in a Bruker silicon low background sample holder with a 20 mm diameter. To facilitate adherence of the sample to the sample holder's surface, a thin layer of conventional cosmetic cream was applied prior to adding the powder. Phase matching was carried out utilizing the International Centre for Diffraction Data (ICDD) PDF2-2004 database[29] and the software DIFFRAC.SUITE EVA provided by Bruker. Rietveld quality PXRD patterns were also acquired for quantitative phase analysis performed in *Chapter I* (*see section 2.6 for more details, p. 75*).

The crystallite size was calculated from (*211*) reflection peak, using the Scherrer equation, $L = 0.9\ \lambda / \beta \cos\theta$; where L is the crystallite size in Å, β is the full-width at half-maximum (FWHM) of the Bragg peak (*211*) plane corrected for instrumental broadening in radians, λ is the wavelength of Cu Kα (1.54178 Å), and θ is the Bragg angle in radians.

2.2.2 N_2 physisorption analysis

Textural properties were determined via N_2 physisorption in the relative pressure (P/Po) region of 0.01-0.99 at -196 °C (77 K), using a Tristar 3000 instrument (Micromeritics). Before analysis, the samples (~0.15 g) were degassed overnight under vacuum (*ca.* 1.3×10^{-4} bar) at 300 °C. The specific surface area (S_{BET}) was evaluated by the *Brunauer-Emmett-Teller* (BET) method in the relative pressure range of 0.05–0.30 (P/Po). The *pore size distribution* (PSD) was obtained from the desorption isotherm branch utilizing the *Barrett-Joyner-Halenda* (BJH) method.

2.2.3 Scanning electron microscopy (SEM)

SEM micrographs were recorded on a JEOL 7600F microscope working between 10-15 kV to analyze the morphology of the samples. Prior to the analysis, the powdered samples were placed on a piece of carbon black tape on an aluminum stub. A chromium sputter coating of *ca.* 16 nm was deposited over the samples under vacuum using a Sputter Metal 208HR (Cressington).

2.2.4 Thermogravimetric analysis-mass spectrometry (TGA-MS)

TGA-MS analysis was performed on a Mettler Toledo TGA/DSC 3+ apparatus coupled with a Pfeiffer Vacuum ThermoStar mass spectrometer. First, the sample was stabilized at 25°C for ca. 15 min under flowing dry air (100 mL·min^{-1}, 80% N_2 and 20% O_2 Alphagaz1, Air Liquide), and then heated from 25 to 900 °C at 10 °C·min^{-1}.

2.2.5 Raman spectroscopy

Raman spectra were collected on an InVia Renishaw spectrometer coupled with a confocal microscope (Leica DM LM) using an *x*50 objective lens, equipped with an 1800 l/mm grating, a slit opening of 65 µm, and a CCD detector. All spectra were recorded between 100-1600 cm^{-1} (low-spectral region) and 3000-4000 cm^{-1} (high-spectral region), operating at an excitation wavelength of 514 nm (green light) and power of *ca.* 50 mW. Each spectrum corresponds to an average of 8 accumulations. No baseline subtraction was performed in any of the spectra. Yet in some cases, the intensity of the spectrum was normalized as described in the corresponding legend of the depicted figures in each chapter.

2.2.6 Electron Paramagnetic Resonance (EPR) spectroscopy

EPR spectra were recorded at ~9.4 GHz microwave frequency (X-band) and 100 kHz modulation frequency at liquid nitrogen temperature (-196 °C) using a Bruker ELEXSYS 500 spectrometer. A microwave power of 2 mW and a modulation amplitude between 0.2-0.5 mT was applied. The spectra processing was carried out using the software provided by Bruker, while the total spin concentrations of paramagnetic species were determined from the second integral of the spectra using a standard. For instance, in *Chapter II* vanadyl sulfate ($VOSO_4 \cdot K_2SO_4$) was employed as a standard, whereas in *Chapter III* copper sulfate ($CuSO_4$) was used. For each spectrum, the relative contributions of superoxide ions (O_2^-), oxygen radical (O^-) or copper(II) species (isolated and clusters Cu^{2+}) were determined by computer simulation (deconvolution) using the program EPRsim32.[104] In some cases, where only O_2^- species was found, the spin concentration was directly obtained after comparing the second integral of the spectrum with the standard. The cumulative error from quantification by

comparison with the standard and the simulation is estimated at *ca.* 20%.

2.2.7 X-ray photoelectron spectroscopy (XPS)

XPS spectra were recorded using an SSX 100/206 spectrometer (Surface Science Instruments, USA) with Al-Kα radiation operated at 10 kV and 20 mA. Powdered samples were pressed into stainless-steel troughs of 6-mm diameter positioned on a ceramic carousel. The pressure in the analysis chamber was ~10^{-6} Pa. The analyzed area was ~1.4 mm² and the pass energy was set at 150 eV. A flood gun set at 8 eV and a Ni grid placed 3 mm above the sample surface were used for charge compensation. The following sequence of spectra was recorded: survey spectrum, C 1s, O 1s, Al 2p, Ca 2p, Cu 2p, and C 1s again to check the stability of charge compensation with time. The binding energy scale was referenced to the C-(C,H) component of the C 1s peak of adventitious carbon contamination fixed at 284.8 eV. Data treatment was performed with the CasaXPS program (Casa Software Ltd, UK). The spectra were decomposed with the least-squares fitting routine provided by the software with a Gaussian/Lorentzian (85/15) product function after subtraction of a non-linear Shirley baseline. Atomic concentrations were calculated using peak areas normalized based on the acquisition parameters and sensitivity factors provided by the manufacturer.

2.2.8 Diffuse reflectance UV-Visible (DR-UV-Vis) spectroscopy

DR-UV-Vis spectra were recorded in the 200-800 nm spectral range, with a sampling interval of 0.5 nm and a slit width of 2 nm, on a UV-Vis-NIR spectrometer UV-3600 Plus (Shimadzu) equipped with a Praying Mantis (Harrick) collection system suitable for solid material analysis. The background of the samples was calibrated using a Spectralon® Diffuse Reflectance Standard Reference pellet. The background measurements were conducted in the same wavelength as the recorded sample spectra. The data manipulation was performed using the Shimadzu UV software package (UVProbe 2.62), and Kubelka–Munk transformation was calculated from the background corrected reflectance data. The position of the absorption edge was determined from the optical absorption edge by plotting the Kubelka–Munk transformation data against the photon energy values. The y-

axis (intensity) of the Kubelka–Munk transformation data were normalized by the maximum value to ease the visualization and comparison of the different spectra.

2.2.9 Temperature programmed reduction (TPR-H_2)

TPR-H_2 experiments were performed on a CATLAB-PCS Microreactor coupled to a QGA mass spectrometer (Hiden Analytical). About 0.1 g of sample was used for the measurements. Prior to the TPR analysis, the samples were heat-treated from 50 to 400 °C (10 °C·min^{-1}) under Ar flow (40 mL·min^{-1}) and held for 1 h, then it was cooled down to 50°C under the same atmosphere. Next, it was subsequently exposed to a flow (50 mL·min^{-1}) of 0.5% H_2/(N_2+Ar) and heated in the range of 50-800 °C at a heating rate of 10 °C·min^{-1}. The detected mass/charge ratios were: 1(H_2); 18(H_2O); 28(CO); 32(O_2); 40(Ar); and 44(CO_2).

2.2.10 Temperature programmed oxygen desorption (O_2-TPD)

O_2-TPD experiments were carried out on a CATLAB-PCS Microreactor coupled to a QGA mass spectrometer (Hiden Analytical). About 0.15 g of sample was used for the measurements. The temperature program was: i) dwelling step at 50°C for 0.5 h under Ar flow (20 mL·min^{-1}); ii) heating from 50 to 900 °C (10 °C·min^{-1}) under the same atmosphere, iii) plateau 900°C for 0.25 h. The detected mass/charge ratios were: 1(H_2); 18(H_2O); 28(CO); 32(O_2); 40(Ar); and 44(CO_2).

2.3 Catalytic performance evaluation

Depending on the aim of each Chapter, a catalytic evaluation system based on the carbon black (as soot model substitute) combustion (*Chapters I and III*) or propane oxidation (*Chapter II*) was selected.

2.3.1 Catalytic carbon black combustion

In *Chapters I* and *III*, the catalytic performance of pristine and Cu-doped C12A7, respectively, was evaluated in CB oxidation reaction. These catalytic experiments were investigated by temperature-

programmed combustion (TPC) employing a frequently used carbon black (CB) powder (Printex U, Degussa) as a diesel soot model.[105,106] Unless otherwise indicated, in each catalytic test, 200 mg of Printex-U and catalyst (5%wt of CB) were hand-mixed in a mortar for ~10 min, defined as tight-contact conditions. Then, 50 mg of resulting mixture were loaded inside a quartz tube (microreactor, i.d. = 0.4 mm) between two layers of silica wool. All the runs were performed under atmospheric pressure from 50 to 800 °C at a heating rate of 10 °C·min^{-1} in a CATLAB-PCS Microreactor (Hiden Analytical) coupled to a QGA (Hiden Analytical) mass spectrometer. The analyzed mass/charge ratios were: 2(He); 18(H_2O); 28(CO); 32(O_2); 40(Ar); and 44(CO_2). Unless otherwise indicated, an inlet gas flow of 5% O_2 balanced with He (Praxair) was fed at a flow rate of 50 mL·min^{-1}. The evolved gases from the CB combustion are typically plotted as TPC curves displaying the evolution of CO_2 and CO as a function of the temperature.

In *Chapters I* and *III,* where the CB oxidation was employed as a reaction probe, one commonly shared activity indicator was the temperature (T_{peak}) at which the highest combustion rate is attained (*i.e.*, maximum production of CO_x), determined from the TPC curves. Besides, other activity indicators were also used to highlight the performance of pristine and doped C12A7 during catalytic CB combustion, which is described in detail in the experimental part of each Chapter. Additionally, the methodology followed in carrying out the recyclability test discussed in Chapter III is described separately in its corresponding experimental part.

The selectivity of CO_2 (S_{CO_2}) to the total amount of produced CO_x from the CB oxidation was defined as:

$$S_{CO_2}(\%) = 100 \times C_{CO_2} / \left(C_{CO_2} + C_{CO}\right)$$

where C_{CO_2} and C_{CO} are respectively the total concentration of CO_2 and CO obtained by integrating the area underneath the corresponding TPC curve.

2.3.2 Propane oxidation reaction

The propane oxidation process was chosen in *Chapter II* to assess the impact of the population distribution of extra-framework oxygen

species on the catalytic performance of C12A7. The tests were performed in catalytic setup working at atmospheric pressure guaranteeing a pressure drop less than 0.1 mbar. Before the test, in the case of porous C12A7, the sample was pelletized, hand-ground using a mortar, and then sieved to obtain a desired fraction with a particle size between 200-315 µm. For the non-porous one, the sample was directly, without pelletizing it, hand-ground and sieved to get the same particle size fraction as in the former case. The catalytic bed was composed of 150 mg of C12A7 catalyst ($200 < d_p < 315$ µm) mixed with 350 mg of fragmented quartz glass ($d_p > 350$ µm) to warrant a plug flow behavior and to avoid heat transfer limitations. The mixture was loaded inside a U-shaped fixed bed quartz reactor and placed at the center of a vertical tubular furnace. The catalytic bed temperature was monitored and controlled using a K-type thermocouple placed in close intimacy with the fixed bed and connected to a PID controller. The catalytic tests were performed between 30 and 650 °C (ΔT = 10 °C·min^{-1}) with consecutive isothermal dwelling stages. The total gas flow was 40 mL·min^{-1} unless otherwise mentioned. The propane and oxygen concentrations were adjusted depending on the experiment conditions. For instance, in a perspective of a total oxidation reaction, the concentration of propane was adjusted to 1000ppmv by diluting with a mixture of oxygen and nitrogen in order to obtain a molar ratio equivalent to synthetic air (80% N_2 and 20% O_2). Conversely, under operational conditions for a selective oxidation reaction, the typical gases concentrations were: 8% C_3H_8, 8% O_2, and 84% N_2, unless otherwise stated. The exhaust gas stream coming from the reactor outlet was periodically analyzed by an on-line gas chromatograph (GC, *vide infra*). At each isothermal plateau where the catalytic performance was evaluated, the temperature was dwelled to warrant at least five injections under steady conditions.

2.3.2.1 *Expression of catalytic performance*

In order to evaluate the catalytic performance, catalytic outcomes were express in terms of conversion and selectivity according to the following equations:

$$\textbf{Conversion (\%)} = X\,(\%) = \frac{n_{i0} - n_i}{n_{i0}} \times 100$$

where, n_{i0} is the initial molar concentration of propane and n_i is the molar concentration of propane at a given reaction time and temperature.

$$\textbf{Selectivity (\%)} = S\ (\%) = \frac{n_j}{\sum n_j} \times 100$$

where, n_j is the molar fraction of carbon in a product *j* (*e.g.*, CO_2) formed at a given reaction time and temperature. $\sum n_j$ corresponds to the sum of all carbon molar fractions connected with all the detected products at a given reaction time and temperature. This latter regard considers that the carbon balance is equivalent to 100%. For those products containing less than three carbon atoms, correction factors were employed to calculate the selectivity (*e.g.*, 1/3 for CO_2 and CO or 2/3 for C_2H_4).

2.3.2.2 *Gas chromatography (GC) equipment*

The reaction outlet gases were analyzed using an on-line GC instrument (VARIAN 3800) equipped with two detectors and three columns. All gaseous compounds in the stream were first separated using a Hayesep column (2m x 1/8'' x 0.085'' Ni packed with Hayesep Q, 80/100 mesh, Restek™). Then, the permanent gases analysis (O_2, N_2, CO and CO_2) were separated and quantified, using a molecular sieve column (5A, 6' x 2mm ID, 80/100 mesh, Restek™) coupled to a thermal conductivity detector (TCD). Besides, the hydrocarbons (CH_4, C_2H_4, C_3H_6, and C_3H_8) were separated and measured employing a Rt®-Silica BOND PLOT column (length: 30m, ID: 0.32 mm, Restek™) and a flame ionization detector (FID). The complete gas analysis lasted 15.2 min per injection.

CHAPTER I

Improving mayenite (C12A7) textural properties by unconventional preparation routes towards an effective improvement of its catalytic activity

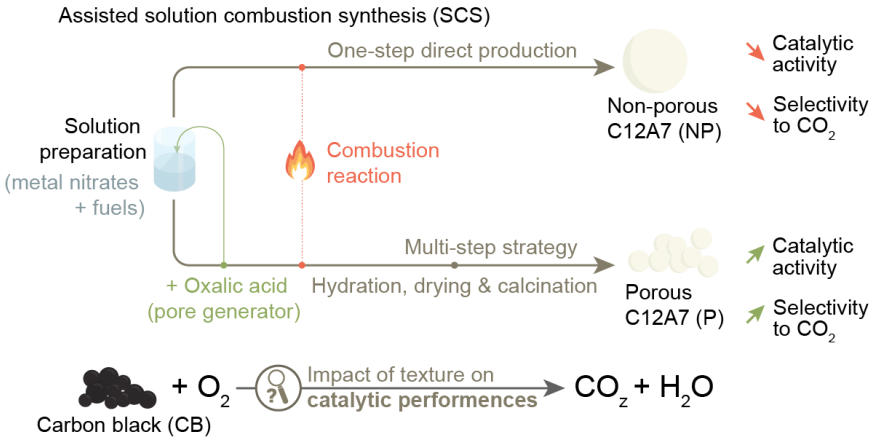

Abstract

This first chapter reports on new, cost-effective, and simple methods for producing mayenite (C12A7) at lower temperatures. In particular, one strategy overcomes the constraints of preparing C12A7 by the conventional ceramic route, leading to enhanced textural properties. In a first attempt, we successfully fabricated C12A7 starting from 250°C by a one-step solution combustion synthesis (SCS) employing Al and Ca nitrates and urea and β-alanine. We showed that a proper selection of the furnace temperature to trigger the ignition permits the control of the phase purity and crystallinity degree of C12A7. However, any variation in the furnace temperature or fuel-to-oxidizer ratio proved ineffective in improving the specific surface area of the prepared C12A7 materials. Consequently, the addition of oxalic acid was implemented in the former protocol, easing the production of porous mayenite by a multi-step protocol based on the preparation of an initial precursor by SCS, which was hydrated, filtered, dried, and calcined. We showed that the textural properties and crystallinity could be tuned by varying the temperature during the calcination step. Hence, this second approach made possible the formation of porous mayenite from temperatures as low as 275°C, reaching remarkably high specific surface areas and large pore volumes. Finally, we demonstrated that mayenite textural properties enhancement effectively promoted its catalytic properties, prompting the carbon black oxidation at low temperatures while at the same time favoring CO_2 production over CO.

Most of the results presented in this chapter have been published in:

Meza-Trujillo, I., Devred, F., & Gaigneaux, E. M. (2019). Production of high surface area mayenite (C12A7) via an assisted solution combustion synthesis (SCS) toward catalytic soot oxidation. Materials Research Bulletin, ***119***, 110542.

1 Introduction

As exposed in the General Introduction (*see section 5, pp. 34-44*), C12A7 shows to be a promising contender in the field of heterogeneous catalysis, in particular in oxidation reactions. Yet, to exploit the full potential of C12A7 as a catalyst, we first needed to explore new preparation routes to tackle the constraints of producing C12A7 via the conventional ceramic route (*e.g.*, low surface area and negligible porosity). In this chapter, we report how we prepared C12A7 with enhanced textural properties, with the underlying aim of effectively improving its catalytic activity (*e.g.*, conversion). To that end, we have synthesized mayenite via two preparation routes based on the solution combustion synthesis (SCS).

In the first case, leveraging on the highly exothermic nature of the self-sustained combustion reaction, we speculated that the former could provide the necessary amount of heat to reach the required temperature to form the C12A7 phase without needing additional input of external heat. Thus, we could circumvent the necessity of calcining the solid for prolonged periods at elevated temperatures, as required in the solid-state synthesis. Consequently, in this first method, we investigated the possibility of producing C12A7 via a double-fuel mixture approach using urea and β-alanine, and Ca and Al nitrates (playing as oxidizers in the SCS). Precisely, we explored the impact of varying the furnace temperature and the fuel-to-oxidizer ratio (ϕ) on the combustion process (type of combustion and duration until the self-sustained ignition) and physicochemical properties of the final product (specific surface area, crystallinity, and phase purity).

In the second stage, based on the outcomes of the optimized method from the first stage, we modified it by adding oxalic acid, aiming at producing porous C12A7 by a multi-step protocol. A previous study related to the synthesis of cobalt ferrite ($CoFe_2O_4$) suggested that oxalic acid can act as a porogeneous and combustion retarding agent, improving the textural properties.[107] Here, we studied the effects of varying the amount of oxalic acid on the combustion process (*e.g.*, intense flame, smoldering, or explosion) and physical properties (color, morphology, and texture) of the synthesized powder obtained after the combustion reaction. Additionally, we investigated the influence of modifying the heat-treatment temperature of the last step (calcination)

of this second multi-stage approach on C12A7 crystallinity degree and textural properties.

Finally, we examined and compared the catalytic performances of the most promising C12A7 catalysts synthesized through the two methods to assess the benefits of boosting the textural properties of C12A7 in the carbon black oxidation reaction. The influence of the contact mode between catalyst and carbon particles is also studied and discussed.

2 Experimental

2.1 Materials

The grade purity and manufacturer of the chemical reagents employed in the C12A7 materials preparation can be found in the general Experimental Section of this thesis (*p. 56*).

2.2 General considerations and overall combustion reaction conception

In this study, hydrated nitrate salts were chosen as sources of Ca and Al since they contain the oxidizing agent (NO_3^-), which is fundamental for the redox reaction, but also because they are highly soluble in water allowing the formation of a homogenous solution. As stated in the general introduction, the successful preparation of the desired material relies on the appropriate fuel selection to react with a specific metal salt (*see General Introduction, section 4.2, pp. 30-34).* Based on the literature,[92] urea (CH_4N_2O) and β-alanine ($C_3H_7NO_2$) were selected as suitable organic fuels to interact with Al and Ca nitrates, respectively.

The combustion reactions between metal nitrates salts and organic fuels selected in this study were conceived based on the propellant chemistry and related thermodynamic calculations, assuming complete combustion, where CO_2, N_2, and H_2O are presumed to be the most likely formed gaseous products over other plausible compounds.[87,108,109] However, during the preparation of our samples, the presence of brown fumes were sometimes observed which may be attributed to the evolution of NO_x from the thermal decomposition of the

reagents. Nevertheless, these gaseous species as well as other secondary plausible gases (i.e., NH_3, and HNCO) were not considered in the following overall stoichiometric reaction calculations, as usually done in the literature.[87] Additionally, considering that both nitrates react separately with each fuel, the following equilibrium combustion reactions are presented below.

$$12Ca(NO_3)_2{\cdot}4H_2O+14Al(NO_3)_3{\cdot}9H_2O + nCH_4N_2O + (3/2\,n - 165/2)O_2 \rightarrow Ca_{12}Al_{14}O_{33} + nCO_2 + (174+2n)H_2O + (33+n)N_2 \quad (1.1)$$

$$12Ca(NO_3)_2{\cdot}4H_2O + 14Al(NO_3)_3{\cdot}9H_2O + mC_3H_7NO_2 + (15/4\,m - 165/2)O_2 \rightarrow Ca_{12}Al_{14}O_{33} + 3mCO_2 + (174+ 7/2\,m)H_2O + (33+ m/2)N_2 \quad (1.2)$$

Based on the method proposed by Jain regarding propellant chemistry, it is possible to calculate the elemental stoichiometric coefficient (ϕ).[108] The latter, also referred to as the fuel-to-oxidizer ratio, is a proportion between the total oxidizing and reducing valences of the metal salts and fuels, respectively. On the one side, metals, carbon, and hydrogen are regarded as reducing partners and are given a positive valence. In this regard, the corresponding reducing valence for metal is taken from its oxidation state in the metal precursor (*e.g.*, in $Ca^{2+}(NO_3)_2$ calcium works with +2), whereas, for carbon (+4), and hydrogen (+1), they come from their oxidation state in the formed by-products. On the other hand, oxygen (oxidizer) possesses a negative valence (-2), whereas nitrogen is assumed to work with neutral valence (0). This latter consideration is accepted from the assumption that only molecular nitrogen is produced by a complete combustion reaction.[87,108] For instance, the reducing valence of 1 mol of urea (CH_4N_2O) is (+4+4+0-2) = +6, whereas the oxidizing valence of 1 mol of Ca nitrate [$Ca(NO_3)_2{\cdot}4H_2O$] is (+2+0-12) = -10. It is worth mentioning that hydration water in the metal salt (*e.g.*, 4 H_2O molecules in calcium nitrate) does not modify the overall compound valence.[87,109] Thus, the *n* moles of urea and *m* moles of β-alanine can be written in terms of ϕ by employing the following equation.

$$\phi = \frac{(-1)\times \text{moles}_{\text{fuel}} \times \sum(\text{valences of all oxidizing and reducing elements in fuel})}{\text{moles}_{\text{oxidizer}} \times \sum(\text{valences of all oxidizing and reducing elements in oxidizer})} \quad (1.3)$$

For instance, the oxidizer-to-fuel ratio for Eq. (1.1) can be calculated as follows:

$$\phi = \frac{(-1)\times n_{\text{moles urea}} \times \sum[1C\times(+4)+4H\times(+1)+2N\times(0)+1O\times(-2)]}{\{12\times\sum[1Ca\times(+2)+2N\times(0)+6O\times(-2)]+14\times\sum[1Al\times(+3)+3N\times(0)+9O\times(-2)]\}}$$

$$\phi = \frac{-n\times(+6)}{12\times(-10)+14\times(-15)} = \frac{-6n}{-330}$$

while for Eq. (1.2), it corresponds to:

$$\phi = \frac{(-1)\times m_{\text{moles }\beta\text{-alanine}} \times \sum[3C\times(+4)+7H\times(+1)+1N\times(0)+2O\times(-2)]}{\{12\times\sum[1Ca\times(+2)+2N\times(0)+6O\times(-2)]+14\times\sum[1Al\times(+3)+3N\times(0)+9O\times(-2)]\}}$$

$$\phi = \frac{-m\times(+15)}{12\times(-10)+14\times(-15)} = \frac{-15m}{-330}$$

Consequently for Eq. (1.1) $n = 55\phi$, whereas for Eq. (1.2) $m = 22\phi$. The respective equilibrium overall combustion expressed as a function of the fuel-to-oxidizer ratio is obtained by combining Eqs. (1.1) and (1.2), assuming an equivalent proportion between both reactions with a fuel ratio, urea/β-alanine=5/2.

$$12Ca(NO_3)_2{\cdot}4H_2O + 14Al(NO_3)_3{\cdot}9H_2O + 55/2\,\phi CH_4N_2O + 11\phi C_3H_7NO_2 + 165/2\,(\phi-1)O_2 \rightarrow Ca_{12}Al_{14}O_{33} + 121/2\,\phi CO_2 + 187/2\,\phi H_2O + 33(\phi+1)N_2 \quad (1.4)$$

The ϕ ratio also reflects the oxygen demand during the combustion reaction. Under stoichiometric conditions (ϕ = 1), it is considered that the combustion reaction does not require an exchange of oxygen with the atmosphere. Conversely, working below (ϕ < 1) or above (ϕ > 1) stoichiometric conditions, molecular oxygen is either produced (low-fuel regime) by the combustion reaction or required to achieve total combustion of the fuel(s) (high-fuel regime), respectively.

2.3 Thermodynamic considerations and calculations

The highly exothermic combustion reaction occurring in this kind of synthesis can lead to exceptionally high temperatures within a very short time due to high rate of reaction. Actually, the reached temperature in the former conditions can be compared to the adiabatic flame temperature. Therefore, the total amount of released heat by the combustion reaction under adiabatic conditions is expressed as the

difference between the enthalpies of formation of products and reagents, also known as heat of reaction (ΔH^{o}_{rx}) (*see* Eq. (1.5)). Besides, the theorical adiabatic combustion temperature (T_{ad}) can be calculated by solving Eq. (1.6). All the calculations were carried out using HSC Chemistry 5.1© software[110] employing existent thermodynamic data summarized in Table 1.1.

$$Q=\Delta H^{o}_{rx}=\sum n_p \Delta H^{o}_{f\ products}-\sum n_r \Delta H^{o}_{f\ reagents} \quad (1.5)$$

where, n is the number of moles of a specific reagent or product dictated by the overall combustion reaction, Eq.(1.4), and ΔH^{o}_{f} is the standard heat of formation of a specific compound.

$$-\Delta H^{o}_{rx}=\int_{To}^{Tad}\left(\sum n_i Cp_i\right)_{products} dT \quad (1.6)$$

where, n_i is the number of moles of a specific product, Cp_i is heat capacity as a function of the temperature under isobaric conditions, T_0 is the initial temperature, usually standard temperature (25 °C), and T_{ad} is the adiabatic combustion temperature.

Table 1.1. Relevant thermodynamic data[a] for calculations

Substance	**ΔH^{o}_{f} (kJ mol^{-1})**	**Cp (J mol$^{-1}\cdot$K^{-1})**
$Ca(NO_3)_2\cdot 4H_2O_{(c)}$	-2132.88	-
$Al(NO_3)_3\cdot 9H_2O_{(c)}$	-3757.10	-
$CH_4N_2O_{(c)}$	-333.10	-
$C_3H_7NO_{2(c)}$	-558.00	-
$12CaO\cdot 7Al_2O_{3(c)}$	-19429.99	$1263.4 + 0.274\cdot T - 2.31x10^{7}\cdot T^{-2}$
$CO_{2(g)}$	-393.51	$22.2 + 5.98x10^{-2}\cdot T - 3.50\ x10^{-5}\cdot T^{2} - 7.46\ x10^{-9}\cdot T^{3}$
$H_2O_{(g)}$	-241.83	$32.2 + 1.92x10^{-3}\cdot T + 1.06\ x10^{-5}\cdot T^{2} - 3.59\ x10^{-9}\cdot T^{3}$
$N_{2(g)}$	0	$28.9 - 1.57x10^{-3}\cdot T + 8.08\ x10^{-6}\cdot T^{2} - 2.87\ x10^{-9}\cdot T^{3}$
$O_{2(g)}$	0	$25.5 + 1.52x10^{-2}\cdot T - 7.15\ x10^{-6}\cdot T^{2} + 1.31\ x10^{-9}\cdot T^{3}$

[a] Data taken from diverse programs and handbooks[110–112]

2.4 Single-step mayenite preparation protocol via solution combustion synthesis using a double fuel-approach

The quantities of all reagents were determined based on the overall combustion reaction Eq. (1.4), assuming to yield 5 g (0.00036 mol) of C12A7. In each synthesis, varying amounts of urea and β-alanine were engaged depending on the selected ϕ ratio, ranging between 0.5 and 2, yet always keeping a constant molar ratio between the fuels (urea/β-alanine:5/2). Stoichiometric amounts of metal nitrates (Ca/Al:12/14) were always kept the same in all the experiments. All reagents were added into a borosil vessel (300 mL) containing *ca.* 10 mL of distilled water. The solution mixture was heated up to 50°C under magnetic stirring to dissolve all precursors. Once a clear solution was obtained, the container was introduced into a pre-heated muffle furnace to trigger the combustion reaction. In this study, several furnace temperatures were tested, varying between 250-500 °C. At first, the solution underwent dehydration and then started to boil and swell, releasing large amounts of fumes and leading to a frothing gel. As soon as the ignition temperature was attained, an exothermic self-sustaining reaction took place (Figure 1.1), giving way to a solid product in a matter of a few seconds (~15 s). Alternatively, the latency time of the sample in the furnace, corresponding to the lapse between the introduction of the container into the furnace and its remotion after the end of the combustion reaction, highly depends on the furnace temperature, reagents amount, and solvent volume. Finally, the solid powder yielded by the combustion reaction was quenched to room temperature, manually ground using an agate mortar, sieved, and stored for further characterization. The samples generated using this approach are designated as ϕ-NP-X, where ϕ represents the fuel-to-oxidizer ratio, and "X" denotes the operational temperature of the preheated furnace during their synthesis. For instance, a sample prepared under stoichiometric conditions at 500°C would be labeled: *1-NP-500*.

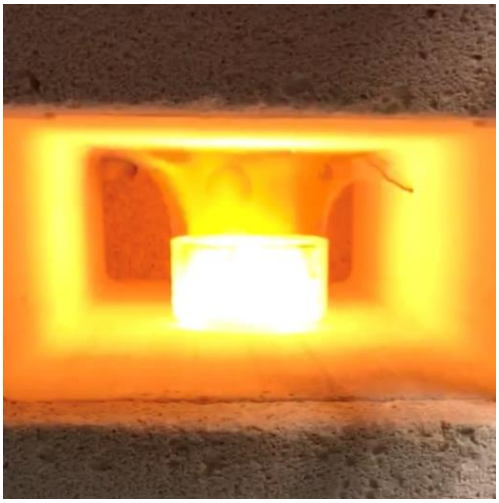

Figure 1.1. Combustion reaction using a double-fuel mixture (urea and β-alanine) under stoichiometric conditions (ϕ = 1)

2.5 Preparation of porous mayenite via a multi-step assisted solution combustion synthesis

The addition of oxalic acid was implemented in a second stage to improve the textural properties of C12A7 inspired from a protocol for the preparation of a cobalt ferrite by SCS.[107] Here, we express the concentration of oxalic acid (afterward denoted as OA) as a weight ratio between the mass of OA and the expected mass of C12A7. In each synthesis, varying amounts of OA were introduced, ranging from 0.25-1 (g OA·g^{-1} C12A7). Based on the overall combustion reaction Eq.(1.4), stoichiometric quantities (ϕ = 1) of metal nitrates (Ca/Al:12/14) and fuels (urea/β-alanine:27.5/11) to produce 5 g of C12A7 were added into a borosil container (300 mL) and dissolved with *ca.* 5 mL of preheated distilled water (80°C) under magnetic stirring at 80 °C. Next, a specific amount of OA (*x* g per g of expected C12A7) was dissolved in ~3 mL of hot distilled water (80°C) and was then added to the former solution until obtaining a homogeneous solution. It is worth mentioning that the addition of OA altered the initial stoichiometric (ϕ = 1) ratio between oxidizers and fuels, promoting a fuel-rich regime, considering that OA can also be regarded as a fuel. Then, the pot containing the precursor solution mixture was placed in a preheated furnace at 500 °C to trigger the combustion reaction. The as-obtained powder from the combustion reaction, denoted *x*@OA

(where "*x*" represents the OA/C12A7 mass ratio), was quenched to room temperature, hydrated with hot distilled water (80 °C, 100 mL $H_2O \cdot g^{-1}$ solid) under magnetic stirring for *ca.* 20 min, filtered, and dried at 110 °C overnight. The resulting as-dried solid (hereafter denoted as *x*@OA-P) was hand-ground and calcined between 300-800°C in a pre-heated furnace for 4 hours under static ambient air. The calcined solid powder (denoted as P-Y, where "Y" stands for the calcination temperature) was cooled down to room temperature, hand-ground, and stored for further characterization.

2.6 Catalyst characterization

C12A7 samples were characterized by PXRD, N_2 physisorption, TGA-MS, and SEM techniques, as described in the general Experimental Section (*p. 56*). Specific analysis conditions used in this Chapter are described hereafter.

Rietveld quality powder X-ray diffraction patterns were recorded on a Bruker-D8 advance diffractometer. The PXRD patterns were acquired in a broad 2θ range: 10-100° with a scanning rate of *ca.* $0.46° \cdot min^{-1}$. A pseudo-Voigt function for the peak profile modeling was used during the refinement, whereas the background was manually selected and not refined. The Rietveld refinements were performed i) to determine the weight fractions of each detected phase in the SCS-derived powders and ii) to calculate the lattice parameters of C12A7. The crystallography data for the refinements were extracted from the crystal information files (CIFs) belonging to the Crystallography Open Database (COD).[28] The FullProf suite and its graphical tool Winplotr were used to accomplish the refinements.[113]

For the high temperature powder X-ray diffraction (HT-PXRD), the XRD instrument configuration was modified by adding an XRK 900 (Anton Paar) chamber, which allows the analysis at different temperatures between room temperature and 900 °C. Prior to the analysis, the as-dried precursor was loaded in a ceramic sample holder inside the chamber and purged with synthetic dry air (alphagaz1: 80% N_2, 20% O_2, Airliquide). A K-type thermocouple coupled to the sample holder was used to control and monitor the sample temperature during the analysis. The temperature was raised from 25 to 800 °C under flowing synthetic dry air, with a heating rate of $10°C \cdot min^{-1}$. At each

measurement, the temperature was dwelled constant during the entire data collection. Reported temperature is the sample temperature and not the set temperature. The diffractograms were collected in a reduced 2θ range, between 10 and 50° with a scanning rate of 4.5°·min^{-1}, to minimize the presence of reflection peaks raising from the Kapton® layer located in the external structure of the chamber. Catalytic performances evaluation.

The catalytic tests were performed as already described in the general Experimental Section (*see section 2.3.1, p. 60*). Still, some specificities of the experiments reported in the present Chapter are described below. In each catalytic test, 50 mg of carbon black and catalyst (5% of the mass of CB used, *i.e.*, 2.5 mg) were either hand-ground in a mortar for *ca.* 10 min (tight-contact conditions) or gently mixed together inside a container using a spatula for *ca.* 2 min (loose-contact conditions). In all the tests, an inlet gas flow of 5% O_2 balanced with He (Praxair) was fed at a flow rate of 50 mL·min^{-1}. The results are typically shown as TPC curves plotting the evolution of CO_2 and CO along the temperature ramp applied. In the case of unimodal TPC curves (*i.e.*, with only one peak of combustion observed), the temperature values corresponding to the start of the oxidation process (T_{onset}) and the one at which the highest combustion rate is attained (*i.e.*, maximum production of CO_x) were taken as activity indicators of the tested catalysts. For multimodal TPC curves (*i.e.*, presence of more than one peak of combustion), the maxima values of all peaks were reported and compared with the former case. The produced amounts of CO_2 and CO were obtained by integrating the area under the corresponding curves obtained from the TPC runs. The selectivity towards CO_2 was calculated according to the equation reported in the general Experimental Section (*p. 60*).

3 Results and discussion

3.1 Single-step preparation of C12A7 via SCS using double-fuel approach

The results presented in this part are related to the first preparation method described in the previous section. Herein, the influence of the fuel-to-oxidizer ratio and the furnace temperature on the combustion process (type of combustion), latency time in the furnace, and

physicochemical properties of the final product (surface area, crystallinity, and phase purity) are investigated and discussed.

3.1.1 Thermodynamic aspects and qualitative analysis of the synthesized powders

Figure 1.2 displays the thermodynamic calculation results by employing several SCS recipes based on the overall combustion reaction (Eq. (1.4)) with ranging values of fuel-to-oxidizer ratio (ϕ). The negative values of the heat of reaction (Figure 1.2a) showed that the combustion reactions with ϕ ranging from 0.75-2 are highly exothermic, whereas at 0.5 the reaction turns out endothermic. It can also be seen that the standard enthalpy of reaction substantially increases with rising the ϕ ratio, where at ϕ = 2, the most exothermic one is noticed. The calculated adiabatic temperature values for those exothermic reactions follow a rising trend, reaching the highest temperature (1727 °C) at the maximum studied ϕ value. It is also noted that the calculated adiabatic temperature magnitude highly depends on the type(s) of fuel(s) considered for the combustion reaction. For instance, under stoichiometric conditions (ϕ = 1), by employing β-alanine as single fuel instead of a mixture, a higher theoretical adiabatic temperature is obtained in contrast to the temperature depicted by using a fuel mixture. Alternatively, by employing urea alone, a lower temperature is shown. Based on this theoretical analysis, using β-alanine as the sole fuel source, instead of urea, should significantly favor the C12A7 phase formation. Additionally, working with fuel-rich compositions while using a mixture of urea and β-alanine should also contribute to the C12A7 phase development, considering that the reaction exothermicity and the adiabatic temperature are boosted with the ϕ ratio increasing. Yet, the experimental results showed a completely different story, as will be discussed in the next section.

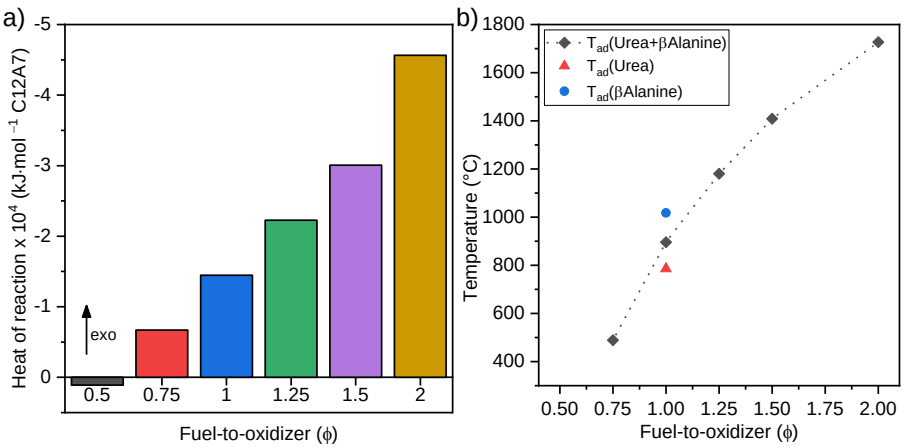

Figure 1.2. Thermodynamic calculated a) standard enthalpy of reaction (heat of reaction), and b) adiabatic combustion temperature (T_{ad}) for varying fuel-to-oxidizer ratios. Additional calculated data employing only a single fuel (urea or β-alanine) are displayed for comparison.

Depending on the composition of the redox mixture, namely the amount of fuel, the fuel-to-oxidizer ratio showed to affect not only the combustion process but also the form and density of the solid produced. Figure 1.3 displays the morphology of the different powders yielded from the combustion reaction using a fuel mixture approach with ranging fuel-to-oxidizer ratios.

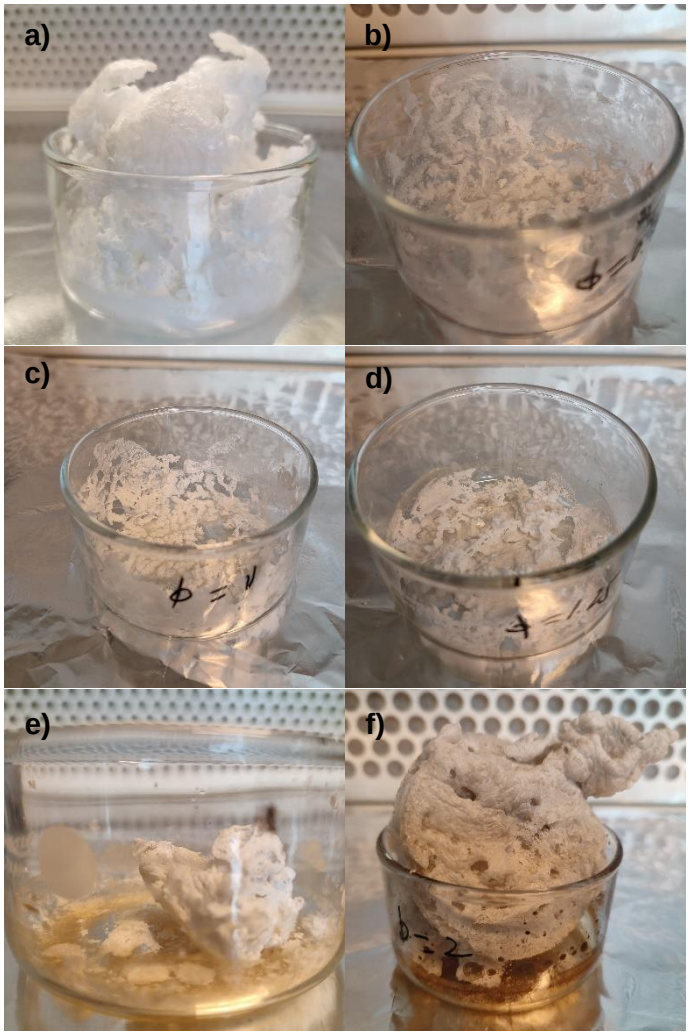

Figure 1.3. As-prepared powders yielded by the combustion reaction with ranging fuel-to-oxidizer ratios: a) 0.5, b) 0.75, c) 1.0, d) 1.25, e) 1.5, and f) 2.0

It can be noticed that the volume occupied by the solid, its morphology, and its color vary as a function of the fuel-to-oxidizer ratio, being more pronounced at the lowest and highest ϕ values. For instance, under stoichiometric conditions (ϕ = 1) and at ϕ values close it, the combustion reaction took place in the entire volume with the appearance of an intense glowing flame (see Figure 1.1) producing a dense colorless coral-like solid (Figures 1.3 b-d). This shows that small variations ϕ did not have a noticeable impact in the way the combustion takes place or in the physical properties of the obtained solids.

Conversely, under lean ($\phi < 0.75$) or fuel-rich ($\phi > 1.25$) conditions, the combustion went into a smoldering mode, while localized flames were sometimes noticed at high ϕ ratios. The products were either colorless (Figure 1.3a, $\phi = 0.5$) or greyish (Figure 1.3f, $\phi = 2$) voluminous powders depending on the fuel content of the initial redox mixture. After the synthesis, the sample containers of those recipes working with high fuel-to-oxidizer ratios ($\phi \geq 1.5$) were coated at the bottom with a brownish layer, which was likely associated with incomplete combustion leading to the formation of residual fuel deposits. The latter colored deposit was also noticed in the containers of those samples prepared at low furnace temperatures (<500°C). The mass of the powders recovered after the combustion reaction was constantly consistent with the expected one (*e.g.,* 5 g) from the stoichiometric calculations. Yet, in some cases, depending on the employed ϕ, the voluminous fluffy powder overflowed the container. Consequently, some losses inevitably occurred.

3.1.2 Characterization of the as-synthesized C12A7 powders

As exposed in the previous section from a thermodynamic perspective, the mayenite synthesis via a single-fuel approach using β-alanine seems to be the best choice to prompt the formation of the C12A7 phase, rather than urea. Nevertheless, the experimental results showed that none of these fuels led to the production of the desired C12A7 phase after the combustion reaction. By employing β-alanine, PXRD analysis revealed that the obtained solid was amorphous (Figure 1.4). In contrast, by using urea, even though the obtained powder was crystalline, all the diffraction lines were attributed to calcium nitrate (Figure 1.4). Thus, in neither of these conditions C12A7 was formed. Similar results have been reported by other authors when preparing distinct calcium aluminate materials via a single-fuel approach.[90,92]

In light of this, our findings demonstrate that when seeking for the best recipe to prepare a chosen material via SCS, the fuel selection cannot be exclusively based on theoretical thermodynamic calculations, such as the adiabatic temperature. Consequently, based on a previous report by Ianoş *et al*.[92] on the successful preparation of single-phase tricalcium aluminate (C3A) via SCS employing a fuel blend, we decided to explore the possibility of producing C12A7 by this

novel approach considering that C3A and C12A7 belong to the same calcium aluminate family.

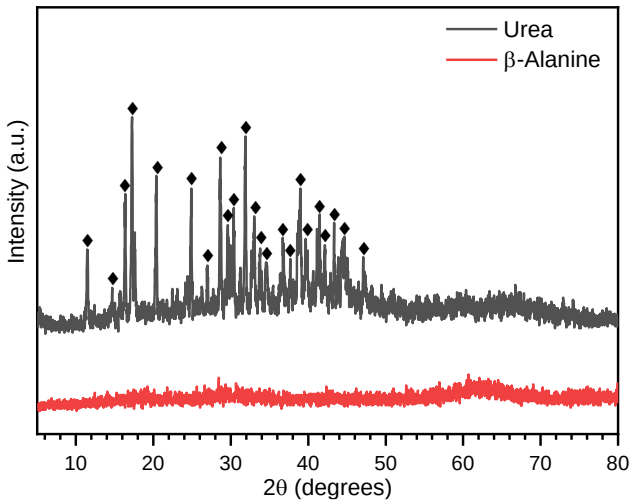

Figure 1.4. PXRD patterns of the synthesized powders by SCS using a single-fuel. The diamond icon represents the peaks of $Ca(NO_3)_2{\cdot}4H_2O$ (JCPDS-card 09-0413).

By firing a solution containing a stoichiometric mixture of fuels and metal nitrates (ϕ = 1) at different furnace temperature, we noticed that the combustion reaction promoted the direct formation of C12A7 as the predominant phase (Figure 1.5 and Table 1.2). At a first glance, PXRD analysis revealed that the mayenite phase was promptly formed from temperatures as low as 250 °C, by comparing our experimental diffractograms with the C12A7 reference pattern (JCPDS-card 09-0413). Besides, the occurrence of two other crystalline phases was also depicted, whose reflections matched with the reference PXRD patterns of monocalcium aluminate ($CaAl_2O_4$: CA; JCPDS-card 23-1036) and tricalcium aluminate ($Ca_3Al_2O_6$: C3A; JCPDS-card 38-1429). However, a careful examination of the diffractograms showed (inset Figure 1.5) that an increase in the furnace temperature from 250°C to 500°C gradually promoted the disappearance of the concomitant minor phases. The latter observation is illustrated by the intensity reduction of the principal reflections of CA and C3A at 30.09° (*123*) and 33.20° (*440*), respectively. Thus, we highlight that an appropriate furnace temperature selection is imperative to effectively promote the C12A7 phase formation over the other side phases. The calculated lattice parameter (*a*) varied between 11.974-11.977 Å for all the samples (entries 1-4, Table 1.2), which are in close agreement with

the one reported in the literature for pure synthetic mayenite (a=11.989 Å)[24–26], confirming once more the occurrence of the C12A7 phase. In addition, the high crystallinity degree of the SCS-derived C12A7 samples was visually assessed by the sharpness of the XRD peaks (Figure 1.5) and, validated by the calculated crystallite size values (entries 1-4, Table 1.2) obtained from the (*211*) strongest peak (2θ = 18.11°) using the Scherrer equation, which ranges between 110-122 nm.

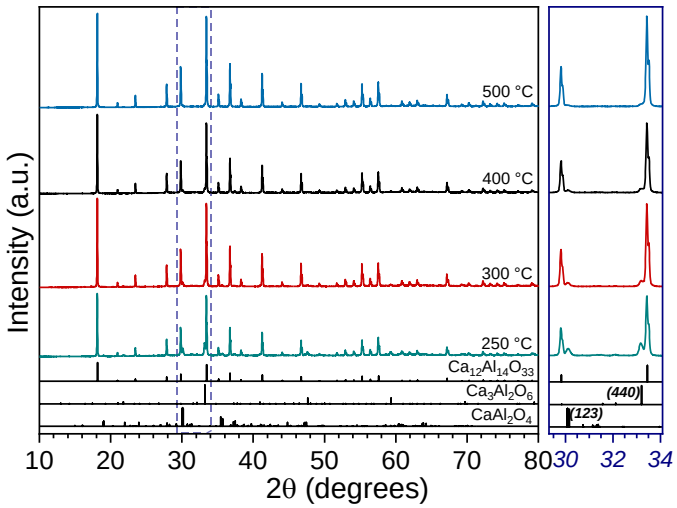

Figure 1.5. PXRD patterns of the powders synthesized via SCS using a fuel mixture produced at different furnace temperatures. Inset: zoomed region in the 2θ range between 28-34°

Table 1.2. SCS parameters, crystallite size, lattice parameter and phase quantification of the SCS derived C12A7 powders produced at different temperatures and with ranging ϕ ratios

Entry	Sample	Temperature (°C)	ϕ ratio	Latency time (min)	Surface area ($m^2 \cdot g^{-1}$).	Crystallite size (nm)	a (Å)	C12A7 (%)	C3A (%)	CA (%)
1	1-NP-250	250	1	25	1	110	11.974	79	10	11
2	1-NP-300	300	1	10	-	116	11.977	92	3	4
3	1-NP-400	400	1	4	-	117	11.974	94	3	3
4	1-NP-500	500	1	1.5	1	122	11.975	98	1	1
5	0.5-NP-500	500	0.5	3.5	-	-	-	-	-	-
6	0.75-NP-500	500	0.75	2.5	<1	109	11.973	93	4	3
7	1.25-NP-500	500	1.25	2.0	1	100	11.973	95	2	4
8	1.5-NP-500	500	1.5	3	-					
9	2-NP-500	500	2.0	3.2	-	-	-	-	-	-

The latency time[3], expressed as the period between the introduction of the container into the furnace and the reaction initiation, appeared to be highly dependent on the selected furnace temperature (entries 1-4, Table 1.2). For example, the total residence time inside the furnace needed to complete the synthesis of C12A7 went from a few minutes (1.5 min) at 500 °C to several dozen (25 min) at the lowest temperature (250 °C). Thus, it was evidenced that the lower the furnace temperature, the longer it takes to trigger the combustion reaction.

The in-depth analysis of PXRD patterns (Figure 1.5) via Rietveld refinement provided evidence of the impact of prolonging the occurrence of the combustion reaction on the phase purity. This effect resulted from selecting a furnace temperature below 500°C. The quantified content of each crystalline phase (C3A, CA, and C12A7) are summarized in Table 1.2. For instance, at the highest tested temperature (500°C), a highly-crystalline pure C12A7 (entry 4, Table) was obtained. In contrast, at temperatures as low as 250 °C, a lower content of C12A7 phase was reflected (entry 1, Table 1.2). Thus, the extended duration of the initial stages (solvent evaporation, gel formation, and thermal decomposition) occurring before the combustion reaction initiation might have modified the original stoichiometric proportions between nitrates and fuels, as explained below. On the one hand, at 250 °C, the lower evaporation rate of the solvent probably led to the early depletion of the most thermo-sensible reagents. According to the literature[114], urea undergoes hydrolysis and thermal decomposition between 134-263 °C yielding ammonia (NH_3) and isocyanic acid (HCNO) as main by-products. As for the aluminum nitrate, Pacewska *et al*. proposed that above 80 °C (melting point) and below 170 °C , $Al(NO_3)_3 \cdot 9H_2O$ thermal decomposition is connected to

[3] The latency time was measured by recording the time between the moment the container was introduced into the furnace (t=0 min) and the beginning of the combustion reaction. The latter event was evidenced by a sudden increase in the furnace temperature deviating from the setpoint value, as depicted by the temperature reader connected to the furnace thermocouple.

occurrence of simultaneous processes such as dehydration of the salt, hydrolysis, and destruction of the nitrate groups.[115] Consequently, at temperatures below 500 °C, the premature depletion of urea and Al-nitrate could entail the formation of other calcium aluminates (CA and C3A) due to the alteration of the initial calculated proportion between fuels and oxidizers. Hence, the lower the furnace temperature the higher the presence of impurities. On the other hand, regarding the CaO-Al_2O_3 phases diagram[15,16,18,116] (see Figure i.2 in General introduction), the narrow region to produce single-phase C12A7 is not only highly dependent on the stoichiometric ratio between CaO: Al_2O_3 (12:7) but also on the temperature (1350 °C for solid-state reaction). So, the heat losses at low temperatures (< 500 °C) could have consumed a part of the total amount of energy released by the exothermic reaction, lowering the attained temperature during the combustion reaction, thus promoting the formation of impurities (CA and C3A) as well.

According to the literature[87,109], SCS method usually allows the formation of nanoporous powders with high surface areas, mainly due to two factors: i) the generation of large amounts of gases during the combustion reaction, and ii) the fast cooling rate once the combustion temperature is attained. Consequently, a substantial volumetric expansion in the solid product is achieved, promoting the formation of finely dispersed nanoparticles, and preventing their agglomeration. However, our N_2 physisorption and SEM analyses revealed a different story. The measured S_{BET} for all C12A7 derived powders were equal to or less than 1 $m^2 \cdot g^{-1}$, regardless of the furnace temperature (entries 1 and 4, Table 1.2). Besides, Figure 1.6 illustrates the morphology and microstructure of the SCS-derived C12A7 powders. For instance, SEM images of the C12A7 sample produced at 500°C showed irregularly shaped aggregates of partially sintered grains and dense solid particles within a large size distribution (1-100 μm). At higher magnifications, the presence of small superficial pores and craters was observed, which were probably left behind after the sudden evaporation of trapped droplets of solvent during the combustion reaction. Likewise, those C12A7 powders synthesized below 500°C displayed similar morphologies and microstructures. Thus, despite the successful production of single-phase C12A7 at low temperature employing a fuel mixture, this synthetic protocol did not lead to the formation of a porous

material, leading instead to a solid with comparable surface area and morphology to those synthesized via the ceramic route[11,52,63].

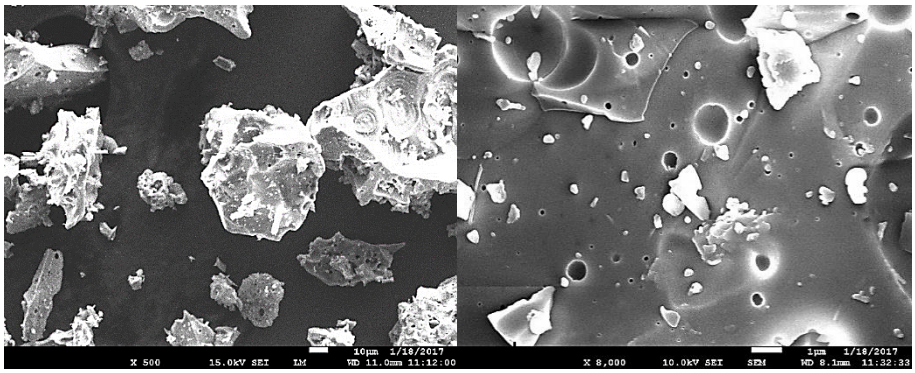

Figure 1.6. Scanning electron microscope (SEM) images of SCS-derived C12A7 produced at 500 °C with ϕ = 1 at different magnifications a) 500x and b) 8000x

According to the literature[117,118], working under rich-fuel conditions, ϕ > 1, not only increases the amount of heat emitted by the reaction (Figure 1.2a) but also stimulates the generation of combustion gases, which has proven to be a key element determining the texture and morphology of the as-synthesized solid. As illustrated in Figures 1.3 c and d, working with enriched fuel compositions promoted the production of a foamy voluminous solid. However, this upsurge of the fuel content also led to a reduction in the maximum attained temperature (Figure 1.2b). Thus, a significant variation of the fuel-to-oxidizer ratio (ϕ < 0.75 or ϕ > 1.25) impeded the development of a crystalline material, as shown by PXRD analysis (Figure 1.7). Besides, a moderate variation (0.75 ≤ ϕ ≤ 1.25) allowed the formation of a highly-pure C12A7, however, it also promoted the development of other calcium aluminate side phases, as revealed by Rietveld analysis (entries 6 and 7, Table 1.2). Nevertheless, no improvement of the textural properties was observed in those crystalline C12A7 samples by modifying the ϕ ratio, exhibiting similar S_{BET} values to the one synthesized under stoichiometric conditions (ϕ = 1).

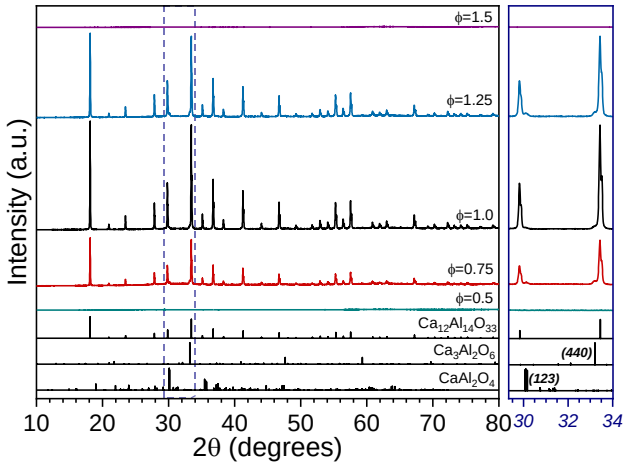

Figure 1.7. PXRD patterns of the as-synthesized powders produced at 500°C via SCS using a fuel mixture with ranging fuel/oxidizer ratios. Inset: zoomed region in the 2θ range between 28-34°

These outcomes revealed for the first time that crystalline C12A7 materials were promptly produced at low temperature (>250°C) via solution combustion synthesis by using a fuel mixture, without requiring an extra post-annealing step as compared with the single-fuel approach. The selection of a proper furnace temperature effectively enhances the C12A7 phase purity and crystallinity degree. Yet, the variations of the furnace temperature and fuel-to-oxidizer ratio proved ineffective in increasing the surface area of SCS-derived C12A7 material.

3.2 Preparation of porous mayenite via a multi-step assisted solution combustion approach

A new approach to produce porous mayenite via a modification of our former SCS protocol was performed by adding oxalic acid (OA). This new strategy was inspired by a previous study related to the synthesis of cobalt ferrite ($CoFe_2O_4$) by SCS.[107] The authors suggested that oxalic acid can act as a porogeneous and combustion retarding agent, improving the textural properties. In this second synthetic approach, we investigated the preparation of C12A7 using a stoichiometric ratio between nitrates (Ca and Al) and fuels (urea and β-alanine), while adding various amount of oxalic acid, expressed as an OA/C12A7 mass ratio, which ranges between

0.25-1 g OA·g^{-1} C12A7. Thus, as in the previous section, we evaluated the impact of on the combustion process and morphology of the as-obtained powders obtained after the combustion reaction is discussed. Figure 1.8 presents a selection of images that illustrates the latter effect, whereas Figure 1.9 shows the PXRD patterns corresponding to the as-prepared powders (*x*@OA) produced by combustion reaction, employing different amounts of OA.

At low concentration (0.25 g OA·g^{-1} C12A7), the combustion reaction took place as a thermal explosion (Figure 1.8a), with the occurrence of a glowing-intense flame. In the same way, PXRD analysis (Figure 1.9) showed that the coral-like solid (Figure 1.8d, 0.25@OA sample) yielded by the combustion reaction was mainly composed of C12A7 along with minor contents of CA and C3A, as hitherto observed when working under lean or rich-fuel compositions near the stoichiometric one ($0.75 \leq \phi \leq 1.25$, Figure 1.7). Besides, by increasing the OA concentrations (≥0.5 g OA·g^{-1} C12A7), the reaction underwent via self-propagating smoldering combustion (Figure 1.8b and c), where a small portion of the frothing gel locally ignited and propagated in the form of a combustion wave through the rest of the gel volume. In this latter case, the obtained fluffy, voluminous white-grayish powders (Figures 1.8e and f) showed to be amorphous (Figure 1.9), which was most likely attributed to the drop of the maximum temperature attained during the combustion reaction. In addition, solid products showed a darker coloration with rising the AO/C12A7 mass ratio. This denoted a higher content of carbonaceous residue due to incomplete combustion, as previously noticed when working at fuel-rich conditions ($\phi > 1$).

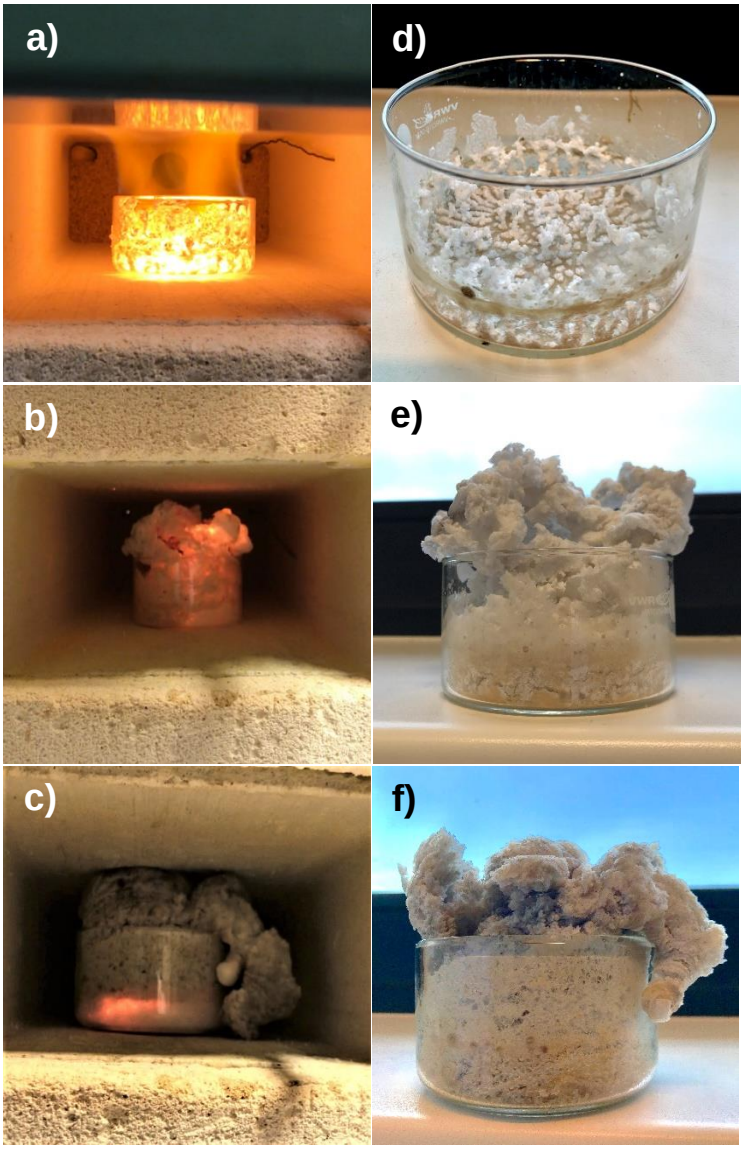

Figure 1.8. Images representing the combustion process and product morphology of the solid powders yielded by the combustion reaction employing different OA amounts: a & d) 0.25@OA; b & e) 0.5@OA; and c & f) 0.75@OA.

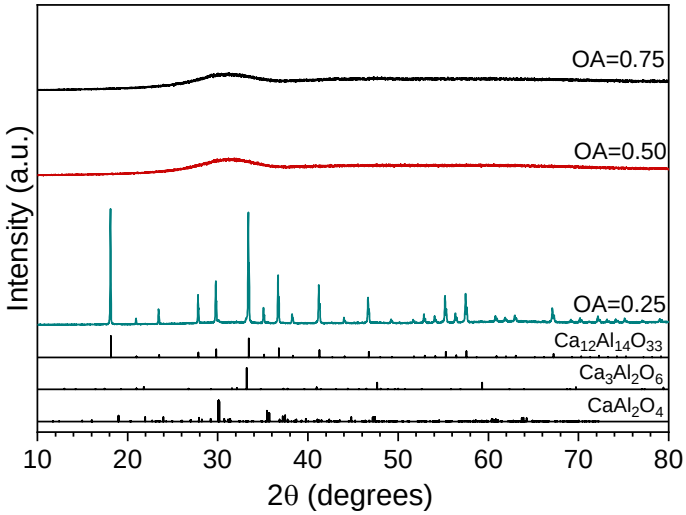

Figure 1.9. PXRD patterns of the synthesized x@AO-SCS powders produced with ranging OA/C12A7 mass ratios.

Similar to what was observed in the previous section, the morphology of the powders and the loss of crystallinity can be explained by two factors: i) a substantial upsurge of the gas volume evolved during the combustion reaction; and ii) a significant reduction in the combustion temperature. N_2 physisorption analysis showed that despite the addition of OA, when working with low mass ratio (0.25@OA), the C12A7 textural properties were not improved. Instead, at higher OA concentrations (0.5-1@OA), the S_{BET} of the combustion-derived amorphous powders was successfully enhanced, exhibiting surface area values in the range of 9-12 $m^2 \cdot g^{-1}$.

In a subsequent step, the amorphous powders obtained with AO/C12A7 ratios ranging from 0.5 to 1 were exposed to hot water at 80°C, resulting in the formation of a suspension. The suspension was then magnetically stirred for *ca.* 20 minutes, while maintaining a constant temperature. This step in our procedure was inspired by the methodology employed in the cobalt ferrite preparation by SCS.[107] Unexpectedly, this hydration process promoted the shaping of crystalline powders from the preceding amorphous powders. Thus, after succeeding filtration and drying steps, the three as-dried precursor powders (Figure 1.10) revealed the presence of three crystalline phases: hydrogarnet [$Ca_3Al_2(OH)_{12}$, JCPDS-card 24-0217], aluminum hydroxide [$Al(OH)_3$, JCPDS-card 33-0018], and calcium

carbo-aluminate hydrate [$Ca_4Al_2(OH)_{12}CO_3{\cdot}5H_2O$, JCPDS-card 41-0219].

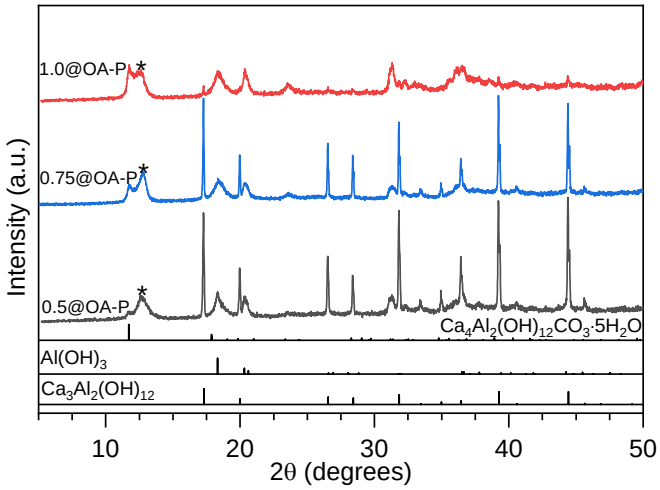

Figure 1.10. PXRD patterns of the as-dried precursor (x@AO-P) powders produced after subsequent hydration, filtration, and drying steps employing the synthesized x@AO produced by the combustion reaction with OA/C12A7 mass ratio ranging between 0.5-1. The symbol ∗ denotes the $Ca_4Al_2(OH)_{12}CO_3{\cdot}xH_2O$ phase, see below for more details.

In a previous study related to the mayenite preparation by hydrothermal approach, the formation of $Ca_3Al_2(OH)_{12}$ was achieved by hydrothermally processing a stoichiometric mixture of calcium and aluminum hydroxides.[80] Thus, Li *et al.* proposed that hydrogarnet could act as a precursor during the obtention of porous C12A7 at lower temperatures.[80] In another study related to mayenite synthesis, Hasegawa *et al.* observed that the formation of $Ca_4Al_2(OH)_{12}CO_3{\cdot}5H_2O$ rather than $Ca_3Al_2(OH)_{12}$ could be favored depending on the type of atmosphere employed during the synthesis. Thus, they associated the formation of calcium carbo-aluminate hydrate with the prompt carbonation of $Ca(OH)_2$ under ambient air, whose formation could be mitigated by employing an N_2 atmosphere.[85] In contrast, we consider that in our case, the formation of carbo-aluminate was related to the hydration of the carbonaceous amorphous residue left behind by the combustion reaction. Even though all three as-dried precursor powders (0.5-1@OA-P) depicted in Figure 1.10 presented the same three crystalline phases. The 0.5@OA-P specimen displayed the lowest content of the carbo-aluminate phase, most likely due to the lower

residual carbon content. Therefore, the 0.5 g OA·g^{-1} C12A7 mass ratio turned out to be the optimal one to minimize the presence of carbonated impurities, also considering that higher OA concentrations did not significantly increase the surface area.

The phase transition during the calcination process of the selected sample (0.5@OA-P) was monitored by high-temperature powder X-ray diffraction (HT-PXRD) and thermogravimetric-mass spectroscopy (TGA-MS) analyses, as displayed in Figure 1.11a and b, respectively.

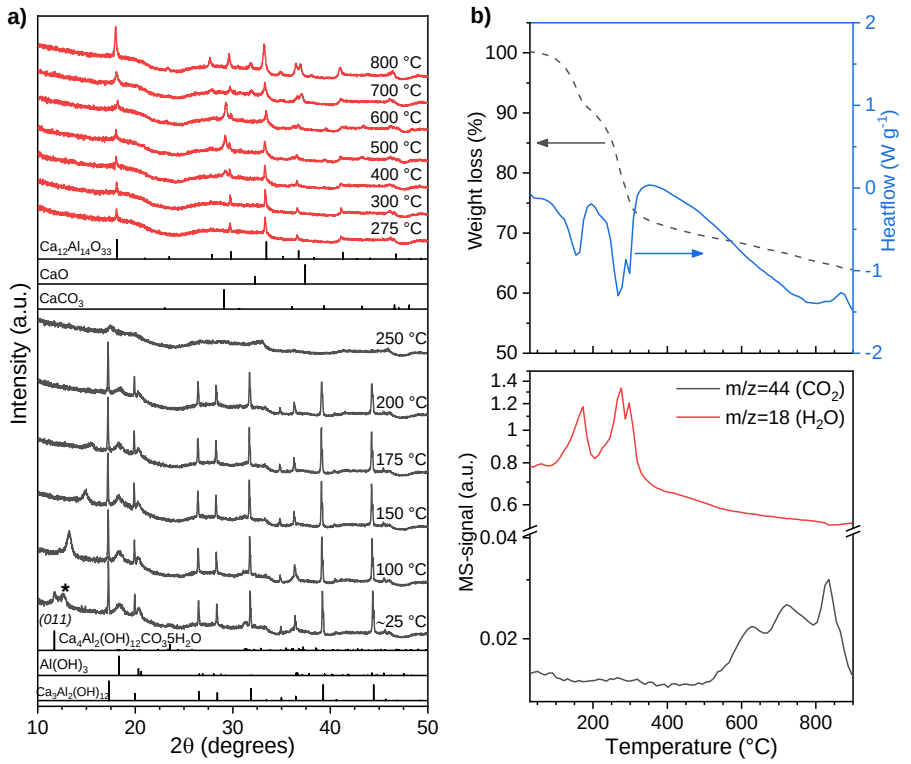

Figure 1.11. Phase transition analysis of the as-dried precursor powder (0.5@OA-P). a) HT-PXRD patterns collected at different temperatures between 25 and 800 °C using an XRK 900 (Anton Paar) chamber under dry air flow with a heating rate of 10 °C·min^{-1}. The data of each PXRD pattern was collected under isothermal conditions. b) TGA-MS analysis under flowing dry air (100 mL·min^{-1}) from 25 to 900 °C with a heating rate of 10 °C·min^{-1}.

Apart from the three hydroxide phases, the as-dried precursor PXRD pattern collected at room temperature (RT, ~25°C) revealed an unidentified peak (∗) partially superposed to the carbo-aluminate

principal reflection (*011*). The former reflection was attributed to the occurrence of a concomitant $Ca_4Al_2(OH)_{12}CO_3 \cdot xH_2O$ phase with a lower hydration content, which was probably formed during the drying step.

Moreover, upon heating, both reflections depicted at RT went missing, whereas a new peak emerged at a higher 2θ angle in diffractograms obtained at higher temperatures (between 100-175°C, Figure 1.11). The position of the latter peak continually shifted towards higher 2θ degrees by increasing the calcination temperature until all reflections related to the carbo-aluminate phase faded out at *ca.* 200 °C. Besides, the intensity and position of hydrogarnet peaks remained unchanged up to 200 °C, whereas the $Al(OH)_3$ reflections seemed less intense, most likely due to loss of structural water. In previous studies,[119,120] carbo-aluminate has been described as a lamellar structure characterized by the presence of stacked positively charged layers of $[Ca_4Al_2(OH)_{12}]^{2+}$ and negatively-charged interlayers of $[CO_3 \cdot 5H_2O]^{2-}$. It has also been stated that the carbo-aluminate basal spacing varies with the shape and size of the anions and the amount of interlayer water. Hence, it is reasonable to correlate the loss of interlayer trapped water upon heating to the basal spacing reduction, shifting the corresponding reflection towards higher angles. In this way, TGA-MS analysis corroborated the latter hypothesis showing that water molecules were released by the sample upon heating via an endothermic process, as displayed by the evolution of its mass-over-charge signal (m/z = 18), which was correlated to the loss of structural water. At 250 °C, a poorly-crystalline powder was observed, yet a few reflections related to the hydrogarnet phase were also depicted (top black-line, Figure 1.11a). Li *et al.*[80] suggested that $Ca_3Al_2(OH)_{12}$ and $Al(OH)_3$ dehydrate from ~300 °C leading to the formation of C3A and AlO(OH) (boehmite), respectively, which are the intermediates in the C12A7 formation at low temperature. Even though the latter intermediates were not found in our study, the occurrence of mayenite was revealed starting from ~275 °C (bottom red-line, Figure 1.11a). Between 200-400 °C, a second mass loss (*ca.* 20%) represented by two successive overlapped endothermic processes was noticed, which was attributed to the water release by $Ca_3Al_2(OH)_{12}$ and $Al(OH)_3$ upon dehydration. From 400°C, the presence of concomitant calcium carbonate ($CaCO_3$; JCPDS-card 05-0586) was evidenced, whereas the rise in the temperature over 600°C produced calcium oxide (CaO;

JCPDS-card 37-1497) via the decarbonation of $CaCO_3$ associated with the release of CO_2 (m/z=44) from 500°C, as observed by HT-PXRD and TGA-MS, respectively. In the same way, mayenite crystallinity was favored with increasing the temperature encouraging the formation of a well-crystallized C12A7 at 800 °C displaying an average crystallite size of 33 nm according to Scherrer equation (Table 1.3). A Rietveld analysis (Figure 1.12) showed that the powder obtained after calcination at 800°C for 4h predominantly contained C12A7 (93%) with a minor presence of CaO (7%), as a concomitant phase.

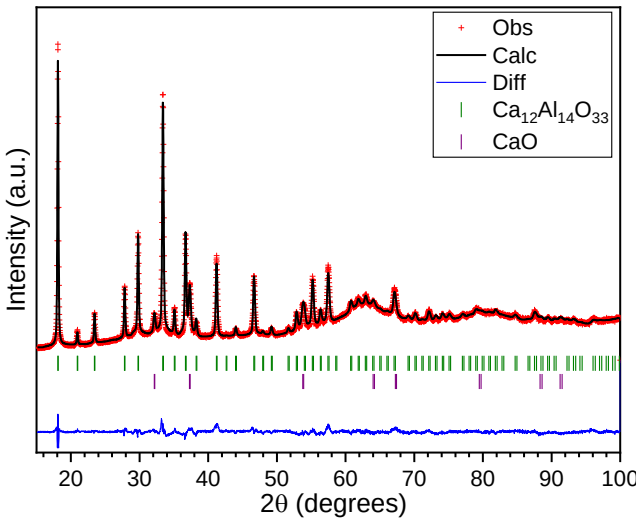

Figure 1.12. Rietveld refinement analysis of pC12A7-80 PXRD pattern. Observed data (red plus symbol), calculated data (solid black line), and the difference between the observed and the calculated patterns (solid blue line) is plotted at the bottom. Reference patterns C12A7 (green bars, JCPDS-card 09-0413) and CaO (purple bars, JCPDS-card 37-1497).

Based on the precedent HT-PXRD study, four temperatures in the range of 300-800°C were selected to perform a separate calcination of the as-dried precursor powder (0.5@OA-P) under static air for 4h, with the resulting samples dedicated for further characterization by N_2 physisorption. All isotherms (Figure 1.13) featured a type IV shape attributed to mesoporous materials and a hysteresis loop of type H3 corresponding to materials composed of non-rigid aggregates with plate-like pores according to the IUPAC[121]. Yet, despite the similar hysteresis loop shapes displayed by all N_2 physisorption isotherms, the C12A7 calcined at 600 °C exhibited an enlarged hysteresis loop down-

shifted to low relative pressures (~0.5-0.8 P/Po), which is likely related to the occurrence of smaller mesopores. Moreover, the slightly higher amounts of adsorbed N_2 at the initial relative pressures by those samples calcined between 300-400°C is associated with the occurrence of some micropores. Meanwhile, the steep N_2 uptake around P/Po = 1 was ascribed to N_2 adsorption within the spaces between constituting particles.

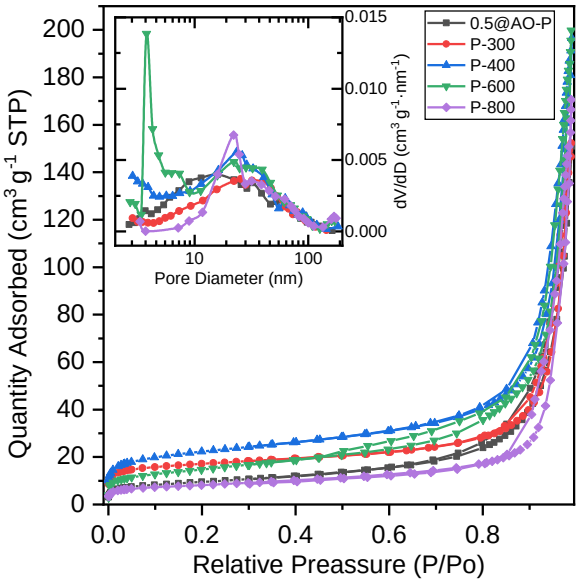

Figure 1.13. N_2-physisorption isotherms of porous C12A7 materials produced after calcination under static ambient air at selected temperatures for 4h. PSD plots (inset) were obtained by the BJH model using the desorption branch.

The pore size distribution (PSD) evolution with rising calcination temperature is shown in Figure 1.13 (inset). Upon heating, the PSD of the calcined C12A7 samples became narrower and less dispersed, showing maxima around 20-30nm, as compared to the as-dried precursor. In the case of the P-600 sample, a distinctive new group of pores leading to a maximum at *ca.* 3.8 nm was also observed. However, this narrow distribution of pores was identified as an artifact produced by the forced closure of the isotherm (green lines in Figure 1.13) upon desorption at P/Po between 0.4–0.5 due to the tensile strength effect.[122] Additionally, the mentioned PSD narrowing towards increased pore sizes, namely at 800°C, was attributed to the

fusion of the smaller pores (interparticle spaces between the grains composing the particles) due to the aggregation of the particles caused by the rising calcination temperature.

The detailed textural properties of the as-dried precursor and C12A7 calcined at different temperatures are summarized in Table 1.3. The 0.5@OA-P sample, obtained after subsequent hydration, filtration, and drying steps, showed a higher BET surface area (33 $m^2 \cdot g^{-1}$) compared to the fluffy 0.5@OA amorphous powder yielded by the combustion reaction (9 $m^2 \cdot g^{-1}$). This enhancement in the specific surface area could be attributed to the rearrangement of the atoms during the formation of the three crystalline phases. Moreover, the calcination of the as-dried precursor at 300 °C (P-300) allowed the formation of mesoporous mayenite displaying a notably high pore volume (0.22 $cm^3 \cdot g^{-1}$), which became enlarged as the temperature increased up to 600 °C (P-600), whereas a heat treatment at a superior temperature slightly decreased the pore volume (entries 2-5, Table 1.3). The specific surface area (S_{BET}) was improved as the calcination temperature increased to 400 °C, displaying a remarkable value of 74 $m^2 \cdot g^{-1}$, while it decreased from thereon due to the sintering and agglomeration of the particles. The latter was reflected by the promoted crystallinity degree of C12A7 with rising calcination temperature, as demonstrated by HT-PXRD analysis. At 800°C, a highly pure crystalline mesoporous C12A7 (P-800) was produced, revealing a specific surface area 30-fold higher than that obtained by our former method and those obtained by the conventional ceramic route.[11,52,63]

Table 1.3. Textural properties of the as-dried precursor and mayenite samples obtained after calcination at different temperatures for 4h under static ambient air.

Entry	Sample	Calcination temperature (°C)	S_{BET} ($m^2 \cdot g^{-1}$)	Pore volume[a] ($cm^3 \cdot g^{-1}$)	Crystallite size[b] (nm)
1	0.5@OA-P	-	33	0.23	-
2	P-300	300	55	0.22	-
3	P-400	400	74	0.29	-
4	P-600	600	52	0.31	17
5	P-800	800	30	0.26	33

[a] Obtained from the desorption branch using the BJH method. [b] Average crystallite size calculated using the Scherrer equation.

The SEM images (Figure 1.14a) of P-800 sample second the N_2 physisorption results showing the presence of aggregates composed by flake-shaped nanoparticles. At higher magnification (Figure 1.14b), it appears that the flake-shaped particles are smaller than 100 nm. A similar structure was observed during the production of mayenite by a sol-gel oxalate precursor method[77]. Thus, probably the use of oxalic acid during the preparation of mayenite leads to the formation of this particular kind of morphology.

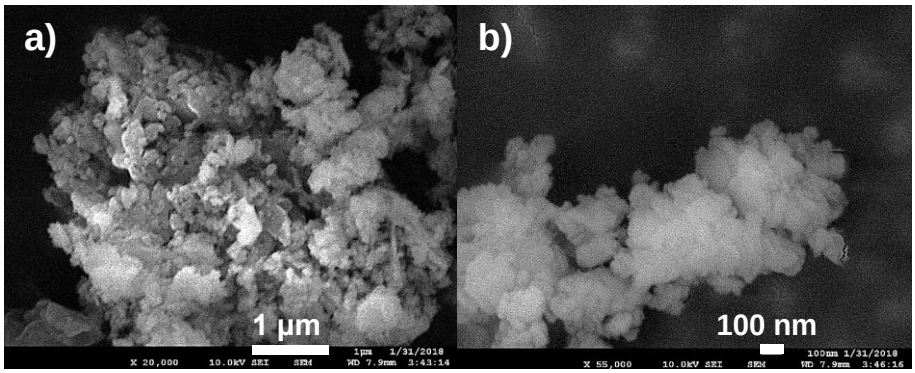

Figure 1.14. Scanning electron microscope (SEM) images of porous mayenite calcined under static air at 800 °C for 4 h with different magnifications a) 20000x and b) 55000x.

3.3 Evaluating the catalytic activity of mayenite in the carbon black (CB) combustion

To fulfill the underlying motivation of this study, which is the improvement of the catalytic activity of C12A7 by enhancing its textural properties, the catalytic performances of selected C12A7 catalysts were evaluated. Such catalysts were synthesized through the two preparation strategies presented in the previous sections (3.1 and 3.2) and tested in the carbon black (soot model surrogate) combustion. The sample selection is justified by the observations summarized in Table **1.4**. Regarding non-porous C12A7 samples, 1-NP-500 was selected as the most representative one of the series considering that it presents the highest crystallinity and purity, and that the S_{BET} of all of them is similar. For simplifying the identification of 1-NP-500 sample in next chapters, it will be referred to simply as NP. Considering porous C12A7, P-600 and P-800 were selected for further research because both present good textural properties, high crystallinity and lower

presence of CaO. In contrast, P-400 (displaying the highest surface area) and P-300 were not evaluated. In fact, these samples still contain a significant amount of calcium carbonate (as shown by PXRD and TGA-MS analyses), which will certainly affect the adequate interpretation of their catalytic activity, since CO_2 will be generated due to the decarbonation of $CaCO_3$ and therefore the CO_2 generated by CB oxidation will be overestimated. Additionally, the textural and structural properties of P-300 and P-400 will certainly be modified during the catalytic test by exposing the sample to temperatures higher than the one employed for their synthesis.

Table 1.4. Summary of non-porous (NP) and porous (P) C12A7 prepared by the two synthesis protocols

Sample	S_{BET} ($m^2 \cdot g^{-1}$)	Observations
1-NP-250	1	C12A7 (79%) containing substantial CA and C3A phases
1-NP-300	-	C12A7 (92%) containing minor CA and C3A phases
1-NP-400	-	C12A7 (94%) containing minor CA and C3A phases
1-NP-500	1	Highest crystallinity and virtually pure C12A7 (98%) phase
0.5-NP-500	-	Amorphous powder
0.75-NP-500	-	C12A7 (93%) containing minor CA and C3A phases
1.25-NP-500	<1	C12A7 as main containing minor CA and C3A phases
1.5-NP-500		Amorphous powder
2-NP-500		Amorphous powder
P-300	55	Very low crystallinity and concomitant presence of $CaCO_3$.
P-400	74	Highest S_{BET}, yet low crystallinity and important presence of CaO and $CaCO_3$.
P-600	52	Competitive surface area, better crystallinity, and lower presence of CaO.
P-800	30	Higher crystallinity degree, higher C12A7 content (93%) and minor presence of CaO.

Figures 1.15a and b assemble the catalytic results of the performed CB oxidation runs under tight and loose contact conditions, respectively. In both cases, the TPC curves of CO_2 and CO (inset) produced during the CB combustion are reported for the selected C12A7 catalysts, along with an uncatalyzed run (α-alumina) for comparison. Additionally, the catalytic indicators such as the onset and peak temperatures and the CO_2 and CO selectivity are summarized in Table 1.5. The TPC CO_2 curve for the uncatalyzed combustion of

Printex-U in the presence of α-alumina showed that CO_2 production started around 486 °C and gradually increased with the rising temperature reaching the highest combustion rate at 655 °C. In comparison, after performing the CB combustion in the presence of either non-porous or porous C12A7, their respective TPC CO_2 curves were shifted down to lower temperatures (Figure 1.15) regardless of the contact mode, implying that all tested materials promoted the CB combustion. For instance, non-porous C12A7 (NP; 1 $m^2 \cdot g^{-1}$) displayed a unimodal TPC curve in both scenarios (tight and loose contacts), showing similar onset and peak temperatures (entries 2-3, Table 1.5). On the contrary, the shape of the TPC curves obtained when porous mayenite catalysts were employed highly depended on the contact mode. In the case of a "tight" contact procedure (Figure 1.15a), the curves displayed a mostly unimodal distribution, whereas the "loose" contact approach (Figure 1.15b) generated dramatically more complex profiles. As expected, a remarkable improvement in the activity was observed when porous mayenite was employed. Under "tight" contact conditions, the CO_x TPC curves (namely CO_2) for C12A7 catalysts calcined at 600 and 800°C showed a significant decrease in the T_{onset} and T_p values as compared to the non-catalytic combustion (entries 4 and 6, Table 1.5). The small peaks appearing in the upper-temperature region between 580-800 °C were attributed to non-catalytic processes involving CO_2 discharge due to $CaCO_3$ decarbonation (*see* Figure A.1 in Appendix A). In the case of P-600, the already present $CaCO_3$ (*see* Figure 1.11) was decomposed upon heating at high temperatures (> 650°C). In contrast, the CO_2 peak at *ca.* 630°C was related to the existing CaO in porous C12A7 catalysts, which captured CO_2 during the CB combustion at low temperatures and then released it with rising temperature. In addition, the absence of CO peaks in the above same temperature region corroborated our latter assessment.

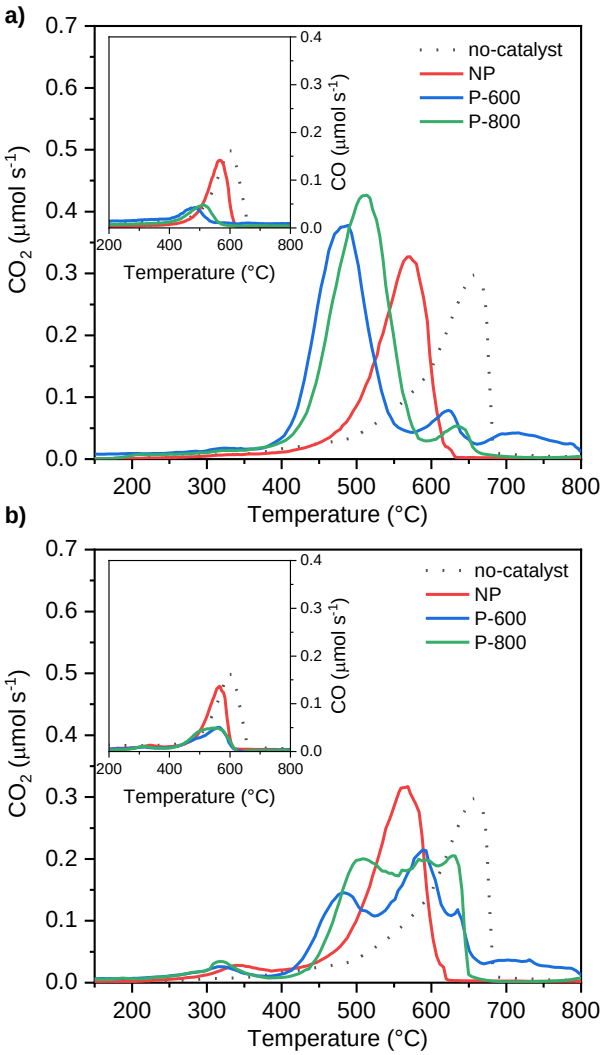

Figure 1.15. CO_2 and CO (inset) evolved gases from the catalytic oxidation of carbon black (Printex-U) under **a)** "tight" and **b)** "loose" contact conditions. Porous C12A7 calcined at different temperatures 600 °C (P-600) and 800 °C (P-800); non-porous mayenite (NP) directly obtained after the combustion reaction at 500 °C (solid red line) under stoichiometric conditions (ϕ = 1). A non-catalytic carbon black combustion (α-alumina+CB) is also displayed for comparison.

On the other hand, under "loose" contact conditions, the TPC CO_2 curves displayed a multimodal shape, revealing the presence of three principal peaks (entries 5 and 7, Table 1.5). We have attributed these different stages in the TPC CO_2 curves to the following situations. The

first peak appeared in the same temperature range as the one obtained under the “tight” contact conditions meaning that a part of the carbon particles was in intimate contact with the catalyst surface, favoring the oxidation at low temperatures. On the contrary, the second peak might be associated with delayed CB oxidation, which occurred at higher temperatures due to the reduced contact between the catalyst and the carbon particles. The latter event could be presumed to be independent of the catalyst texture as it always fell at similar temperatures whatever the catalysts used. Thus, it cannot be used to compare the catalytic performance between our different samples. As for the last peak, we have related it to the release of CO_2 due to decarbonation of calcium carbonate, as already reported under “tight” contact conditions (*vide supra*).

Table 1.5. CB combustion activity and selectivity results under tight contact for different C12A7 catalysts

Entry	Sample	Contact mode	T_{onset} (°C)	T_p (°C)	S_{CO_2} (%)	S_{CO} (%)
1	Non-catalytic run	-	486	655	66	34
2	NP	Tight	479	571	71	29
3		Loose	480	570	70	30
4	P-600	Tight	405	488	92	8
5		Loose	426	485/588/635	85	15
6	P-800	Tight	437	514	91	9
7		Loose	446	512/590/631	84	16

Furthermore, the improvement in the textural properties also showed to positively influence the selectivity towards CO_2 during the CB oxidation, reducing the CO formation up to 4-fold and 3-fold concerning the uncatalyzed run and that catalyzed by non-porous C12A7, respectively (Table 1.5). In addition, only slightly inferior CO_2 selectivities were obtained when working under “loose” contact.

The above-reported improved C12A7 catalytic performances in the CB oxidation were undoubtedly attributed to enhancement in the textural properties and morphology of C12A7. Our statements are supported by a previous study in which Yang *et al.* suggested that the desorption of reactive oxygen species in mayenite occurs more readily with decreasing the particle size. They found that the mobility and the desorption of the oxygen species are limited by the mass transport in the bulk of C12A7.[11] In addition, as mentioned in the General

Introduction (*pp. 22-28*), the formation/regeneration of reactive oxygen species (O_2^-, O^-, and O_2^{2-}) only occurred at temperatures over 400°C.[9,70] Supported by these facts and considering that the catalytic carbon black oxidation took place at temperatures in the same range at which the reactive oxygen species are formed, it is consistent to consider these oxygen species as responsible for the CB oxidation over C12A7.

4 Conclusive remarks

We revealed that crystalline C12A7 materials were promptly produced at temperatures as low as 250°C via one-step solution combustion synthesis using a fuel mixture of urea and β-alanine without requiring an additional high-temperature calcination step, as compared with the single-fuel approach. The selection of a proper furnace temperature effectively enhances the C12A7 phase purity and crystallinity degree. Yet, the variations of the furnace temperature and fuel-to-oxidizer ratio proved ineffective in increasing the surface area of the as-synthesized C12A7 materials via the one-step SCS methodology.

Furthermore, we successfully developed a new, efficient, and potentially scalable method to produce highly pure crystalline porous mayenite with a high specific surface at mild conditions by adding oxalic acid as a pore generator. We showed that the textural properties and crystallinity can be tuned by varying the calcination temperature making possible the formation of porous mayenite from temperatures as low as 275°C, reaching a remarkable specific surface area of 74 $m^2 \cdot g^{-1}$ at 400°C and displaying a large pore volume of 0.3 $cm^3 \cdot g^{-1}$, which had never been reported before.

Finally, in this first chapter, we demonstrated that the improvement of mayenite textural properties effectively promoted its catalytic activity and selectivity, prompting the total CB oxidation at low temperatures while favoring CO_2 production over CO. Even though we confirmed that mayenite is active in CB combustion and a promising catalyst in oxidation catalysis, we did not address the implications that the chemical identity and relative concentration of the extra-framework species could have on the catalytic performance of C12A7. Yet, this aspect will be covered in detail in Chapter II.

CHAPTER II

Modulation of the population distribution of extra-framework oxygen species inside C12A7 as a way to control its catalytic performance in an oxidation reaction

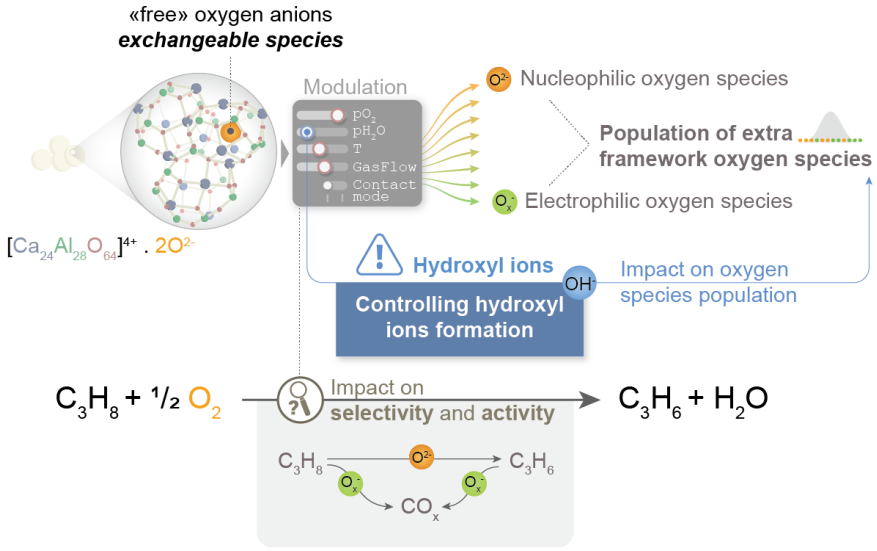

Abstract

In this chapter, we investigate the effect that controlling the population distribution of extra-framework oxygen species within C12A7 could have on its catalytic performances in an oxidation reaction, namely its selectivity towards total *vs.* partial oxidations. To study the effect of several operational parameters (*e.g.*, calcination temperature, atmosphere composition, gas/solid contact mode, and gas flow rate) on the control of the population distribution of the oxygen species inside C12A7 cages, we examine several sets of them denoted as methods A, B, C, and D. The nature and the relative abundance of the distinct extra-framework species obtained in each non-porous or porous C12A7 sample are systematically evaluated by EPR, Raman, and DR-UV-vis spectroscopies. For the first time reported in the literature, we evidenced the benefits of increasing the oxygen flow rate on the modulation of the oxygen species. Among the different studied conditions, the calcination at high temperatures (800-900°C) under a pure dry oxygen atmosphere employing either a crossflow configuration (method C) or high flow rates (method D) shows to be pivotal in the dehydroxylation of C12A7 (*i.e*., elimination of OH^- inside the cages), promoting the formation of electrophilic oxygen species (O_2^- and O^-). On the contrary, the O^{2-} (nucleophilic) enrichment is successfully achieved by calcining C12A7 containing electrophilic oxygen species above 650°C under inert gas (N_2). The evaluation of C12A7 catalytic performances reveals that a rise in the relative concentration of electrophilic oxygen species partially improves its activity in the propane oxidation reaction. This improvement was only observed when the catalyst had an optimal combination of textural and structural characteristics (*i.e.*, higher specific surface area and smaller particle size). However, the stability of this positive effect proved not to be long-lasting over time because its persistency highly depends on the difference between the consumption and regeneration rates of oxygen species. Besides, we demonstrate that the initial chemical identity (*i.e.,* whether it is nucleophilic or electrophilic in nature) of the dominant extra-framework species in C12A7 does not influence the selectivity of the catalyst, which invalidates our hypothesis. The main reason behind this outcome seems to be that the extra-framework population distribution is constantly re-equilibrated with the reaction medium during the oxidation process.

1 Introduction

In the previous Chapter, we demonstrated that the enhancement of the textural properties of C12A7 boosted its catalytic performance in an oxidation reaction. Yet, we did not evaluate the influence that the chemical identity and relative concentration of the entrapped extra-framework anionic oxygen species could have on its catalytic behavior. The nature of the oxygen species involved on the catalyst surface is understood to play a central role in the overall catalytic process, particularly on its selectivity. During a catalytic cycle, several surface oxygen species can be generated by the interactions between molecular oxygen (gas) and the catalyst surface (solid). These oxygen species can be distinguished by their electronic nature with evolving order of decreasing nucleophilicity/increasing electrophilicity, from electron-rich (O^{2-}, nucleophilic species) to electron-poor ($O_2^- > O_2^{2-} > O^-$, electrophilic species), where each one of them possesses distinct properties and reactivity. For instance, in the oxidation of a hydrocarbon nucleophilic species are related to partial oxidation reactions (oxidation without involving the C-C bond rupture), whereas the electrophilic ones predominantly lead to total oxidation processes because they tend to attack and break the C-C bonds, forming CO_x.[1,3,5,7] Generally, more than one type of these oxygen species is simultaneously found at the catalyst surface during an oxidation reaction.

As exposed in the General Introduction (*see section 2.2, p. 20*), C12A7 presents a peculiar crystal structure featured by a positively charged framework $[Ca_{12}Al_{28}O_{64}]^{4+}$ and capable of simultaneously hosting distinct oxygen species (O_2^-, O^-, O_2^{2-}, O^{2-}, and OH^-) as counter-anions to preserve charge neutrality of the material.[8–11,13,24,35,123] It has been demonstrated that the chemical identity and relative concentration of these anionic species can be manipulated by fine-tuning the synthesis or post-treatment conditions (*e.g.*, temperature and atmosphere composition in terms of pO_2 and pH_2O under which an annealing is applied). Hosono's group[9–11,13,35,123] has established that large quantities of reactive oxygen species (O_2^- and O^-) can be accommodated inside mayenite structural cages by heat-treating C12A7—containing clathrated "free" oxygen ions (O^{2-})—under an oxygen atmosphere at temperatures over 400°C, as revealed by electron paramagnetic resonance (EPR) and Raman spectroscopies.[11]

This oxygen radicals formation is accomplished by an electron transfer from O^{2-} to $O_{2(g)}$, as described in the General introduction (*see section 3.1, p. 22*).[9,10] For practical reasons, Eq. (i.1) (General Introduction) is here recalled and renamed as Eq. (2.1).

$$O^{2-}_{(cage)} + O_{2\,(atmosphere)} \rightleftharpoons O^{-}_{2(cage)} + O^{-}_{(cage)} \quad (2.1)$$

However, when the objective is to promote the incorporation of the latter species, controlling the water vapor in the atmosphere is of pivotal importance since its presence during the annealing of C12A7 can considerably reduce the formation of the oxygen species, as exposed in the General Introduction (*see section 3.2, p. 28*). As expressed above, in this case, Eq (i.5) is recalled and renamed as Eq. (2.2).[10,35,36]

$$O^{2-}_{(cage)} + [null]_{(cage)} + H_2O_{(atmosphere)} \rightleftharpoons 2OH^{-}_{(cage)} \quad (2.2)$$

Therefore, in this second chapter, we intend to verify our hypothesis that there is a possibility to control the catalytic activity and selectivity of C12A7 in an oxidation reaction by modulating its population distribution of extra-framework oxygen species. To do so, we have divided this study into two consecutive parts.

In Part I, by employing several spectroscopic techniques (Raman, EPR, and DR-UV-vis), we evaluated the possibility of modulating the speciation and relative abundance of the extra-framework oxygen species by applying several sets of combinations, where distinct parameters, including the calcination temperature, partial pressures of oxygen and water, and the way of contact between the solid material and the gas stream employed during the annealing process (parallel or cross-flow configuration). Inspired by our preparation approaches from Chapter I, we designed and compared three different methods (A, B, and C) to prepare or post-activate porous and non-porous C12A7, respectively, intending to generate distinct population distribution of oxygen extra-framework species. Next, in a first attempt to appraise the relationship between the population distribution of oxygen species and the catalytic performance of C12A7, we examined the catalytic activity and selectivity of selected specimens in the propane oxidation reaction. However, this first screening showed that even though we significantly increased the oxygen species concentration using

method C**,** the overall population distribution of extra-framework in C12A7 was still dominated by hydroxyl ions.

Therefore, in Part II, to decisively assess whether or not the modulation of the oxygen species population can be exploited to control the selectivity of C12A7, we developed a new strategy (method D) to promote the dehydroxylation of the cages and, thus maximize the preponderance of one oxygen species over any other extra-framework species. For the first time reported in the literature, we evidenced the benefits of increasing the oxygen flow rate on the modulation of the oxygen species. Additionally, we evaluated the impact of preparing porous C12A7 at a higher temperature (900°C) on its structural and textural properties. Finally, by employing the most promising catalysts presenting a population distribution governed by reactive oxygen anions, we disclosed the catalytic outcomes of these samples under catalytic conditions towards either the total or partial oxidation of propane.

2 Experimental

2.1 Materials

The grade purity and manufacturer of the chemical reagents and gases employed in the preparation and post-activation of C12A7 materials can be found in the general Experimental Section of this thesis (*p. 56*).

2.2 Preparation methods

In this section, **non-porous C12A7** and **porous C12A7** (hereafter denoted as **NP** and **P**, respectively) materials were used to investigate the influence of several preparation parameters on the modulation of the extra-framework oxygen species distribution inside the C12A7 structure. In this aim, the **atmosphere composition, annealing temperature, gas/solid contact mode (parallel or cross flow), and total flow rate** were varied to evaluate their individual effect on the fine-tuning of the different targeted oxygen species. When working with non-porous C12A7 samples, a post-activation (annealing) step under specific set of conditions was carried out employing the pristine NP powder directly obtained after the combustion synthesis as a starting raw material. In the case of porous C12A7 specimens, the preparation

conditions were directly varied during the last stage (*i.e.*, calcination) of the synthesis process, thus avoiding the addition of an extra-step as in the former case. The methods used in this chapter and their corresponding parameter combinations are illustrated in Scheme 2.1.

Method A: This preparation protocol relates to the one previously used in Chapter I (*see section 2.5 p. 74*) for the calcination of the as-dried precursor to produce porous C12A7. However, to easily differentiate between the different procedures employed to post-activate or synthesize C12A7 in this second chapter, we have renamed this method as A. Briefly, the calcination step was accomplished under an uncontrolled atmosphere, where the moisture in the ambient atmosphere was neither measured nor controlled. In each experiment, the sample (*ca.* 1 g) contained in an alumina crucible was introduced in a preheated muffle working at two different temperatures (600 and 800 °C) and dwelled for 4h under static ambient air. Then, the crucible was removed from the furnace and quenched to room temperature inside a desiccator. Once the sample was cooled, it was transferred to a glassware container which was stored inside a desiccator -until it was analyzed or tested.

Method B: The C12A7 materials were thermally treated inside a horizontal tubular furnace under flowing dry oxygen. The sample (ca. 1 g) was loaded in an alumina boat and was positioned inside a quartz tube (I.D. 30 mm) at the center of a tubular furnace, and then it was closed, and the inlet and outlet gas lines were connected. Before calcination, the tube was flushed for *ca.* 5 min with flowing dry oxygen, and the presence of any possible leak was verified. Then, the sample was heated from 25 to 800 °C at a heating rate of 10 °C·min^{-1} and dwelled for 4h at 800 °C, the sample was constantly exposed to a parallel flow of dry O_2 (pO_2=1 atm) at a flow rate of 50 mL·min^{-1}. The temperature was controlled by a K-type thermocouple placed at the center of the furnace above the sample container (the ΔT in the zone where the boat was positioned was always inferior to 4 °C). Finally, the sample was quickly removed out of the heated zone to one end of the tube and quenched to room temperature under the same atmosphere. Once cooled, the sample was stored in a desiccator inside a closed glassware container until it was analyzed or tested.

Method C: The C12A7 materials were calcined under crossflowing dry oxygen. The sample (*ca.* 1 g) was loaded inside a U-shaped tube quartz reactor on a sintered fixed quartz disc, and the reactor was placed at the center of a vertical tubular furnace. Before heating, the reactor was flushed for *ca.* 5 min with dry oxygen. Then, the sample was heated from 25 to 800 °C at a heating rate of 10 °C·min^{-1} and dwelled for 4h at 800 °C, a continuous crossflow of dry O_2 of 50 mL·min^{-1} was constantly fed across the fixed bed. The temperature was controlled by a K-type thermocouple placed in close intimacy to the fixed bed. Finally, the sample was quickly moved out of the heated zone by pulling down the vertical furnace and quenched to room temperature under the same atmosphere. Once cooled, the sample was stored in a desiccator inside a closed glassware container until it was analyzed or tested.

Method D: This method employed the same tubular furnace mentioned above in Method B. Yet, three main modifications related to the different varied parameters are described as follows. In this procedure, a high dry oxygen flow rate of *ca.* 1.4 L·min^{-1} was used during the entire heat-treatment. The sample was treated at temperatures ranging from 600 to 900 °C for a dwell-time of 4h, after which it was cooled down inside the furnace to room temperature under the same atmosphere. Besides, in some cases, after the 4 h of dwelling, an additional step was added, where the type of gas was varied in order to modulate the extra-framework species distribution to a targeted species. For instance, pure dry O_2 (pO_2 = 1 atm) was always used during the entire calcination at 900°C to boost the concentration of electrophilic oxygen species (O_2^-, O^-), whereas a subsequent calcination step at 650°C under inert gas (N_2) or humid N_2 (pH_2O = 0.1 atm) for 1h was added after the first 4h of calcination to prompt the formation of nucleophilic oxygen species (O^{2-}) or hydroxyl ions (OH^-), respectively. At the end of the last calcination step, the sample was cooled down to room temperature under the same atmosphere employed in the last annealing step (*e.g.*, dry oxygen in the case of electrophilic formation, dry N_2 for the nucleophilic enrichment or humid N_2 for the annihilation of the oxygen species). After cooling, the material was kept in a closed glassware container within a desiccator for later analysis or testing.

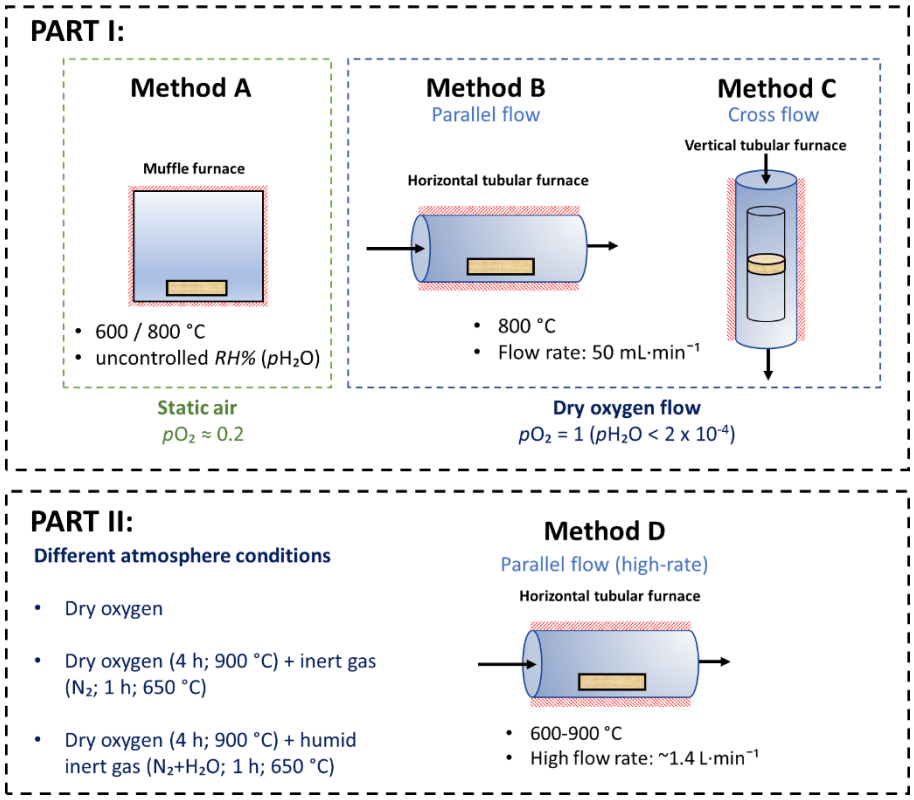

Scheme 2.1. Schematic representation of the methods used for the post-activation or preparation of non-porous and porous C12A7 specimens. The zones drawn in red represent the position of the heating jacket of the respective furnaces.

2.3 Catalyst characterization

C12A7 samples were characterized by PXRD, N_2 physisorption, Raman, EPR, DRUV-Vis spectroscopies, TPR-H_2 and O_2-TPD analyses, as described in the general Experimental Section (*pp. 56-60*). Specific analysis conditions used in this Chapter are described hereafter.

EPR spectra were recorded as described in section 2.2.6 (*p. 58*). The spin concentrations of paramagnetic oxygen species were determined from the second integral of the spectra using $VOSO_4{\cdot}K_2SO_4$ as standard. To determine the relative contribution of each paramagnetic species (O_2^- and/or O^-), the experimental spectrum was reproduced and deconvoluted by computer simulation using the

program EPRsim32.[104] It is worth mentioning that each performed simulation of the experimental EPR spectrum of a corresponding sample must not be regarded as a simple fitting. Instead, the obtained computer-simulated spectrum is the result of a complex iterative process (employing a minimization algorithm) in which several parameters determining the line shape of the EPR powder pattern and the position of the feature lines (g-values) are refined independently in order to obtain the best fitting between the experimental and simulated spectra.

EPR adsorption-reactivity tests were carried out using propylene as a probe molecule under anaerobic conditions (*i.e.*, oxygen-free). Before the probe molecule adsorption, *ca.* 0.025 g of catalyst was introduced into an EPR quartz cell probe and heated up to 200 °C (10°C·min^{-1}) under dynamic vacuum (< 4 x 10^{-7} bar) and dwelled for 1h to evacuate and clean the surface of any adsorb molecule (surface activation). Then, the cooled and evacuated cell was introduced in a liquid N_2 bath, and *ca.* 25 Torr of C_3H_6 was adsorbed at -196 °C. The gas excess that was not adsorbed was evacuated, and the cell was sealed. Next, the EPR cell probe, containing the sample with $C_3H_{6(ads)}$, was exposed to several consecutive heat-treatment under static conditions at different temperatures ranging from 200-550°C, unless otherwise mentioned. For each selected temperature (T_r), the cell was heated from room temperature to T_r at 10°C·min^{-1} and maintained at that temperature for 0.5 h. Once the total annihilation of the oxygen species was accomplished (*i.e.*, no EPR signal), the reduced sample (dark gray colored) was reoxidized. In this case, the cell was degassed under dynamic vacuum (< 4 x 10^{-7} bar) at 200 °C for 1 h. Then, 140 Torr of oxygen were introduced into the cell and adsorbed by the sample at liquid nitrogen temperature (-196 °C). Finally, the EPR cell was heated to 600°C and held for 1h. Before and after each treatment (*e.g.*, evacuation, adsorption, heat treatment, reoxidation) applied to the sample, an EPR spectrum was collected at -196 °C to evaluate any modification in the shape and/or intensity of the spectrum due to the consumption of the paramagnetic oxygen species. Quantitative evaluation of the concentration of oxygen species present in the spectra was performed by double integration of the corresponding EPR spectra and comparison with a vanadyl sulfate standard.

2.4 Catalytic activity evaluation

The catalytic performance of selected C12A7 catalysts prepared in this Chapter were evaluated in the propane oxidation reaction as described in the general Experimental Section (*see section 2.3.2, p. 61*). The catalytic outcomes expressed in terms of propane conversion and selectivity were calculated according to the equations reported in the general Experimental Section.

Part I: First insight into the modulation of the distribution of extra-framework oxygen species and its implication in the catalytic behavior of C12A7.

3 Results and discussion

3.1 Assessing the nature and relative concentration of the extra-framework species inside C12A7 samples

This section aims to settle the ground for straightforward identification and quantification of the different oxygen species that can coexist inside the C12A7 cages. To do so, we have first examined by electron paramagnetic resonance (EPR) and Raman spectroscopies our three samples previously investigated in Chapter I. Figure 2.1 displays the EPR spectra collected at -196 °C of pristine non-porous C12A7 (**NP**) and porous C12A7 prepared at 600 °C (**P-600-A**) and 800 °C (**P-800-A**) for 4 h under static ambient air ($pO_2 = 0.2$ and uncontrolled humidity content).

All spectra showed an asymmetric signal with an orthorhombic shape, typical feature of superoxide radicals (O_2^-).[8] The characteristic *g*-values of the O_2^- ion ($S = ½$, $g_{xx} = 2.004$, $g_{yy} = 2.009$, $g_{zz} = 2.073$) obtained by computer simulation (see red dotted-line in Figure 2.1) demonstrated to be in good agreement with those reported in the literature.[8,9,11] In contrast, we excluded the existence of O^- radicals since its distinctive feature rising at $g = \sim 2.04$ was not observed in any of the spectra of this set. Besides, the absolute concentration of paramagnetic species normalized by the mass (solely attributed to O_2^- radicals) was determined by comparing the double integral of each spectrum with the one of vanadyl sulfate ($VOSO_4 \cdot K_2SO_4$) used as standard. The superoxide anions quantification showed that **P-800-A** contained the highest amount of O_2^- radicals (4×10^{17} spin·g^{-1}) among all three specimens, being *ca.* one order of magnitude higher than the lowest O_2^- content displayed by **P-600-A** (5×10^{16} spin·g^{-1}).

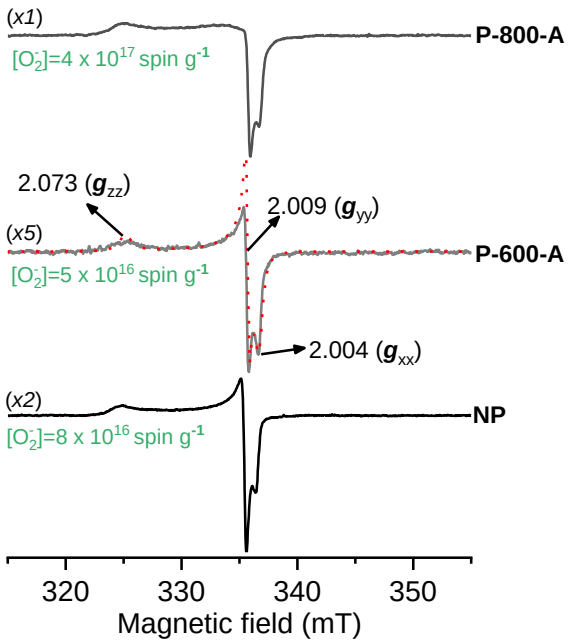

Figure 2.1. EPR spectra collected at -196 °C of non-porous C12A7 (NP) and porous C12A7 calcined at 600 °C (P-600-A) and 800 °C (P-800-A) under static ambient air. The simulated spectrum of P-600-A is also depicted (red dotted-line). The corresponding total concentration of superoxide ions are shown beneath each spectrum (green).

The Raman bands appearing in the low-spectral region (200-1000 cm^{-1}, *black dashed lines*) of the spectra shown in Figure 2.2 were ascribed to the C12A7 framework modes assigned to the Al-O framework vibrations, as reported in the literature.[102,103,124] It is worth mentioning that none of the spectra appearing in Figure 2.2 have undergone any baseline background correction, so avoiding any modification of the Raman bands. For **NP** and **P-800-A**, the most dominant Raman mode attributed to the symmetric vibration of bridged oxygen (Al-O-Al) between tetrahedra $(AlO_4)^{5-}$ appeared at 520 and 518 cm^{-1}, respectively. Meanwhile, the latter band was shifted to lower frequencies (513 cm^{-1}) in the **P-600-A** spectrum. By analyzing the Raman spectra of three different **P-600-A** obtained from different batches and on different dates (*see the Appendix*, Figure B.1), we observed that in all the cases the maxima for the most dominant Raman mode of C12A7 appeared shifted to lower frequencies (510-513 cm^{-1}). This observation led to investigate the possible reasons

behind this modification in the position of the Raman bands. A detailed comparison between **porous** and **non-porous C17A7** spectra revealed several less evident differences. For instance, by comparing the band intensity of those shown at 840 and 883 cm^{-1}, we observed that the former band seemed more prominent in the porous C12A7 spectra. This observation could be related to the higher hydration degree of porous C12A7 as a result of its preparation pathway (*i.e.*, porous C12A7 was obtained by calcining a solid precursor composed of hydroxides). Consequently, a modification in the number of hydroxyl groups occupying the cages associated with this higher hydration degree of the crystal structure (Al-OH...Al-O unit)[125] could have led to the intensity change in the latter bands, as will be discussed in the following sections. Besides, the bands emerging in the region below 1000 cm^{-1} observed in the porous C12A7 spectra (*purple dashed lines*), while absent in the **NP** spectrum, might be associated with the CaO phase also present in **P-600-A** and **P-800-A** specimens (*vide infra*).

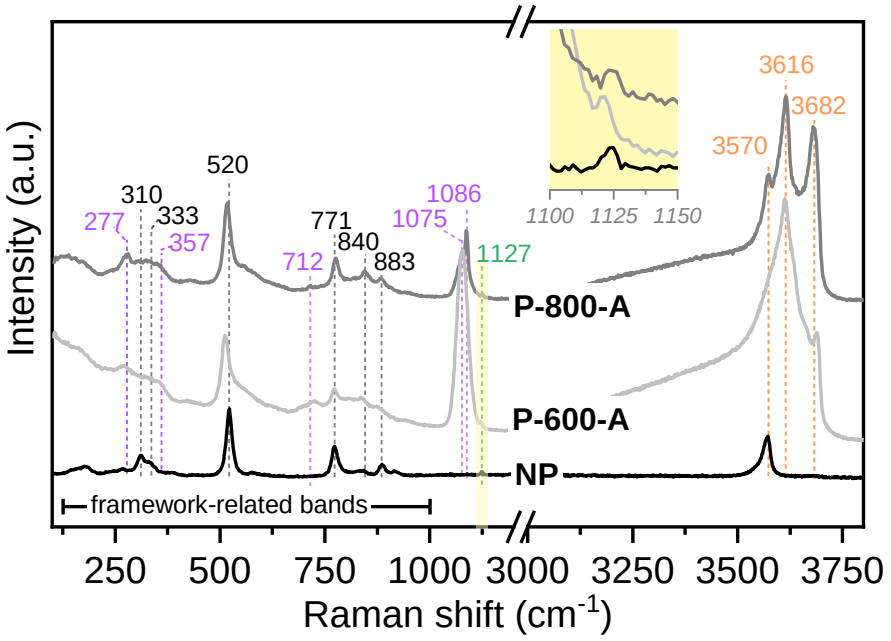

Figure 2.2. Raman spectra in the low- and high-frequency regions of non-porous C12A7 (**NP**) and porous C12A7 calcined at 600 °C (**P-600-A**) and 800 °C (**P-800-A**) under static ambient air. Inset in yellow displays the spectral region corresponding to the vibrational mode of O_2^- radical. None of the Raman spectra presented here were baseline correction.

In the low-frequency region above 1000 cm^{-1}, non-porous and porous C12A7 samples spectra displayed a small peak at ~1127 cm^{-1} (*see inset in yellow*, Figure 2.2). While porous C12A7 spectra (**P-600-A** and **P-800-A**) also showed a broad prominent band centered at 1075 cm^{-1} and a sharp superposed band at 1086 cm^{-1} (**P-800-A**). According to Che *et al.*[69], the stretching vibration of superoxide species on the surface of metal oxides can be found in the spectral region between 1075-1195 cm^{-1}. Regarding pristine C12A7, Hosono's group[9,11,12,102] has assigned a Raman band between 1125-1135 cm^{-1} to the vibrational stretching mode of O_2^- radical occluded inside mayenite cages. In contrast, several other research groups[56,82,84,98] working with bare- and doped-mayenite derivatives (*e.g.*, Si-C12A7) have attributed a band positioned between 1075-1085 cm^{-1} to the Raman mode of encaged O_2^- ions. For instance, if we focus only on the **P-600-A** spectrum, which portrays the most prominent peak at 1075 cm^{-1} among all C12A7 specimens, we could anticipate that this sample possesses the largest concentration of O_2^- ions. Yet, this hypothesis was proved inaccurate by two facts. First, the above-presented EPR analysis showed that **P-600-A** displayed the lowest concentration of superoxide species. Besides, **NP**, possessing a slightly higher content of O_2^- ions than **P-600-A**, exhibited no Raman modes at 1075 or 1086 cm^{-1}. Therefore, we may deduce that the band appearing ~1127 cm^{-1} in our spectra is the one ascribable to O_2^- ions in agreement with Hosono's group[9,11,12,102] interpretation.

To support the latter elucidation, we have compared the Raman spectra of **NP** and **P-800-A** (*see the Appendix*, Figure B.2) with experimentally obtained spectra of lime-based compounds, considering that porous C12A7 (**P-600-A** and **P-800-A**) also contained CaO as a minor phase (*see section 3.2 in Chapter I, p. 92*). However, knowing that CaO does not generate any Raman active mode because all spectral features can be attributed to either $Ca(OH)_2$ and $CaCO_3$,[101] we have employed the latter compounds in a more detailed analysis of our spectra. We noticed that $Ca(OH)_2$ displayed two distinct features at 1075 and 1086 cm^{-1}, whereas $CaCO_3$ only showed a sharp one at 1086 cm^{-1}. In a previous report related to the analysis of lime-based materials, Schmid *et al.*[101] assigned these vibrational modes to the CO_3^{2-} stretching vibration in crystalline (1086 cm^{-1}) and amorphous (1080 cm^{-1}) calcium carbonate. Consequently, in opposition to the

presumed attribution of the bands in the region between ~1070-1090 cm^{-1} to superoxide anions,[43,98] we have determined that these Raman features belong to the CaO phase (superficially carbonated) and the coexistent amorphous carbonated. Meanwhile, the differences in band intensity (1075 cm^{-1}) shown between the spectra of **P-600-A** and **P-800-A** could be associated with the significantly higher content of amorphous domains in the former sample due to calcination at a lower temperature.

In the high-frequency region related to the vibrational modes of hydroxyl groups, three distinct bands around 3570, 3616, and 3682 cm^{-1} (*orange dashed lines*) were observed in the spectra (Figure 2.2). Besides, a broad band rising from the background below *ca.* 3550 cm^{-1} was also revealed in **P-600-A** and **P-800-A**. On the one hand, the occurrence of extra-framework OH^- ions was confirmed by the band at 3570 cm^{-1} attributed to the stretching vibration of OH^- inside C12A7 nanocavities.[35,45] The incorporation of OH^- ions in our samples can be explained as follows. The C12A7 preparation by solution combustion synthesis unavoidably employed water as a solvent for the precursors dissolution, which was evaporated during the combustion reaction promoting the presence of water vapor during the formation of the as-burnt solid (*i.e*., preparation of pristine **NP** or amorphous precursor). Besides, during the last stage of preparation of **P-600-A** and **P-800-A** upon calcination of the as-dried solid precursor, mainly formed of hydrogarnet ($Ca_3Al_2(OH)_{12}$), substantial amounts of $H_2O_{(g)}$ were released during the formation of C12A7 and CaO (*see section 3.2 in Chapter I*, *p. 92)*. On the other hand, the two other bands located above 3600 cm^{-1} showing maxima at ~3616 and ~3682 cm^{-1} (not observed in **NP**) might be attributed to the presence of CaO (*see Appendix B*, Figure B.2, $Ca(OH)_2$ spectrum) and associated with structural “hydrogarnet” defects. Several reports studying anhydrous and partially hydrated mayenite minerals hosting halide ions (*i.e*., C12A7 containing Cl^- or F^-*,* as counter-anions),[21,125–127] have proposed that the latter bands can be linked to OH groups interacting with the C12A7 framework rather than being entrapped as counter-anions. Galuskin *et al*.[21] proposed that the hydration capacity of mayenite might be more significant than anticipated. They suggested that C12A7 might be capable of incorporating up to six hydroxyl anions per mayenite formula unit—considering that each unit cell ($Ca_{24}Al_{28}O_{66}$) contains two C12A7 units—according to the following reaction:

$Ca_{12}Al_{14}O_{33} + 3H_2O \rightarrow Ca_{12}Al_{14}O_{30}(OH)_6$. However, for the above said to occur, two oxygens in *O2* position (non-bridging between tetrahedra) might be substituted by three hydroxyls each of them, producing a change in the coordination of two Al atoms composing the *T1* tetrahedron from a tetrahedral (AlO_4) to octahedral ($AlO_3(OH)_3$) configuration. Additionally, they have proposed that this structural modification in mayenite upon total hydration ($Ca_{12}Al_{14}O_{30}(OH)_6$) could be considered the initial step towards the consecutive formation of a hydrogarnet phase.[21,125–127] Therefore, considering that **P-600-A** and **P-800-A** were produced by calcining a solid, mainly formed of $Ca_3Al_2(OH)_{12}$, we might assume that these bands at ~3616 and ~3682 cm^{-1} are associated with structural hydrogarnet defects..[21] Moreover, the broad band below 3550 cm^{-1} has been assigned to the symmetric and antisymmetric vibrations of molecular H_2O adsorbed at the superficial cages of C12A7.[125] Consequently, the occurrence of these bands in the hydroxyl region and their connections with a hydrated “defected” C12A7 phase could also explain our observations linked to the low-frequency shifts and intensities variations of the Al-O vibrations in porous C12A7, in which were predominantly observed in **P-600-A**.

The electronic properties of the three C12A7 samples were analyzed by DR-UV-Vis spectroscopy. We examined the position of the optical absorption edge to determine the predominant extra-framework species in each sample of this set. Figure 2.3 shows the absorption spectra (obtained by Kubelka-Munk transformation of diffuse reflectance spectra) of non-porous and porous C12A7 prepared under static ambient air. We observed that the edge of the optical absorption band for **NP** (5.2 eV) appeared at lower energy compared with **P-600-A** (5.7 eV) and **P-800-A** (5.7 eV). Hayashi *et al.*[123] demonstrated that the position of the absorption edge, ranging between ~4-6 eV, is strongly influenced by the chemical identity of the predominant clathrated extra-framework species. They found that the absorption edge shifts to higher energy with an increase in OH^- and concomitant decrease in O^{2-} ion contents. They established that when C12A7 almost exclusively possessed encaged oxide ions (C12A7:O^{2-}), the absorption edge was positioned at *ca.* 4.9 eV. This absorption band was attributed to the electronic transition from the oxide ion (O^{2-}) localized state to the framework conduction band ($O^{2-} \rightarrow$ FCB). On the opposite, C12A7 predominantly containing OH^- (C12A7:$2OH^-$) showed

an optical absorption band edge at ~5.7 eV, which was related to the strong electronic transition from OH^- → FCB (see inset Figure 2.3). Thus, in our case, the observed differences in the position of the absorption edge between non-porous and porous C12A7 samples could be explained as follows. The absorption edge values obtained for specimens **P-600-A** and **P-800-A,** in close agreement with the absorption edge position for C12A7:$2OH^-$, indicated that porous C12A7 prepared under static ambient air predominantly contains clathrated OH^- ions. In the case of **NP**, (i) a lower content of OH^- ions and (ii) the coexistence of O^{2-} ions could induce a shift in the position of the optical absorption edge, becoming closer to the one for C12A7:O^{2-}.

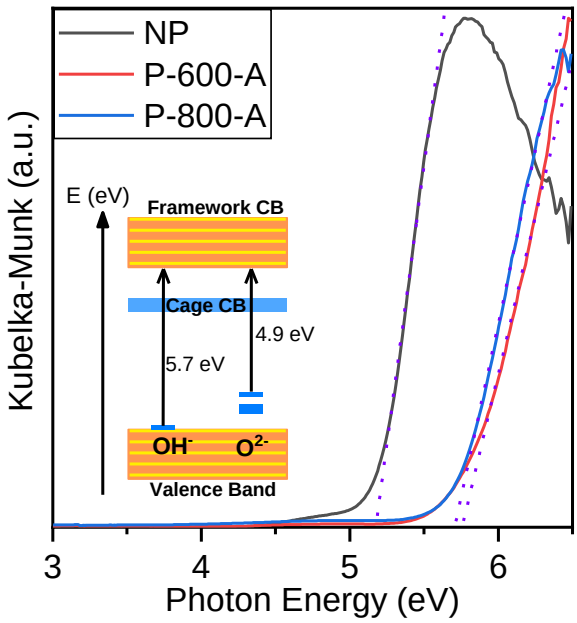

Figure 2.3. Optical absorption spectra obtained by Kubelka-Munk transformation of the DR-UV-Vis spectra of **NP** (black line), **P-600-A** (red line), and **P-800-A** (blue line) prepared under static ambient air. The y-axis values of the DR-UV-Vis spectra were normalized by the maximum value to facilitate their visualization. Electronic structures of C12A7 containing encaged OH^- or O^{2-} ions are shown in the inset. Optical transitions of each anion to the framework conduction band (CB) are shown with solid arrows.[123]

In summary, even though we undoubtedly identified and quantified O_2^- ions (electrophilic species) in this set of samples, their concentrations were significantly lower in contrast to OH^- ions. In the

case of porous C12A7, both **P-600-A** and **P-800-A**, prepared under static air with uncontrolled humidity (method **A**), had an extra-framework population distribution dominated by OH^- ions. In opposition, the pristine **NP**, aside from having a substantial content of hydroxyl anions in its cages, also contained O^{2-} ions.

3.2 Influence of the preparation/post-treatment conditions on the modulation of the extra-framework species distribution

Based on the detailed analysis related to the identification of the different extra-framework species described in the previous section, herein we investigate and discuss the effects that modifying the preparation or post-activation conditions could have on the control of the extra-framework species distribution and determine to what extent we can modulate the oxygen species population in C12A7. To this end, we have studied several setup methods (*described in section 2.2, p. 108*), varying the preparation conditions such as the calcination temperature, atmosphere composition, and contact configuration between the solid sample and the gas stream (parallel or cross-flow setup). These varied set of conditions are summarized in Table 2.1.

Table 2.1. Sample setup conditions for the post-activation of **non-porous C12A7** and the preparation of **porous C12A7**

Sample	Atmosphere	Type	Temp. (°C)	pO_2 (atm)	pH_2O (atm)
P-600-A[a]	Static ambient air	Porous	600	0.2	~0.026[d]
P-800-A[a]	Static ambient air	Porous	800	0.2	~0.026[d]
P-800-B	Parallel flowing O_2	Porous	800	1.0	(<2 x 10^{-4})[e]
P-800-C	Cross-flowing O_2	Porous	800	1.0	(<2 x 10^{-4})[e]
NP[b]	Static ambient air	Non-porous	-	0.2	~0.026[d]
NP-600-A[c]	Static ambient air	Non-porous	600	0.2	~0.026[d]
NP-800-A[c]	Static ambient air	Non-porous	800	0.2	~0.026[d]
NP-800-B[c]	Parallel flowing O_2	Non-porous	800	1.0	(<2 x 10^{-4})[e]
NP-800-C[c]	Cross-flowing O_2	Non-porous	800	1.0	(<2 x 10^{-4})[e]

[a] Samples **P-600-A** and **P-800-A** referred to the samples produced by assisted SCS approach described in Chapter I (*see section 2.5, p. 74*). [b] Sample **NP** was produced by SCS using a double fuel-approach ($\phi = 1$) described in Chapter I (*see section 2.4, p. 73*). [c] Sample **NP** was used as starting material. [d] Estimated value considering an average room temperature of 22 °C. [e] Water content provided by the gas supplier (AirLiquide).

To assess the presence of either O_2^- and OH^- ions, the two sets of C12A7 samples were analyzed by Raman spectroscopy. The normalized spectra of non-porous (post-activated) and porous (prepared) C12A7 specimens obtained under the three different methods are displayed in Figure 2.4a and b, respectively. The vibrational band at *ca.* 1127 cm^{-1} assigned to the stretching mode of O_2^- radical (*highlighted in yellow*) was reflected in all spectra of each set, thus confirming the successful incorporation of superoxide anions. Among the different strategies used to modulate the relative population of the oxygen species in this study, method **C** showed to be particularly effective in promoting the formation of O_2^- ions inside C12A7 cages, which was revealed by the greater intensity of the band peaking at ~1127 cm^{-1} observed in **NP-800-C** and **P-800-C** spectra. Additionally, regarding porous C12A7 samples (Figure 2.4b), we observed some differences concerning to bands previously attributed to $CaCO_3$ and $Ca(OH)_2$ Raman-active modes displayed by the CaO phase. For instance, the band at ~1086 cm^{-1}—stretching mode of CO_3^{2-} moiety in crystalline $CaCO_3$—noticeable in the **P-800-A** spectrum was diminished from the **P-800-C** one. This observation suggests that CaO carbonation was avoided since the calcination was performed under pure dry $O_{2(g)}$, *i.e.*, free of ambient $CO_{2(g)}$. The latter statement demonstrates, once again, that those bands present in porous C12A7 are not, in any manner, related to superoxide ions.

In the hydroxyl spectral region (above 3000 cm^{-1}, Figure 2.4a and b), the band rising at 3570 cm^{-1} undoubtedly confirmed the occurrence of encaged OH^- ions in all the C12A7 specimens. This observation showed that the hydroxyl species incorporation could not be prevented under any of the studied combinations of conditions and setups, even when the calcination was performed under pure dry $O_{2(g)}$ at 800 °C (methods **B** and **C**). However, by employing method **C**, the broad band below ~3550 cm^{-1} and the other one at 3682 cm^{-1}, associated with a higher hydration degree of the C12A7 structure were noticeably reduced in **P-800-C** as compared to **P-800-A** and **P-800-B**. In contrast, **NP-600-A** was the only specimen presenting the hydration “defective” band (3682 cm^{-1}) in the set of non-porous C12A7, which could be correlated to the calcination at low temperature in the presence of water (static ambient air), thus promoting a structural deformation of Al tetrahedra by changing the Al coordination,[21] as earlier discussed.

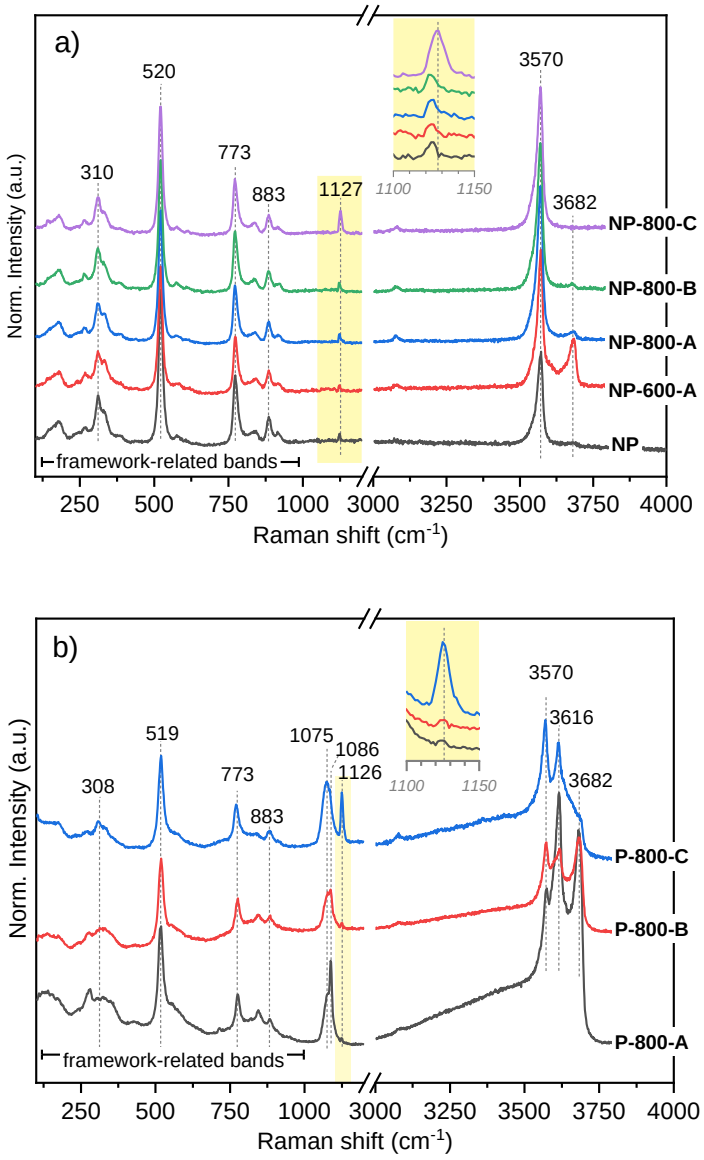

Figure 2.4. Raman spectra of a) **non-porous** and b) **porous C12A7** samples either post-activated or prepared according to the experimental conditions summarized in Table 2.1. Each spectrum was normalized by the intensity of the band at *ca.* 520 cm^{-1} corresponding to the most dominant Raman mode of the C12A7 framework (symmetric vibration of bridged oxygen, Al-O-Al). None of the Raman spectra presented here were baseline correction.

Unlike Raman analysis, EPR spectroscopy allowed us to assess the relative concentration of superoxide species (O_2^-) and to evidence

and quantify the oxygen ion radicals (O^-) possibly incorporated in each sample of the two studied sets. The collected experimental spectra are shown in Figure 2.5a and b, whereas the total spin concentrations of paramagnetic oxygen species are plotted in Figure 2.6a and b.

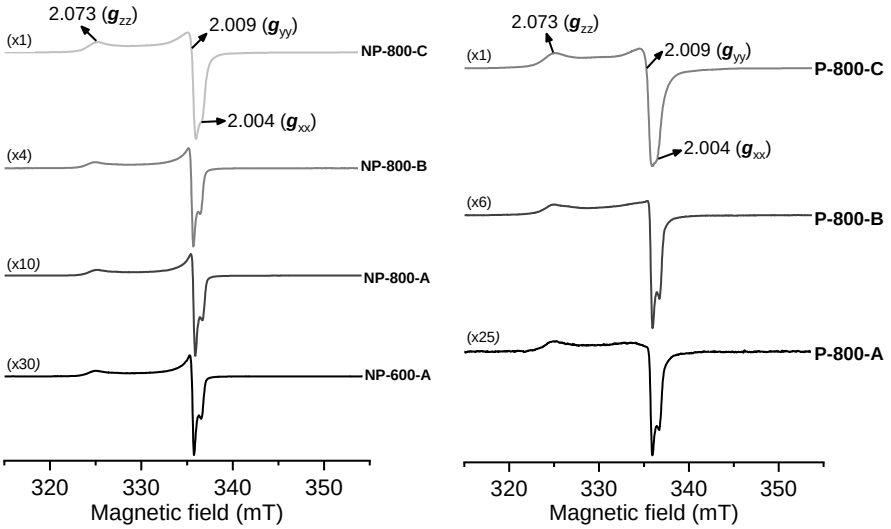

Figure 2.5. EPR spectra of a) **non-porous** and b) **porous C12A7** prepared under several setup conditions summarized in Table 2.1.

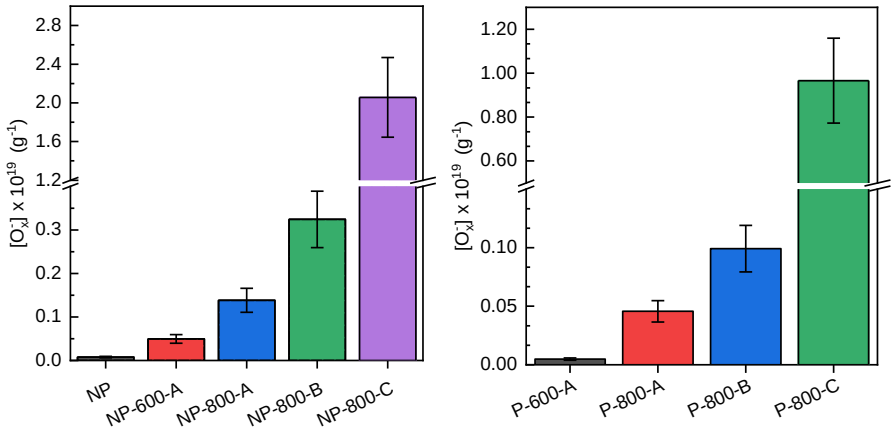

Figure 2.6. Total concentration of paramagnetic oxygen species for a) **non-porous** and b) **porous C12A7** specimens obtained by double integration of EPR spectra shown in Figure 2.5. Error bars represent the cumulative error from quantification analysis.

We noticed that all samples essentially contained superoxide anions, irrespective of the method employed for their post-activation/formation and their texture, as illustrated by the asymmetric sharp shape of the EPR lines ascribable to O_2^- species, validating the Raman results (*vide supra*). In the previous section, we observed that the rise of the calcination temperature favored the formation of these oxygen species, which is also confirmed in the case of non-porous C12A7 specimens, showing a rise in the concentration of O_2^- ions by increasing the temperature in the post-annealing treatment. Besides, by comparing samples treated at the same calcination temperature (*i.e.,* 800°C) but under different atmosphere compositions (method **A** vs. **B**) within each set, we observed that by increasing the oxygen partial pressure from 0.2 to 1.0, the absolute oxygen species concentration was also enhanced (Figure 2.6a and b).

Furthermore, consistent with the Raman observations, the EPR analysis demonstrated that method **C** played a significant role in enhancing the concentration of reactive oxygen species (ROS). This was evident from the intensity of the spectra (Figure 2.5) and the absolute concentration of paramagnetic oxygen radicals observed in the **NP-800-C** and **P-800-C** samples (Figure 2.6). For instance, in the case of non-porous C12A7, **NP-800-C** possessed a concentration *ca.* 6-fold higher in oxygen radicals than **NP-800-B,** both post-activated under the same atmosphere ($pO_2 = 1.0$), but employing a different gas/solid contact configuration, namely cross flow for **C** vs. parallel flow for **B**. In contrast, the porous C12A7 prepared by cross flow configuration (**P-800-C**) showed approximately a 10-fold increase in ROS concentration compared to the one produced using parallel flow (**P-800-B**). These suggest that the type of contact between the solid and the gas stream is of pivotal importance for the modulation of the extra-framework species inside C12A7. It is noteworthy to mention that the increasing trends in the concentration of oxygen radicals, achieved by raising the temperature, oxygen partial pressure, or modifying the contact mode, remained consistent despite the associated error value (approximately 20%) in the analysis.

A more detailed evaluation of the **NP-800-C** and **P-800-C** spectra by computational simulation revealed that both samples also contained clathrated O^- radicals (*see Appendix B*, Figure B.3). The EPR lines of each sample (at the top of Figure 2.5a and b) were deconvoluted into

two superposed components, attributable to O_2^- (g_{xx} = 2.004, g_{yy} = 2.009, g_{zz} = 2.073) and O^- (g_{xx} = g_{yy} = 2.035, g_{zz} = 1.997) species. However, the $[O^-]/[O_2^-]$ ratios values obtained for **NP-800-C** (~0.12) and **P-800-C** (~0.15) samples reflected a predominance of O_2^- species in both samples. In earlier reports, Hosono *et al.*[9–11] noticed that superoxide radicals tended to be more stable and to form more promptly than oxygen anions at low temperatures and oxygen partial pressures. However, they found nearly equivalent amounts of both species ($[O^-]/[O_2^-] \approx 1$) when C12A7—containing almost exclusively oxide ions (O^{2-}) as extra-framework species—was calcined under a pure dry oxygen atmosphere at elevated temperature (1350 °C) and high pressure (400 atm). Thus, since all our experiments were conducted at low temperatures (utmost 800 °C) and atmospheric pressure (1 atm), and also considering that our C12A7 samples contained considerable amounts of OH^- ions as depicted by Raman analysis, it is consistent that we have observed a prevalent or sole presence of superoxide anions in our samples.

To go deeper in investigating the effect of controlling the atmosphere composition on the modulation of the population distribution of extra-framework species, we examined the position of the optical absorption edge of selected C12A7 specimens (Figure 2.7). In the case of non-porous C12A7, we observed the rise of a new absorption band around 4.7 eV, clearly visible in the **NP-800-C** spectrum. In an earlier report, Hayashi *et al.* [123] associated this band with the oxygen radicals formation, namely O_2^- ions. They proposed that this band could be related to i) an intramolecular transition in O_2^- ions from the occupied state π_u to the unoccupied state π_g (green arrow in inset b, Figure 2.7) or ii) a transition from the VB to the unoccupied state π_g of the superoxide anion (purple arrow in inset b, Figure 2.7). Therefore, based on the verified presence of O_2^- ions by EPR and Raman analyses, we have consistently attributed the latter band to the occurrence of superoxide anions in our samples. Additionally, the absorption edge for the **NP-800-C** specimen post-treated under pure dry oxygen, in contrast to **NP-800-A** post-activated under ambient air, showed a slight shift to lower energy, suggesting a higher presence of O^{2-} ions in the former sample. Conversely, the noticeable lower prevalence of the absorption band at *ca.* 4.7 eV in the spectrum of **P-800-C** (see inset a, Figure 2.7)—which presents the second highest

relative concentration of O_2^- ions—could be presumptively related to the strong predominance of the absorption edge related to OH^- ions, masking the O_2^- absorption band. However, by contrasting **P-800-C** and **P-800-A** spectra, we noticed that the edge position was slightly moved down for the former sample, denoting a lesser presence of OH^- ions due to the calcination under pure dry oxygen, thus somewhat promoting the dehydroxylation of the cages. Even though the increase in the oxygen partial pressure (pO_2 from 0.2 to 1.0) led to a substantial rise in the relative concentration of oxygen radicals (*ca.* 100-200 times more ROS, Figure 2.6b), **P-800-C** specimen obtained by method **C** still displayed an extra-framework species distribution preponderated by OH^- ions. The latter might be related to the high stability of OH^- ions inside the mayenite structure even at high temperatures (over ~1000°C), owing to the unique great hydration enthalpy of C12A7 (-228 ± 40 kJ·mol^{-1}).[35]

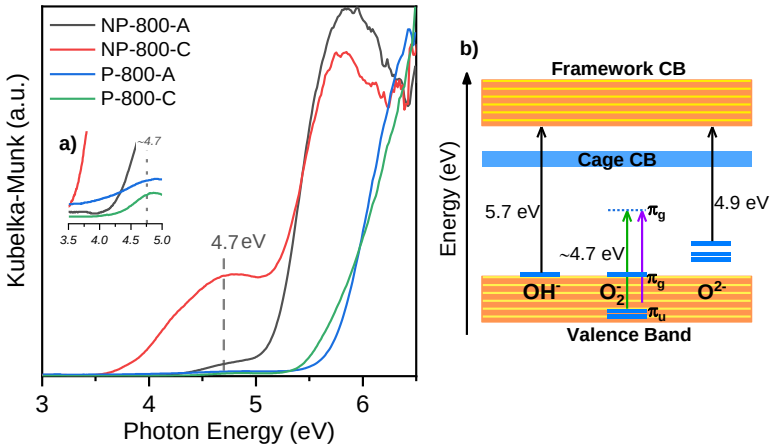

Figure 2.7. Optical absorption spectra obtained by Kubelka-Munk transformation of the DR-UV-Vis spectra of **NP-800-A** (black line), **NP-800-C** (red line), **P-800-A** (blue line), and **P-800-C** (green line) prepared by methods **A** (calcined under ambient air) and **C** (calcined under pure dry oxygen). The y-axis values of the DR-UV-Vis spectra were normalized by the maximum value to facilitate their visualization. Insets show a) zoomed region of the Kubelka-Munk transformation plot, b) the electronic structures of C12A7 containing encaged OH^-, O_2^-, and O^{2-} ions.[123]

3.3 Catalytic performance: propane oxidation

Selected catalysts presenting distinct structural properties and varying concentration of reactive oxygen species, were tested in the

propane oxidation reaction. This reaction, in opposition to the carbon black oxidation reaction studied in Chapter I, is expected to help us elucidate the effect that the nature of the oxygen species (*i.e.,* electrophilic or nucleophilic) inside C12A7 and their relative concentrations could have on its catalytic activity, but most importantly, on the modulation of its selectivity by analyzing the entire distribution of products at steady conditions under different reaction temperatures. In this section, we have focused on the catalytic performance of C12A7 specimens under operational conditions for propane total oxidation (*i.e.,* low propane concentration *ca.* 1000 ppmv balanced with synthetic air), knowing that the different investigated methods in the previous sections mainly led to the incorporation of electrophilic oxygen species and hydroxyl ions inside C12A7 cages.

From the light-off curves presented in Figure 2.8—showing the propane conversion over time at different reaction temperatures—we observed that pristine non-porous C12A7 **(NP)** appeared as the least active catalyst. At temperatures below 550°C, **NP** showed to be inactive, while from there on, it showed a marginal increase in its activity, reaching an overall conversion of 15% at 650°C, slightly superior to the propane conversion obtained without any catalyst (Blank run, X_{C3H8} = 10% at 650°C). Given that only inert SiO_2 chips were loaded into the catalytic reactor in the blank run, the observed activity is attributed to homogenous gas phase reactions, which occur from 550°C.[1] The low catalytic activity displayed by **NP** is probably associated with the diffusional limitations of the extra-framework species in the bulk of C12A7, as will be discussed below.

Moreover, porous C12A7 samples (**P-600-A** and **P-800-A**) annealed under static ambient air (uncontrolled humidity) showed to be active from 400°C and reached total propane conversion at 650 °C—100 degrees below the respective temperature for complete oxidation without a catalyst. **P-600-A** was revealed to be more efficient at converting propane in the temperatures range between 400-600 °C, as compared to **P-800-A** (Figure 2.8). On the one hand, if we consider that **P-600-A** presented the lowest concentration of superoxide anions (electrophilic species) among all C12A7 specimens, as revealed by EPR analysis (Figure 2.6), we would have expected to observe an opposite trend in the catalytic behavior of the two latter samples. On the other hand, we also have to consider that both specimens have distinct textural properties. For instance, **P-600-A** possesses a higher

S_{BET} and smaller crystallite size than **P-800-A** *(see Table 1.3 in Chapter I, p. 96*), which showed to be crucial parameters influencing the catalytic performance of C12A7, as previously revealed in Chapter I. Therefore, based on the relative importance of these factors, at low ROS contents, we may suggest that the physical properties (specific surface area and morphology) preponderate the role played by oxygen radicals in the catalytic activity. However, considering the relatively low concentrations of ROS (*ca*. 100-200 times lesser) displayed by **P-600-A** and **P-800-A**, in contrast to **P-800-C**, it cannot be generalized that an increase in the relative concentration of oxygen radicals is not an effective way to promote the catalytic activity of C12A7.

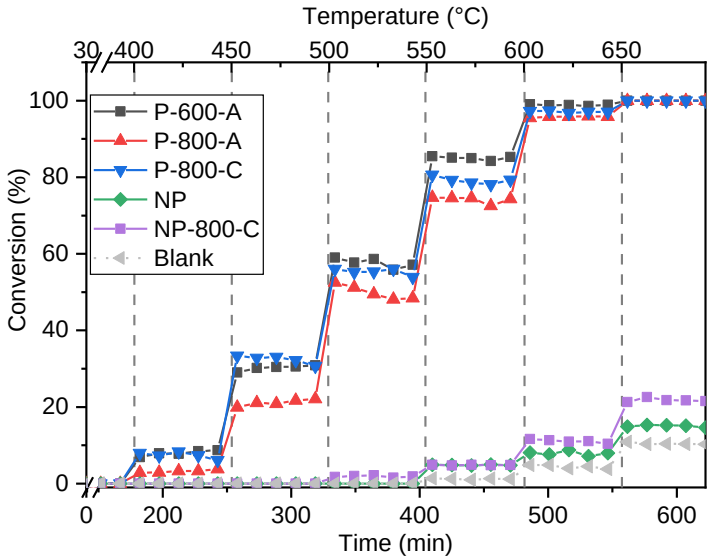

Figure 2.8. Catalytic activity of selected C12A7 materials prepared or post-activated according to the conditions summarized in Table 2.1. A blank run (reactor loaded only with inert SiO_2 chips) is also depicted for comparison, the complete oxidation, not shown here, was reached at 750°C. Catalytic test conditions: total flow rate of 40 mL·min^{-1} containing 1000 ppmv C_3H_8 balanced with synthetic dry air; catalytic bed composed by 0.15 g of catalyst diluted with 0.35 g of SiO_2 chips.

As evidenced in the General Introduction (*see section 5.1.2, p. 41*), there are only a few studies reporting on the effect of the amount of reactive oxygen species on the activity of C12A7 for oxidation applications. For instance, Fujita *et al.*[82] reported that the amount of occluded oxygen anions could be manipulated by changing the Si/Al

ratio by preparing and examining various Si-doped C12A7 derivatives ($Ca_{12}Al_{14-x}Si_xO_{33+0.5x}$, $0 \leq x \leq 4$). However, they found that as the doping degree increased (*i.e.*, higher content of reactive O_2^- and O_2^{2-} species), the activity of Si-C12A7 derivatives in the oxidation of several hydrocarbons gradually decreased with the increase in the Si/Al ratio instead of improving.[58,98] Yet the authors did not provide further interpretation about this unexpected outcome. On the opposite, in a most recent study, Intiso *et al.*[56,84] examined the catalytic performance of C12A7 prepared by different synthetic strategies for the trichloroethylene oxidation reaction. They proposed that an adequate combination of high surface area and high number of active species (superoxide radicals) can improve the activity of mayenite.

Consequently, to elucidate if a substantial increase in the content of ROS could lead to a noticeable enhancement in the catalytic activity (*i.e.,* high oxidation rate at lower temperatures), we further investigated the catalytic behavior of **NP-800-C** and **P-800-C** specimens, each of which had the highest concentration of electrophilic oxygen radicals (O^- and O_2^-) within their corresponding set. For instance, **NP-800-C** performance was expected to be markedly improved since an almost 260-fold increase in the concentration of ROS was observed, as compared to pristine non-porous C12A7 (**NP**). Yet the forecast outcome was not reflected. Albeit the significant gap in the ROS concentration between the two latter catalysts (Figure 2.6a), **NP-800-C** showed to be inactive under 550 °C, and only a modest improvement in its activity was noticed from there on, reaching a propane conversion of *ca.* 20% at 650 °C, faintly superior to that of **NP** (Figure 2.8). Conversely, even though **P-800-C** possessed approximately half the content of oxygen radicals displayed by **NP-800-C**, the former sample exhibited a notably better catalytic activity than the latter. These divergent behaviors between porous and non-porous specimens can be related to their distinct textural and structural properties. For instance, the relatively low S_{BET} (1 $m^2 \cdot g^{-1}$) and bulky morphology of non-porous mayenite, presenting large particle sizes (*ca.* 1-100 microns, *see Figure 1.6 in Chapter I, p. 86*), could act as a mass transport barrier, preventing the desorption of the occluded reactive oxygen species at low temperatures. On the contrary, the smaller particles (agglomerated grains with a size less than 100 nm, *see Figure 1.14 in Chapter I, p. 97*) and higher S_{BET} could facilitate the desorption of the oxygen species by reducing the diffusion pathway

inside the C12A7 bulk. Yang *et al.*[11] observed that the desorption of the entrapped oxygen species in the C12A7 structure is mainly limited by the mass diffusion of the ROS from its bulk to the outmost layer at the surface of C12A7. To sustain this hypothesis, we thus performed a TPR-H_2 analysis with **NP-800-C** and **P-800-C** to determine at which temperature the occluded oxygen species is readily available to react with hydrogen (*see Appendix B*, Figure B.4). By doing so, we noticed that **P-800-C** reduction (T_{red} ≈ 590 °C) occurred around 150 degrees below that of **NP-800-C** (T_{red} ≈ 750 °C), demonstrating that the enhanced structural properties of porous C12A7 promoted the desorption of the ROS and thus rendered them accessible to react with H_2. Overall, this last observation proved the prevailing importance of the textural and structural properties on the catalytic activity.

Moreover, to properly evidence the benefits of increasing the concentration of oxygen radicals on the C12A7 catalytic performance, we first needed to exclude the influence of textural properties. To that end, the light-off curves of the porous specimens (Figure 2.8) were normalized by their specific surface area (30 $m^2 \cdot g^{-1}$, presented in Chapter I, Table 1.3), shown in Figure 2.9. By doing so, we directly observed that **P-600-A** normalized activity was the lowest among the three samples, corroborating that the improvement in its performance was due to its higher surface area. When comparing **P-800-C** and **P-800-A**, presenting equivalent surface areas but distinct amounts of oxygen species due to their preparation conditions (cross-flowing oxygen vs. static ambient air), we observed some distinctions in their catalytic behaviors. For instance, between 400-600 °C, we noticed that **P-800-C** outcompeted the other catalysts, which was associated with its higher content of oxygen radicals. In addition, we also observed a progressive decay in the activity gap between the two latter catalysts with rising the reaction temperature, whereas from 600°C equivalent propane conversions were exhibited. This activity loss might be caused by the premature depletion of the initially incorporated oxygen radicals in **P-800-C** during the propane oxidation at low temperatures and due to the impossibility of regenerating these species at the same rate as they were consumed. We tentatively associated the latter premise with two factors: i) the lower oxygen partial pressure (synthetic air, pO_2 = 0.2) in the reaction atmosphere during the catalytic test compared to the one used to prepare **P-800-C** (cross-flowing dry oxygen; pO_2 = 1, and ii) the incorporation of OH^- ions inside the cages as a result of the

water formation during the oxidation of propane. Thus, to confirm this statement, we investigated the catalytic behavior of the **P-800-C** catalyst during a second consecutive run (*see Appendix B*, Figure B.5). By doing so, we evidenced that the gain in the activity observed at low temperatures for the fresh catalyst vanished from the light-off curve of the spent one. As a result, it was revealed that the reduced catalytic performance exhibited by the spent **P-800-C** catalyst was proportional to that displayed by the C12A7 specimen produced under ambient air (**P-800-A**). According to the latter, we might suggest that the reaction medium to which **P-800-C** was exposed during the first catalytic run regenerated a substantially lower number of oxygen radicals inside the cages, somewhat close to the concentration of ROS obtained by preparing C12A7 by method **A**. Based on this experiment, we can presume that the initial concentration of ROS found in the fresh catalyst was not restored after the first run because the reaction conditions impeded their adequate regeneration.

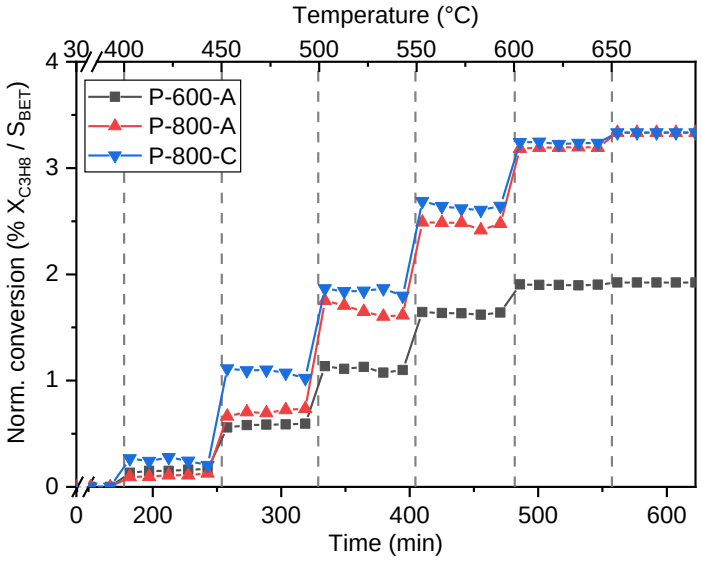

Figure 2.9. Catalytic activity of selected samples, after normalization by the specific surface area (S_{BET}).

In summary, we can conclude that the rise in the concentration of oxygen species can stimulate the activity of C12A7, but for this to occur, a tailored set of textural and structural properties is required. However, the steadiness of this promotion effect seems to be restricted by the regeneration rate of the extra-framework species under the

reaction conditions as will be confirmed in the second part of this chapter.

Finally, to examine the effect of the relative concentration of reactive oxygen species on the catalysts selectivity, we analyzed the product distribution obtained during the propane oxidation over time at different reaction temperatures as shown in Figure 2.10. For instance, when comparing the selectivities of **P-600-A** (Figure 2.10a) and **P-800-A** (Figure 2.10b), both catalysts revealed similar product distribution profiles, entirely dominated by total combustion products (CO and CO_2), where only small fractions of olefins (C_3H_6 and C_2H_4) were found. Additionally, we noticed an incremental upsurge in the CO_2 selectivity as the reaction temperature rose, outpacing CO generation above 550°C. Meanwhile, a virtually 100% CO_2 selectivity was achieved at 650°C (*i.e.*, complete conversion). In the case of **P-800-C**, in spite of its substantial higher content of oxygen radicals, its products distribution profile remained nearly the same as for the two other previous catalysts. This suggests that even though the concentration of oxygen radicals can influence the catalytic activity, it has no or rather limited impact on the selectivity of the catalyst. Yet before precipitating us in that conclusion, we also need to consider that the overall extra-framework population distribution of the investigated C12A7 specimens was dominated by OH^- radicals, as shown by DR-UV-Vis analysis (Figure 2.3 and Figure 2.7), where the oxygen radicals represented only a small fraction of the overall population of encaged species. For example, if we compared the ROS concentration of **P-800-C** (~1 x 10^{19} spin·g^{-1}) with the theoretical maximum capacity of C12A7 framework[4], which is about 8.66 x 10^{20} spin·g^{-1} (2.3 x 10^{21} spin·cm^{-3}, considering its theoretical density of 2.68 g·cm^{-3}),

[4] C12A7 theoretical maximum concentration $\left(\text{spin}\cdot g^{-1}\right) = \frac{C \times \rho}{V}$
where
V = unit cell volume, considering the C12A7 cubic structure (a^3 = 1.72 x 10^{-21} cm^3)
C = maximum charge of the C12A7 framework (4+)
ρ = C12A7 theoretical density (2.68 $cm^3 \cdot g^{-1}$)

the amount of oxygen radicals in **P-800-C** represents only ~1% of the entire population

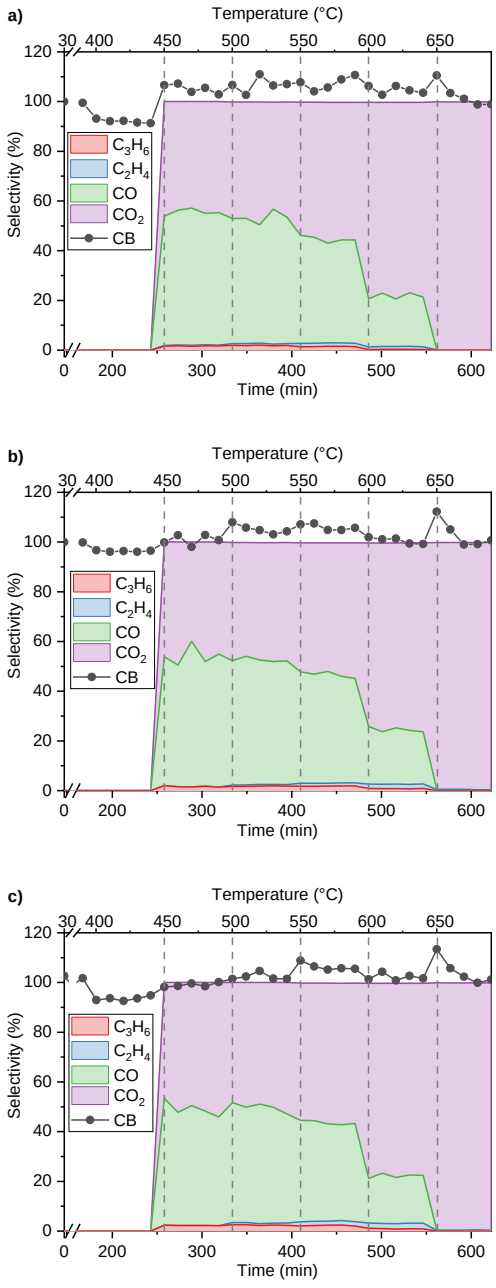

Figure 2.10. Selectivity and C-balance (CB) for **a)** P-600-A, **b)** P-800-A, and **c)** P-800-C catalysts. The presence of CH_4 at the level of traces was also noticed from 500°C.

In short, even though method **C** significantly increased the oxygen species concentration compared to the two other protocols (**A** and **B**)**,** the extra-framework population distribution of C12A7 was still dominated by hydroxyl radicals. Therefore, to assess whether or not the modulation of the oxygen species population can serve as a tool to control the selectivity of C12A7, we need to find a new strategy to promote the dominance of oxygen radicals over any other species. The latter is addressed in the second part of this chapter.

Part II: Mastering the control of the oxygen species distribution in C12A7.

4 Results and discussion

As exposed in the General Introduction (*see section 3.2, p. 28*),[35,36] the incorporation of OH^- ions in mayenite can severely reduce the presence of oxide anions (O^{2-}) inside C12A7, as described by Eq (2.2). Conversely, the formation of the reactive oxygen species (O_2^- and O^-) according to Eq (2.1) compulsorily requires the pre-existence of O^{2-} ions as extra-framework species.[10] In part I, despite all our efforts to effectively increase the concentration of O_2^- and O^- species within C12A7, we witnessed that all our preceding methods were ineffective in achieving this, because we systematically observed an extra-framework population distribution dominated by OH^- species. This matter can be associated with the fact that the preparation conditions (mainly the calcination temperature) employed in our different procedures were insufficient to promote a significant dehydroxylation of the C12A7 cages. According to the literature,[9,35] the latter process can be accomplished by increasing the calcination temperature over 1050 °C in a dry oxygen-rich atmosphere ($pO_2 \geq 1$), shifting the equilibrium to the left side of Eq (2.2). However, a calcination step at such elevated temperatures can be detrimental to the textural properties of mayenite.

Therefore, in this second part, we investigated a new protocol denoted method **D**, in which the calcination step for the preparation of porous mayenite was performed at milder conditions than that required for the complete dehydroxylation, namely at 900 °C under a dry oxygen atmosphere. In addition, we also examined the influence of the flow rate on the modulation of the oxygen species. Despite the benefits of employing a cross-flow setup as shown in part I (*see section 3.2, pp. 121-127*), herein, we selected a parallel flow configuration since it allowed us to modulate the flow rate without generating an appreciable pressure drop in the system.

Figure 2.11a shows the evolution of the oxygen species concentration with varying oxygen flow rates, which were obtained by double integration of the EPR spectra displayed in Figure 2.11b. We noticed that as the flow rate increased, the total concentration of

oxygen radicals in cages increased noticeably. For instance, when a considerably high flow rate (*ca*. 1.4 $L \cdot min^{-1}$) was employed during the preparation of C12A7 (hereafter denoted as **P-900-D-O_2**), annealed at 900 °C for 4h, a remarkable total ROS concentration of ~3.5 x 10^{20} $spin \cdot g^{-1}$ was obtained. This concentration was two-order of magnitude higher than the one displayed by a C12A7 specimen prepared under the same conditions but only employing 50 $mL \cdot min^{-1}$ of dry oxygen (as used in part I). Thus, we demonstrated that by applying a high oxygen flow rate during the calcination step, we could boost the overall concentration of oxygen species up to *ca.* 40% of the theoretical maximum content of extra-framework species within C12A7. In addition, we provided evidence that rising the calcination temperature up to 900 °C (Figure 2.11c), was also crucial to promote the concentration of oxygen radicals.

Moreover, one can see from the EPR spectra (Figure 2.11b) that the spectral shape and intensity of the signals also changed with increasing the oxygen flow rate. In particular, the line shape of the blue spectrum (**P-900-D-O_2**) highly differs from the two others—which show a typical line shape attributed to superoxide ions—suggesting the presence of more than one kind of paramagnetic oxygen species. In a previous report,[10] this specific spectral shape (a nearly single Lorentzian shape) was also shown by a C12A7 sample prepared under 400 atm of dry oxygen at 1350 °C for 2 h, which contained a high concentration of oxygen radicals ($[O^-]/[O_2^-] \approx 1$) representing *ca.* 75% of the theoretical maximum content. Hayashi *et al.* proposed that this g-anisotropy loss in the spectral shape could be related to the dipolar broadening between the O_2^- and O^- species when there are found in very high concentrations. Consequently, based on this report we can attribute the obtained spectrum (blue line) to the occurrence of both oxygen radicals in equivalent proportions (*i.e.*, the respective concentration of each species was about 1.75 x 10^{20} $spin \cdot g^{-1}$).

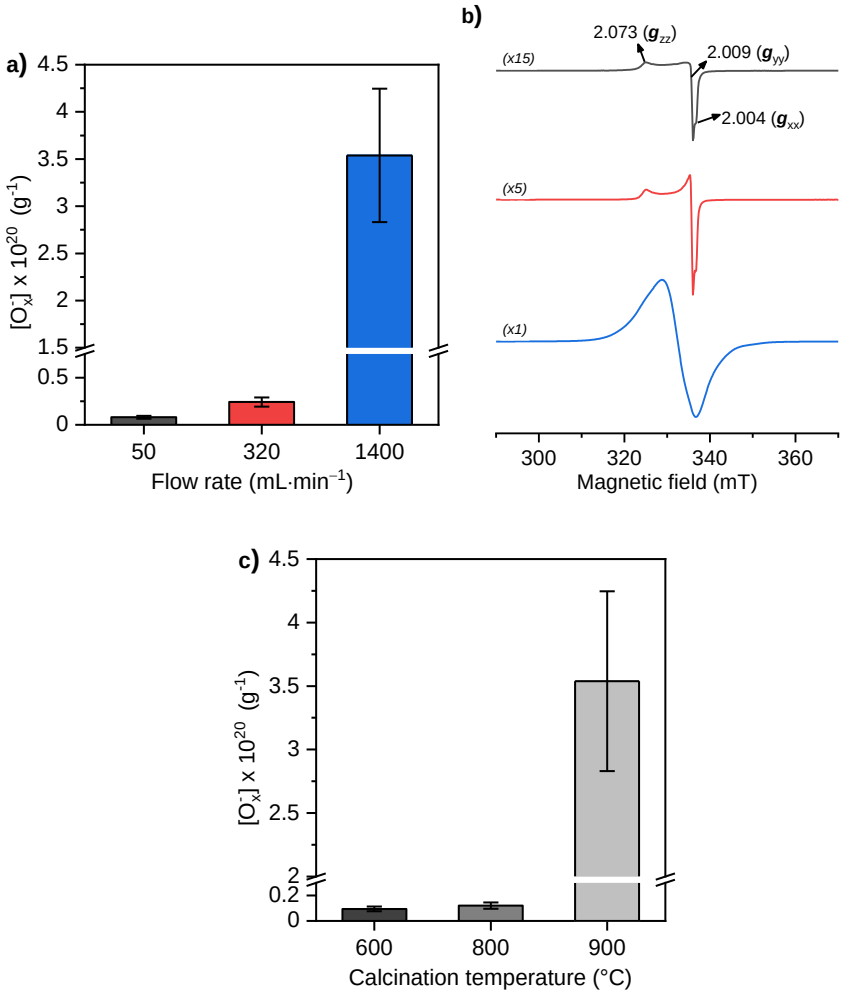

Figure 2.11. a) Evolution of the oxygen species concentration with ranging the total flow rate of oxygen. b) EPR spectra of samples prepared at 900°C for 4h under dry oxygen atmosphere employing different total flow rate. c) Total concentration of oxygen radicals in porous C12A7 obtained by using a high-flow rate (1.4 L·min^{-1}), as function of the calcination temperature. Error bars represent the cumulative error from quantification analysis.

To unveil the nature of the remaining fraction of extra-framework species, corresponding to *ca.* 60% of the theoretical maximum capacity (8.66 x 10^{20} spin·g^{-1}), we analyzed **P-900-D-O$_2$** by Raman and DR-UV-vis spectroscopies. In agreement with the EPR analysis, Figure 2.12 a and b corroborated the remarkable presence of superoxide ions in this specimen, as confirmed by the prominent Raman band at 1127 cm^{-1}

and the rising absorption band *ca.* 4.7 eV reflected in the DR-UV vis spectrum. The presence of encaged OH^- ions was confirmed by the band rising at 3570 cm^{-1} (Figure 2.12a). However, this latter band seems less intense than those OH^- vibration modes observed in Part I when compared with the principal Raman mode of the C12A7 framework at ~520 cm^{-1} (Figure 2.5), which could indicate a lesser occurrence of these moieties. In addition, the optical absorption edge at ~4.9 eV (Figure 2.12b) provided evidence of a predominant occurrence of oxygen oxide (O^{2-}) anions. These observations demonstrate that **P-900-D-O_2** presented an overall population distribution governed by oxygen species rather than hydroxyl anions, revealing that method **D** is an effective way to dehydroxylate the cages of C12A7.

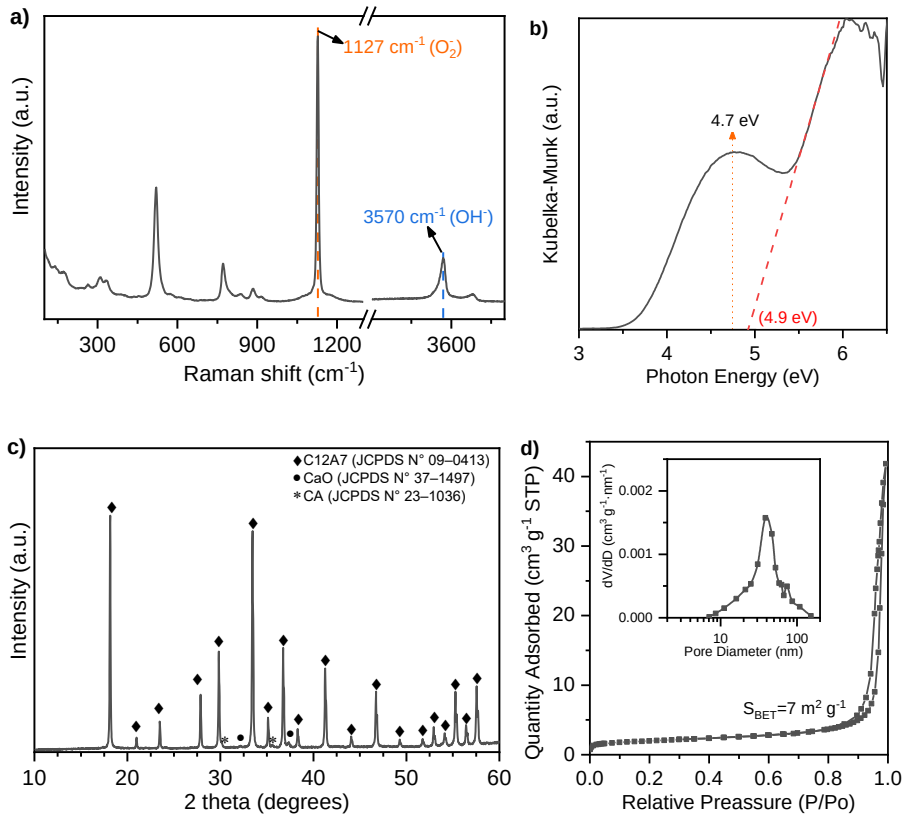

Figure 2.12. a) Raman, b) UV-vis spectra, c) PXRD diffractogram, and d) N_2 adsorption-desorption isotherms of **P-900-D-O_2**.

Overall, the observed outstanding total concentration of ROS in **P-900-D-O_2** could be explained as follows. We understood, from part I, that the annealing conditions were crucial in modulating the distribution population of extra-framework species. So, considering that our synthetic approach to producing porous C12A7 involves the calcination of a hydroxide precursor—which possesses a large number of hydroxyl moieties—it was imperative to quickly remove them before being incorporated during the formation of mayenite upon calcination. Thus, by employing a high flow rate of dry oxygen ($pO_2 = 1$; $pH_2O < 2 \times 10^{-4}$), the OH^- species coming from the decomposition of the hydroxides were more effectively evacuated than by using a low-rate flow, impeding in a great extent their incorporation within C12A7 framework. As a result, oxide ions (O^{2-}) were clathrated instead, which acted as an intermediate species being oxidized in the presence of oxygen (atmosphere), leading to the ultimate incorporation of superoxide and oxygen ion radicals in a significant quantity.

To evaluate the impact of increasing the calcination temperature on the structural and textural properties of C12A7, we examined **P-900-D-O_2** by PXRD and N_2 physisorption. The diffractogram (Figure 2.12c) showed well-defined reflection peaks associated with the C12A7 phase (♦). A negligible occurrence of a calcium aluminate phase (CA, ∗) was also depicted, whereas the concomitant presence of the CaO phase (•), previously observed in samples calcined at lower temperatures (600-800 °C, Figure 1.11a), was considerably diminished upon calcination at 900 °C. Additionally, the proportion of amorphous domains was significantly reduced. The absence of Raman mode between 1075-1085 cm^{-1} (Figure 2.12a) otherwise attributed to the amorphous carbonate moiety supported the latter. Thus, these observations revealed that **P-900-D-O_2** possessed superior phase purity and crystallinity, probably the highest among the porous specimens studied in the previous sections. Furthermore, as anticipated, the texture of **P-900-D-O_2** was notably changed. N_2 adsorption-desorption curves (Figure 2.12d) nearly corresponded to a Type II isotherm (*i.e.,* non-porous or macroporous adsorbent)[121] because it presented almost no hysteresis loop. As a result, the PSD representing its porosity (*i.e.,* interparticle spaces between the grains conforming the particles) was also altered. It revealed a larger average size of *ca.* 50 nm and a negligible pore volume (0.07 $cm^3 \cdot g^{-1}$) due to the sintering of the particles with increasing calcination temperature,

as described in Chapter I. Additionally, the specific surface area was significantly reduced (7 $m^2 \cdot g^{-1}$), being more than 4 times lower than the one displayed by **P-800-A** calcined at 800°C (Figure B.6, *see Appendix B*).

To decisively assess whether C12A7 catalytic performance could profit from modulating the extra-framework species population towards a distribution preponderated by oxygen radicals within C12A7, we evaluated the performance of **P-900-D-O_2** in the propane total oxidation reaction under the same test conditions as in part I. Figure 2.13 displays the light-off curve, representing the C_3H_8 conversion over time evaluated at different reaction temperatures. At low temperatures (< 500°C), the fresh catalyst showed steady activity over time, which increased with rising reaction temperature. Conversely, between 500-600 °C, the conversion decayed over time under isothermal conditions, showing a significant drop in the propane conversion of about 20% at 550°C, whereas the activity profile leveled off from thereon. At 650 °C, the complete conversion of propane was not achieved, as we previously observed when employing a porous sample (Figure 2.8); instead, an X_{C3H8} = 92% was obtained. When contrasting the **P-900-D-O_2** activity with the one displayed by **P-600-D-O_2**—which possessed a notably lower content of ROS (Figure 2.11c) and a population distribution governed by hydroxyl anions—we could attest that the latter outperformed the former, despite the prevalent fraction of oxygen radicals in **P-900-D-O_2**. We interpreted this lower activity as a consequence of increasing the calcination temperature, which unavoidably reduced the textural properties of the catalyst while growing its particle size. As a result, at temperatures below 500°C, the large number of encaged oxygen radicals located at the bulk of the C12A7 were not readily available to react with propane, as it was the case for those clathrated at the outermost layer of the solid (*i.e.*, superficial cages). When the oxygen radicals from the bulk became accessible at the surface of the C12A7 particle, they promoted the reactivity of mayenite between 500 and 600°C. However, this promotion was not long-lasting, as a rapid decay of the activity over time was reflected at each isothermal stage, probably because the oxygen radicals were consumed faster than they were generated, making it difficult to sustain a high and stable conversion.

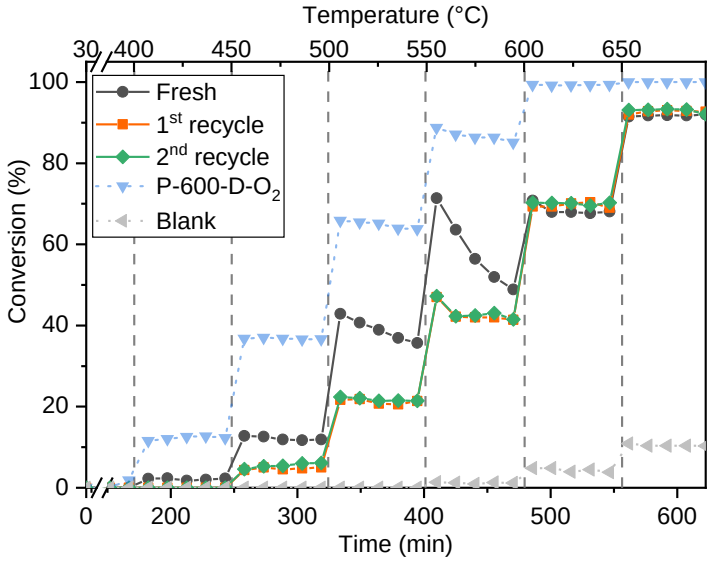

Figure 2.13. The catalytic activity of **P-900-D-O₂** (fresh) and two recycle tests are also shown. The catalytic activity of **P-600-D-O₂** (light blue curve) is also depicted for comparative reasons, this sample was also prepared employing method **D** but was calcined at lower temperature (600°C) to preserve the textural properties. Catalytic test conditions: total flow rate of 40 mL·min^{-1} containing 1000 ppmv C_3H_8 balanced with synthetic dry air; catalytic bed composed by 0.15 g of catalyst diluted with 0.35 g of SiO_2 chips.

Aiming to corroborate our latter interpretation, we examined samples **P-900-D-O₂** and **P-600-D-O₂** by thermo-programmed desorption analysis (TPD). The obtained O_2-TPD curves are shown in Figure 2.14. To illustrate the effect of particle bulkiness on the mobility of the oxygen species, we also analyzed a non-porous C12A7 specimen post-activated by method **D** (**NP-900-D-O₂**). Besides, the TPD signals of H_2O and CO_2 from the three previous samples can be found in Appendix B (Figure B.7). We observed that the O_2 desorption started from 400 °C for porous samples (a) and (b), whereas for the non-porous one (c), it set off from 600°C. In the case of the latter sample, as expected, the maximum was attained at higher temperatures (727°C), considering the dense structure and negligible texture of non-porous mayenite. Concerning the O_2-TPD signal (Figure 2.14a), its interpretation was not straightforward as for the former sample. In this case, the considerable amount of H_2O and CO_2 desorbed from **P-600-D-O₂** (Figure B.7a) complexified the (a) curve profile, masking the O_2 desorption. For example, the water released

showing peaks at ~150°C and ~570 °C attributed to adsorbed water at the surface cages and OH groups in high coordination with the Al framework atoms (structural defects), respectively, were also reflected in the O_2-TPD curve (Figure B.7a). While above 750 °C, two peaks (772 and 866 °C) related to the CO_2 emission from the decomposition of crystalline and amorphous calcium carbonate—present in samples calcined at 600°C—additionally modified the shape of the O_2-TPD curve. Therefore, by decomposing signal (a) considering the individual contribution of H_2O and CO_2, we could attribute a peak rising at 490 °C to the desorption of oxygen species. As for curve (b), given its asymmetric desorption profile, it was decomposed in two peaks with maxima at 550 and 595 °C. The first peak corresponded to oxygen species extracted from the most external (superficial) layer of the C12A7 particle, whereas the second came from those species located in its bulk, as described in an earlier study.[11] As a result, we could establish that the complete desorption of the oxygen radicals occurred more readily from the less bulky sample **P-600-D-O_2**, followed by **P-900-D-O_2** and **NP-900-D-O_2**. In summary, our findings agree with the above-mentioned report from Hosono's group.[11] They proposed that the oxygen species have limited mobility in C12A7 and suggested that the diffusion of the oxygen radicals is controlled by the mass transport in the bulk of C12A7 particles. Consequently, to release the oxygen species encapsulated at the deepest region of the C12A7 particles to the gas phase, more time and higher temperatures are required, in contrast to those situated at the outermost layer of the solid.

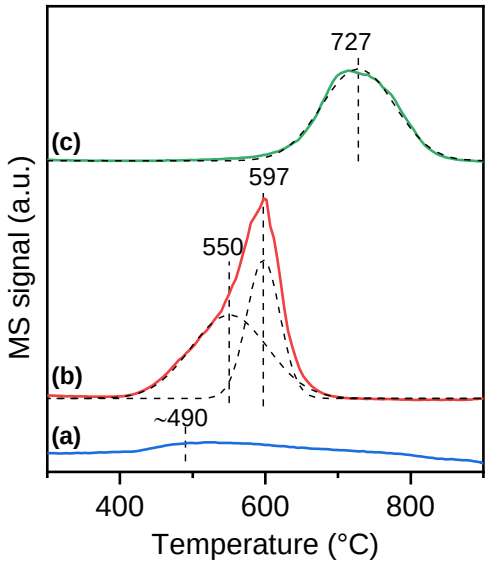

Figure 2.14. O_2-TPD profiles of samples prepared/post-activated employing method D (a) P-600-D-O_2, (b) P-900-D-O_2, and (c) NP-900-D-O_2.

Moreover, by analyzing the recyclability tests of **P-900-D-O_2** (Figure 2.13), we noticed that the light-off curves of the 1st and 2nd recycles were remarkably alike. Yet, an activity loss was witnessed, as compared to the fresh catalyst. We interpret these outcomes as follows. During the first run of **P-900-D-O_2** (pristine catalyst), the main fraction of the oxygen radicals, clathrated in C12A7 during its synthesis, were consumed by reacting with propane mainly between ~450-600°C. In parallel, the reaction medium conditions (*i.e.*, the presence of water vapor as a subproduct; a low total flow rate, 40 mL·min^{-1}; and a reduced oxygen partial pressure, 0.2) seemed to inhibit the regeneration of the oxygen radicals in a way to sustain their dominance on the population distribution at the end of the first catalytic run. Instead, the incorporation of hydroxyl species within the cages located at the outermost layer of the solid was favored. These assumptions are supported by a pronounced decrease in the intensity of the superoxide anion vibrational mode (1027 cm^{-1}) after the first catalytic cycle while the band (3570 cm^{-1}) assigned to the encaged hydroxyl ions increased (Figure 2.15). Consequently, based on these modifications in the population distribution of the extra-framework species between the fresh catalyst and the spent catalyst, the activity during the first recycle was reduced but leveled off after the second

one. All these findings support our observations and arguments disclosed in the first part of this chapter (*see section 3.3, p. 127*).

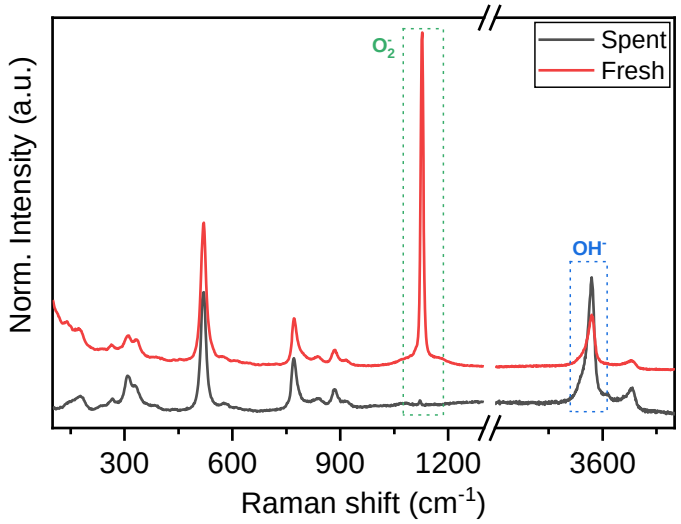

Figure 2.15. Raman spectra of **P-900-D-O₂** before (fresh) and after (spent) the first catalytic run. Each spectrum was normalized by the height of the most intense band of the C12A7 framework at 520 cm^{-1}.

To provide further evidence related to the modification of the extra-framework species population distribution upon a depletion-regeneration cycle. We have studied by EPR spectroscopy the catalyst reactivity under static anaerobic conditions (25 Torr of C_3H_6) at different reaction temperatures and its post-reoxidation under pure oxygen (140 Torr of O_2) at 600°C for 1h. More details about this procedure can be found in the experimental section. For instance, if we focus on the EPR spectra of **P-900-D-O₂** before and after the adsorption of C_3H_6 (Figure 2.16a), it can be noticed that the shape and intensity of the signal remain unchanged. However, upon heating starting from 350°C, we observed a decrease in the spectrum intensity (see embedded percentages in Figure 2.16a) which implied that the paramagnetic oxygen species were consumed by reacting with propene. Considering that the test was carried out in the absence of oxygen, the oxygen species could not be regenerated, leading to a gradual intensity loss. Concerning the EPR spectral shape, one can observe that the nearly isotropic form (*i.e.*, lack of g-anisotropy) of the EPR signal detected before C_3H_6 adsorption was retained up to 200°C. While from 350 °C, singular spectral features attributable to the paramagnetic oxygen

species encapsulated in C12A7 started to be shown from thereon. For instance, the superoxide g_{zz} component was depicted at higher *g*-values, whereas the g_{xx} and g_{yy} components stayed unresolved in the lower region. In the case of the O^- radical, its parallel feature (g_{xx}=g_{yy}) was also shown, while its perpendicular component (g_{zz}) was masked by the dominant part of superoxide anions. As the reaction temperature increased, the ratio between the two oxygen radicals was modified, revealing a faster consumption of O^- ions, most likely due to their lower stability and higher mobility in contrast to O_2^- species, as described in the literature.[10,72] From 500°C, a new symmetric and narrow signal rising around $g \approx 2.002$ was noticed. In earlier studies examining the C12A7 reduction under anaerobic conditions by EPR, a similar feature was depicted at *ca.* $g \approx 2.01$ in the EPR spectra of the lean-oxygen C12A7 specimens.[52,103] Alternatively, another study examining the coke formation in zeolites under anaerobic conditions also reported an EPR signal at $g \approx 2.002$ and attributed it to the presence of coke.[128] Hence, it appears coherent to assimilate this EPR signal in our spectra to the coke formation in C12A7 when exposed to reductive anaerobic conditions. Lastly, at 550°C, the EPR signal from the oxygen radicals vanished, and only the coke signal was visible, implying that all the encaged oxygen radicals were annihilated. Meanwhile, the unreacted propene was deposited as coke due to the increase in the temperature in the absence of oxygen.

Moreover, by employing samples presenting distinct characteristics in terms of texture and extra-framework population distribution, as we previously did for the TPD analysis (**P-600-D-O_2** and **NP-900-D-O_2**), we could observe some differences in their behavior. Even though we noticed that the O^- radicals were more rapidly consumed at lower temperatures, regardless of the particle bulkiness of the sample, we did observe disparities in the depletion rate of the oxygen radicals as a function of the C12A7 particle bulkiness. For instance, the entrapped oxygen species from the specimen showing smaller particles and thereby higher surface area (*i.e.*, **P-600-D-O_2**) were consumed at a faster rate than from the non-porous one (**NP-900-D-O_2**), as illustrated in Figures B.8a and b. Additionally, we could assess that the required temperature for achieving the complete consumption of the paramagnetic oxygen species was lower for **P-600-D-O_2** (~500 °C) than for **NP-900-D-O_2** (*ca*. 650 °C). Therefore, all these findings corroborate our interpretations from the O_2-TPD analysis.

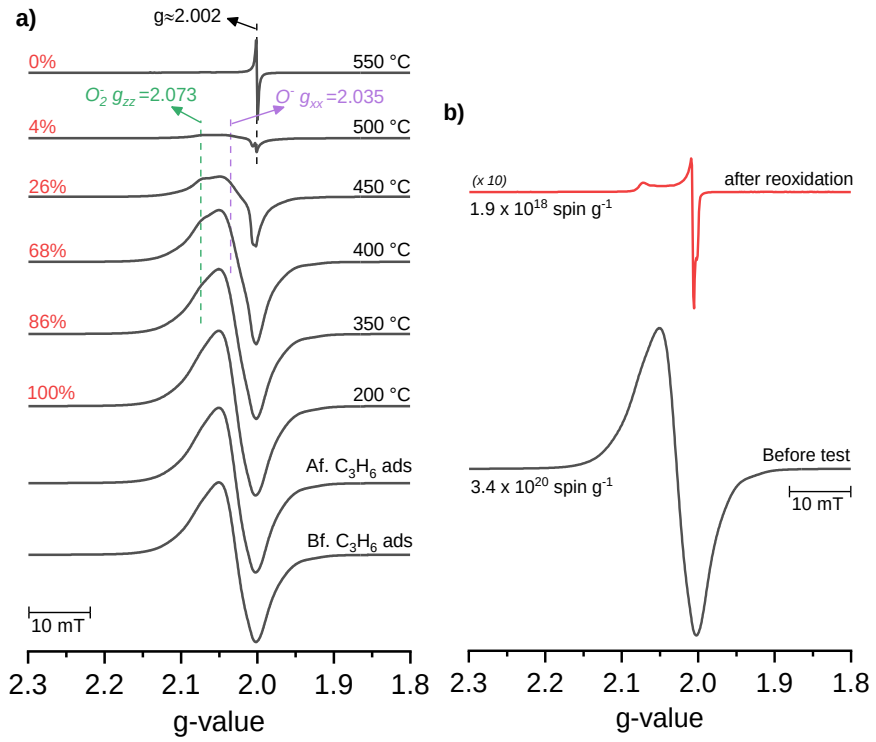

Figure 2.16. Variation of EPR spectra from **P-900-D-O₂** obtained at different temperatures during the anaerobic reactivity test (25 Torr C_3H_6). All the EPR spectra were collected at -196 °C. The EPR cell was sealed and kept isolated from the ambient atmosphere during the whole experiment. EPR spectra of **P-900-D-O₂** before the reactivity test and after reoxidation with oxygen (140 Torr) at 600°C for 1h. The EPR spectrum after the reoxidation was magnified 10 times to facilitate its visualization. The total concentration of oxygen species is found beneath the spectra.

Furthermore, by performing the reoxidation of the coked samples—which showed a light-gray coloration at the end of the reactivity test—we could notice that the regeneration of the oxygen species toward their initial concentration was not achieved. As revealed by Figure 2.16b and Figures B.8 c-d, a significantly lower total concentration of oxygen species (~10^{17} - 10^{18} spin·g^{-1}) was exhibited in all re-oxidized samples, where only superoxide ions were detected. This result proves, once and for all, that if the treatment (or reaction medium) conditions during the regeneration of the oxygen species in terms of annealing temperature, oxygen and water partial pressures, flow rate, and so on, are not equivalent to those used during the initial incorporation of these species, their complete restitution would not be possible. Instead, a new population distribution would be established

in equilibrium with the atmosphere conditions used during the regeneration.

Concerning the product distribution obtained by testing **P-900-D-O_2** (fresh) (Figure 2.17a), we may have expected to observe a prevailing formation of CO_2 considering the remarkable concentration of reactive oxygen species, particularly O^- radicals. However, between 450-600°C, the obtained distribution profile displayed almost equivalent selectivities for CO and CO_2. In addition, a higher presence of olefins (C_3H_6 and C_2H_4) was also detected, in contrast to their almost unnoticed occurrence in the former catalytic tests employing samples with a population distribution dictated by hydroxyl anions (Figure 2.10). At 650 °C, instead of reflecting a 100% CO_2 selectivity as previously observed, we noticed a slightly lesser presence of CO and an upsurge in the C_2H_4 selectivity. The latter is probably due to the cracking of C_3H_6 taking place at high temperatures, which is consistent with the lowered selectivity toward C_3H_6 with rising the reaction temperature. Last but not least, the presence of olefins—which are associated with the selective oxidation of propane—might lead us think that the occurrence of O^{2-} ions in **P-900-D-O_2**, as revealed by UV-vis analysis, could have promoted the formation of such products. Yet, by examining the product distribution of the first (Figure 2.17b) and second (not shown due to the similarities with the first one) catalytic recycles, we could notice that the C_3H_6 and C_2H_4 selectivities remained unchanged, whereas the only change corresponded to the higher selectivity of CO_2 showed by the spent catalyst in contrast to the fresh one. Thus, knowing that the recycled catalyst presented an extra-framework population distribution governed by OH^- ions, we could suggest that the presence of superficial hydroxyl species might be beneficial to preferentially form CO_2 rather than CO as a total oxidation product. Consequently, we estimated that the concomitant existence of O^{2-} ions in the fresh **P-900-D-O_2** seemed not to be the origin of the production of propene and ethylene (*vide infra*). We believe, instead, that all these results might be related to the structural and textural modifications that **P-900-D-O_2** underwent due to its calcination at higher temperature, which resulted in the formation of bigger particles, delaying the desorption of the oxygen radicals located at the deeper regions inside the C12A7 particles to interact with propane. Thereby, the distribution of the products was also impacted by this mass transport limitation. Thus, we may presume that when the oxygen radicals from the deeper

regions within the mayenite mass were mobilized to the outermost superficial layer of the catalyst, only a part of them (those closer to the superficial layer) participated in the propane total oxidation, whereas the other fraction were recombined, producing clathrated oxide ions and molecular oxygen (reverse Eq (2.1)), where the latter was directly released to the atmosphere. This assumption is based on the desorption mechanism of oxygen species proposed by Yang *et al*.[11]

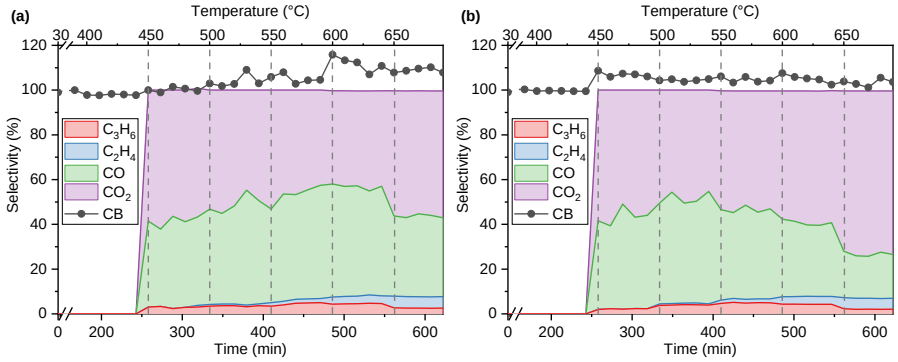

Figure 2.17. Selectivity and C-balance for P-900-D-O_2, **(a)** 1st run and **(b)** 2nd run or (1st recycle). The presence of CH_4 at the level of traces was also noticed from 600°C.

In summary, we demonstrate with all the above-exposed results that despite having a population dominated by “electrophilic” oxygen radicals in C12A7, it was not possible to enhance its catalytic activity neither to control its selectivity, as expected, since promoting the incorporation of these species during the preparation of mayenite decreased its textural properties resulting in the formation of bulkier particles, which had an impact on the mobility of oxygen species by prolonging their desorption from the bulk to the particle surface due to the increased particle thickness.

As a last illustrative example, we present the catalytic evaluation of a series of catalysts possessing different population distributions of extra-framework species under operational conditions usually employed in a partial oxidation reaction, *i.e.*, 8% C_3H_8, 8% O_2 (balanced with N_2) (Figure 2.18). Thus, based on the ability of C12A7 to exchange its extra-framework species as a function of the heat-treatment conditions, we performed a post-calcination step at 650°C under pure dry nitrogen after annealing the sample at 900 °C for 4h under high flow of dry oxygen. The latter procedure was carried out to

desorb the encapsulated oxygen radicals (O_2^- and O^-) formed during the first stage and to promote the formation of oxide ions (O^{2-}) by driving the equilibrium to the left side of Eq (2.1). The produced sample was denoted as **P-900-D-O_2+N_2**. A similar procedure was done, but instead of using dry N_2 as in the former case, we employed humid N_2 to annihilate all the oxygen species and exclusively incorporate OH^- ions, as illustrated by Eq (2.2). The obtained sample was labeled as **P-900-D-O_2+humid N_2**.

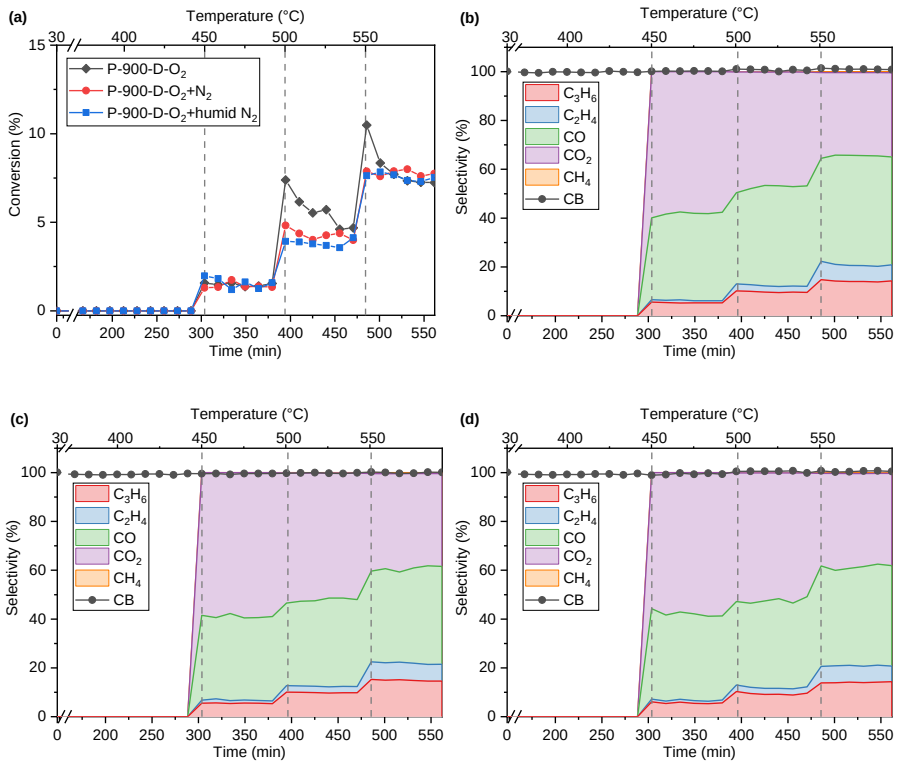

Figure 2.18. a) Light off curves of two catalysts prepared by method **D** but employing different atmosphere conditions to promote distinct population distribution of extra-framework species: **P-900-D-O_2** (electrophilic species) and **P-900-D-O_2+N_2** (nucleophilic species), and **P-900-D-O_2+humid N_2** presenting a population distribution governed by OH^- ions (*see Figure 2.18*). Catalytic test conditions: total flow rate of 40 mL·min^{-1} containing 8% C_3H_8, 8% O_2 and balanced with N_2; catalytic bed composed by 0.15 g of catalyst diluted with 0.35 g of SiO_2 chips. Selectivity and C-balance of b) **P-900-D-O_2**, c) **P-900-D-O_2+N_2**, and d) **P-900-D-O_2+humid N_2**.

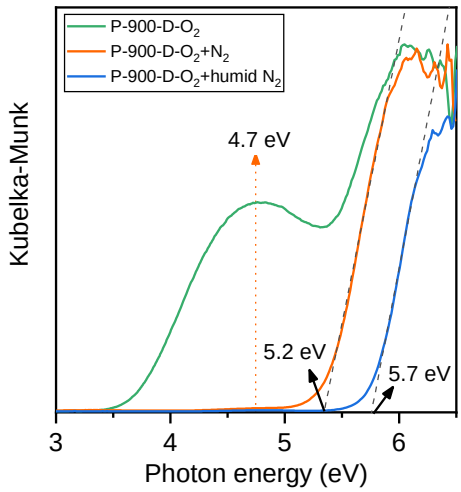

Figure 2.19. Optical absorption spectra obtained by Kubelka-Munk transformation of the DR-UV-Vis spectra of C12A7 samples prepared by method D possessing different population distributions of extra-framework species. **P-900-D-O_2+N_2** (dominated by O^{2-} species), **P-900-D-O_2+humid N_2** (dominated by OH^- ions) and **P-900-D-O_2** (containing O_2^- radicals). The intensity of the spectra was normalized by their maximum value.

The nature of the dominant extra-framework species in each of the previous samples was confirmed by UV-vis analysis, as shown in Figure 2.19. The optical absorption edge of the former sample was shifted down to lower energy (5.2 eV) in contrast to the latter (5.7 eV). These results confirmed the formation of O^{2-} and OH^- ions in **P-900-D-O_2+N_2** and **P-900-D-O_2+humid N_2**, respectively. Besides, the absence of the band at ca. 4.7 eV confirmed that the procedures employed to prepare the last two samples effectively annihilated the oxygen radicals incorporated during the first stage of the preparation.

By analyzing the catalytic performances of the three different catalysts in Figure 2.18, we observed, first, that the catalytic activity of **P-900-D-O_2** over time at 500 and 550°C could not be sustained due to faster desorption/consumption of the oxygen radicals in contrast to their regeneration, as previously observed under total oxidation conditions (Figure 2.13). However, under the present test conditions (8% C_3H_8, 8% O_2 and balanced with N_2) in comparison to the former ones (1000 ppmv C_3H_8 in dry synthetic air), a quicker decay in the activity was noticed, probably due to the higher concentration of propane. Second and last, the initial chemical identity (*i.e.,* nucleophilic or electrophilic nature) of the dominant extra-framework species did not

influence the selectivity of the catalysts because very similar product distributions were obtained (Figure 2.18 b-d), despite the confirmed different nature of the encaged dominant species in each catalyst. Thus, these results invalidate our hypothesis and demonstrate that C12A7 selectivity could not be controlled by modulating its population distribution of extra-framework species. The main reason behind this outcome seems to be that the extra-framework population distribution was in a dynamic equilibrium with the reaction medium during the oxidation process, where a lower partial pressure of oxygen ($pO_2 = 0.08$) as compared with the one ($pO_2 = 1$) used during the preparation of the catalyst, as well as the presence of water vapor (byproduct). As a result, at the end of each catalytic run, proportional amounts of superficial OH^- and, in a lesser number, O_2^- species were formed in equilibrium with the partial pressures of water vapor and oxygen in the gas phase (reaction atmosphere), as above-confirmed by EPR and Raman analyses.

5 Conclusive remarks

In this chapter, porous and non-porous C12A7 specimens presenting distinct population distributions of extra-framework species were successfully obtained using multiple strategies (A, B, C, and D). Herein, we systematically investigated by employing Raman, EPR, and DR-UV-vis spectroscopies the effect on the modulation of the population distribution of extra-framework species by fine-tuning several operational parameters, such as the atmosphere composition (oxygen and water partial pressures), calcination temperature, contact mode between the solid and the gas stream (parallel or cross-flow configuration) and total flow rate.

In part I, by analyzing the specimens obtained by methods A and B, we demonstrated that the rise in the calcination temperature and oxygen partial pressure promoted the formation of reactive oxygen species while reducing the incorporation of OH^- ions within the cages. Most importantly, we showed that the effective removal of the hydroxyl species released by the C12A7 precursor (*i.e.*, hydrogarnet) upon calcination during the preparation of porous C12A7 could be handled using a cross-flow configuration (method C). However, this first screening showed that even though we significantly increased the relative concentration of reactive oxygen species (O_2^- and O^-), in

particularly by method C**,** the overall population distribution of extra-framework in all C12A7 samples was still dominated by hydroxyl species, regardless of the strategy employed.

In a first attempt to appraise the relationship between the population distribution of oxygen species and the catalytic performance of C12A7 in the propane oxidation reaction, we showed that the rise in the concentration of oxygen species promoted the activity of C12A7 to some extent. This improvement was only detected when the catalyst displayed a suitable combination of textural and structural characteristics (*i.e*., higher specific surface area and smaller particle sizes). However, the steadiness of this promotion effect was not long-lasting over time. The latter was associated with the regeneration mechanism of the extra-framework species under the reaction medium conditions, where the oxygen radicals were consumed faster than they were generated, making it difficult to sustain a high and stable conversion.

Besides, we showed that the modulation of the oxygen radicals concentration had no or relatively limited impact on the selectivity of the catalyst because similar product distributions, dominated by CO_x, were obtained regardless of the sample employed. This issue was eventually associated with the lowered number of oxygen radicals in the overall population distribution of extra-framework, where hydroxyl anions were the dominant species.

In part II, by employing method D, we demonstrated that by operating at a high temperature (900 °C) and high-flow rate (1.4 $L \cdot min^{-1}$) of pure dry oxygen during the calcination step, we could maximize the relative concentration of electrophilic oxygen species, revealing a high occurrence of both O_2^- and O^- ions, thus, reverting the dominance of hydroxyl ions over the population distribution of extra-framework species within C12A7. In contrast, by performing additional annealing under an inert atmosphere over 650 °C, we promoted the formation and hegemony of O^{2-} ions (nucleophilic oxygen species), in agreement with the radical formation mechanism described in the literature.

By evaluating the catalytic performance of the catalysts prepared by method D, we demonstrated that despite having a population

dominated by “electrophilic” oxygen radicals in C12A7, it was not possible to enhance its catalytic activity nor to control its selectivity, as initially hypothesized. The latter was associated with the modification of mayenite textural and structural properties since promoting the incorporation of these species during its preparation unavoidably reduced its specific surface area and resulted in the formation of bulkier particles, thus impacting the mobility of oxygen species, and prolonging their desorption from the bulk to the particle surface due to the increased particle thickness. Finally, we decisively demonstrated that the initial chemical identity (*i.e.,* nucleophilic or electrophilic nature) of the dominant extra-framework species in C12A7 cannot influence the selectivity of the catalyst, invalidating our hypothesis. The main reason behind this outcome seems to be that the extra-framework population distribution is constantly re-equilibrated with the reaction medium during the oxidation process.

CHAPTER III

Nature and role of Cu(II) species in doped C12A7 catalysts for carbon black (soot model) oxidation

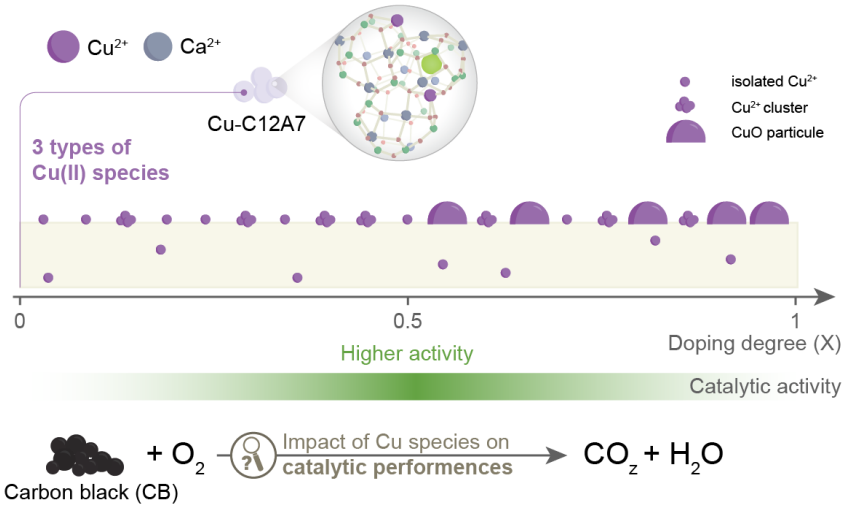

Abstract

In this last chapter, we present the preparation of copper-doped mayenite catalysts (Cu-C12A7) and appraise the effect that the nature and abundance of the different copper species could have on their catalytic performances in the carbon black (CB) oxidation reaction employing Printex-U as soot model. In addition, the influence of the atmosphere composition of the reaction medium, precisely the presence of water, was also studied. Leveraging on the assisted solution combustion synthesis of porous C12A7 presented in Chapter I, herein, we investigate the modification of this approach by partially replacing calcium nitrate with copper (II) nitrate to promote the insertion of Cu^{2+} entities within the C12A7 framework. By controlling the calcination temperature and the amount of copper precursor, two series of Cu-C12A7 catalysts ($Cu_x:C_{12-x}A_7$) containing various Cu loadings ($0.06 \leq x \leq 1$) were prepared at 600 and 800 °C. EPR, Raman, PXRD, and XPS analyses revealed that Cu(II) interacted with the C12A7 matrix in three structurally different forms: isolated-Cu^{2+}, clustered-Cu^{2+}, and bulky CuO particles. Cu-C12A7 catalysts exhibited enhanced activity over bare-C12A7, boosting the CB oxidation at low temperatures and maximizing the CO_2 selectivity. The control over the dispersion of Cu, textural properties, and superoxide species concentration of the Cu-C12A7 catalysts achieved by adjusting the Cu loading and calcination temperature showed to be crucial in promoting the catalytic performance. We concluded that the well-dispersed clustered Cu^{2+} is the most likely active species responsible for the improved activity under dry and wet conditions.

The results presented in this chapter were partially carried out by Eng. Arnaud Mary during his master thesis (2019) and have been published in:

Meza-Trujillo, I., Mary, A., Pietrzyk, P., Sojka, Z., & Gaigneaux, E. M. (2022) Nature and role of Cu(II) species in doped C12A7 catalysts for soot oxidation, Appl. Catal. B Environ. **316** 121604.

1 Introduction

As demonstrated in the preceding chapters, the catalytic performance of C12A7 in oxidation reactions can be effectively enhanced through two different approaches. Firstly, by improving its textural properties (discussed in Chapter I) and, secondly, by increasing the relative concentration of reactive oxygen species (as explored in Chapter II). Nevertheless, in the latter case, this enhancement could not be sustained over time due to the slow regeneration of the extra-framework species under the reaction conditions leading to decrease in the number of available oxygen species and therefore to the decrease in the catalytic activity of C12A7. Moreover, the inclusion of foreign cations within the framework of C12A7 as dopants (via a cationic substitution) has shown to be an applicable way to improve the electronic and catalytic properties of mayenite, as mentioned in the General Introduction (*p. 42*). To the best of our knowledge, none of the studies documented in the literature have portrayed a relationship between the enhancement of the catalytic activity of Cu-doped C12A7 and the role played by the copper species in an oxidation reaction. Nor has it been reported what influence the speciation of copper entities of different natures could have on the catalytic behavior of Cu-C12A7 catalysts.

In the present Chapter, we have selected the CB oxidation reaction to study the effect of doping mayenite on its catalytic behavior, considering that regardless of the nature of the extra-framework species initially incorporated in C12A7, the predominant species formed under the reaction medium conditions were always hydroxyl and superoxide radicals, as discussed in Chapter II, while the latter species are known to participate in the total oxidation of a substrate such as carbon black. Taking advantage of the synthesis approach for the preparation of porous C12A7 proposed in Chapter I, herein, we have investigated the outcomes of preparing Cu-C12A7 catalysts with ranging copper contents, presenting different textural properties and superoxide concentrations by controlling the calcination temperature and the initial amount of copper precursor. Additionally, we have attempted to assess which copper species (isolated Cu^{2+}, well-dispersed Cu^{2+} clusters, or segregated bulk CuO particles) are responsible for the enhancement of the catalytic CB conversion and CO_2 selectivity via a comprehensive analysis of the physicochemical

properties of the Cu-C12A7 catalysts using an array of diverse analytical techniques, namely PXRD, N_2 physisorption, XPS, EPR, and Raman spectroscopies. Finally, to evaluate the influence that the atmospheric composition of more realistic combustion engine exhaust gases (*i.e.*, significantly higher water vapor content) could have over the catalytic activity of our Cu-C12A7 catalysts, the CB oxidation was also performed in the presence of water vapor ($5\%H_2O/5\%O_2$/He, wet conditions) to be contrasted with our outcomes obtained under dry conditions ($5\%O_2$/He).

2 Experimental

2.1 Materials

The grade purity and manufacturer of the chemical reagents employed in the Cu-C12A7 materials synthesis can be found in the general Experimental Section of this thesis (*p. 56*).

2.2 Cu-doped C12A7 preparation

The protocol for preparing porous Cu-doped C12A7 catalyst (also referred to as Cu-C12A7 for brevity) by one-pot assisted solution combustion synthesis is illustrated in Scheme 3.1. The Cu-C12A7 catalysts prepared in this chapter are denoted as Cu(*x*)-P-*Y*, where "*x*" stands for the nominal molar fraction of Ca replaced by Cu, "P" symbolizes porous C12A7 as employed in the previous chapters, and "*Y*" represents the calcination temperature. Concerning non-doped C12A7 porous samples, we prepared them according to the synthesis procedure described in Chapter I (*see section 2.5, p. 74*).

All reagent amounts, except oxalic acid, were calculated based on the overall combustion reaction, Eq. (3.1), considering an oxidizer/fuel ratio equal to 1 ($\phi = 1$, stoichiometric conditions). The resulting overall combustion reaction employed for the preparation of Cu-C12A7 is described as follows:

$$\begin{aligned} &x\mathrm{Cu(NO_3)_2} + (12\text{-}x)\mathrm{Ca(NO_3)_2} + 14\mathrm{Al(NO_3)_3} + \\ &55/2\,\phi\mathrm{CH_4N_2O} + 11\phi\mathrm{C_3H_7NO_2} + 165/2\,(\phi\text{-}1)\mathrm{O_2} \rightarrow \\ &\mathrm{Cu_xCa_{(12\text{-}x)}Al_{14}O_{33}} + 121/2\,\phi\mathrm{CO_2} + 187/2\,\phi\mathrm{H_2O} + 33(\phi{+}1)\mathrm{N_2} \end{aligned} \qquad (3.1)$$

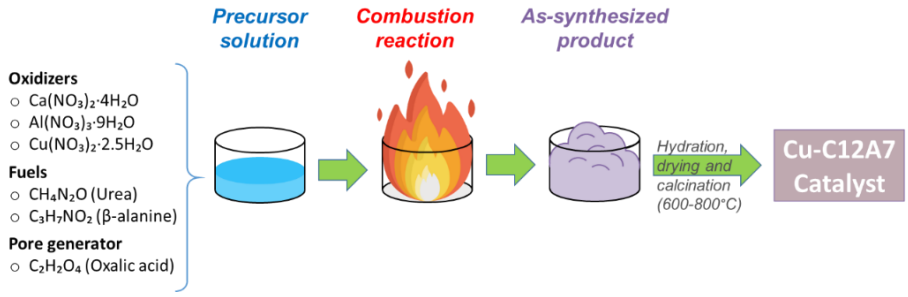

Scheme 3.1. Step by step preparation of Cu-C12A7 catalysts via one-pot assisted solution combustion synthesis.

In the present study, the nominal doping degree (x) represents the moles of Ca replaced by Cu from the total of 12 moles of Ca present per mol of C12A7. For example, for x = 0.5 (2.3%wt Cu), 11.5 moles of Ca and 0.5 moles of Cu are employed, keeping invariant the 12 moles of divalent cations required to yield 1 mol of Cu-doped C12A7. Accordingly, five distinct nominal molar fractions of copper ranging between $0.06 \leq x \leq 1$ were employed. Based on Eq. (3.1), for a given doping degree, stoichiometric quantities of metal nitrates (Cu, Ca, and Al) and fuels (urea and β-alanine) to produce 5 g of Cu-C12A7 per batch were added into a borosil container (300 mL) and dissolved with *ca.* 5 mL of preheated distilled water (80°C) under magnetic stirring at 80 °C. Next, a specific amount of oxalic acid (OA) (0.5 g per g of Cu-C12A7 to be produced) was dissolved in ~3 mL of preheated distilled water (80°C) and added to the former solution. Once a whitish light blue solution was obtained, the solution-containing vessel was placed in a preheated furnace at 500°C to trigger the combustion reaction. As soon as the ignition temperature was attained, an exothermic self-sustaining reaction took place with the occurrence of glowing reddish flames (Figure. B.1), giving way to a solid product in a matter of a few seconds (~15 s). The as-synthesized powder was manually ground and mixed with distilled water (80°C) to form a slurry with a mass ratio of 1g/100g (solid/water) and stirred for about 20 min. Then, the slurry was filtered, and the retained wet solid was dried overnight at 120°C. Finally, the as-dried powder was grounded and calcined at either 600 or 800°C in a preheated furnace for 4h under static ambient air, then cooled to room temperature in a desiccator, hand-ground, and stored in a closed glassware container for further characterization or catalytic evaluation.

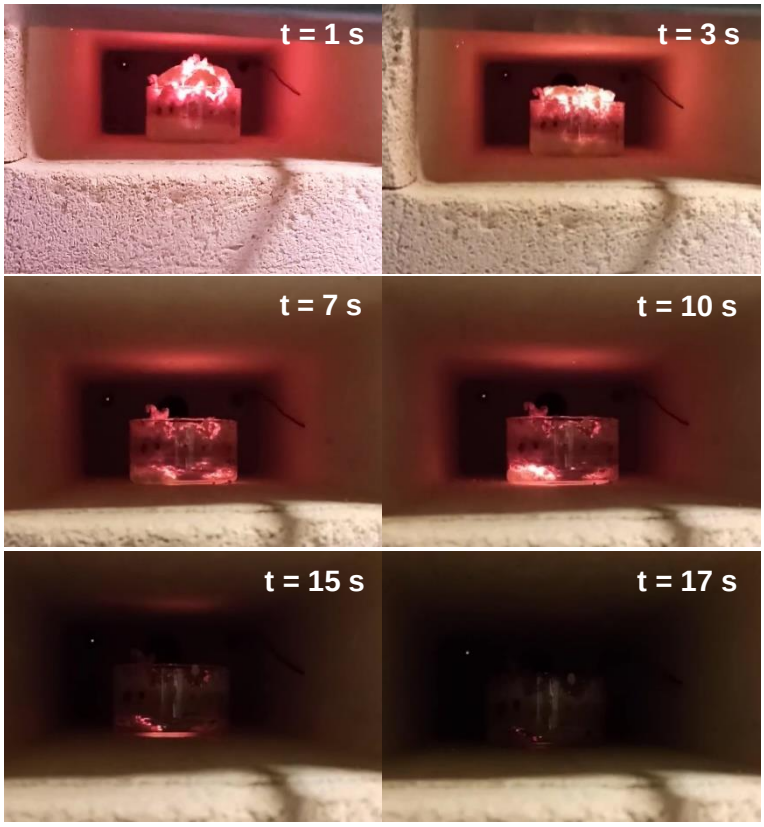

Figure 3.1. Image sequence extracted from a video clip recorded during the combustion reaction stage of the solution to prepare Cu(x)-C12A7 materials (x = 0.24).

2.3 Catalyst characterization

Pristine and Cu-doped C12A7 samples studied in this Chapter were characterized by PXRD, N_2 physisorption, Raman, EPR, XPS analyses, as described in the general Experimental Section (*pp. 56-60*). Specific analysis conditions used in this Chapter are described hereafter.

EPR spectra were obtained according to the procedure described in section 2.2.6 of the general Experimental Section (*p. 58*). In this Chapter, the total spin concentrations of paramagnetic species were determined from the second integral of the EPR spectra using $CuSO_4$ as a standard. For each spectrum, the relative contributions of superoxide ions (O_2^-) and copper(II) species (isolated and clusters

Cu^{2+}) were determined by computer simulation (deconvolution) using the program EPRsim32.[104]

2.4 Catalytic performance evaluation

The catalytic tests were performed according to the procedure described in the general Experimental Section (*see section 2.3.1, p. 60*). Still, some specificities of the experiments reported in the present Chapter are described below. In each catalytic test, 50 mg of a mixture of carbon and catalyst (5%wt of CB) obtained solely under tight-contact conditions were employed. For dry conditions, an inlet gas flow of 5% O_2 in He (Praxair) was fed at a flow rate of 50 mL·min^{-1}. For the experiments performed in the presence of water (wet conditions), the same inlet flow of dry gases went through a saturator (continuous bubbling system) kept inside a thermostatic bath at 33 °C (pH_2O = 0.05 atm) to humidify the gas stream. All tubing lines, downstream the saturator, were heated at 50°C to prevent vapor condensation. Temperatures corresponding to 10, 50, and 90% CB conversion (denoted as T_{10}, T_{50}, and T_{90}, respectively), as well as the temperature (T_{peak}) at which the highest combustion rate is attained (*i.e.*, maximum production of CO_x), determined from the TPC curves, were used as indicators of the activity of the tested catalysts. The produced amounts of CO_2 and CO were obtained by integrating the area under the corresponding curves obtained from the TPC runs. The selectivity towards CO_2 was calculated according to the equation reported in the general Experimental Section (*p. 61*).

The recyclability tests were performed as follows. After each cycle, the spent catalyst was recovered from the reactor and separated from the two layers of silica wools, and the obtained catalyst mass was measured. As a function of the recovered spent catalyst mass, an adequate amount of CB (5% of the catalyst weight) and both powders were poured into a mortar and ground for ~10 min. Then, the resulting mixture was loaded into the reactor for a consecutive catalytic run (recycle) under dry or wet conditions, depending on the test requirements. In this way, for each recycle test, the weight ratio between the catalyst and carbon black remained constant and equivalent 19:1, respectively.

3 Results and discussion

3.1 Catalytic combustion of carbon black (soot model)

The catalytic performances of the two sets of Cu-C12A7 catalysts, calcined at 600 and 800° C, were evaluated in the CB oxidation reaction. The catalytic performances of undoped C12A7 samples (x = 0) annealed under the same conditions as presented in Chapter I, are here used for comparison. All catalysts were evaluated by the thermo-programmed combustion (TPC) method under tight-contact conditions (*i.e*., carbon hand mixed with the catalysts in a mortar) because it ensures, better reproducibility than loose contact conditions when preparing the solid mixture, even though it is a less representative approximation of the contact between carbon particles and catalyst in realistic conditions. As shown in Chapter I, the analysis of the CB combustion profiles obtained under loose-contact conditions (*i.e*., Printex-U carbon hand mixed with the catalysts with a spatula) resulted in more complex multimodal curves, which could impede us from drawing reliable comparisons between the different catalysts, whereas tight-contact permits a better understanding of the intrinsic reactivity, as reported in the literature.[106,129] This being said, the obtained catalytic results, in addition to an uncatalyzed CB combustion experiment (Printex-U alone), are shown in Figures 3.1, 3.2, B.1, and Table 3.1. The conversion profiles (Figure 3.2) were obtained by integrating the area under the TPC CO_x curves (*see Appendix C*, Figure C.1) in the temperature range between ~350-580 °C, which is undoubtedly associated with the CO_x produced by the catalytic combustion of CB over Cu-C12A7 catalysts. As justified in Chapter I, the minor peaks emerging above *ca.* 580 °C in the TPC curves were correlated to CO_2 evolving from the decarbonation of calcium carbonate (*i.e*., $CaCO_{3(s)} \xrightarrow{\Delta} CaO_{(s)} + CO_{2(s)}$) upon heating over 600°C approximately. While the latter was formed at lower temperatures through CO_2 (from CB oxidation) capture by CaO, found in all catalysts (*vide infra*).

Table 3.1. Catalytic activity indicators and CO_2 selectivity of Cu-C12A7 catalysts.

Entry	Catalyst	Doping degree (x)	T_{10} (°C)	T_{50} (°C)	T_{90} (°C)	T_{peak} (°C)	S_{CO_2} (%)
1	P-600	0.0	432	480	527	489	92
2	Cu(0.06)-P-600	0.06	435	481	533	473	92
3	Cu(0.12)-P-600	0.12	433	474	528	468	96
4	Cu(0.24)-P-600	0.24	427	468	525	461	100
5	Cu(0.50)-P-600	0.50	431	468	516	461	100
6	Cu(1.00)-P-600	1.00	440	491	538	496	100
7	P-800	0.0	448	503	547	514	91
8	Cu(0.06)-P-800	0.06	443	491	531	496	92
9	Cu(0.12)-P-800	0.12	440	489	525	493	95
10	Cu(0.24)-P-800	0.24	425	474	510	477	100
11	Cu(0.50)-P-800	0.50	416	460	498	464	100
12	Cu(1.00)-P-800	1.00	425	474	515	486	100
13	CB (no catalyst)		537	599	639	606	34

In the absence of a catalyst or any other "inert" material (*e.g.*, α-alumina employed in Chapter I), the highest combustion rate for Printex-U was attained at 606 °C (T_{peak}), while the T_{10}, T_{50}, and T_{90} were 537, 599, and 639 °C, respectively (entry 13, Table 3.1). Besides, after performing the CB combustion in the presence of a catalyst, the CB conversion curve shifted to lower temperatures (Figure 3.2), implying that all tested catalysts promote CB combustion. The latter was confirmed by examining the T_{50} (Figure 3.3a) and T_{peak} (Figure 3.3b) values, demonstrating that all Cu-containing C12A7 samples exhibited T_{50} and T_{peak} values at least 100 degrees below those revealed by the uncatalyzed CB oxidation. A reproducibility test of Cu(0.5)-P-800 is shown in Figure C.2 (see Appendix C). As could be observed, the repetitions done with three different samples show comparable TPC curves, which denotes the satisfactory repeatability of the tests.

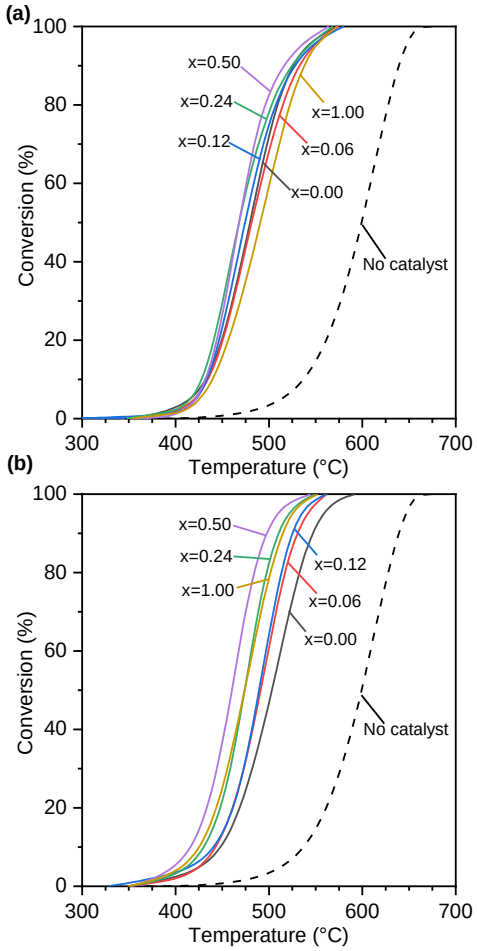

Figure 3.2. Profiles of CB conversion over Cu-C12A7 catalysts calcined at a) 600 and b) 800 °C.

By comparing the catalytic activity of Cu-doped C12A7 catalysts with those displayed by undoped C12A7 shown in Chapter I (recalled in Table 3.1, entry 1 and 6), one can notice that the activity was enhanced, showing T_{peak} values downward shifted up to 28 and 50 °C for those annealed at 600 and 800 °C, respectively. This positive effect on the catalytic activity (*i.e.,* T_{50} or T_{peak} reduction) increases with rising the copper loading until the highest activity is observed at $x = 0.5$. Further increments in the copper content ($x = 1.0$) led to activity loss, accomplishing the oxidation of CB at higher temperatures (entries 6 and 12, Table 3.1).

Similarly, the calcination temperature also had an impact on the catalytic activity. As a general trend, better results, in terms of T_{10} (onset temperature), were shown by the set of Cu-doped catalysts calcined at 600°C in contrast to those heat-treated at 800°C. In the case of the former group, the obtained onset temperatures were shown to be very similar among samples, regardless of the copper content. Meanwhile, in the Cu-C12A7 set calcined at 800°C, a noticeable reduction in the onset temperature was observed as copper loading increased, displaying the lowest T_{10} at x = 0.5 (entry 11), which turned out to be even lower than the one obtained by its analog calcined at 600 °C. Regarding the T_{peak}, as the copper content approached x = 0.5, the materials calcined at 600°C seemed to attain a plateau, exhibiting the same catalytic performance (T_{peak}=461 °C) in the range 0.24-0.5. As for the Cu(x)-P-800 series, the lowest temperature (*i.e.,* highest activity) was attained at x = 0.5 (T_{peak}=464 °C), showing a similar catalytic behavior as the one annealed at 600 °C with equivalent copper loading. In contrast, from $x \geq 0.5$, the differences in terms T_{50} observed between the two Cu-C12A7 series calcined at 600 and 800 °C revealed an inverted behavior, where those annealed at high temperatures exhibited a higher activity (*i.e*., lower T_{50}). As exposed before, the highest copper content (x = 1.0) led to a lessened catalytic activity. However, Cu(1.00)-P-600 (entry 6, Table 3.1) showed to be even less active than the undoped one (x = 0, entry 1) heat-treated at the same temperature (600°C). Conversely, Cu(1.00)-P-800 specimen (entry 12), despite its lower activity, still performed better than bare C12A7 prepared at 800°C (entry 7).

Finally, both series of Cu-doped C12A7 catalysts showed a dominant production of CO_2 over CO with regards to the uncatalyzed combustion reaction where CO (66%) was predominantly formed (entry 13, Table 3.1). Increasing the copper content further promoted the CO_2 selectivity reaching 100% as the doping degree came close to x = 0.24 and remained at maximum from thereon. Additionally, we found that, regardless of the calcination temperature, equivalent CO_2 selectivities were found between each pair of catalysts for a given copper doping degree, indicating that the catalyst selectivity was unaffected by its heat treatment history. This enhancement in the CO_2 selectivity might be associated with the enhanced redox properties of Cu-C12A7 catalysts compared to bare-C12A7 (either P-600 or P-800)

due to the introduction of copper, which is known for accelerating the oxidation of CO to CO_2.[130]

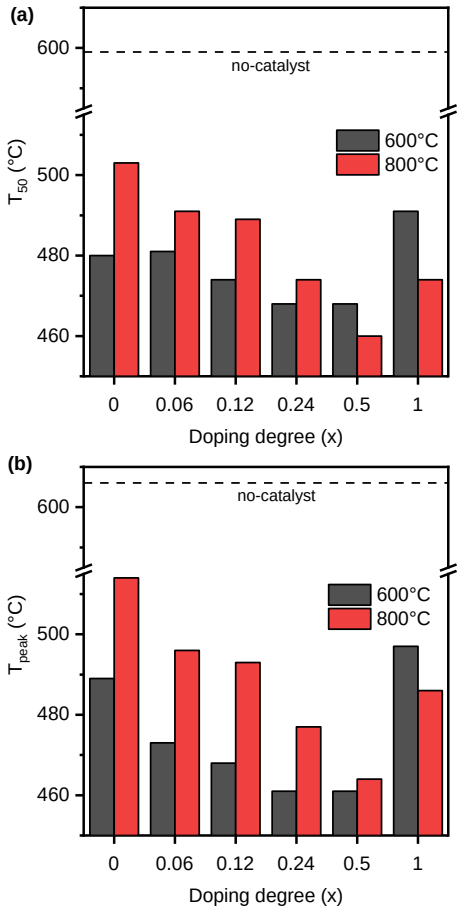

Figure 3.3. Comparison of the activity indicators a) T_{50} and b) T_{peak} among the two sets of Cu-C12A7 catalysts.

From the above-exposed results, we may determine that the optimum copper content for the oxidation of carbon black with Cu-C12A7 catalysts is close to $x = 0.5$. Therefore, aiming to understand the relationship between the catalytic behavior of the studied Cu-C12A7 materials and the copper-mayenite interactions, we have thoroughly examined the physicochemical properties of these catalysts in the following sections.

3.2 Catalyst characterization

3.2.1 Structural analysis by powder X-ray diffraction (PXRD) and Raman spectroscopy

The effect of the copper loading and calcination temperature on the crystalline structure of Cu-C12A7 catalysts was investigated by PXRD. Figure 3.4a and b show the diffractograms of the two series of Cu-doped C12A7 samples calcined under static ambient air at 600 and 800 °C, respectively. Additionally, Table 3.2 gathers several structural parameters evaluated from the PXRD patterns. The diffractograms of both Cu-doped C12A7 sets (600 and 800°C) exhibited typical reflections of mayenite-crystal cubic centered structure (*I-43d*), which were identified with the JCPDS N° 09-0413 database reference for this material.[25] The principal peaks at 2θ= 18.1, 29.7, 33.4, 36.7, 41.2, and 46.6° corresponding to the (*2 1 1*), (*4 0 0*), (*4 2 0*), (*5 2 1*) and (*6 1 1*) planes, respectively, along with other low-intensity labeled peaks (*) were attributed to C12A7 crystal structure. Besides, minor XRD peaks (●) were identified and ascribed to the CaO crystal phase (JCPDS N° 37–1497). As reported in Chapter I, the production of pristine porous C12A7 by the transformation of a hydrogarnet ($Ca_3Al_2(OH)_{12}$/C3AH6) precursor led to the segregation of the CaO, as a side-phase. In this case, the formation of the C3AH6 phase after hydration and drying of the copper-containing combustion product (*see* Scheme 3.1) was also evidenced by PXRD, as indicated in Figure C.3 (*see Appendix C*), proving the CaO origin in Cu-C12A7 samples.

Moreover, the characteristic peaks of CuO likely to appear at 35.5° and 38.7° were not distinguished in samples presenting low doping degrees ($x \leq 0.24$). However, at high Cu loadings ($x \geq 0.5$), the formation of a segregated CuO phase (♦) was pointed out, which was readily distinguishable on the series calcined at 600°C due to the lower intensity of C12A7 reflections, as compared to the catalysts calcined at higher temperatures (800 °C) (see insets in Figure 3.4a and b). Hence, the absence of copper-related reflections in the PXRD patterns at low doping degrees suggested that copper was either well-incorporated in the C12A7 matrix forming a solid solution or well-dispersed on C12A7 surface. Conversely, at high contents, the presence of CuO reflections indicated the segregation of at least a fraction of the initial amount of copper involved in the synthesis of Cu-C12A7 as a concomitant oxidic phase.

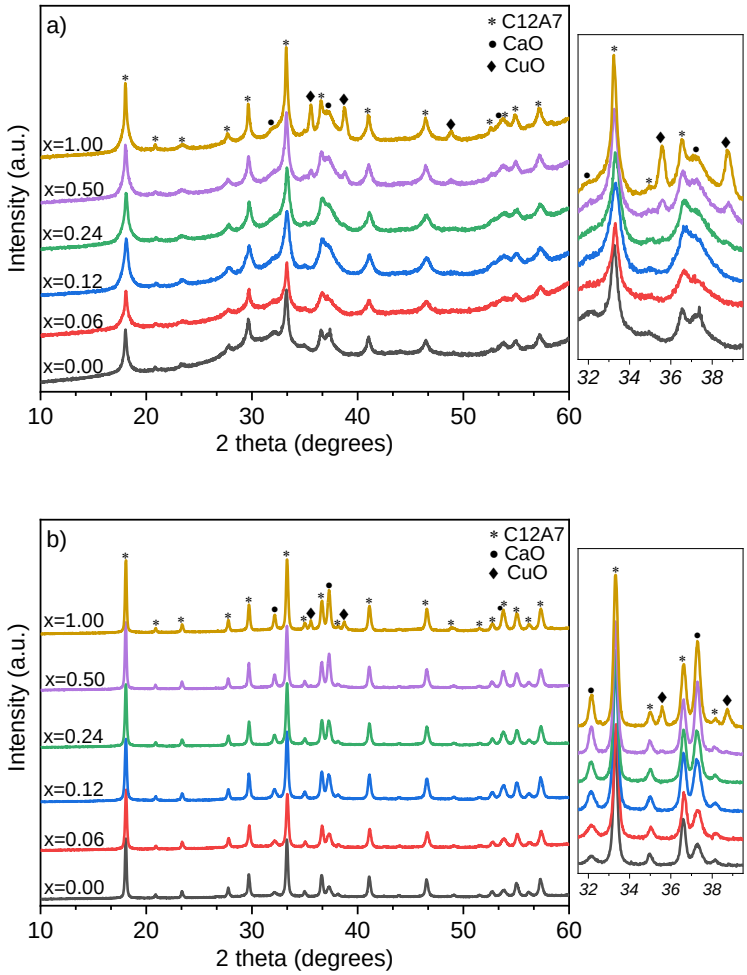

Figure 3.4. PXRD patterns of Cu-C12A7 samples calcined at a) 600 and b) 800 °C for 4h in static ambient air. For comparison, diffractograms of pristine C12A7 (x = 0) are shown at the bottom line of each graph. Insets are displayed to guide the reader through the identification of the different phases.

Although both series of Cu-doped mayenite samples exhibited very similar diffractograms among each set, we could notice that the calcination temperature and doping degree influence the structural properties of the Cu-C12A7 catalysts as follows. For instance, at low temperatures (600°C), the slight presence of an amorphous domain tended to disappear with increasing copper loading, as illustrated by the small broad signal in the background line between 25-35° (2θ). Besides, in the enlarged 2θ regions of the set calcined at 800 °C (inset Figure 3.4b), the intensity of CaO peaks at 2θ= 32.2 (*1 1 1*) and 37.3°

(*2 0 0*) continuously increased with the rising of the Cu nominal content as compared to the pristine C12A7 (P-800). These two observations could correlate with modification of the reaction stoichiometry through partial substitution of Ca for Cu by inducing vacancies in the mayenite framework, thus promoting Cu^{2+} insertion. It seems that the alteration in the stoichiometry, from one side, favored the formation of CaO as the doping degree increased for the series calcined at high temperature, while from the other side, at low temperature, the amorphous phase content was reduced, as will be confirmed by Raman spectroscopy (*vide infra*). In addition, with the increase in the calcination temperature, the C12A7 diffraction peaks became narrower and more intense due to the agglomeration and sintering of the grains. As an outcome, the average crystalline size of C12A7 noticeably increased by almost a factor of two (Table 3.2). Therefore, the calcination temperature offers a way to control the crystallinity and crystal size of Cu-C12A7 materials.

The calculated lattice parameter for undoped and Cu-doped C12A7 catalysts are summarized in Table 3.2. Regardless of the copper content and the temperature at which they were treated, the samples present unit cell values (~12.0 Å) closer to the most quoted one for synthetic C12A7:$2O^{2-}$ (a = 11.989 Å).[25] In the literature, it has been suggested that partial cationic substitution of Ca^{2+} ions (1.0 Å) by smaller Cu^{2+} ions (0.73 Å) can lead to a contraction of the lattice (a = 11.974 Å).[45] However, it has also been shown that the anionic substitution of O^{2-} extra-framework species occluded within the nanocages by another kind of active oxygen species (*i.e.*, OH^-, O_2^-, and O^-) can promote a contraction of the unit cell (*e.g.*, a = 11.977 Å for C12A7:OH^-).[8,24,26,47] Thus, the correlation between an effective cation doping and the lattice size modification without considering the influence of the anion substitution should be avoided. In our case, no apparent relationship could be settled between the increase in doping degree and the variation in lattice value. Meanwhile, the slight lattice expansion observed in our materials could be attributed to the presence of structural defects and lower crystallinity as compared to stoichiometric C12A7:O^{2-} synthesized by solid-state reaction.[25]

Cu-C12A7 catalysts were further examined by Raman spectroscopy to ensure the mayenite structure and the chemical identity of the occluded extra-framework anions within the C12A7

cages. Raman spectra recorded for the Cu-C12A7 samples annealed at 600 and 800 °C are shown in Figure 3.5 a and b, respectively. All spectra recorded in the low-spectral region (200-1000 cm^{-1}) displayed the characteristic Raman modes of the C12A7 framework, which were assigned to the Al-O framework vibrations, as discussed in Chapter II.[102,103,124] Herein, the most dominant band attributed to the symmetric vibration mode of Al–O–Al bridged oxygen between $(AlO_4)^{5-}$ tetrahedra was also shifted to higher frequencies with the rise of the calcination temperature, as observed for pristine C12A7 in Chapter II (Figure 2.2, p. 116). The latter observation was related to the prevalence of structural defects (*i.e.*, Al-OH...Al-O unit) at low temperatures due to a change in the coordination of Al atoms.[21] This structural modification related to a higher hydration degree of the C12A7 structure was lessened by raising the calcination temperature, as shown in Chapter II, as will be corroborated by the hydroxyl vibration region analysis of the Cu-C12A7 specimens (*vide infra*).

In the spectral range below 500 cm^{-1}, three low-intense bands belonging to the C12A7 framework at 268, 310, and 330 cm^{-1} were observed (Figure 3.5 a and b). The C12A7 bands in this low spectral region have been related to the Ca breathing mode and the localized vibrations of framework O^{2-} ions.[102] Nonetheless, one can notice that these bands appeared broader and less resolved in the set calcined at 600 °C compared to the 800°C set. Moreover, peaks at 285, 331, and 616 cm^{-1} not attributable to the C12A7 structure were also distinguished in the set calcined at 600°C (Figure 3.5a). These bands were identified as CuO fingerprints in close agreement with those band positions reported in the literature at 296, 346, and 631 cm^{-1}.[131] Conversely, in the spectra of Cu(*x*)-P-800 samples (Figure 3.5b), no apparent incidence of CuO-related bands were detected, even for the highest loading ($x = 1.0$), despite the identified existence of CuO crystals by PXRD from $x \geq 0.5$ (Figure 3.4). However, by increasing the copper content, the C12A7-related bands within the set prepared at 800 °C displaced to lower frequencies. In addition, the principal Raman mode (Al-O-Al, ~518 cm^{-1}) of the C12A7 framework became asymmetric, showing a long low-frequency tail. Likewise, a shoulder at the right side of the latter band (~518 cm^{-1}) was noticed, which upsurged and got broader with the Cu loading increase.

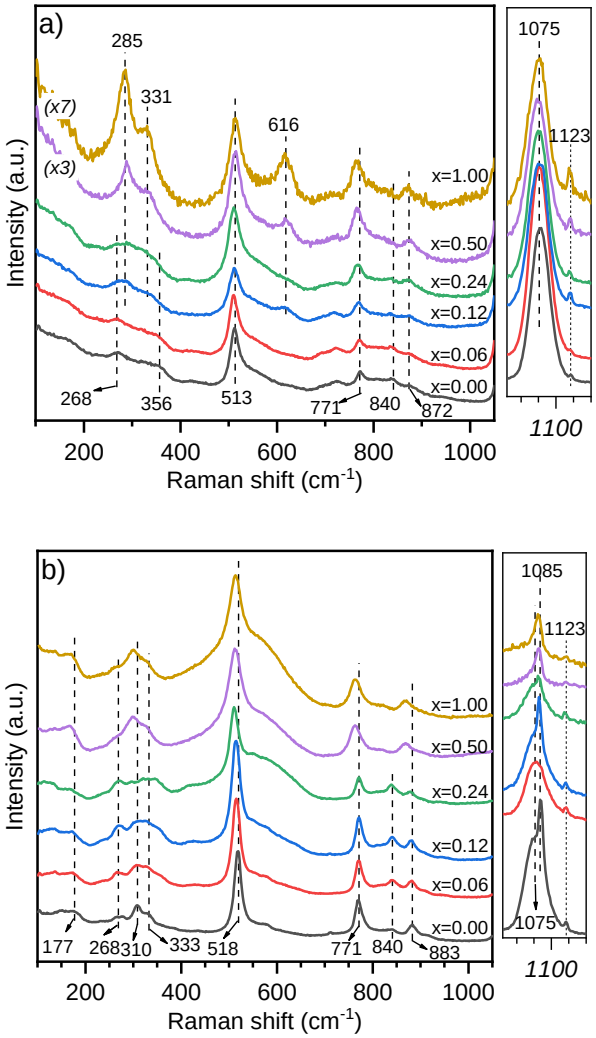

Figure 3.5. Raman spectra of Cu-doped C12A7 samples calcined at a) 600 °C and b) 800 °C. None of the Raman spectra shown here present any background baseline correction or intensity normalization.

In the region above 1000 cm^{-1} (zoomed regions, Figure 3.5a and b), regardless of the calcination temperature or copper content, we corroborated the existence of encaged superoxide ions (O_2^-) by the band appearing at 1123 cm^{-1}, in agreement with our interpretation from Chapter II. However, we could not distinguish by Raman spectroscopy any variation in the incidence of the O_2^- species among each set of catalysts due to their lower presence. Nevertheless, their relative

concentrations have been assessed by EPR (*vide infra*). Moreover, the manifestation of the CaO phase, presenting not active Raman modes[101], was revealed by the vibrational stretching modes of CO_3^{2-} emerging at 1075 and 1085 cm^{-1}. The former band originated from the superficially carbonated CaO phase, whereas the latter emerged from the amorphous carbonated phase, as described in Chapter II (*see section 3.1, pp. 114-121*). It can also be noticed that the band at 1075 cm^{-1} was predominant in the catalysts calcined at 600°C, whereas in those prepared at 800°C, its intensity decreased with rising the copper loading. The latter observation was correlated with the lowered presence of amorphous domains at higher loading degrees, as shown by PXRD.

In the high-frequency region related to the hydroxyl groups, three peaks around 3570, 3614, and 3680 cm^{-1} were observed in the spectra of both Cu-C12A7 sets, as depicted in Figure C.4 (*see Appendix C*). The band rising at 3570 cm^{-1} undoubtedly confirmed the presence of encaged OH^- radicals in all the Cu-C12A7 samples, regardless of the copper content or calcination temperature at which they were prepared. As discussed more in detail in Chapter II, the existence of OH^- ions inside the cages of our catalysts could be explained by two factors. (i) The annealing was performed under an ambient atmosphere (*i.e.*, in the presence of atmospheric humidity during the calcination), and (ii) C12A7 was produced by the decomposition of a hydrated precursor (C3AH6), which released water upon heating. Moreover, the two other bands located above 3600 cm^{-1} showing maxima at ~3614 and ~3680 cm^{-1} might be attributed to structural defects and superficial adsorbed hydroxyls, which can lead to a change in the coordination of a fraction of Al atoms from tetragonal to octahedral.[21] However, we noticed that with rising in the copper content ($x \geq 0.5$), the latter bands associated with a higher hydration degree of the C12A7 structure were significantly reduced, mainly in the set calcined at 800 °C, which suggests that the rise in the copper content somehow prevents the structural deformation of Al tetrahedra.

Table 3.2. Characterization results of Cu-C12A7 catalysts by PXRD and N_2 physisorption.

Sample	Lattice parameter [a] (Å)	Crystallite size [b] (nm)	S_{BET} ($m^2 \cdot g^{-1}$)	Pore volume [c] ($cm^3 \cdot g^{-1}$)
P-600	12.022(±0.006) [e]	26	52[d]	0.31[d]
Cu(0.06)-P-600	12.018	26	45	0.38
Cu(0.12)-P-600	12.024	19	54	0.18
Cu(0.24)-P-600	12.011(±0.005)	20	49	0.26
Cu(0.50)-P-600	12.036(±0.010)	22	56	0.22
Cu(1.00)-P-600	12.039(±0.004)	31	51	0.19
P-800	12.019(±0.003)	47	31[d]	0.26[d]
Cu(0.06)-P-800	12.016	45	22	0.23
Cu(0.12)-P-800	12.013	42	22	0.18
Cu(0.24)-P-800	12.012(±0.010)	45	27	0.18
Cu(0.50)-P-800	12.018(±0.005)	47	25	0.22
Cu(1.00)-P-800	12.017(±0.005)	53	25	0.20

[a] The lattice parameter was determined using the cubic symmetry of C12A7 by Eq.: $a = d_{hkl} \times \sqrt{h^2 + k^2 + l^2}$, where *a* is the lattice parameter (Å), *d* is the basal distance (Å). The Miller indexes (*h*, *k*, *l)* correspond to the reflecting plane used to measure the crystallite size as reported in reference JCPDS N° 09-0413. [b] The crystallite size was estimated from the peak reflection (*2 1 1*) using the Scherrer equation. [c] N_2 volume taken up at -196°C and relative pressure of 0.99.[d] Data taken from Chapter I. [e] Values in brackets represent the standard deviation (N=3)

3.2.2 N_2 physisorption analysis

The impact of the calcination temperature and doping degree on the textural properties was studied by N_2 physisorption. The adsorption-desorption isotherms of Cu-C12A7 catalysts heat-treated at 600 and 800°C containing different copper doping degrees are given in Figure 3.6a and b, respectively, whereas the detailed textural properties are listed in Table 3.2.

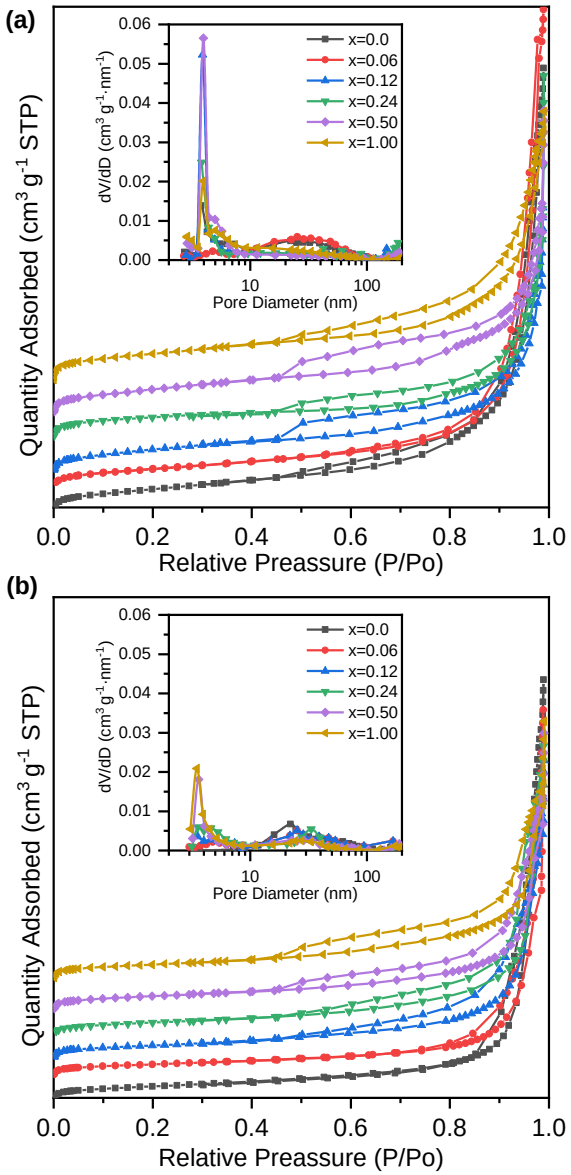

Figure 3.6. N_2 physisorption isotherms of Cu-C12A7 catalysts calcined a) 600 °C and b) 800 °C. Pore size distributions (PSD) based on the desorption branch are shown in insets. The isotherms are Y-axis offset to facilitate their visualization.

All isotherms exhibit a type IV shape and a hysteresis loop of type H3 (Figure 3.6). The shape of the isotherms is typically associated with mesoporous material, while the steep N_2 uptake near P/Po = 1 is connected to the N_2 adsorption within the interparticle spaces between

the constituting particles forming aggregates. Besides, the hysteresis loop shape can be attributed to capillary condensation in a non-rigid texture within the interparticle voids[121], and cannot be assigned to any intra-particular mesoporosity. The latter observation agrees with our findings in Chapter I (*p. 87*), related to the production of porous pristine C12A7, where aggregates of flake-shaped nanoparticles were found. In the catalysts set calcined at 600 °C, we observed a perceptible hysteresis loop at lower relative pressures (P/Po ~ 0.5-0.8), except for the sample with the lowest copper content ($x = 0.06$), which was associated with the condensation-decondensation of N_2 within smaller mesopores. On the other hand, the catalysts calcined at high temperatures (800°C) displayed a narrower hysteresis loop in the same region. In addition, within the latter set, a shift in the hysteresis loop towards lower P/Po values was noticed as the doping degree increased, which was not the case for the former one. These observations are supported by the analysis of pore size distributions (PSD). Here, we observed two groups of PSDs. The first group showing a maximum at *ca.* 3.5-4 nm, as mentioned in Chapter I, is produced by the forced closure of the isotherm upon desorption at P/Po between 0.4–0.5, attributed to tensile strength effect, leading to the formation of this artificial PSD. The second group was characterized by a large PSD between *ca.* 10-100 nm associated with the interparticle porosity. Moreover, when comparing the series calcined at 600 and 800 °C, a decrease of the pore volume (P_v) was evidenced with increasing calcination temperature for the lowest doping degree (x=0.06). Nevertheless, over this copper content no differences were observed among the two series. The specific surface area (S_{BET}) results revealed a noticeable difference between the two series as a function of the calcination temperature. For instance, the Cu-C12A7 catalysts annealed at 600 °C displayed specific surface area values up to two-fold higher than those treated at 800°C, which is in line with our findings from Chapter I related to the production of pristine (undoped) porous C12A7. Nevertheless, no correlation between the doping degree and the S_{BET} was found in either set of catalysts.

3.2.3 X-ray photoelectron spectroscopy (XPS) analyses

XPS measurements were conducted to evaluate the Cu surface dispersion and the homogeneity of the different Cu-C12A7 catalysts.

Figure 3.7 shows the XPS Cu 2p doublet spectra of both sets of samples (600 and 800°C). The two peaks of the doublets appeared at binding energies (BE) of ca. 932–934 eV for the first, and at higher BE between ca. 952–954 eV for the second, corresponding to the Cu $2p_{3/2}$ and Cu $2p_{1/2}$ components, respectively. Besides, a small broad shakeup satellite emerged close to the Cu $2p_{3/2}$ peak at higher BE around 242 eV, which gained in intensity as the copper content increased ($x \geq 0.5$). The occurrence of this satellite peak has been recognized as a distinctive feature of Cu(II) species.[132,133] Consequently, whatever the copper loading and the calcination temperature, the same typical Cu 2p profile was observed, presenting a $2p_{3/2}/2p_{1/2}$ doublet and a satellite, which corresponded to Cu^{2+} cationic species. Yet, a subtle shift to lower BE in the Cu $2p_{3/2}$ peak was noticed (Figure 3.7), as compared to the reported BE value for bulk CuO (933.6 ±0.4 eV).[132]

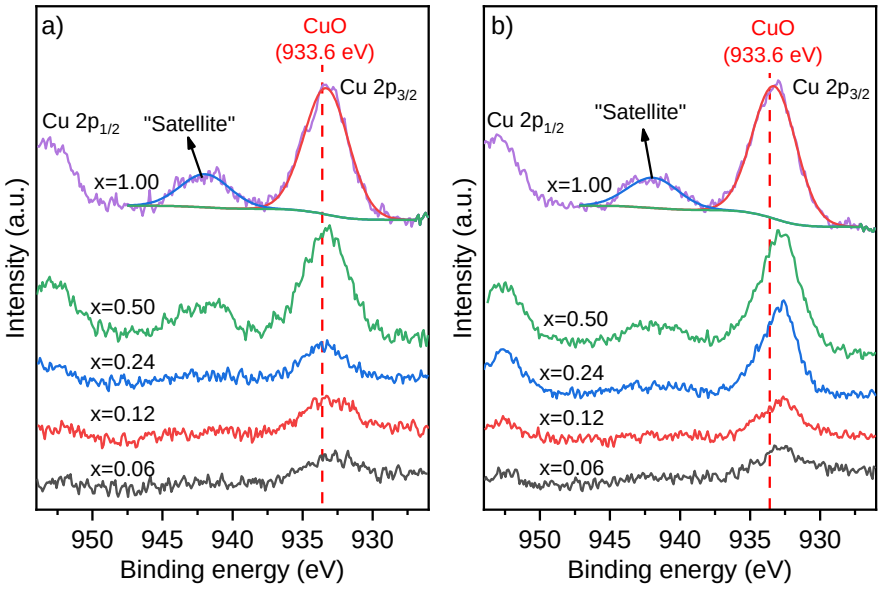

Figure 3.7. Cu 2p region XPS spectra of the Cu-C12A7 catalysts calcined at a) 600 and b) 800°C.

The individual BE values for the Cu $2p_{3/2}$ peak summarized in Table 3.3 corroborated the latter observation, which could be attributed to a partial reduction of the Cu(II) species due to the ultrahigh-vacuum or the photoionization inside the XPS chamber. Since only small BE

shifts between the different copper species can be expected, the decomposition of the Cu $2p_{3/2}$ peak to accurately evaluate the Cu speciation (Cu^{2+}, Cu^{+}, and Cu^{o}) is likely to be avoided due to the overlapping binding energies when Cu^{2+} is the most abundant species.[132]

Table 3.3. Cu $2p_{3/2}$ binding energy (BE), bulk atomic ratios based on the nominal doping degree (*x*), and surface atomic ratios based on XPS elemental quantification.

Sample	Cu $2p_{3/2}$ BE (eV)	Nominal bulk Cu/(Ca+Cu+Al) atomic ratio	Surf. Cu/(Ca+Cu+Al) atomic ratio	Surf. $(CO_3)^{2-}$/(Ca+Cu) atomic ratio
Cu(0.06)-P-600	933.0	0.002	0.004	0.51
Cu(0.12)-P-600	933.2	0.005	0.004	0.53
Cu(0.24)-P-600	933.5	0.009	0.008	0.55
Cu(0.50)-P-600	933.3	0.019	0.016	0.42
Cu(1.00)-P-600	933.3	0.038	0.014	0.36
Cu(0.06)-P-800	932.8	0.002	0.004	0.21
Cu(0.12)-P-800	932.9	0.005	0.008	0.23
Cu(0.24)-P-800	932.9	0.009	0.016	0.18
Cu(0.50)-P-800	932.9	0.019	0.028	0.16
Cu(1.00)-P-800	933.3	0.038	0.026	0.26

Table 3.3 shows the surface atomic Cu/(Cu+Ca+Al) ratios for all catalysts calculated based on the XPS surface elemental quantifications tabulated in Table C.1 (*see Appendix C*). The Cu quantification was performed based on the decomposition of Cu 2p spectra considering the Cu $2p_{3/2}$ peak and its satellite. Bulk (nominal) and surface (XPS) atomic Cu/(Cu+Ca+Al) ratios were very close for the Cu(*x*)-P-600°C catalysts set, suggesting that a good homogeneity was obtained, except for the sample with the highest copper loading ($x = 1.0$) where a lower surface ratio is observed. On the contrary, at high temperatures (800°C), the Cu surface content increased, displaying surface atomic Cu/(Cu+Ca+Al) ratios almost two-fold superior to the bulk ratios. This latter observation was probably associated with the migration of copper from the inner volume of the catalysts to their surface due to the rise in the temperature during the calcination. In both series, the highest Cu surface content was reached at intermediate Cu loadings ($x = 0.5$). However, the increasing trend in the Cu surface concentration with increasing *x* was disrupted at the maximum nominal loading ($x = 1$), indicating a lower Cu surface

content. The latter might be interpreted as a decrease in CuO dispersion resulting from the formation of bigger particles (segregated CuO crystallites). Moreover, the XPS measurements also confirmed that the surface content of adventitious carbonate moieties decreases by increasing the calcination temperature (Table 3.3), in agreement with our PXRD and Raman observations.

3.2.4 Assignment and quantification of Cu^{2+} and O_2^- species by electron paramagnetic spectroscopy (EPR)

To learn more about the nature of the copper species and how the calcination temperature affects the relative distribution of the various copper species and superoxide (O_2^-) ions present in the two series of Cu-C12A7 catalysts, EPR measurements were carried out. Figure 3.8 shows the EPR spectra obtained at -196 °C for the two series of Cu-doped C12A7 samples annealed at 600 (a) and 800°C (b). All EPR spectra, regardless of the doping degree and calcination temperature, were composed of the same overlapped asymmetric signals ascribable to the paramagnetic Cu^{2+} and O_2^- ions. In the low magnetic field region (260-310 mT), a main axial signal (denoted as A) and another one (hereafter A') contributing to a lower extent were observed, presenting a four-line hyperfine structure as illustrated by their parallel components (A_{zz}) due to the interactions of odd electrons with copper nuclei (S = 1/2, I = 3/2).[134–136] Meanwhile, the perpendicular features of these axial signals (A and A') appeared between 320-340 mT, exhibiting broad line widths with unresolved hyperfine splitting structure. In addition, a broad superimposed anisotropic signal (denoted as B) between *ca.*300-330 mT was also detected. The latter presented large line widths, which have been ascribed to the dipolar interactions between neighboring Cu^{2+} ions accommodated inside Cu(II)-containing aggregates of oxidic type.[134–136] Yet, considering that antiferromagnetic coupling between Cu^{2+} ions within well-crystallized large CuO particles produces EPR silent species, signal B was reasonably ascribed to small clusters where this antiferromagnetic character is not fully established.[134–136] In the high magnetic field region (~330-340 mT), a sharper signal was present in both sets. According to previous literature, this feature was assigned to g_{xx} and g_{yy} components of the orthorhombic signal belonging to O_2^- ions clathrated inside the C12A7 cages, whereas the g_{zz} feature was covered under the dominant perpendicular component of the Cu^{2+} species.[45] The

intensity of the superoxide signal was superior in the spectra of the catalysts calcined at high temperatures (800°C), suggesting that the rise in the temperature promoted the formation of this oxygen species due to the partial dehydroxylation of OH^- ions inside cages at the outermost layer of the grains, which was already understood to occur from Raman spectroscopy. The latter assessments agreed with our analysis described in Chapter II related to undoped pristine C12A7 (x = 0), where the rise in the calcination temperature showed to be of pivotal significance in the oxygen species formation (*pp. 121-127*).

Based on computer simulations of the experimental spectra, the fitted EPR parameters are reported in Table 3.4. The ***g***-tensor values of the A and A' signals corresponded well to those previously reported by Maurelli *et al.*[45] for isolated Cu^{2+} ions within the C12A7 framework. Moreover, the observed unresolved hyperfine splitting of the perpendicular component of both signals might be attributed to the line bonding associated with the microheterogeneity in the local structural environment of Cu(II) species accommodated in the C12A7 framework.[45] Besides, the average ***g***-tensor, $\langle g \rangle$=2.16, for signal B is similar to those of signals A and A', confirming that signal B belongs to Cu(II) ions. Finally, the determined ***g***-tensors for O_2^- ions showed to be in good agreement with those found in the literature[10,11,13,102], confirming its assignment.

Table 3.4. EPR parameters of copper (II) and superoxide paramagnetic species in Cu-C12A7 catalysts obtained by computer simulation of the spectra.

Signal	**g-tensors**				**Hyperfine constant** [b]	**structure**
	g_{xx}	g_{yy}	g_{zz}	$\langle g \rangle$ [a]	A_{xx} [c] (MHz)	A_{zz} (MHz)
isolated Cu^{2+} (A)	2.071	2.071	2.350		426	15
isolated Cu^{2+} (A')	2.066	2.066	2.309		512	16
clustered Cu^{2+} (B)				2.16		
O_2^- (superoxide)	2.005	2.008	2.074			

[a]Average ***g***-tensor for the anisotropic signal B. [b]A (MHz)= 2.802495 x g/g_e x A (G), where g_e=2.00232. [c]$A_{xx}=A_{yy}$ considering an axial symmetry.

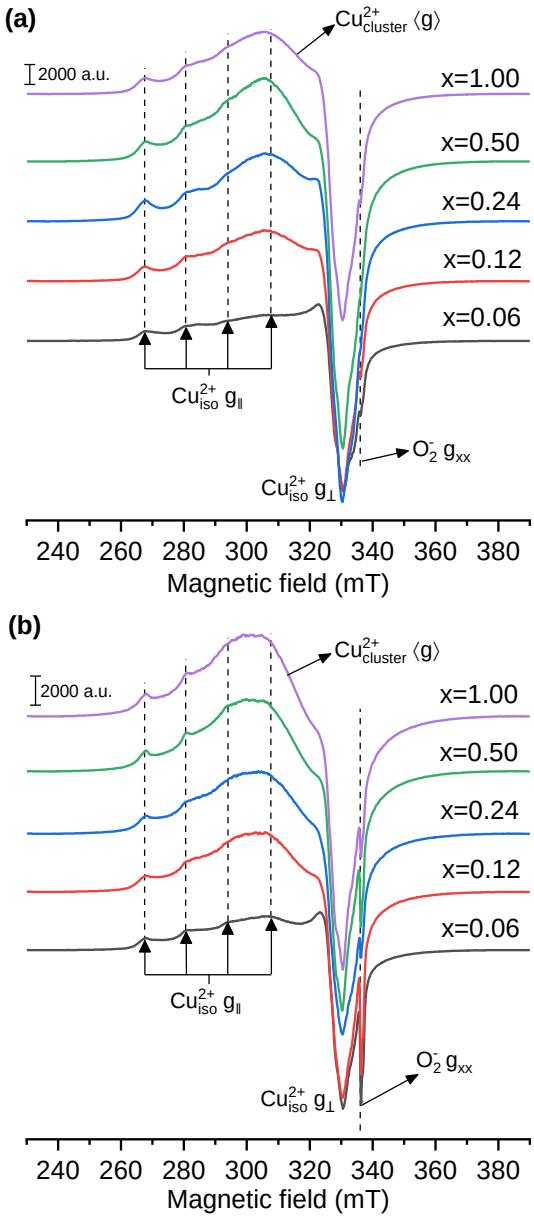

Figure 3.8. EPR spectra of two sets of Cu-C12A7 catalysts calcined at a) 600 and b) 800 °C.

Figure 3.9a shows the absolute concentration of EPR active copper species (Cu^{2+}_{iso} and $Cu^{2+}_{clusters}$) normalized by the catalyst mass determined by the double integration of the spectra and compared with

the $CuSO_4$ standard. In both sets, the specific concentration of the EPR active copper species increased monotonically with rising the doping degree. Yet, for the catalysts calcined at 600°C, a superior concentration and a steeper increase were noticed, attaining a maximum value at $x = 0.5$, then the concentration dropped from thereon. Our interpretation is that the excess of Cu induced the formation of bulky CuO species diminishing the dispersion and prompting the agglomeration of the small clusters at the surface of C12A7, which produced a loss in the integral EPR intensity. As aforesaid, these larger CuO particles are EPR-undetectable, thus decreasing the EPR signal concerning the Cu loading. This statement was confirmed by the presence of segregated CuO at higher doping degrees ($x \geq 0.5$) as revealed by PXRD.

Figure 3.9b displays the relationship between the doping degree and the total amount of EPR active Cu^{2+} species normalized by the nominal number of Cu atoms (Cu_{total}). Consequently, if all the Cu atoms loaded in each catalyst were detected by EPR, this ratio should be equal to 1 (100%). Even though the EPR active Cu^{2+}/Cu_{total} proportion was close to the expected value at the lowest doping degree ($x = 0.06$), as the doping degree increased this ratio declined monotonically, with a loss of nearly ten-fold at the highest x value. This observation confirmed that an increase in the doping degree unambiguously promoted the formation of bigger CuO particles due to the coalescence and aggregation of the well-dispersed Cu^{2+} species (isolated and clusters). While the loss of dispersion was intensified at higher temperature due to the migration of Cu atoms from the bulk to the surface, as confirmed by XPS.

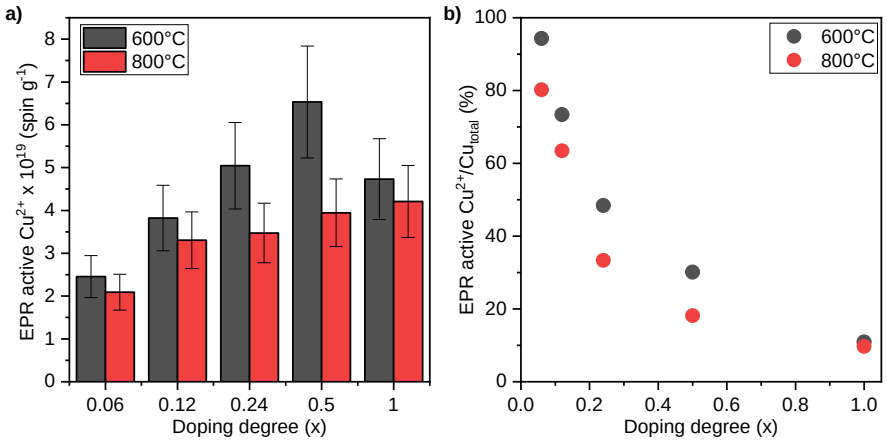

Figure 3.9. a) Total concentration of EPR active Cu^{2+} ions as a function of the doping degree. b) Relationship between the EPR active Cu^{2+}/Cu_{total} and the doping degree, where Cu^{2+}/Cu_{total} represents the relation between the EPR active Cu^{2+} species to the nominal copper loading. Error bars represent the cumulative error rising from the quantification analysis.

Lastly, Figure 3.10 assembles the relative contribution of each paramagnetic species (Cu^{2+} isolated, Cu^{2+} cluster, and O_2^-) concerning the normalized total spin concentration shown in Figure 3.9a, which was obtained by computer simulation. The clustered Cu^{2+} ions were the most abundant species, except at the lowest Cu loading (x = 0.06), where nearly equivalent contributions between the isolated and the clustered Cu^{2+} species were observed, being even slightly predominant at lower temperatures (600 °C). As a result, raising the calcination temperature and the Cu loading promoted the production of Cu^{2+} clusters while diminishing the isolated ones. The contribution of superoxide ions (~10^{16}-10^{17} spin g^{-1}, inset Figure 3.10) was marginal regarding the absolute spin concentration (~10^{19} spin g^{-1}), yet higher concentrations were detected at elevated temperatures (800 °C), which was associated with a higher partial replacement of OH^- by O_2^- via an anionic-exchange process, as described in detail in Chapter II.

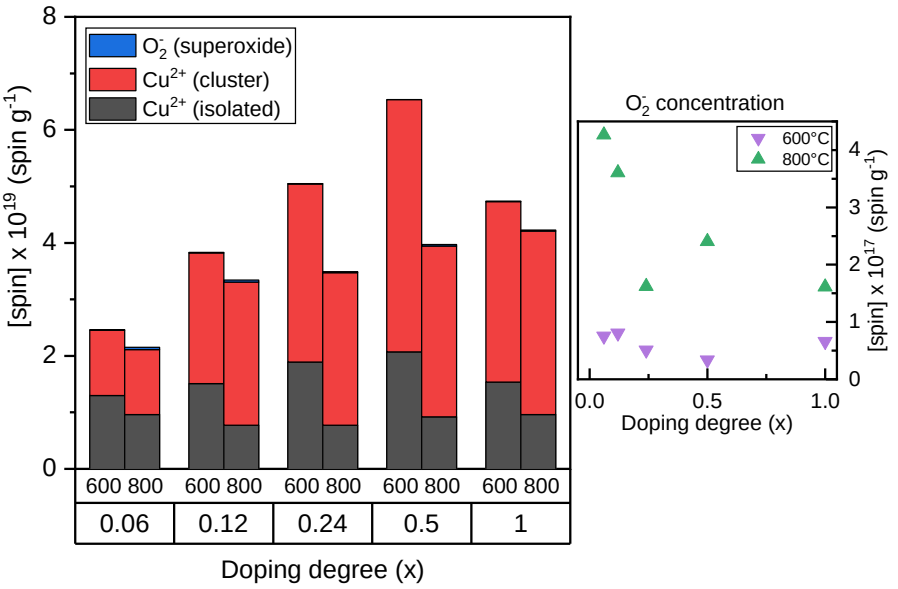

Figure 3.10. Contribution of signals Cu^{2+} isolated, Cu^{2+} cluster and O_2^- extracted from computer simulations of the EPR spectra of Figure 3.8, as a function of the doping degree for the two series of Cu-C12A7 catalysts. For a better visualization the superoxide concentrations are shown in the inset.

3.3 Nature and role of the different Cu(II) species

Considering the distinct nature of the Cu species interacting at different degrees with C12A7, a plausible correlation of their nature with their role in catalytic CB oxidation is here discussed. Two parameters seem to have a significant impact on the catalytic activity of Cu-C12A7 materials toward the combustion of carbon black: (i) the calcination temperature; (ii) the nature, abundance, and dispersion of copper. As shown in the previous sections by EPR, Raman, PXRD, and XPS analyses, copper is present as fully oxidized (Cu^{2+}) in three structurally different Cu(II) entities: well-dispersed Cu^{2+} species (isolated and clustered) and segregated CuO particles, whose relative concentrations vary as a function of the doping degree and the calcination temperature.

At low doping degrees ($0 < x < 0.24$), only *ca.* 60-95% of the total nominal amount of copper was detected and characterized by EPR. For instance, the slightly predominant presence of isolated Cu^{2+} was only observed at low temperatures (600 °C) and low Cu loading

(x = 0.06). The residual EPR-undetected copper fraction, which was superior in samples calcined at higher temperatures (800 °C), could be due to the presence of small CuO particles, considering that Cu species magnetically interacting with each other, decreases the EPR intensity [134–136]. Concerning the catalytic performance of the samples in this Cu loading range, an improved catalytic activity, gauged by lower T_{peak} and T_{50} values, was observed as the Cu loading was raised. This positive effect could be related to the increase in the relative concentration of clustered Cu^{2+} species since the content of isolated ones remain almost the same within each set of catalysts with the increasing nominal copper content. On the contrary, the noticed differences in the catalytic activity, at equivalent doping degrees between the two series of catalysts calcined at 600 and 800 °C, could be associated with the superior specific surface area exhibited by the samples calcined at lower temperatures, as previously reported for pristine non-doped C12A7 in Chapter II.

Moreover, by increasing the Cu content ($x \geq 0.24$), the occurrence of a separated CuO crystalline phase was detected from x = 0.24 and x = 0.5 for the catalysts calcined at 600 and 800 °C, respectively. Thus, confirming the association of the undetected fraction with the formation of segregated CuO particles, which grow with the excess of Cu via the coalescence and agglomeration of the well-dispersed Cu(II) species, as shown by EPR, Raman, and PXRD. Similarly, when rising the Cu loading, the catalytic activity continued to improve until x = 0.5, where the lowest T_{peak} values were attained in both series of catalysts. Meanwhile, any Cu excess from thereon hampered the catalytic activity. These evolutions of the catalytic performance might be related to two facts: (i) the highest concentration of EPR Cu^{2+} active species (predominant Cu^{2+} clusters) was also achieved at x = 0.5, (ii) the segregated CuO reached the maximum at the highest loading (x = 1.0).

In previous studies related to the catalytic behavior evaluation of supported CuO materials in several reaction systems such as soot combustion[137], NO_x reduction[138] and CO oxidation[133–135], the ameliorated catalytic performances of these Cu-promoted catalysts were associated with the formation of CuO amorphous patches (Cu^{2+} clusters) over the surface of the support. It was suggested that clustered Cu(II) is easily reduced due to the presence of both Cu-O-Metal and Cu-O-Cu interactions, while the isolated Cu^{2+} species

strongly interacting with the support are less reducible due to their higher stability in the solid matrix and the absence of Cu-O-Cu interactions. On the contrary, the loss of dispersion due to the agglomeration of copper, and thus the formation of segregated bulky CuO particles, notably reduces the Cu-O-Metal interactions, which negatively impacts the redox capacity of the catalysts [133–135,137,138]. Therefore, we may speculate that in our case, the three structurally different Cu species located at the surface of C12A7 interact in a similar way as those in the other CuO-supported systems, explaining the catalytic activity enhancement with the increase of clustered Cu^{2+} species, while the activity loss is attributed to the lower interactions between the segregated CuO particles with C12A7. Moreover, the comparable catalytic activity displayed by the Cu(0.50)-P-600 and Cu(0.50)-P-800, although the one calcined at 800°C presented a lower concentration of clustered Cu^{2+} species and lower surface area, could be attributed to the higher concentration of superoxide ions promoted by the annealing at elevated temperatures (inset, Figure 3.10). In a previous study, Sato *et al*. suggested that the incorporation of Cu as a dopant in a Si-containing C12A7 derivative enhanced the reactivity of the occluded native O_2^- species.[44] Thus, we may propose that a synergic effect between the well-dispersed Cu^{2+} species and the clathrated O_2^- ions in our catalysts improves the catalytic activity also in our system.

3.4 Influence of water on the catalytic performance of Cu-C12A7 catalysts

Considering that water vapor is unavoidably present in combustion exhaust gases, including those of gasoline engines, it is necessary to corroborate that the above-stated observations and findings concerning our catalysts tested in the CB oxidation under dry conditions (5% O_2/He) remain consistent when working under more representative conditions (*i.e.,* in the presence of water vapor). Therefore, several specimens from the series of catalysts calcined at 800°C were tested under wet conditions (5% H_2O+5% O_2/He). The selected water content in this examination falls in the range of those reported in the literature (*e.g.*, 1-30%) to simulate the composition of the exhaust gases from a diesel combustion engine.[139–141] The CB conversion profiles are displayed in Figure C.5 (*see Appendix C*) and the activity indicators are compared (wet *vs.* dry conditions) in Table

3.5. Above all, we noticed that the previously observed relationship between the doping degree and the catalytic activity under dry conditions remained unchanged in the presence of water, showing that the best catalytic activity was achieved at a copper loading equal to 0.5 where the clustered Cu^{2+} species were dominant. In addition, we observed that the presence of water in the reaction medium accelerated the reaction rate for all the tested catalysts, regardless of the copper content. As shown in Figure C.5, all CB conversion profiles obtained under wet conditions shifted to low temperatures as compared to those acquired under dry conditions. The latter was confirmed by the activity indicators summarized in Table 3.5. For instance, lower T_{50} values were achieved when CB was oxidized in the presence of water vapor. Last but not least, water also seemed to promote the formation of CO_2 over CO, as observed at low copper loadings where lower CO_2 selectivity values were obtained under dry conditions.

Table 3.5. Comparison between the activity indicators for Cu-C12A7-800 catalysts tested under dry and wet conditions in the CB oxidation reaction.

Atmosphere composition	**Catalytic indicators**	**Doping degree (*x*)**			
		0.00	0.06	0.50	1.00
Wet conditions ($5\%O_2/5\%H_2O$/He)	T_{10}	436	430	408	416
	T_{50}	476	476	439	450
	T_{90}	511	511	469	489
	T_{peak}	474	480	437	445
	S_{CO_2}	99	99	100	100
Dry conditions ($5\%O_2$/He)	T_{10}	448	443	416	425
	T_{50}	503	491	460	474
	T_{90}	547	531	498	515
	T_{peak}	514	496	464	486
	S_{CO_2}	91	92	100	100

In previous studies, this improvement in the catalytic activity during the soot oxidation reaction in the presence of water vapor within the reaction medium has already been observed.[139–141] For instance, it has been reported that the presence of water during the oxidation of soot is much more important that is concentration in the exhaust gases. In a recent isotopic study[141], Yang *et al.* proposed that water participates in the carbon oxidation reaction as an accelerator rather than an

oxidant. They suggested that the improved activity under wet conditions is related to (i) the higher capability of water vapor to be adsorbed and dissociated at the catalyst surface, as compared to dioxygen; and (ii) its ability to boost the regeneration of oxygen vacancies. Conversely, as described in the general introduction, C12A7 is known for its capacity to host within its structure (*i.e.*, clathrated cages) a wide variety of anions as countercharges to maintain its charge neutrality. Among them, OH^- ions can be easily incorporated by an anionic exchange reaction between water vapor and the encaged oxygen radicals inside C12A7 when the material is annealed in an atmosphere containing water in a wide range of temperatures (~400-900 °C)[35], as reviewed in Chapter II. Therefore, we suggest that the superficial cages might act as active sites in the OH* formation, which promotes the formation of surface-oxygen complexes (SOCs) at the contact points between the surfaces of C12A7 and primary carbon particles, boosting the catalytic activity. However, this hypothesis needs to be corroborated, yet this forthcoming study falls out of the scope of the present thesis.

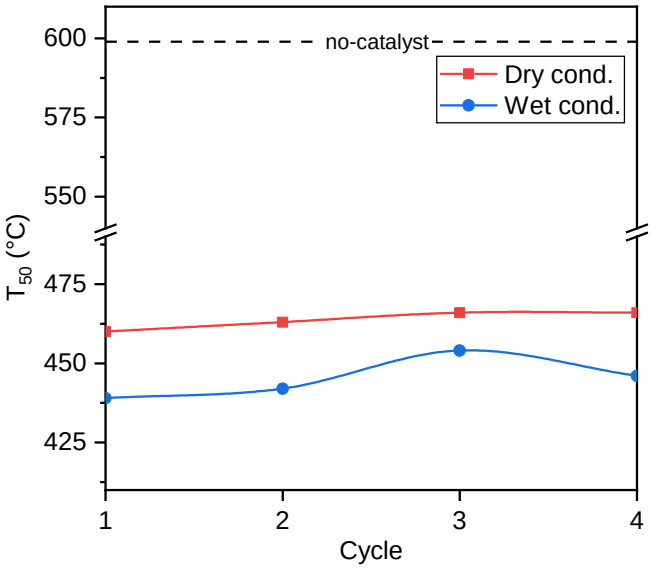

Figure 3.11. T_{50} in consecutive CB combustion cycles performed under dry (5%O_2+He) and wet (5%H_2O+5%O_2+He) conditions employing Cu(0.5)-P-800 catalyst (x = 0.5).

The long-term stability of our best catalyst, Cu(0.50)-P-800 (x=0.5), was evaluated during four consecutive CB combustion cycles under dry (O_2/He) and wet (H_2O/O_2/He) conditions, with the obtained T_{50} values in each run being reported in Figure 3.11). The catalytic activity under dry conditions remained almost unchanged after four cycles, demonstrating the robustness of our catalyst. Under wet conditions, a slight deactivation (if significant) was observed during the first three cycles, after which the catalytic activity leveled off.

4 Conclusive remarks

This last Chapter showed that Cu-doped C12A7 materials displaying well-dispersed Cu^{2+} species and enhanced textural properties were effectively prepared by one-pot assisted solution combustion synthesis. We could demonstrate that copper loading and calcination temperature noticeably impacted the relative abundance of the different Cu species, their degree of dispersion, and the textural and structural properties of the Cu-C12A7 catalysts, significantly influencing their catalytic performance in the CB oxidation. After carefully examining the physicochemical properties of Cu-C12A7 catalysts, we assessed that these materials contained three structurally distinct forms of copper species: isolated Cu^{2+} (within the framework), clusters of Cu^{2+}, and segregated CuO particles. We showed that the Cu-doped porous C12A7 catalysts prepared in this chapter were notably more active than the undoped porous C12A7 ones presented in Chapter I. We found that an optimal doping level of x = 0.5 led to the best catalytic output, also showing an improved selectivity towards CO_2 with rising the Cu loading. We suggested that the enhancement in the catalytic activity is related to the increase in the relative concentration of the well-dispersed clustered Cu^{2+} species in close interaction with C12A7. We also evidenced that an excessive doping degree diminished the catalyst performance due to the loss of dispersion of the active species and the concomitant segregation of CuO.

Overall, an appropriate balance of the dispersion degree of the Cu species, textural properties, and superoxide species of the Cu-doped C12A7 catalysts allowed an improvement of their catalytic performance in the CB oxidation reaction. The presence of water vapor during the CB oxidation reaction brought a positive effect on the catalytic

performance of our catalysts, but the relationship performance-Cu species remained identical, whatever under wet or dry conditions. Additionally, the reflected long-term thermal stability of Cu-doped C12A7 makes it a promising candidate to uphold the high temperatures attained inside the catalytic filter at localized hot spots.

GENERAL CONCLUSION AND OUTLOOK

1. General conclusion

In oxidation catalysis, the control over the nature of the available oxygen species (electrophilic or nucleophilic) at the surface of a metal oxide is considered to have an important role in the catalytic performance, particularly on its selectivity. In this context, this thesis aimed to evaluate the possibility of modulating the activity and selectivity of an oxidation process by controlling the population distribution of extra-framework oxygen species of mayenite (C12A7), considering the capacity of this calcium aluminate to modify the nature of the occluded extra-framework anions inside its structure as a function of external conditions (*e.g.*, temperature and atmosphere). Therefore, we have hypothesized that by adjusting the nucleophilic or electrophilic character of the population distribution of extra-framework oxygen species, we might have a possibility of favoring a total or partial oxidation reaction.

In the pathway to the main purpose of this thesis, firstly, we needed to develop a preparation method to tackle the known limitations of synthesizing C12A7 through the conventional ceramic route (*i.e.*, solid-state reaction), which is known to produce mayenite with limited textural properties (*first objective*). Hence, two preparation strategies based on solution combustion synthesis (SCS) were investigated and successfully developed in *Chapter I*. These synthetic approaches revealed that i) C12A7 could be prepared directly and cost-effectively without requiring high temperatures for its formation, and ii) C12A7 with enhanced texture and controlled crystallinity could also be produced by optimizing the first methodology. These findings were crucial as they later facilitated the preparation of Cu-doped C12A7 catalysts with improved textural and structural properties (*Chapter III*). Yet, more importantly, they also allowed a better understanding of the relationship between textural properties, modulation of the extra-framework oxygen species distribution, and catalytic behavior of C12A7 (*Chapter II*).

To eventually appraise the influence of the extra-framework oxygen species distribution on the catalytic performance of C12A7 in an oxidation reaction, we needed to assess if this population distribution could be modulated in C12A7 materials obtained by a wet-chemistry approach and up to which extent (*second objective*). In *Chapter II*, several strategies were designed and tested to analyze the impact of

multiple parameters on controlling the oxygen species population profile. It was evidenced, in agreement with the literature, that increasing the temperature under a controlled atmosphere (*e.g.*, high partial pressure of oxygen and low water content) is an effective way to promote the formation of active oxygen species while significantly reducing the presence of entrapped hydroxyl anions. In this matter and for the first time in the literature, it was revealed that the oxygen flow rate and the type of configuration between the inlet gas stream and the solid (C12A7 or its precursor) during the heat treatment are relevant parameters towards a better control of the oxygen species distribution. Nevertheless, promoting the dominance of the oxygen species over the hydroxyl anions unavoidably impacted the textural and structural properties of C12A7 due to the higher temperature required for this purpose.

All chapters together showed that the texture, concentration of extra-framework oxygen species, and structural modifications by cationic doping in C12A7 had an influence on its catalytic performance (*third objective*). Firstly, the benefit of improving the mayenite textural properties, namely its specific surface area, was evidenced in the carbon black and propane total oxidation reactions. In both catalytic systems, porous C12A7 showed better conversions than the non-porous one at lower temperatures. Additionally, in the CB oxidation, the selectivity toward CO_2 also showed to be favored from this improvement (*Chapter I*). Secondly, isolating the effect of increasing the concentration of oxygen species was only achieved by carefully examining the catalytic performance of C12A7 without considering the influence of the textural properties (*Chapter II*). Hence, it was evidenced that increasing the quantity of entrapped oxygen species indeed promoted the catalytic activity of C12A7, nevertheless, this effect was not long-lasting over time. Thirdly, the structural modification by introducing copper within C12A7 structure developed in this work also provided valuable insights. Overall, an appropriate balance between the dispersion degree of the Cu(II) species, textural properties, and superoxide species in the Cu-doped C12A7 catalysts was shown to be decisive to their catalytic performance in the CB oxidation reaction. Lastly, the presence of water in the oxidation medium during the CB oxidation showed to be beneficial for the overall performance of pristine and Cu-doped C12A7.

Although bare and Cu-doped C12A7 catalysts are somewhat less efficient compared to conventional oxidation catalysts such as CeO_2 or supported noble metals, it is necessary to highlight that the latter kind relies on rare, critical, and expensive elements. Conversely, our mayenite-based catalysts contain mainly earth-abundant and cost-effective metals (Ca and Al), while only small fractions of copper are incorporated (where x = 0.5 corresponds to only 2.3%wt Cu). Besides, regarding a potential application in catalytic CB combustion, the lower activity of C12A7 could be compensated by increasing the amount of loaded catalyst in the filter trap considering its significantly lower cost. However, the assessment of the Cu-C12A7 catalytic behavior in the presence of other pollutants (NO_x and H_2S) and under less ideal conditions (*i.e.*, loose contact mode) are required to establish the potential application.

Finally, the multiple findings in *Chapter II* demonstrated that the initial chemical identity (*i.e*., nucleophilic or electrophilic nature) of the dominant extra-framework species in C12A7 could not influence the selectivity of the catalyst. This outcome has been associated with the fact that catalysis is a dynamic process. Therefore, the initial distribution population is dynamically re-equilibrated with the oxidation medium upon reaction conditions. As a result, the medium promotes the most stable species (OH^- and in less amount O_2^-) under these precise conditions and prevents control over the oxygen species distribution during the reaction process.

The results presented in this work highlighted the potential of C12A7 as an oxidation catalyst. We have provided fundamental insights that will contribute to a better understanding of the relationship between the physicochemical properties of C12A7 and its catalytic behavior in oxidation reactions. Nonetheless, the close dependency between stability and speciation control of the C12A7 extra-framework population regarding the surrounding medium during an oxidation reaction frustrated our intentions of controlling the product distribution (selectivity) by modulating the distribution profile of oxygen species, thus invalidating our hypothesis.

In summary, C12A7 is a competitive catalyst in specific oxidation reactions, namely for air control applications. The fact that mayenite is based on abundant earth metals (Ca and Al) positioned it as a cost-

effective, robust, and environmentally friendly material. Its unique structure and its capacity to modulate the nature and abundance of its extra-framework species provide versatility to this calcium aluminate. However, depending on the dedicated application, this material can also present several disadvantages. For instance, the catalytic performance of C12A7 in oxidation reactions may be sensitive to specific reaction conditions, such as temperature, pressure, and reactant composition (presence of water). Deviating from the optimal conditions may result in reduced catalytic activity. Its stability under long-term operation can also be impacted. While C12A7 initially shows promising catalytic performance, maintaining its enhanced activity over extended periods can be challenging. Factors like the re-equilibration of reactive oxygen species and the potential for catalyst deactivation may limit its stability under prolonged operation. Additionally, C12A7 can present selectivity issues. Depending on the reaction system, C12A7 may exhibit lower selectivity (*i.e.,* partial oxidation reaction), leading to the formation of undesired by-products. Thus, C12A7's suitability as an oxidation catalyst is mainly limited to certain oxidation reactions (*e.g.,* VOC total oxidation) and may not be the optimal choice for all oxidation processes.

1. Outlook of future work

Herein, we present a few examples of new prospects to further elucidate various aspects of C12A7 behavior as a catalyst or investigate novel preparation techniques to improve it.

i. Concerning the synthesis of C12A7 via SCS (*Chapter I*), it would be appealing to look into the conception of more sophisticated preparations methods such as:

   - An aerosol spray pyrolysis approach could open a way to further improve the textural and structural properties of bare and doped mayenite through a one-step procedure. This method could prevent the aggregation and sintering of the grains during the combustion reaction by shaping aerosol droplets. In the literature, it has been shown that metal oxide hollow particles with improved texture are likely obtained by employing this versatile and scalable approach.[87,95]

- The usage of soft-templating agents such as cotton (cellulose) fibers or polymer beads to promote a hierarchical porosity within C12A7. This could prompt the formation of three-dimensional ordered macroporous (3-DOM) structured catalysts, promoting the contact between C12A7 and carbon black (soot model substitute) particles while enhancing the catalytic performance.

ii. Regarding the control over the selectivity of an oxidation reaction, an alternative that could be investigated concerns the employment of mild oxidants such as N_2O and CO_2 instead of O_2 (*Chapter II*) to limit the direct and consecutive total oxidation reactions. For instance, using CO_2 as a soft oxidant presents a double advantage *i)* control over the selectivity by preventing the overoxidation of the partial product and *ii)* the CO_2 valorization, which is in line with the current driving force for carbon capture, utilization and storage.[6,142] In this regard, it has been shown that mayenite electride form (C12A7:e^-) is capable of activating and splitting CO_2 even at room temperature.[143] However, it is necessary to evaluate the capacity of C12A7 (oxidic form) to activate CO_2 and to employ it in the partial oxidation of an hydrocarbon.

iii. In *Chapter III*, it was noticed that the presence of water in the reaction medium during CB combustion promoted the catalytic activity and selectivity of bare and doped C12A7. However, the reasons behind this improvement were not elucidated in this work. Therefore, a dedicated study to further understand the latter is still required. Additionally, examining the Cu-C12A7 catalytic behavior in the presence of other pollutants (NO_x and H_2S) and under less ideal conditions (*i.e.*, loose contact mode) should also be considered.

iv. Lastly, it has been recently revealed that Ru/C12A7:OH^- was more active in the CO_2 methanation reaction than its electride derivative (Ru/C12A7:e^-).[61] The authors proposed that altering the anionic species in C12A7 would be a beneficial strategy for enhancing the catalytic activity of the metallic sites. In light of this, it would be worth evaluating other reaction systems where hydroxyl species, often underestimated, could be beneficial,

thus employing C12A7:OH^- as a bulk catalyst or active support. In this case, a catalytic system in the gas phase reaction might be preferred knowing that the immersion of C12A7 in water for extended periods unavoidably leads to its total hydration and subsequent formation of a hydrogarnet phase (C3AH6).[39,63,127] Nonetheless, liquid phase reactions in anhydrous conditions, such as the transesterification of oils into biodiesel using methanol, could be envisaged. In this regard, a few reports have unveiled that hydrocalumite-type compounds and composite materials made of C12A7 and CaO are active for this reaction [144–146]. In addition, calcium aluminates (CA and C12A7) promoted with KOH have also been studied.[147,148] Even though the benefits of the basicity of these materials on the transesterification reaction have been highlighted, none of these studies have yet reported on the possible effect of the clathrated hydroxyl ions on the catalytic behavior of C12A7 for this catalytic system.

REFERENCES

1. Centi, G., Trifiro, F. & Cavani, F. *Selective oxidation by heterogeneous catalysis*. (2001).

2. Armor, J. N. A history of industrial catalysis. *Catal. Today* **163**, 3–9 (2011).

3. Bielanski, A. & Haber, J. Oxygen in Catalysis on Transition Metal Oxides. *Catal. Rev. Sci. Eng.* **19**, 1–41 (1979).

4. Haber, J. Fundamentals of Hydrocarbon Oxidation. in *Handbook of Heterogeneous Catalysis* (eds. Ertl, G., Knözinger, H., Weitkamp, F. & Schüth, J.) 3359–3384 (Wiley-VCH Verlag GmbH& Co. KGaA, 2008).

5. Vedrine, J. C. Heterogeneous catalytic partial oxidation of lower alkanes (C1 – C6) on mixed metal oxides. *J. Energy Chem.* **25**, 936–946 (2016).

6. Gambo, Y. *et al.* Catalyst design and tuning for oxidative dehydrogenation of propane – A review. *Appl. Catal. A Gen.* **609**, (2021).

7. Grant, J. T., Venegas, J. M., McDermott, W. P. & Hermans, I. Aerobic Oxidations of Light Alkanes over Solid Metal Oxide Catalysts. *Chem. Rev.* **118**, 2769–2815 (2018).

8. Hosono, H. & Abe, Y. Occurrence of superoxide radical ion in crystalline calcium aluminate $12CaO{\cdot}7Al_2O_3$ prepared via solid-state reactions. *Inorg. Chem.* **26**, 1192–1195 (1987).

9. Hayashi, K., Hirano, M., Matsuishi, S. & Hosono, H. Microporous crystal $12CaO{\cdot}7Al_2O_3$ encaging abundant O^- radicals. *J. Am. Chem. Soc.* **124**, 738–739 (2002).

10. Hayashi, K., Matsuishi, S., Ueda, N., Hirano, M. & Hosono, H. Maximum incorporation of oxygen radicals, O^- and O_2^-, into $12CaO{\cdot}7Al_2O_3$ with a nanoporous structure. *Chem. Mater.* **15**, 1851–1854 (2003).

11. Yang, S. *et al.* Formation and Desorption of Oxygen Species in Nanoporous Crystal $12CaO{\cdot}7Al_2O_3$. *Chem. Mater.* **16**, 104–110 (2004).

12. Matsuishi, S., Hayashi, K., Hirano, M., Tanaka, I. & Hosono, H. Superoxide Ion Encaged in Nanoporous Crystal $12CaO{\cdot}7Al_2O_3$ Studied by Continuous Wave and Pulsed Electron Paramagnetic Resonance. *J. Phys. Chem. B* **108**, 18557–18568 (2004).

13. Hayashi, K., Hirano, M. & Hosono, H. Excess Oxygen in $12CaO{\cdot}7Al_2O_3$ Studied by Thermogravimetric Analysis. *Chem. Lett.* **34**, 586–587 (2005).

14. Hayashi, K., Matsuishi, S., Hirano, M. & Hosono, H. Formation of oxygen radicals in $12CaO{\cdot}7Al_2O_3$: Instability of extraframework oxide ions and uptake of oxygen gas. *J. Phys. Chem. B* **108**, 8920–8925 (2004).

15. Rankin, G. A. & Wright, F. E. The Ternary System $CaO\text{-}Al_2O_3\text{-}SiO_2$. *Am. J. Sci.* **39**, 1–79 (1915).

16. Hewlett, P. *Lea's Chemistry of Cement and Concrete*. *Science* **58**, (2004).

17. Lagerqvist, K., Wallmark, S. & Westgren, A. X-ray Study of the Systems CaO–Al2O3 and SrO–Al2O3. *Z. Anorg. Allg. Chem.* 1–16 (1937).

18. Nurse, R. W. Phase Equilibria and Constitution of Portland Cement. in *Chemistry of Cement: Proceedings of the Fourth International Symposium* 9–37 (National Bureau of Standards, 1960).

19. Ruszak, M., Witkowski, S., Pietrzyk, P., Kotarba, A. & Sojka, Z. The Role of Intermediate Calcium Aluminate Phases in Solid State Synthesis of Mayenite ($Ca_{12}Al_{14}O_{33}$). *Funct. Mater. Lett.* **04**, 183–186 (2011).

20. Eufinger, J.-P., Schmidt, A., Lerch, M. & Janek, J. Novel anion conductors – conductivity, thermodynamic stability and hydration of anion- substituted mayenite-type cage compounds C12A7:X (X = O, OH, Cl, F, CN, S, N). *Phys. Chem. Chem. Phys.* **17**, 6844–6857 (2015).

21. Galuskin, E. V. *et al.* A reinvestigation of mayenite from the type locality, the Ettringer Bellerberg volcano near Mayen, Eifel district, Germany. *Mineral. Mag.* **76**, 707–716 (2012).

22. Galuskin, E. V. *et al.* Mayenite supergroup, part I: Recommended nomenclature. *Eur. J. Mineral.* **27**, 99–111 (2015).

23. Büssem, W. & Eitel, A. "Die Struktur des Pentakalzium- trialuniinats" (Structui e of Pentacalcium Trialuminate). *Z. Krist.* 175–188 (1936).

24. Jeevaratnam, J., Glasser, F. P. & Dent Glasser, L. S. Anion Substitution and Structure of $12CaO{\cdot}7Al_2O_3$. *J. Am. Ceram. Soc.* **47**,

105–106 (1964).

25. Bartl, H. & Scheller, T. Zur Struktur des $12CaO{\cdot}7Al_2O_3$. *Neues Jahrb. fur Mineral.* 547–552 (1970).

26. Boysen, H., Lerch, M., Stys, A. & Senyshyn, A. Structure and oxygen mobility in mayenite ($Ca_{12}Al_{14}O_{33}$): a high-temperature neutron powder diffraction study. *Acta Crystallogr. Sect. B Struct. Sci.* **63**, 675–682 (2007).

27. Palacios, L. *et al.* Crystal Structures and in-Situ Formation Study of Mayenite Electrides. *Inorg. Chem.* **46**, 409–416 (2007).

28. Graulis, S. *et al.* Crystallography Open Database - An open-access collection of crystal structures. *J. Appl. Crystallogr.* **42**, 726–729 (2009).

29. Gates-Rector, S. & Blanton, T. The Powder Diffraction File: a quality materials characterization database. *Powder Diffr.* **34**, 352–360 (2019).

30. Lacerda, M., Irvine, J. T. S., Glasser, F. P. & West, A. R. High oxide ion conductivity in $Ca_{12}Al_{14}O_{33}$. *Nature* **332**, 525–526 (1988).

31. Irvine, J. T. S., Lacerda, M. & West, A. R. Oxide ion conductivity in $Ca_{12}Al_{14}O_{33}$. *Mater. Res. Bull.* **23**, 1033–1038 (1988).

32. Hayashi, K., Matsuishi, S., Kamiya, T., Hirano, M. & Hosono, H. Light-induced conversion of an insulating refractory oxide into a persistent electronic conductor. *Nature* **419**, 462–465 (2002).

33. Matsuishi, S. *et al.* High-Density Electron Anions in a Nanoporous Single Crystal: $[Ca_{24}Al_{28}O_{64}]^{4+}(4e^-)$. *Science (80-.).* **301**, 626–629 (2003).

34. Dong, Y., Hosono, H. & Hayashi, K. Formation and quantification of peroxide anions in nanocages of $12CaO{\cdot}7Al_2O_3$. *RSC Adv.* **3**, 18311 (2013).

35. Hayashi, K., Hirano, M. & Hosono, H. Thermodynamics and Kinetics of Hydroxide Ion Formation in $12CaO{\cdot}7Al_2O_3$. *J. Phys. Chem. B* **109**, 11900–11906 (2005).

36. Li, J. *et al.* High Density Hydroxyl Anions in a Microporous Crystal: $[Ca_{24}Al_{28}O_{64}]^{4+}{\cdot}4(OH^-)$. *Chem. Mater.* **17**, 2771–2774 (2005).

37. Matsuishi, S., Hayashi, K., Hirano, M. & Hosono, H. Hydride ion as photoelectron donor in microporous crystal. *J. Am. Chem. Soc.* **127**, 12454–12455 (2005).

38. Salasin, J. R. & Rawn, C. Structure property relationships and cationic doping in [Ca24Al28O64]4+ framework: A review. *Crystals* **7**, 1–25 (2017).

39. Jiang, D., Zhao, Z., Mu, S., Phaneuf, V. & Tong, J. Simple and Efficient Fabrication of Mayenite Electrides from a Solution-Derived Precursor. *Inorg. Chem.* **56**, 11702–11709 (2017).

40. Chung, J. H., Ryu, J. H., Eun, J. W., Choi, B. G. & Shim, K. B. One-Step Synthesis of a $12CaO{\cdot}7Al_2O_3$ Electride via the Spark Plasma Sintering (SPS) Method. *Electrochem. Solid-State Lett.* **14**, E41 (2011).

41. Khan, K. *et al.* A comprehensive review on synthesis of pristine and doped inorganic room temperature stable mayenite electride, [Ca 24 Al 28 O 64] 4+ (e −) 4 and its applications as a catalyst. *Prog. Solid State Chem.* **54**, 1–19 (2019).

42. Kitano, M. *et al.* Ammonia synthesis using a stable electride as an electron donor and reversible hydrogen store. *Nat. Chem.* **4**, 934–940 (2012).

43. Sato, K. *et al.* Reactivity of superoxide ions (O_2^-) occluded in micropores of calcium aluminosilicate varied via substitution with transition metal ions. *Stud. Surf. Sci. Catal.* **158**, 2001–2008 (2005).

44. Sato, K., Yamaguchi, M., Fujita, S., Suzuki, K. & Mori, T. Enhancement of the activity of calcium aluminosilicate ($Ca_{12}Al_{10}Si_4O_{35}$) for the combustion of diesel soot via the substitution of Ca^{2+} ions with transition metal ions. *Catal. Commun.* **7**, 132–135 (2006).

45. Maurelli, S. *et al.* Spectroscopic CW-EPR and HYSCORE investigations of Cu^{2+-} and O_2^- species in copper doped nanoporous calcium aluminate ($12CaO{\cdot}7Al_2O_3$). *Phys. Chem. Chem. Phys.* **12**, 10933–10941 (2010).

46. Huang, J., Valenzano, L. & Sant, G. Framework and Channel Modifications in Mayenite ($12CaO{\cdot}7Al_2O_3$) Nanocages by Cationic Doping. *Chem. Mater.* **27**, 4731–4741 (2015).

47. Palacios, L., Bruque, S. & Aranda, M. A. G. Structure of gallium-doped mayenite and its reduction behaviour. *Phys. Status Solidi Basic Res.* **245**, 666–672 (2008).

48. Yang, Z., Zhao, Z., Shi, Y. & Wang, Y. A novel red phosphor $Ca_{12}Al_{14}O_{32}$:Eu^{3+} for near UV white light-emitting diodes. *Mater. Res. Bull.* **48**, 4048–4050 (2013).

49. Tõldsepp, E. *et al.* Synthesis and luminescence properties of Ce3+ doped nanoporous 12CaO??7Al2O3 powders and ceramics. *Opt. Mater. (Amst).* **32**, 784–788 (2010).

50. Hosono, H., Hayashi, K. & Hirano, M. Active anion manipulation for emergence of active functions in the nanoporous crystal $12CaO{\cdot}7Al_2O_3$: A case study of abundant element strategy. *J. Mater. Sci.* **42**, 1872–1883 (2007).

51. Fujita, S. *et al.* Oxidative destruction of hydrocarbons on a new zeolite-like crystal of $Ca_{12}Al_{10}Si_4O_{35}$ including O_2^- and O_2^{2-} radicals. *Chem. Mater.* **15**, 255–263 (2003).

52. Ruszak, M. *et al.* Selective N_2O removal from the process gas of nitric acid plants over ceramic $12CaO{\cdot}7Al_2O_3$ catalyst. *Catal. Letters* **126**, 72–77 (2008).

53. Meza-Trujillo, I., Devred, F. & Gaigneaux, E. M. Production of high surface area mayenite (C12A7) via an assisted solution combustion synthesis (SCS) toward catalytic soot oxidation. *Mater. Res. Bull.* **119**, 110542 (2019).

54. Meza-Trujillo, I., Mary, A., Pietrzyk, P., Sojka, Z. & Gaigneaux, E. M. Nature and role of Cu(II) species in doped C12A7 catalysts for soot oxidation. *Appl. Catal. B Environ.* **316**, 121604 (2022).

55. Cucciniello, R. *et al.* Total oxidation of trichloroethylene over mayenite ($Ca_{12}Al_{14}O_{33}$) catalyst. *Appl. Catal. B Environ.* **204**, 167–172 (2017).

56. Intiso, A. *et al.* A Novel Synthetic Route to Prepare High Surface Area Mayenite Catalyst for TCE Oxidation. *Catalysts* **9**, 27 (2019).

57. Intiso, A., Rossi, F., Proto, A. & Cucciniello, R. The fascinating world of mayenite ($Ca_{12}Al_{14}O_{33}$) and its derivatives. *Rend. Lincei* **32**, 699–708 (2021).

58. Fujita, S., Nakano, H., Suzuki, K., Mori, T. & Masuda, H. Oxidative destruction of hydrocarbons on $Ca_{12}Al_{14-x}Si_xO_{33+0.5x}$ ($0 \leq x \leq 4$) with radical oxygen occluded in nanopores. *Catal. Letters* **106**, 139–143 (2006).

59. Lemonidou, A. A. & Vasalos, I. A. Preparation and evaluation of catalysts for the production of ethylene via steam cracking. Effect of

Operating Conditions on the Performance of 12CaO-7Al_2O_3 Catalyst. *Appl. Catal.* **54**, 119–138 (1989).

60. Pant, K. K. & Kunzru, D. Catalytic Pyrolysis of n-Heptane: Kinetics and Modeling. *Ind. Eng. Chem. Res.* **36**, 2059–2065 (1997).

61. Wu, H. *et al.* CO2 methanation over Ru/12CaO·7Al2O3 catalysts: Effect of encaged anions on catalytic mechanism. *Appl. Catal. A Gen.* **595**, 117474 (2020).

62. Li, C., Hirabayashi, D. & Suzuki, K. A crucial role of O2- and O22- on mayenite structure for biomass tar steam reforming over Ni/Ca12Al14O33. *Appl. Catal. B Environ.* **88**, 351–360 (2009).

63. Yang, S. *et al.* Partial oxidation of methane to syngas over promoted C12A7. *Appl. Catal. A Gen.* **277**, 239–246 (2004).

64. Li, J. *et al.* Chlorine-Tolerant Ruthenium Catalyst Derived Using the Unique Anion-Exchange Properties of 12CaO·7Al_2O_3 for Ammonia Synthesis. *ChemCatChem* **9**, 3078–3083 (2017).

65. Vagia, E. C. & Lemonidou, A. A. Hydrogen production via steam reforming of bio-oil components over calcium aluminate supported nickel and noble metal catalysts. *Appl. Catal. A Gen.* **351**, 111–121 (2008).

66. Inoue, Y. *et al.* Direct Activation of Cobalt Catalyst by 12CaO·7Al2O3 Electride for Ammonia Synthesis. *ACS Catal.* **9**, 1670–1679 (2019).

67. Zhang, Z., Kong, Z., Liu, H. & Chen, Y. Mayenite supported perovskite monoliths for catalytic combustion of methyl methacrylate. *Front. Chem. Sci. Eng.* **8**, 87–94 (2014).

68. Somekawa, S., Yanagi, S., Yamanaka, T. & Hayashi, H. Preparation of Ni/12CaO·7Al2O3 honeycomb-type catalyst for continuous production of hydrogen by methane decomposition. *Inorg. Chem. Commun.* **140**, 10–13 (2022).

69. Che, M. & Tench, A. J. Characterization and Reactivity of Molecular Oxygen Species on Oxide Surfaces. *Adv. Catal.* **32**, 1–148 (1983).

70. Hayashi, K., Ueda, N., Hirano, M. & Hosono, H. Effect of stability and diffusivity of extra-framework oxygen species on the formation of oxygen radicals in 12CaO-7Al2O3. *Solid State Ionics* **173**, 89–94 (2004).

71. Sushko, P. V., Shluger, A. L., Hayashi, K., Hirano, M. & Hosono, H. Mechanisms of oxygen ion diffusion in a nanoporous complex oxide $12CaO{\cdot}7Al_2O_3$. *Phys. Rev. B* **73**, 014101 (2006).

72. Hosono, H., Hayashi, K., Kajihara, K., Sushko, P. V. & Shluger, A. L. Oxygen ion conduction in $12CaO{\cdot}7Al_2O_3$: O^{2-} conduction mechanism and possibility of O^- fast conduction. *Solid State Ionics* **180**, 550–555 (2009).

73. Inoue, Y. *et al.* Highly Dispersed Ru on Electride $[Ca_{24}Al_{28}O_{64}]^{4+}(e^-)_4$ as a Catalyst for Ammonia Synthesis. *ACS Catal.* **4**, 674–680 (2014).

74. Ude, S. N. *et al.* High temperature X-ray studies of mayenite synthesized using the citrate sol-gel method. *Ceram. Int.* **40**, 1117–1123 (2014).

75. Gong, L. *et al.* Synthesis and characteristics of the C12A7-O^- nanoparticles by citric acid sol-gel combustion method. *Mater. Lett.* **64**, 1322–1324 (2010).

76. Rashad, M. M., Mostafa, A. G., Mwakikunga, B. W. & Rayan, D. A. Tunable optical properties of some rare earth elements-doped mayenite Ca12Al14O33 nanopowders elaborated by oxalate precursor route. *Appl. Phys. A Mater. Sci. Process.* **123**, 1–7 (2017).

77. Rashad, M. M., Mostafa, A. G. & Rayan, D. A. Structural and optical properties of nanocrystalline mayenite $Ca_{12}Al_{14}O_{33}$ powders synthesized using a novel route. *J. Mater. Sci. Mater. Electron.* **27**, 2614–2623 (2016).

78. Raab, B. & Poellmann, H. Heat flow calorimetry and SEM investigations to characterize the hydration at different temperatures of different $12CaO{\cdot}7Al_2O_3$ (C12A7) samples synthesized by solid state reaction, polymer precursor process and glycine nitrate process. *Thermochim. Acta* **513**, 106–111 (2011).

79. Ozawa, K., Sakamoto, N., Wakiya, N. & Suzuki, H. Fabrication of $12CaO{\cdot}7Al_2O_3$ powders with high specific surface area by sol – gel and ball-milling method. *J. Ceram. Soc. Japan* **119**, 480–463 (2011).

80. Li, C., Hirabayashi, D. & Suzuki, K. Synthesis of higher surface area mayenite by hydrothermal method. *Mater. Res. Bull.* **46**, 1307–1310 (2011).

81. Fujita, S., Suzuki, K. & Mori, T. Preparation of high-performance Co3O4catalyst for hydrocarbon combustion from Co-containing hydrogarnet. *Catal. Letters* **86**, 139–144 (2003).

82. Fujita, S. *et al.* Controlling the Quantity of Radical Oxygen Occluded in a New Aluminum Silicate with Nanopores. *Chem. Mater.* **15**, 4879–4881 (2003).

83. Fujita, S., Suzuki, K., Mori, T. & Masuda, H. Preparation of aluminum silicate, $Ca_{12}Al_{10}Si_4O_{35}$, using waste materials and its activity for combustion of hydrocarbons. *J. Eur. Ceram. Soc.* **25**, 3479–3484 (2005).

84. Intiso, A., Martinez-Triguero, J., Cucciniello, R., Rossi, F. & Palomares, A. E. Influence of the synthesis method on the catalytic activity of mayenite for the oxidation of gas-phase trichloroethylene. *Sci. Rep.* **9**, 1–9 (2019).

85. Hasegawa, G. *et al.* Topotactic Synthesis of Mesoporous $12CaO{\cdot}7Al_2O_3$ Mesocrystalline Microcubes toward Catalytic Ammonia Synthesis. *Chem. Mater.* **30**, 4498–4502 (2018).

86. Farin, B., Monteverde V., A. H. A., Specchia, S. & Gaigneaux, E. M. Bismuth molybdates prepared by solution combustion synthesis for the partial oxidation of propene. *Catal. Today* **257**, 11–17 (2015).

87. Varma, A., Mukasyan, A. S., Rogachev, A. S. & Manukyan, K. V. Solution Combustion Synthesis of Nanoscale Materials. *Chem. Rev.* **116**, 14493–14586 (2016).

88. Matović, B. *et al.* Synthesis and densification of single-phase mayenite (C12A7). *J. Eur. Ceram. Soc.* **36**, 4237–4241 (2016).

89. Fumo, D. a., Morelli, M. R. & Segadães, A. M. Combustion synthesis of calcium aluminates. *Mater. Res. Bull.* **31**, 1243–1255 (1996).

90. Tas, A. C. Chemical Preparation of the Binary Compounds in the Calcia–Alumina System by Self-Propagating Combustion Synthesis. *J. Am. Ceram. Soc.* **81**, 2853–2863 (1998).

91. Mukasyan, A. S. & Dinka, P. Novel approaches to solution-combustion synthesis of nanomaterials. *Int. J. Self-Propagating High-Temperature Synth.* **16**, 23–35 (2007).

92. Ianoş, R., Lazău, I., Păcurariu, C. & Barvinschi, P. Fuel mixture approach for solution combustion synthesis of $Ca_3Al_2O_6$ powders. *Cem. Concr. Res.* **39**, 566–572 (2009).

93. Kingsley, J. J., Suresh, K. & Patil, K. C. Combustion synthesis of fine-particle metal aluminates. *J. Mater. Sci.* **25**, 1305–1312 (1990).

94. Patil, K., Aruna, S. T. & Ekambaram, S. Combustion synthesis. *Curr. Opin. Solid State Mater. Sci.* **2**, 158–165 (1997).

95. Wen, W. & Wu, J. Nanomaterials via solution combustion synthesis: a step nearer to controllability. *RSC Adv.* **4**, 58090–58100 (2014).

96. Deshpande, K., Mukasyan, A. & Varma, A. Direct Synthesis of Iron Oxide Nanopowders by the Combustion Approach : Reaction Mechanism and Properties. *Chem. Mater.* **16**, 4896–4904 (2004).

97. Peng, R. *et al.* Tailoring the stability of Ni-Fe/mayenite in methane – Carbon dioxide reforming. *Fuel* **284**, 118909 (2021).

98. Fujita, S. *et al.* Oxidative destruction of hydrocarbons on a new zeolite-like crystal of Ca12Al10Si4O35 including O2- and O22- radicals. *Chem. Mater.* **15**, 255–263 (2003).

99. Kitano, M. *et al.* Ammonia synthesis using a stable electride as an electron donor and reversible hydrogen store. *Nat. Chem.* **4**, 934–940 (2012).

100. Pant, K. K. & Kunzru, D. Catalytic pyrolysis of methylcyclohexane: kinetics and modeling. *Chem. Eng. J.* **70**, 47–54 (1998).

101. Schmid, T. & Dariz, P. Shedding light onto the spectra of lime: Raman and luminescence bands of CaO, $Ca(OH)_2$ and $CaCO_3$. *J. Raman Spectrosc.* **46**, 141–146 (2014).

102. Kajihara, K., Matsuishi, S., Hayashi, K., Hirano, M. & and Hideo Hosono. Vibrational Dynamics and Oxygen Diffusion in a Nanoporous Oxide Ion Conductor $12CaO{\cdot}7Al_2O_3$ Studied by ^{18}O Labeling and Micro-Raman Spectroscopy. *J. Phys. Chem. C* **111**, 14855–14861 (2007).

103. Ruszak, M., Witkowski, S. & Sojka, Z. EPR and Raman investigations into anionic redox chemistry of nanoporous $12CaO{\cdot}7Al_2O_3$ interacting with O_2, H_2 and N_2O. *Res. Chem. Intermed.* **33**, 689–703 (2007).

104. Spalek, T., Pietrzyk, P. & Sojka, Z. Program EPRsim32. *J. Chem. Ifn. Model* **45**, 18–29 (2005).

105. Bueno-López, A., Krishna, K., Makkee, M. & Moulijn, J. A. Active oxygen from CeO2 and its role in catalysed soot oxidation. *Catal. Letters* **99**, 203–205 (2005).

106. Bueno-López, A. Diesel soot combustion ceria catalysts. *Appl. Catal.*

B Environ. **146**, 1–11 (2014).

107. Ianoş, R., Bosca, M. & Lazău, R. Fine tuning of $CoFe_2O_4$ properties prepared by solution combustion synthesis. *Ceram. Int.* **40**, 10223–10229 (2014).

108. Jain, S. R. Energetics of Propellants, Fuels and Explosives; a chemical valence approach. *Propellants Explos.* **12**, 188–195 (1987).

109. González-Cortés, S. L. & Imbert, F. E. Fundamentals, properties and applications of solid catalysts prepared by solution combustion synthesis (SCS). *Appl. Catal. A Gen.* **452**, 117–131 (2013).

110. Roine, A. HSC Chemistry 5.1. (2002).

111. Barin, I., Knacke, O. & Kubaschewski, O. *Thermochemical properties of inorganic substances*. *Thermochemical properties of inorganic substances (Supplement)* (Ssprnger-Verlag Berlin Heidelberg GmbH, 1977).

112. Sandler, S. I. *Chemical, Biochemical, and Engineering Thermodynamics*. *October* **158**, (Wiley, 2017).

113. Rodríguez-Carvajal, J. Recent advances in magnetic structure determination by neutron powder diffraction. *Phys. B Condens. Matter* **192**, 55–69 (1993).

114. Biamino, S. & Badini, C. Combustion synthesis of lanthanum chromite starting from water solutions: Investigation of process mechanism by DTA-TGA-MS. *J. Eur. Ceram. Soc.* **24**, 3021–3034 (2004).

115. Pacewska, B. & Keshr, M. Thermal transformations of aluminium nitrate hydrate. *Thermochim. Acta* **385**, 73–80 (2002).

116. Hallstedt, B. Assessment of the CaO-Al_2O_3 System. *J. Am. Ceram. Soc.* **73**, 15–23 (1990).

117. Civera, A., Pavese, M., Saracco, G. & Specchia, V. Combustion synthesis of perovskite-type catalysts for natural gas combustion. *Catal. Today* **83**, 199–211 (2003).

118. Specchia, S., Galletti, C. & Specchia, V. Solution Combustion Synthesis as intriguing technique to quickly produce performing catalysts for specific applications. in *Studies in Surface Science and Catalysis* **175**, 59–67 (2010).

119. Fischer, R. & Kuzel, H. J. Reinvestigation of the system $C_4A{\cdot}nH2O$-$C_4A{\cdot}CO_2{\cdot}nH_2O$. *Cem. Concr. Res.* **12**, 517–526 (1982).

120. François, M., Renaudin, G. & Evrard, O. A cementitious compound with composition $3CaO{\cdot}Al_2O_3{\cdot}CaCO_3{\cdot}11H_2O$. *Acta Crystallogr. Sect. C Cryst. Struct. Commun.* **54**, 1214–1217 (1998).

121. Thommes, M. *et al.* Physisorption of gases, with special reference to the evaluation of surface area and pore size distribution (IUPAC Technical Report). *Pure Appl. Chem.* **87**, 1051–1069 (2015).

122. Groen, J. C., Peffer, L. A. A. & Pérez-Ramírez, J. Pore size determination in modified micro- and mesoporous materials. Pitfalls and limitations in gas adsorption data analysis. *Microporous Mesoporous Mater.* **60**, 1–17 (2003).

123. Hayashi, K. *et al.* Nanoporous crystal $12CaO{\cdot}7Al_2O_3$: A playground for studies of ultraviolet optical absorption of negative ions. *J. Phys. Chem. B* **111**, 1946–1956 (2007).

124. McMillan, P. & Piriou, B. Raman spectroscopy of calcium aluminate glasses and crystals. *J. Non. Cryst. Solids* **55**, 221–242 (1983).

125. Środek, D., Dulski, M. & Galuskina, I. Raman imaging as a new approach to identification of the mayenite group minerals. *Sci. Rep.* **8**, 1–14 (2018).

126. Galuskin, E. V. *et al.* Mayenite supergroup, part III: Fluormayenite, $Ca_{12}Al_{14}O_{32}$ $[\square_4F_2]$, and Fluorkyuygenite, $Ca_{12}Al_{14}O_{32}[(H_2O)_4F_2]$, two new minerals from py. *Eur. J. Mineral.* **27**, 123–136 (2015).

127. Dulski, M. *et al.* Different route of hydroxide incorporation and thermal stability of new type of water clathrate: X-ray single crystal and Raman investigation. *Sci. Rep.* **7**, 1–9 (2017).

128. Pradhan, A. R. *et al.* EPR and NMR studies of coke induced selectivation over H-ZSM-5 zeolite during ethylbenzene disproportionation reaction. *J. Catal.* **184**, 29–38 (1999).

129. Fino, D., Bensaid, S., Piumetti, M. & Russo, N. A review on the catalytic combustion of soot in Diesel particulate filters for automotive applications: From powder catalysts to structured reactors. *Appl. Catal. A Gen.* **509**, 75–96 (2016).

130. Alcalde-Santiago, V., Davó-Quiñonero, A., Bailón-García, E., Lozano-Castelló, D. & Bueno-López, A. Copper-Lanthanum Catalysts for NOx

and Soot Removal. *ChemCatChem* **12**, 6375–6384 (2020).

131. Debbichi, L., Marco De Lucas, M. C., Pierson, J. F. & Krüger, P. Vibrational properties of CuO and Cu 4O 3 from first-principles calculations, and raman and infrared spectroscopy. *J. Phys. Chem. C* **116**, 10232–10237 (2012).

132. Biesinger, M. C. Advanced analysis of copper X-ray photoelectron spectra. *Surf. Interface Anal.* **49**, 1325–1334 (2017).

133. Martínez-Arias, A., Fernández-García, M., Soria, J. & Conesa, J. C. Spectroscopic study of a Cu/CeO2 catalyst subjected to redox treatments in carbon monoxide and oxygen. *J. Catal.* **182**, 367–377 (1999).

134. Giamello, E., Fubini, B., Lauro, P. & Giuria, V. P. Investigation on the State of Copper. *Appl. Catal.* **21**, 133–147 (1986).

135. Harrison, P. G., Ball, I. K., Azelee, W., Daniell, W. & Goldfarb, D. Nature and surface redox properties of copper(II)-promoted cerium(IV) oxide CO-oxidation catalysts. *Chem. Mater.* **12**, 3715–3725 (2000).

136. Martínez-Arias, A., Cataluña, R., Conesa, J. C. & Soria, J. Effect of copper-ceria interactions on copper reduction in a Cu/CeO2/Al2O3 catalyst subjected to thermal treatments in CO. *J. Phys. Chem. B* **102**, 809–817 (1998).

137. Feng, X. *et al.* Stable CuO/La2Sn2O7 catalysts for soot combustion: Study on the monolayer dispersion behavior of CuO over a La2Sn2O7 pyrochlore support. *Chinese J. Catal.* **42**, 396–408 (2021).

138. Sakai, M., Nagai, Y., Aoki, Y. & Takahashi, N. Investigation into the catalytic reduction of NOx at copper-ceria interface active sites. *Appl. Catal. A Gen.* **510**, 57–63 (2016).

139. Sun Park, C. *et al.* Promoting effect of H2O over macroporous Ce-Zr catalysts in soot oxidation. *Mol. Catal.* **474**, 110416 (2019).

140. Christensen, J. M., Grunwaldt, J. D. & Jensen, A. D. Effect of NO2 and water on the catalytic oxidation of soot. *Appl. Catal. B Environ.* **205**, 182–188 (2017).

141. Yang, W. *et al.* Water accelerates and directly participates soot oxidation: An isotopic study. *Appl. Catal. B Environ.* **302**, 120837 (2022).

142. Atanga, M. A., Rezaei, F., Jawad, A., Fitch, M. & Rownaghi, A. A. Oxidative dehydrogenation of propane to propylene with carbon dioxide. *Appl. Catal. B Environ.* **220**, 429–445 (2018).

143. Toda, Y. *et al.* Activation and splitting of carbon dioxide on the surface of an inorganic electride material. *Nat. Commun.* **4**, 1–8 (2013).

144. Campos-Molina, M. J. *et al.* Base catalysts derived from hydrocalumite for the transesterification of sunflower oil. *Energy and Fuels* **24**, 979–984 (2010).

145. Kuwahara, Y. *et al.* Transesterifications using a hydrocalumite synthesized from waste slag: An economical and ecological route for biofuel production. *Catal. Sci. Technol.* **2**, 1842–1851 (2012).

146. Sánchez-Cantú, M. *et al.* Green synthesis of hydrocalumite-type compounds and their evaluation in the transesterification of castor bean oil and methanol. *Fuel* **110**, 23–31 (2013).

147. Nayebzadeh, H., Haghighi, M., Saghatoleslami, N., Tabasizadeh, M. & Binaeian, E. Influence of carbon source content on the structure and performance of KOH/Ca12Al14O33–C nanocatalyst used in the transesterification reaction via microwave irradiation. *J. Alloys Compd.* **743**, 672–681 (2018).

148. Nayebzadeh, H., Saghatoleslami, N. & Tabasizadeh, M. Optimization of the activity of KOH/calcium aluminate nanocatalyst for biodiesel production using response surface methodology. *J. Taiwan Inst. Chem. Eng.* **68**, 379–386 (2016).

APPENDICES

Appendix A

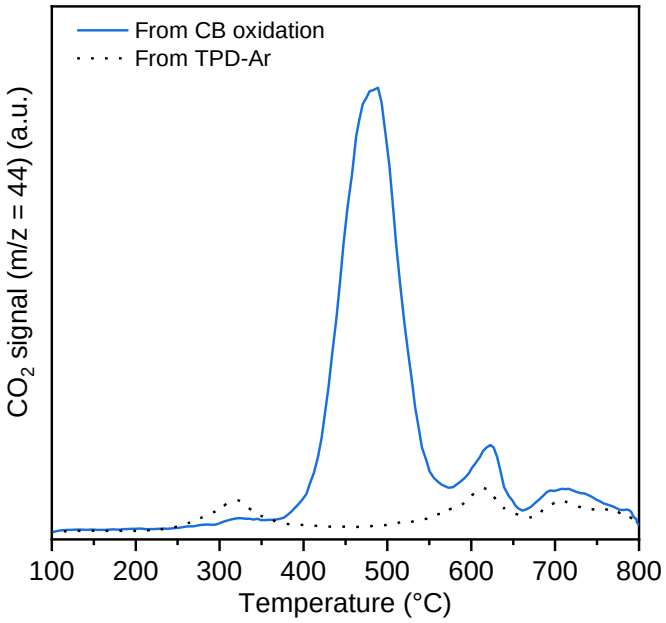

Figure A.1. Thermo-programmed curves for **P-600** sample. The solid blue line represents the CO_2 evolving from the CB oxidation under tight contact conditions (5%wt CB) This TPC curve is the same as the one shown in Figure 1.15a. The dotted black line denotes the CO_2 coming from a TPD test under flowing Ar without the presence of CB. The peaks over 600 °C evidence that the CO_2 production comes from the $CaCO_3$ contained in **P-600**.

Appendix B

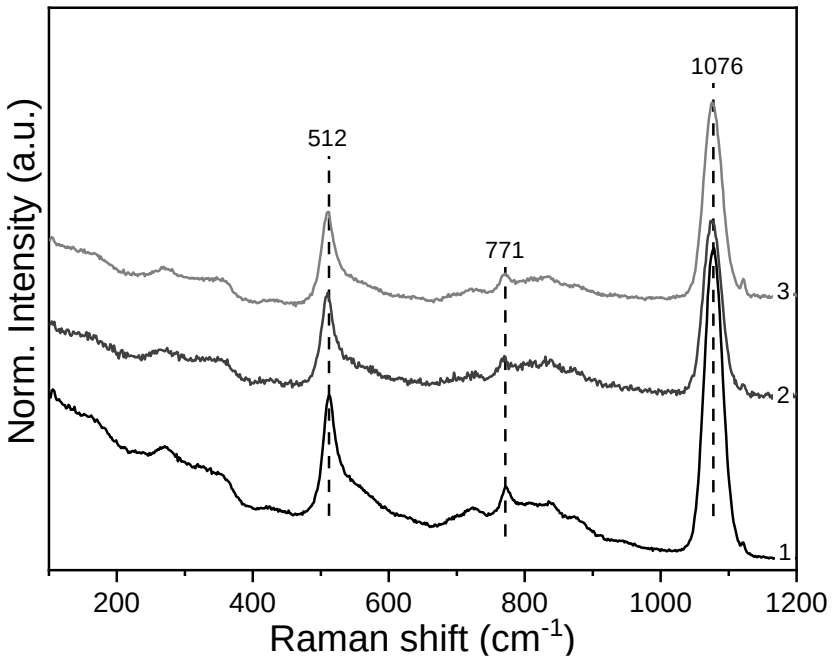

Figure B.1. Raman spectra of three porous C12A7 **(P-600-A)** obtained after calcination at 600 °C under static ambient air. Each spectrum corresponds to a different batch measured on distinct dates. The one at the bottom (spectrum 1) corresponds to the same one that is displayed in Figure 2.2 (Chapter II). The variation in the position for the main mode of C12A7 usually appearing at 520 cm^{-1} are instead displayed between 510-513 cm^{-1}.

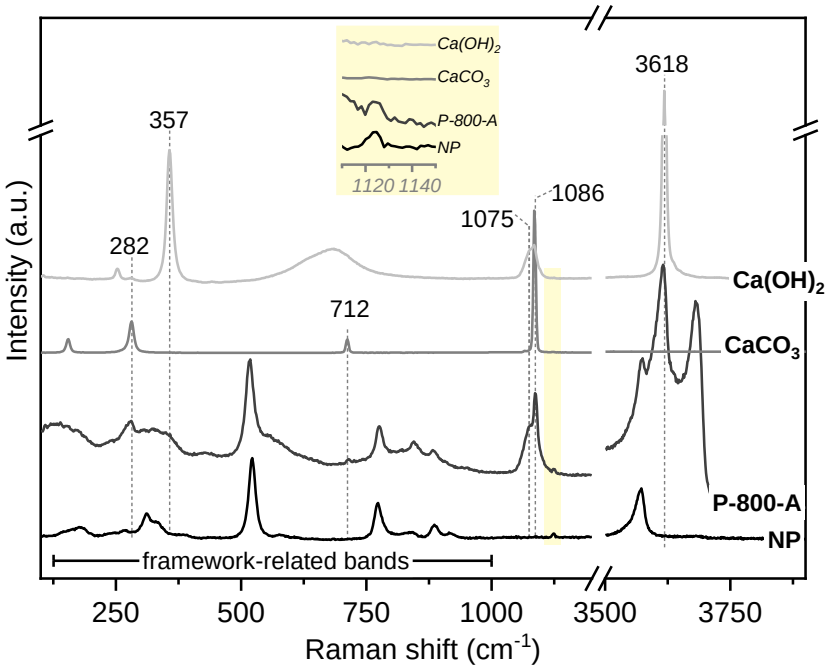

Figure B.2. Raman spectra of non-porous C12A7 **(NP)** as-synthesized after SCS (ϕ = 1; 500 °C) and porous C12A7 **(P-800-A)** obtained after calcination at 800 °C under static ambient air. Raman spectra of $Ca(OH)_2$ and $CaCO_3$ are shown for comparison. The yellow highlighted spectral region is depicted as a zoomed region (inset), which displays the band associated with the occurrence of superoxide anion (~1127 cm^{-1}; O_2^-). As shown, this band is only observed in the spectra of C12A7 samples but not in those from $Ca(OH)_2$ and $CaCO_3$.

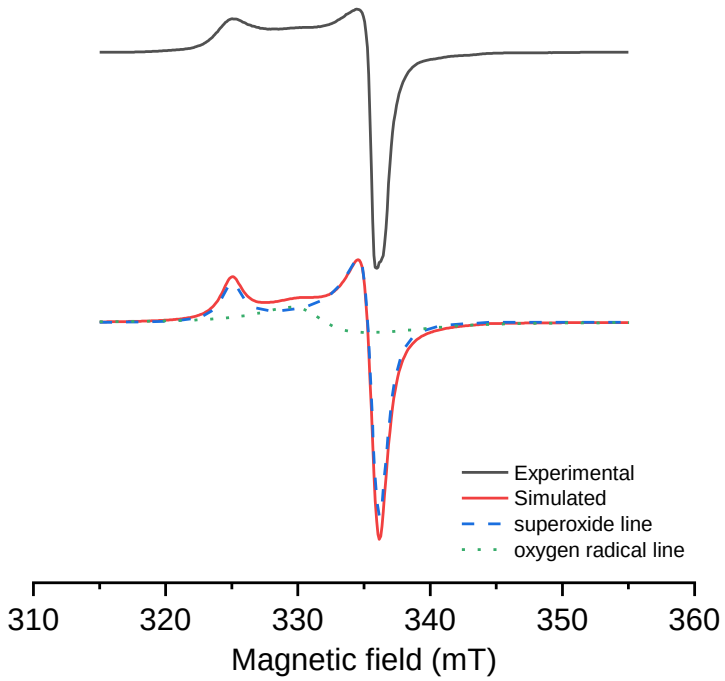

Figure B.3. EPR spectrum of **P-800-C** (above, solid black line). EPR spectrum of **P-800-C** obtained by computational simulation (below, red solid line), the superposed lines are those calculated powder patterns of O_2^- (blue dashed-line) and O^- (green dotted-line).

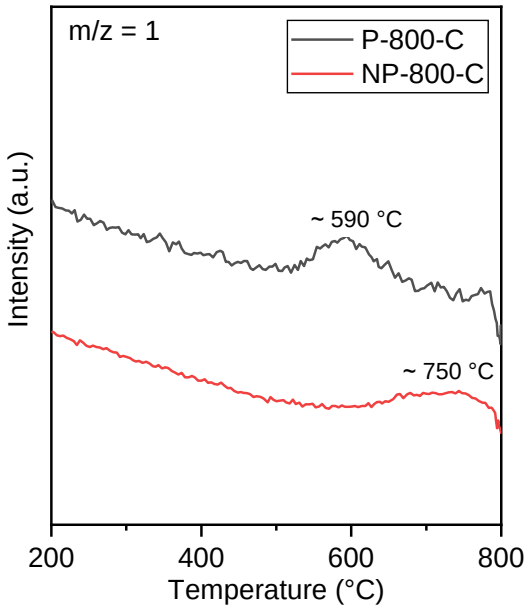

Figure B.4. TPR-H_2 analysis of **P-800-C** and **NP-800-C** samples. The samples were first heat-treated from 50 to 400 °C and held for 1h under Ar flow (50 mL·min^{-1}). After cooling down, the samples were exposed to 0.5% H_2/(N_2+Ar) flow (50 mL·min^{-1}) from 50 to 800 °C employing heating rate of 10 °C/min. The y-axis has been inverted to facilitate the peak visualization.

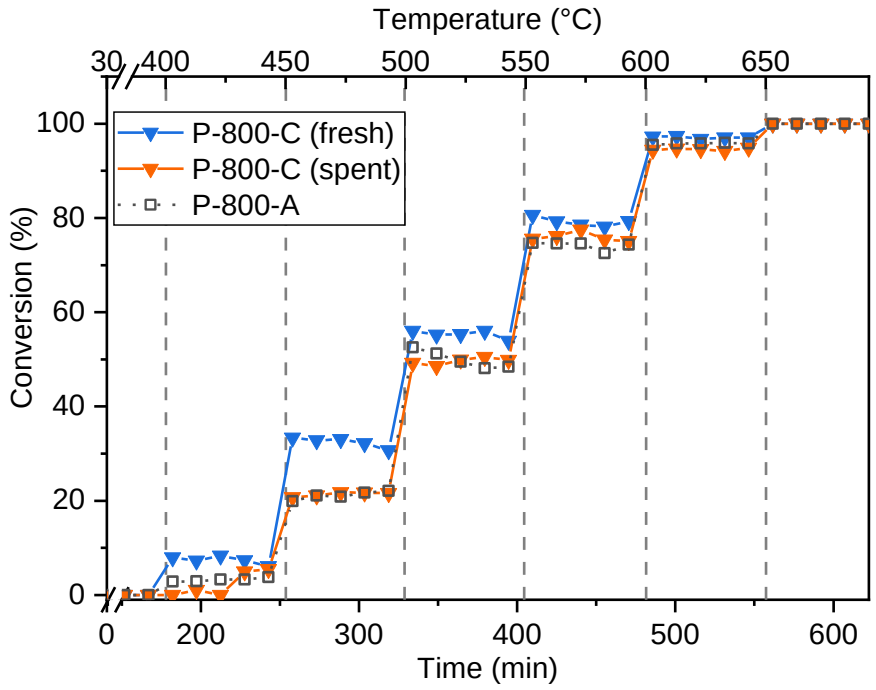

Figure B.5. Catalytic activity of **P-800-C** fresh (1st run) and spent (2nd run). **P-800-A** (C12A7 prepared under ambient static air) light-off curve is also depicted for comparison. Catalytic test conditions: total flow 40 mL·min^{-1} containing 1000 ppmv C_3H_8 balanced with synthetic dry air; 0.15 g of catalyst diluted with 0.35 g of SiO_2 chips.

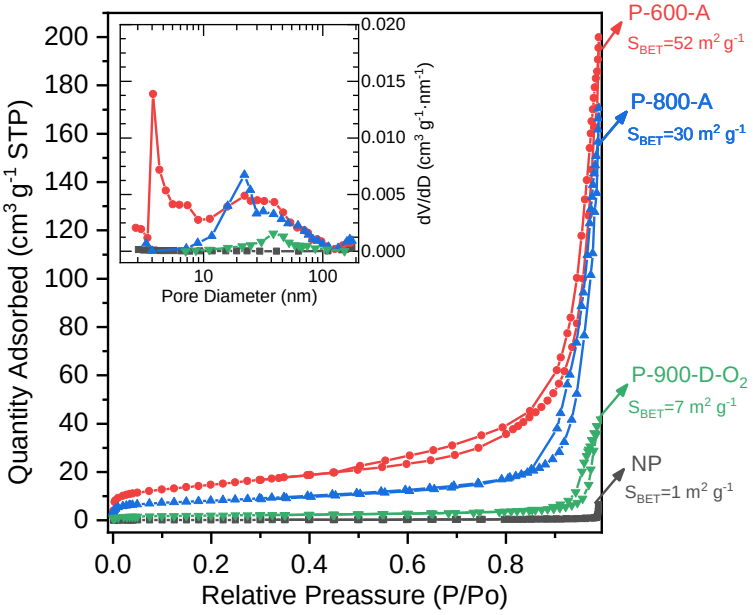

Figure B.6. N_2-physisorption isotherms of C12A7 materials produced at different conditions (referred to Chapter II for further details). PSDs plots (inset) were obtained by the BJH model using the desorption branch.

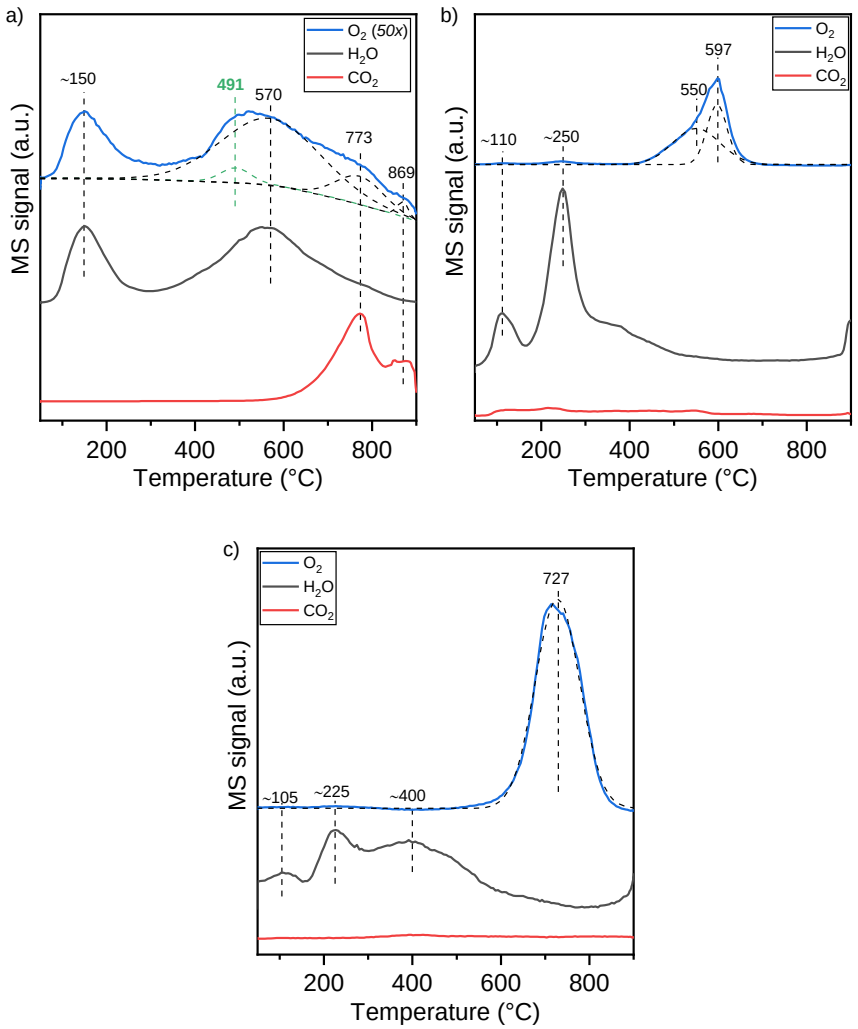

Figure B.7. Thermo-programmed desorption (TPD) curves of several mass-over-charge signals (O_2, H_2O and CO_2) obtained from samples prepared/post activated employing method D **a)** P-600-D-O_2, **b)** P-900-D-O_2, and **c)** NP-900-D-O_2. In the case of P-600-D-O_2, the O_2 signal was magnified (50x) to help its visualization regarding CO_2 and H_2O signals. The samples were heat-treated from 50 to 900 °C under Ar flow (50 mL·min^{-1}), employing a heating rate of 10 °C·min^{-1}.

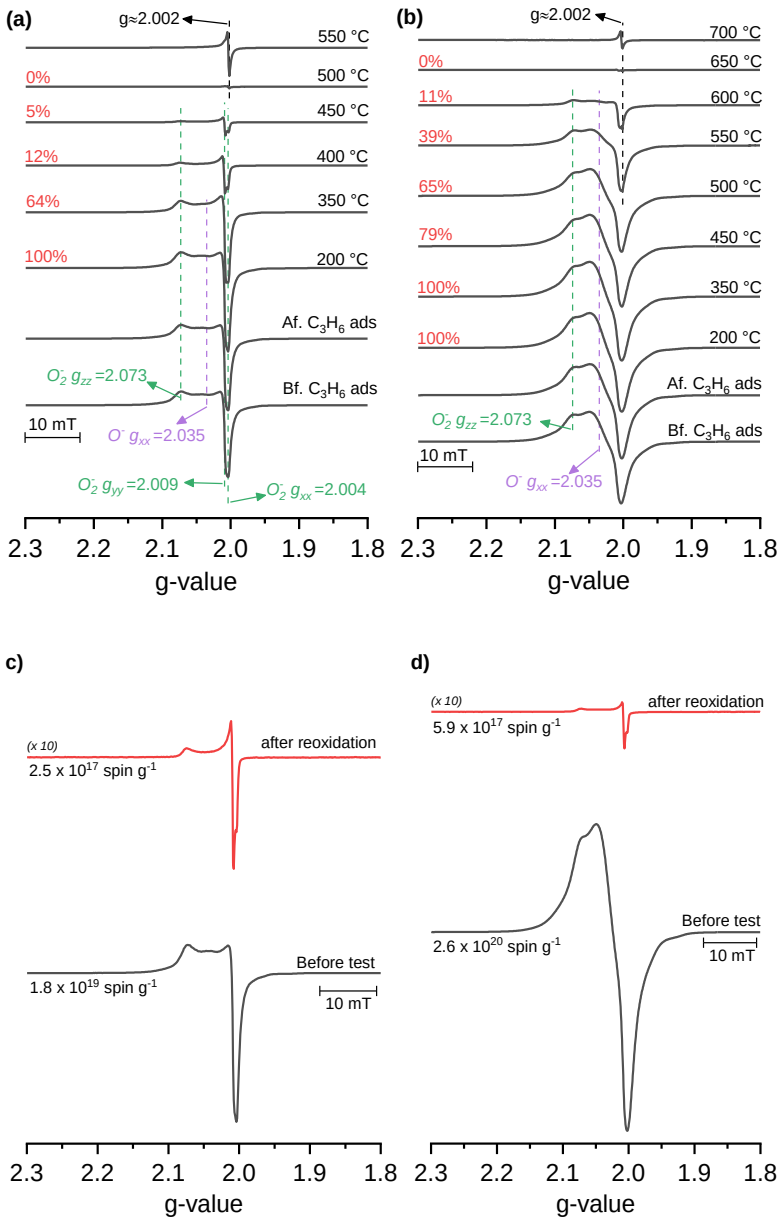

Figure B.8. Variation of EPR spectra of a) **P-600-D-O₂** and b) N**P-900-D-O₂** obtained at different temperatures during the anaerobic reactivity test (25 Torr C_3H_6). All the EPR spectra were collected at -196 °C. The EPR cell was sealed and kept isolated from the surrounding ambient atmosphere during the whole experiment. EPR spectra of **P-**c) **P-600-D-O₂** and d) N**P-900-D-O₂** before the reactivity test and after reoxidation with oxygen (140 Torr) at 600°C for 1h. The EPR spectrum after the reoxidation was magnified to facilitate its visualization. The total concentration of oxygen species is found beneath the spectra.

Appendix C

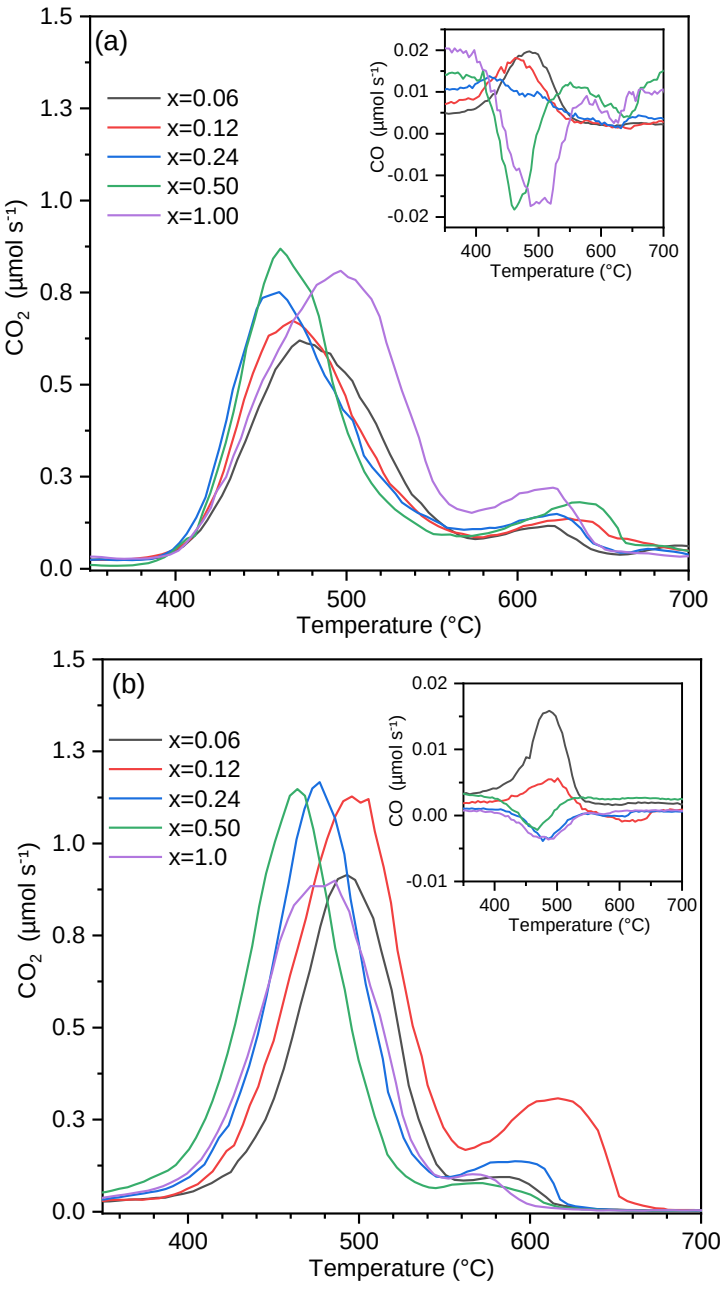

Figure C.1. TPC CO_x curves obtained from carbon black (CB, Printex-U) combustion experiments employing Cu-C12A7 catalysts calcined at a) 600, and b) 800 °C.

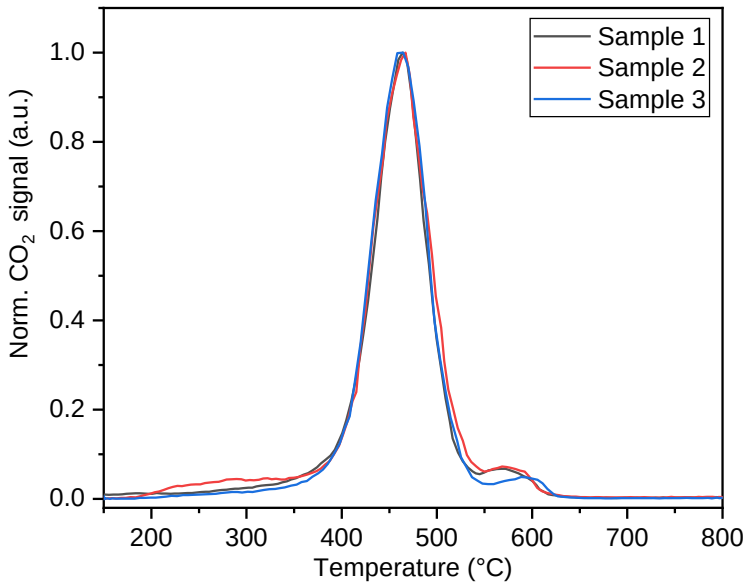

Figure C.2. Reproducibility test showing TPC CO_2 curves obtained from carbon black (CB, Printex-U) combustion employing Cu(0.50)-P-800. N=3

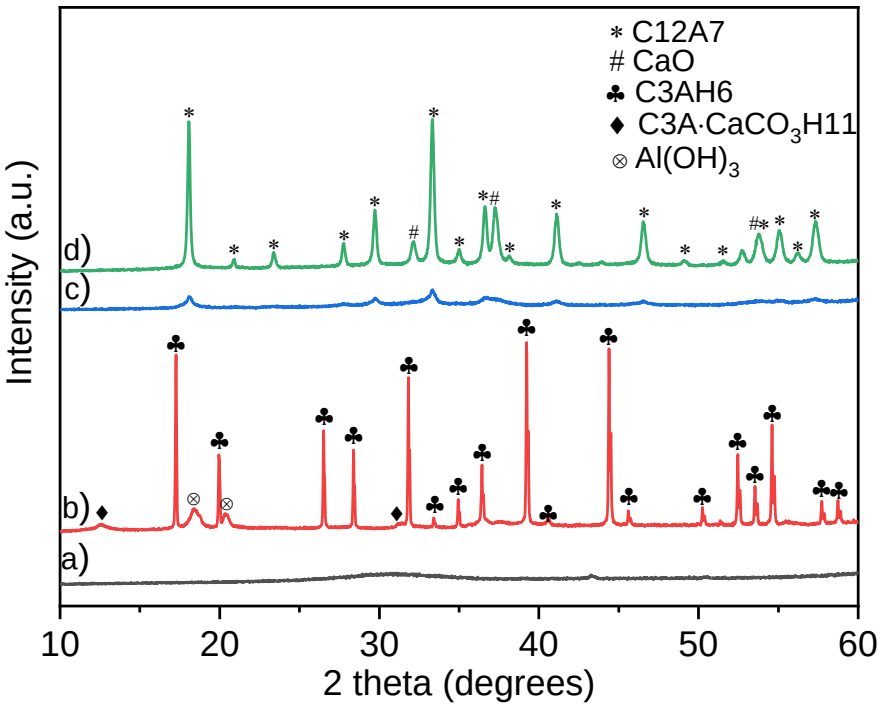

Figure C.3. PRXD patterns obtained from the solid powder during different consecutive stages of the synthesis protocol to prepare Cu(x)-P catalyst (x =0.24): a) solid powder obtained after the combustion reaction in a preheated furnace at 500 °C; b) as-dried precursor after hydration filtration and drying (120 °C overnight); and after subsequent calcination of the as-dried precursor for 4h at c) 600 or d) 800°C under ambient air.

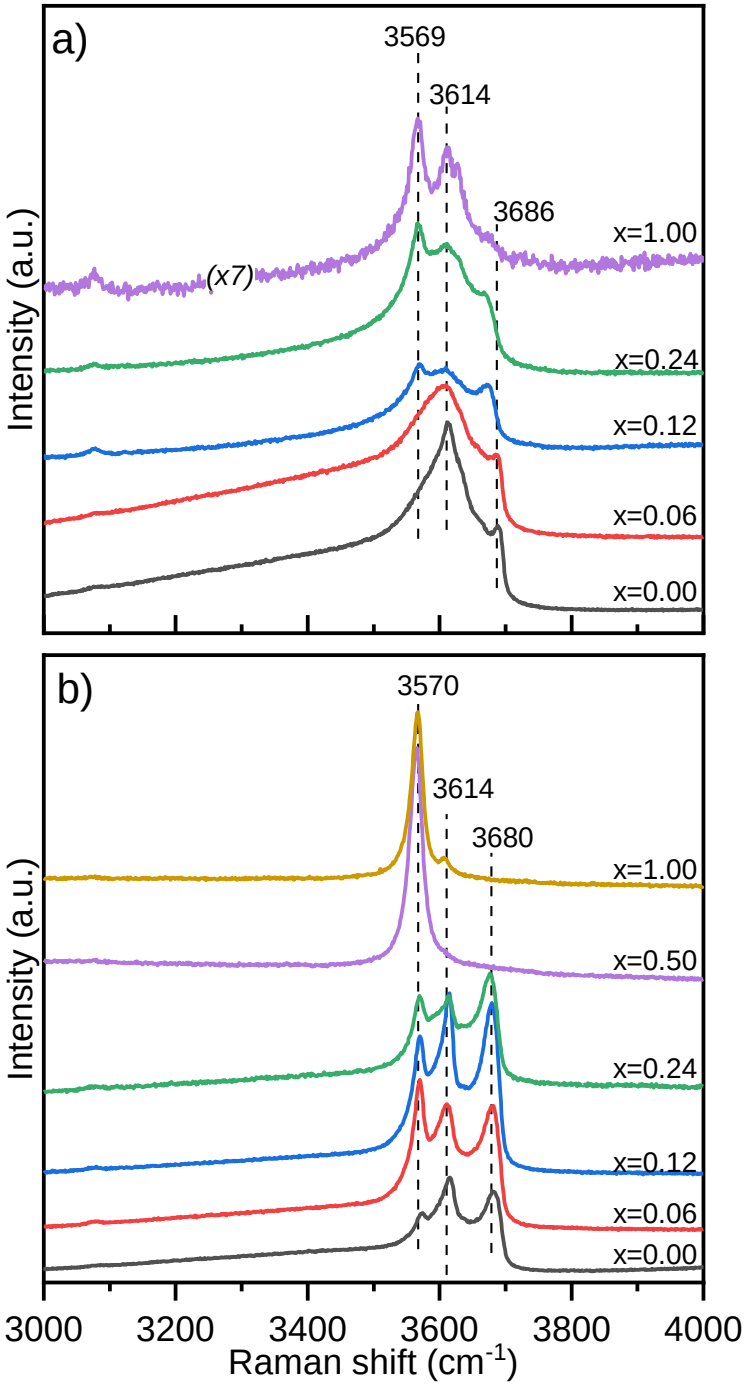

Figure C.4. Raman spectra in the high-frequency region of Cu-C12A7 catalysts series calcined at a) 600, and b) 800°C.

Table C.1. XPS surface elemental quantification

Catalyst	Cu at. %	Ca at. %	Al at. %	O at. %	C (of which carbonates) at. %
Cu(0.06)-P-600	0.1	8.2	19.5	50.0	22.2 (4.2)
Cu(0.12)-P-600	0.1	10.5	16.3	48.4	24.7 (5.6)
Cu(0.24)-P-600	0.2	9.9	16.2	45.6	28.1(5.6)
Cu(0.50)-P-600	0.4	10.8	14.6	48.3	25.8 (4.7)
Cu(1.00)-P-600	0.4	8.6	19.1	49.6	22.2 (3.2)
Cu(0.06)-P-800	0.1	10.0	14.2	51.7	24.1 (2.1)
Cu(0.12)-P-800	0.2	10.2	14.0	55.7	19.8 (2.4)
Cu(0.24)-P-800	0.4	11.0	13.5	54.5	20.5 (2.0)
Cu(0.50)-P-800	0.7	10.7	13.6	50.2	24.7 (1.8)
Cu(1.00)-P-800	0.7	9.2	17.5	44.4	28.3 (2.6)

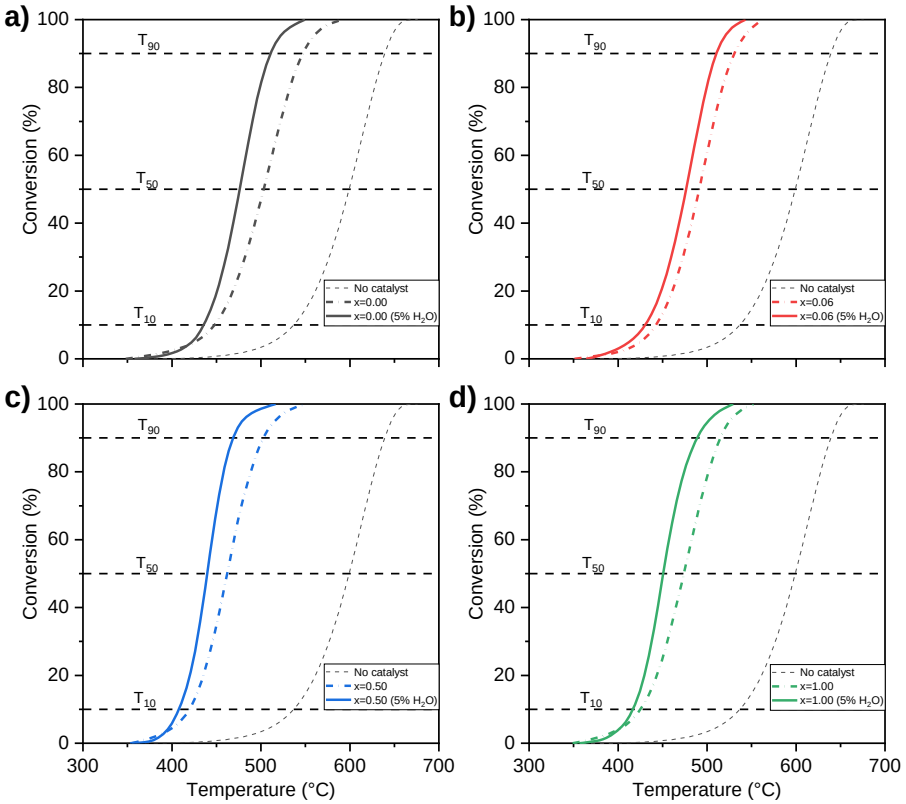

Figure C.5. Catalytic carbon black (CB) conversion profiles for a) bare P-800 (x = 0) and b-d) Cu(x)-P-800 catalysts under dry (dot-dashed lines) and wet conditions (solid lines). CB conversion profile without catalyst under dry conditions is also depicted for comparison (dashed line).

Articles

Scientific articles

- Meza-Trujillo, I., Devred, F., Gaigneaux, E.M., Production of high surface area mayenite (C12A7) via an assisted solution combustion synthesis (SCS) toward catalytic soot oxidation, *Mater. Res. Bull*. 119 (2019) 110542.
  DOI: https://doi.org/10.1016/j.materresbull.2019.110542

- Meza-Trujillo, I., Mary, A., Pietrzyk, P., Sojka, Z., Gaigneaux, E.M., Nature and role of Cu(II) species in doped C12A7 catalysts for soot oxidation, *Appl. Catal. B Environ*. 316 (2022) 121604.
  DOI: https://doi.org/10.1016/j.apcatb.2022.121604

Press articles

- Bientôt des pots d'échappement dénués de métaux nobles et de terres rares ?, *Daily. Science*. October 6th, 2022. https://dailyscience.be/06/10/2022/bientot-des-pots-dechappement-denues-de-metaux-nobles-et-de-terres-rares/
- Voiture : bientôt des pots catalytiques sans métaux critiques ?, *Le Vif*. December 4th, 2022. https://www.levif.be/societe/environnement/voiture-bientot-des-pots-catalytiques-sans-metaux-critiques/

Communications

Oral communications

- Isaac Meza-Trujillo, and Eric Gaigneaux. *Exploring the control of C12A7 oxygen species as a catalytic tool*. 9th World Congress on Oxidation Catalysis: Oxidation for a Sustainable Future and Clean Environment (WCOC 2022), Cardiff (United-Kingdom), September 4-8th, 2022.

- Isaac Meza-Trujillo, Arnaud Mary, Piotr Pietrzyk, Zbigniew Sojka, and Eric Gaigneaux. *Nature and role of copper inside Cu-doped mayenite (Cu-C12A7) catalysts for soot oxidation*.11th International Conference on Environmental Catalysis (ICEC 2020), Manchester (United Kingdom), September 6-9th, 2020. (*Held online due to COVID pandemic*)

- Isaac Meza-Trujillo, and Eric M. Gaigneaux. *Regulating the extra-framework oxygen species in C12A7 as a tool to adjust the selectivity of an oxidation process*. 17th International Congress on Catalysis (ICC2020), San Diego (United Stated), June 14-19th, 2020.(*Cancelled due to COVID pandemic*)

- Isaac Meza-Trujillo, and Eric M. Gaigneaux. *Study of mayenite potentialities as an oxidation catalyst: towards an oxidation process with adjustable selectivity by controlling the reactive oxygen species of the material*. Ph.D. student Day 2019 (Ph.D. Day 2019), Louvain-la-Neuve (Belgium), May 29th, 2019.

Poster communications

- Isaac Meza-Trujillo, and Eric M. Gaigneaux, *Improving mayenite (C12A7) textural properties via an assisted solution combustion toward an enhancement of its catalytic performance in soot combustion*, 14th European Congress on Catalysis (EuropaCat 2019), Aachen (Germany), August 18-23rd, 2019.

- Isaac Meza-Trujillo, and Eric M. Gaigneaux. *Production of high surface area mesoporous mayenite (C12A7) via an oxalic acid assisted solution combustion synthesis (SCS)*, 12th International Symposium on the Scientific Bases for the Preparation of Heterogeneous Catalysts (PREPA 2018), Louvain-la-Neuve (Belgium), July 8-12th, 2018

- Isaac Meza-Trujillo, and Eric M. Gaigneaux. *Tuning Textural Properties of a Mesoporous Mayenite (C12A7) Catalyst via a Modified Solution Combustion Synthesis (SCS)*. Ph.D. student Day 2018 (Ph.D. Day 2018), Louvain-la-Neuve (Belgium), May 25th, 2018.

- Isaac Meza-Trujillo, and Eric M. Gaigneaux. *Production of higher surface area mesoporous Mayenite (C12A7) via the solution combustion synthesis (SCS)*. Journée Scientifique of the Société Royale de Chimie, Louvain-la-Neuve (Belgium), October 12th, 2017.